

Measurement and Modeling of Fire Behavior in Leaves
and Sparse Shrubs

Dallan Ronald Prince

A dissertation submitted to the faculty of
Brigham Young University
in partial fulfillment of the requirements for the degree of
Doctor of Philosophy

Thomas H. Fletcher, Chair
David R. Weise
David O. Lignell
Bradley C. Bundy
William G. Pitt

Department of Chemical Engineering

Brigham Young University

July 2014

Copyright © 2014 Dallan Ronald Prince

All Rights Reserved

ABSTRACT

Measurement and Modeling of Fire Behavior in Leaves and Sparse Shrubs

Dallan Ronald Prince
Department of Chemical Engineering, BYU
Doctor of Philosophy

Wildland fuels and fire behavior have been the focus of numerous studies and models which provide operational support to firefighters. However, fuel and fire complexity in live shrubs has resulted in unexpected and sometimes aggressive fire behavior. The combustion of live fuels was studied and modeled, and the results were assimilated into a shrub-scale fire behavior model which assumes fire spread by flame-fuel overlap. Fire spread models have usually assumed that radiation heat transfer is responsible for driving fire spread, but that assumption is a topic of continuing debate, and appears to contradict some experimental observations. A convection-based shrub-scale fire spread model has been developed, building on a heritage of experiments and modeling previously performed at Brigham Young University. This project has (1) characterized fundamental aspects of fire behavior, (2) integrated the resulting submodels of fire behavior into an existing shrub model framework, and (3) produced shrub-scale fire spread experiments and (4) made model comparisons. This research models fire spread as a convection-driven phenomenon and demonstrates strategies for overcoming some of the challenges associated with this novel approach.

Keywords: wildfire, wildland fire, modeling, L-systems, shrub geometry, kinetics, devolatilization, mass release, heat transfer, convection, flame merging, moisture content, live fuels, shrubs, sparse vegetation.

ACKNOWLEDGMENTS

I thank my advisor Tom Fletcher for guiding and motivating me in this research. I am grateful for his mentoring and friendship on both an academic and personal level. I also thank David Weise for taking time to serve on my graduate committee while continuing his responsibilities as a researcher at the USDA Forest Service Pacific Southwest (PSW) Research Station in Riverside, CA. The insights, expertise and resources he contributed were crucial to this project. I thank David Lignell, Bill Pitt and Brad Bundy for serving on my graduate committee and for providing insightful feedback and support.

I thank Wesley Cole and Brandon Andersen for developing a first generation bush fire spread model and orienting me on this project. I thank Wesley Cole and McKaye Dennis for performing wind tunnel burn measurements that were used for model comparison, including a correlation to determine number of leaves from moisture content and shrub mass. These efforts provided a launching point for my work. I also credit Wesley Cole with measuring moisture contents of leaves quenched after precise heating times.

I'm grateful for Joey Chong and Gloria Burke of the Forest Service for collecting and shipping me live plant samples from the California chaparral and for their assistance with fire spread experiments in the wind tunnel at the PSW Research Station.

I thank Marianne Fletcher for developing a chamise fuel placement code under my supervision, for developing the first version of a Utah juniper leaf placement code, and for writing a quality draft for publication. I thank my fellow graduate student Chen Shen for helping me to interpret his measurements of Utah juniper shrubs for a fuel placement code. I'm grateful for Kelsey Wooley for assisting with the 2010 wind tunnel experiments in Riverside, CA, and for her data analysis and write up.

I thank all the undergraduate researchers who assisted with me with this project: McKaye Dennis, Corinne Olsen, Mitch Withers, Kelsey Wooley, Ganesh Bhattari, Jay Liu, Kenneth Alford, Eddie Overy, Amelia Rapp, Merete Capener, Kellen Rowberry, Jared Little, Cory Bowen, Victoria Lansinger, Marianne Fletcher, Kristen Nicholes, Sydney Hansen, and Jenalyn Clegg. Their contributions were an integral part of this project.

I thank my dear wife Carrie, who has provided constant support and optimism during this project. I would also like to thank our daughter Leah for being a beacon of happiness since joining us in 2013. I am grateful for my parents and siblings for their continual friendship and support.

This work was funded in part by the Joint Fire Sciences Program (JFSP) under contracts 11-JV-11272167-044 and 11-JV-11272167-054 and National Science Foundation Grant CBET-0932842. Any opinions, findings, and conclusions or recommendations expressed in this dissertation are those of the graduate student and advisor and do not necessarily reflect the views of the National Science Foundation or any other government funding agency. Neither the NSF nor any other agency has approved or endorsed the content in this dissertation.

TABLE OF CONTENTS

LIST OF TABLES	xi
LIST OF FIGURES	xiii
NOMENCLATURE.....	xxii
1. Introduction.....	1
2. Literature review.....	5
2.1 Heat transfer mechanisms in wildland fires and wildland fire modeling	5
2.2 History of wildland fire modeling	7
2.3 Wildland fire modeling using ignition zones.....	11
2.4 Shrub fuel structure.....	14
2.5 Fire spread in live vegetation.....	17
2.6 Modeling fire characteristics of live vegetation	20
2.7 Devolatilization behavior and models for biomass.....	22
2.8 Role of water in biomass and wildland fire	25
2.9 Merging of multiple flames	27
2.10 Summary	29
3. Objectives and tasks	31
3.1 Objective.....	31
3.2 Tasks	31
4. Evaluation of a semi-empirical multi-leaf fire spread model and comparison to wind tunnel experiments	33
4.1 Methods	34
4.1.1 Single-leaf experiments	34
4.1.2 Shrub-scale wind tunnel experiments.....	37
4.2 Multi-leaf fire spread simulator	40

4.2.1	Fuel element location models	40
4.2.2	Fuel element physical parameters model	42
4.2.3	Fuel element flame behavior model.....	44
4.2.4	Fluid flow model.....	46
4.2.5	Flame-flame interactions model	48
4.3	Model evaluation methods.....	49
4.3.1	Bulk density	49
4.3.2	Modeling shrub-scale wind tunnel experiments	50
4.3.3	Full factorial sensitivity analysis	53
4.4	Results and discussion	53
4.4.1	Effect of bulk density.....	53
4.4.2	Model comparison to shrub-scale wind tunnel experiments.....	55
4.4.1	Full factorial sensitivity analysis	64
4.5	Conclusions.....	68
5.	Detailed fuel placement models for sparse shrubs.....	69
5.1	Methods	70
5.2	Measurements, observations and correlations	71
5.2.1	Description of chamise	71
5.2.2	Description of Utah juniper	74
5.3	Overview of models.....	76
5.3.1	Chamise model.....	76
5.3.2	Utah juniper model	80
5.4	Results and discussion	82
5.4.1	Chamise.....	82
5.4.2	Utah juniper	87

5.5	Summary and conclusion.....	92
6.	Effects of moisture on the combustion behavior of dead versus live foliage	95
6.1	Experimental methods	96
6.1.1	Fuel description.....	96
6.1.2	Experimental apparatus and instrumentation.....	98
6.2	Results.....	99
6.2.1	Heating pattern.....	99
6.2.2	Differences in early temperature distribution	100
6.2.3	Effects of moisture content and moisture history	102
6.2.4	Effects of moisture content on temperature plateaus.....	103
6.2.5	Use of mode as a moisture marker.....	104
6.2.6	Additional evidence of moisture release during the temperature plateau.....	105
6.2.7	Differences in mass release.....	109
6.3	Discussion.....	110
6.4	Summary and conclusions	111
7.	Kinetic modeling of mass release from dead and live foliage	113
7.1	Model formulation	113
7.1.1	Leaf surface temperature.....	114
7.1.2	Internal leaf temperature	116
7.1.3	Composition estimation and component modeling.....	118
7.1.4	Devolatilization models	118
7.1.5	Moisture release models	123
7.1.6	Internal heat and mass transfer considerations	126
7.2	Results and discussion	127
7.2.1	Water release at 100 °C	129

7.2.2	Diffusion-limited water release: conversion-dependent diffusivity	134
7.2.3	Diffusion-limited water release: temperature-dependent diffusivity	137
7.2.4	Arithmetic mean temperature and mean kinetic temperature	143
7.2.5	One-step dry matter mass release	145
7.2.6	Modeled and measured mass release comparison for all runs	147
7.3	Conclusions	150
8.	Improved semi-empirical shrub-scale fire spread model.....	153
8.1	Model overview	155
8.2	Physics-based submodel and flame parameter scaling	156
8.2.1	Physics-based heat transfer and mass release submodel.....	156
8.2.2	Flame parameter scaling	162
8.3	Flame-flame interactions model and flame geometry	163
8.3.1	Flame height.....	163
8.3.1	Flame radius and downward extension.....	166
8.3.2	Flame angle.....	167
8.3.3	Flame-fuel overlap and pseudo-radiation	167
8.4	Miscellaneous model details.....	168
8.5	Wind tunnel simulation cases	168
8.6	Results and discussion	169
8.6.1	Physics-based submodel for scaling flame parameters.....	170
8.6.2	Comparison of improved bush model with wind tunnel experiments	177
8.7	Discussion and conclusions	183
9.	Summary and conclusions.....	185
9.1	Evaluation of first-generation shrub combustion model.....	185
9.2	Detailed fuel placement	185

9.3	Dead versus live leaf combustion measurements	186
9.4	Modeling combustion of live versus dead leaves	187
9.5	Improved shrub combustion model	188
REFERENCES.....		189
Appendix.....		205
A. Fire behavior of shrub-like fuel arrangements in a wind tunnel.....		207
A.1	Methods.....	208
A.1.1	Fuel selection and arrangement.....	208
A.1.2	Experimental apparatus.....	209
A.2	Results and discussion	211
A.2.1	Flame angle	211
A.2.2	Flame length.....	214
A.2.3	Burn time and change in mass	216
A.2.4	Burn temperature.....	219
A.2.5	Preheating effects	220
A.2.6	Rate of spread.....	225
A.2.7	Moisture in unburned leaves.....	227
A.2.8	Seasonal observations	227
A.3	Conclusion	229
B. Radiation correction of thermocouple measurements.....		233
C. Manzanita single-leaf experiments at two temperatures.....		237
D. Leaf clump experiments		241
D.1	Leaf settling of manzanita leaves connected to branches	242
D.2	Heat shielding of upper, interior leaves	244
D.3	Correlating leaf placement to maximum flame height	245

E. Multi-leaf column and plane fire propagation experiments	249
E.1 Single column experiments	249
E.2 Skewed leaf experiments in a plane	252
F. Improved bush model code (MATLAB)	257
G. L-systems fuel placement code for Utah juniper	285
H. L-systems fuel placement code for chamise.....	295

LIST OF TABLES

Table 4-1. Summary of wind tunnel fire spread experiments through simulated manzanita shrubs.....	39
Table 4-2. Summary of wind tunnel fire spread experiments through simulated manzanita shrubs.....	40
Table 4-3. Wind tunnel stream-wise velocity (m/s) measured using a Kestrel 3000. Values in parentheses were estimated. Species are chamise (Ch.) and manzanita (Ma.). Location number correspond to Figure 4-9.	47
Table 4-4. Ignition volume left and top bounds.....	51
Table 4-5. Criteria for fire spread evaluation.....	52
Table 4-6. Factors and coded values used in the full factorial design.	53
Table 4-7. Average, minimum and maximum standard deviation (and relative standard deviation) of t_{burn} , X_s , and $\Delta z_{f,max}$ for each model configuration.	64
Table 5-1. The coefficients for each size class (by diameter) used in Equation 3 for Chamise.	74
Table 5-2. The coefficients for h_{shrub} versus d_{crown} (Equation 5-2). Alternatively, h_{shrub} may be specified directly in the model.	74
Table 5-3. The coefficients for correlations by Shen (2013) and Mason and Hutchings (1967) data used in Equation 5-6. The R^2 for Shen's correlation is based on its fit to individual measurements, while the R^2 for Mason and Hutchings is for its fit to average measurements for all loam soil types.	76
Table 5-4. L-systems rules governing symbol interpretation for Utah juniper according to string location. 'F' length is scaled from the given value to achieve the specified shrub diameter and conical shape.....	82
Table 5-5. L-systems rules governing symbol replacements for Utah juniper. The derivation(s) when each rule is active and its anatomical result are also summarized.....	82
Table 5-6. Measurements of the chamise shrub in Figure 5-5(a) versus the modeled shrub in Figure 5-5(b).....	83
Table 5-7. A comparison of the measurements of the shrub and the modeled shrub shown in Figure 5-11.	88

Table 6-1. Statistics on average leaf temperature distributions after 3 seconds of heating. (*Dispersion is represented by the interquartile range, which is appropriate for lognormal distributions (Shoemaker, 1999)).....	101
Table 6-2. Summary of water content measurements for nitrogen-quenched manzanita leaves of various heating intervals ($m_{w,q}$ = mean mass of moisture at quenching, m_0 = mean initial leaf mass, \pm 95% confidence interval, n = number of measurements).....	109
Table 7-1. Parameters of single-component one step devolatilization models.....	121
Table 7-2. Multicomponent one-step devolatilization parameters (m_i = mass of component or part, m_{dry} = mass of dry matter).....	122
Table 7-3. Summary of modeling results by section	128
Table A-1. Analysis of variance for flame angle vs. species and wind speed.....	212
Table A-2. Average flame angle (θ) vs. wind speed (combining both species).....	212
Table A-3. Flame angle correlations.....	213
Table A-4. Analysis of variance for flame length vs. species and wind speed.....	216
Table A-5. Analysis of variance for burn time vs. species and wind speed	217
Table A-6. Analysis of variance for burn temperature vs. species and wind speed	219
Table B-1. MathCAD calculation.....	234
Table C-1. Gas flow rate settings for standard and low temperature flat flame burner conditions at 300 K.....	237

LIST OF FIGURES

Figure 2-1. Sequence showing the propagation of ignition zones in a multi-leaf shrub model. Horizontal lines are unburned, burning and burned out leaves, indicated by green, blue and black, respectively. Rectangles are ignition zones. (Pickett et al., 2009).	13
Figure 2-2. Comparison of fire path through a dry Christmas tree (left) and through a modeled manzanita shrub (right). Unburned, burning and extinguished leaves are represented in the model results by blue, green and red dots, respectively (Cole et al., 2009).	13
Figure 4-1. Leaves of a Manzanita shrub – Beatrice F. Howitt © California Academy of Sciences (Howitt, 2008).	35
Figure 4-2. The experimental apparatus is shown configured for no wind (left) and wind-blown (right) experiments. A mass balance (A), leaf (B), video camera (C), IR camera (D), flat-flame burner on movable cart (E), square duct with fan and honeycomb mesh (F), and an alligator clip for holding fuel samples (G) are identified.	36
Figure 4-3. Design and dimensions of wind tunnel. Sections, beginning on the left, are: (a) fan; (b) flow conditioner; (c) open-roofed test section with load cell floor panels and fire bricks; and (d) exit Lozano et al. (2010).	37
Figure 4-4. Shrubs just after excelsior ignition but before starting the fan for Riverside 2009 manzanita Runs 1 (top left), 2 (top right), 3 (bottom left), and 4 (bottom right). The striped stick at the left of each image marks 25 cm intervals. Viewed through open doors from the same perspective as Figure 4-9.	38
Figure 4-5. Leaves distributed based on an image of the second shrub shown in Figure 4-4. Each rectangle is a single leaf with a unique length, width and thickness.	42
Figure 4-6. Histogram of the experimental leaf masses (dry) compared to the best-fit beta probability density function (PDF) and its cumulative distribution function (CDF).	43
Figure 4-7. Sample modeled flame height profile for a manzanita leaf.	45
Figure 4-8. Frames showing a single-leaf combustion sequence, including the leaf and flame. At 2 s, the leaf is still preheating, the maximum flame height is reached at about 11 s, and burnout occurs just after 17 s.	46
Figure 4-9. Schematic of wind tunnel indicating wind measurement locations relative to shrub location. Also see Figure 4-4.	47

Figure 4-10. Schematic of the flame coalescence model. Horizontal bars are burning leaves, their original flames are solid-lined rectangles and their overlapping volume is cross-hatched. The added volume is striped and the final adjusted flame boundaries are dashed. Not to scale.....	49
Figure 4-11. Ignition volume defined by left and top bounds. The ignition volume spans the entire y -dimension.....	51
Figure 4-12. Illustration of $\Delta z_{f,max}$ for experiments (left) and the model (right). The shrub area is highlighted with a box in both cases and the flame height is indicated. The largest value of Δz_f for each simulation or experiment was reported as $\Delta z_{f,max}$	52
Figure 4-13. Model predictions of fraction of fuel (leaves) burned versus bulk density at 45% MC (dry basis) and 0 m/s wind for a 30 x 30 x 50 cm shrub. Small dots are individual simulations and open circles are mean values with ± 1 standard deviation error bars.	54
Figure 4-14. $\Delta z_{f,max}$ comparison of model simulations (box plots of minimum, first quartile, median, third quartile and maximum) and wind tunnel experiments (dots).....	56
Figure 4-15. X_s comparison of model simulations (box plots of minimum, first quartile, median, third quartile and maximum) and wind tunnel experiments (dots).....	59
Figure 4-16. Burn time comparison of model simulations (box plots of minimum, first quartile, median, third quartile and maximum) and wind tunnel experiments (dots).....	60
Figure 4-17. Run 1 flame path of the wind tunnel experiment (left) and a model simulation (right) viewed from the side (x - z perspective). Time is represented by color shading. White contours mark 15 s intervals. The dark patterned area is unburned vegetation while the light patterned area was void.....	61
Figure 4-18. Run 2 flame path of the wind tunnel experiment (left) and a model simulation (right) viewed from the side. See figure caption to Figure 4-17.	61
Figure 4-19. Run 3 flame path of the wind tunnel experiment (left) and a model simulation (right) viewed from the side. See figure caption to Figure 4-17.	62
Figure 4-20. Run 4 flame path of the wind tunnel experiment (left) and a model simulation (right) viewed from the side. See figure caption to Figure 4-17.	63
Figure 4-21. Response of t_{burn} , X_s , and $\Delta z_{f,max}$ to n_L , R_c , MC , and U . Each point represents the average of 36 runs. Each legend applies to its entire row.....	65
Figure 5-1. An example of the strings resulting from three derivations and the interpreted geometry. In each derivation, ‘X’ was replaced with ‘F+X-XFX.’ The	

commands replaced in each derivation are shown in a different color. Where included, dots mark the ends of a step.	70
Figure 5-2. A picture of a chamise shrub after the branches have been cut off showing that multiple primary branches emerge from the ground. Arrows point to cut branch ends.	72
Figure 5-3. Measured and modeled distribution of segment thicknesses for chamise.	73
Figure 5-4. An example of a plant with seven primary branches to illustrate how the values of (a) φ and (b) θ evenly divide the three-dimensional space.	78
Figure 5-5. A visual comparison of (a) a chamise shrub (b) and an example of a modeled chamise shrub.	83
Figure 5-6. This graph shows the relationship between crown diameter and the number of primary branches for a chamise shrub.	84
Figure 5-7. Chamise shrubs generated based on crown diameter. (a) 300 cm crown diameter with 98 primary branches, (b) 350 cm crown diameter with 117 branches, (c) 400 cm crown diameter with 139 branches, and (d) 450 cm crown diameter with 166 primary branches.	85
Figure 5-8. Results from the L-systems model compared to the data from Countryman and Philpot for chamise. “Fuel” in the model was defined as all segments with a thickness less than a quarter inch.	85
Figure 5-9. Total predicted and measured shrub mass as a function of crown diameter for chamise.	86
Figure 5-10. Predicted and measured bulk density of chamise as a function of crown diameter for chamise.	87
Figure 5-11. Visual comparison of (a) a Utah juniper shrub and (b) a shrub geometry generated by the L-systems approach having 35 branches.	88
Figure 5-12. (a) A close-up of the Utah juniper shrub and (b) a close-up of a modeled juniper.	89
Figure 5-13. Dry mass data (individual measurements from Shen and mean \pm 2 standard deviations for Mason and Hutching) and dry mass of modeled Utah juniper shrubs using each dry mass correlation for various crown diameters.	90
Figure 5-14. Juniper shrubs generated for three classifications of fuel denseness with 1.0 m diameters and 1.6 m heights: (a) sparse with 76 branches; (b), medium with 106 branches; and (c) dense with 152 branches.	90

Figure 5-15. Utah juniper bulk density data from Shen and bulk density of modeled juniper shrubs using each dry mass correlation (see Equation 5-6) for various crown diameters.....	91
Figure 6-1. Plotted thickness of a dry dead manzanita leaf superimposed on an image of the leaf. The measurement locations are marked and correspond to the plots.	97
Figure 6-2. Schematic of experimental setup. A leaf is held on the tip of a rod extending from a mass balance through a slot cut in the far glass panel. The FFB is pulled under the glass duct and leaf to begin heating. Temperature and flame behavior are recorded with IR and video cameras. The IR is shot through a 1-inch diameter hole in the glass.	99
Figure 6-3. IR thermal images of a fresh live manzanita leaf during heating at 2 s intervals. Temperature maps such as these were averaged with other runs to produce the histograms in Figure 6-4 and Figure 6-5. The bright dot in middle is a metal needle skewering the leaf. The arrows show direction of upward gas flow.....	100
Figure 6-4. Temperature histograms of all the temperature data across the whole leaf face at 3 s of heating, averaging all 18-19 runs for (a) dry dead leaves, (b) rehydrated dead leaves, (c) dehydrated live leaves, and (d) fresh live leaves. Error bars represent 95% CIs on the fraction of leaf area. Fraction of leaf area is determined by pixel counting of the IR images.	102
Figure 6-5. Traces of temperature histograms for all temperature data across the whole leaf at 2 s, 4 s, 6 s and 8 s, averaging all 18-19 runs for (a) dry dead leaves, (b) rehydrated dead leaves, (c) dehydrated live leaves, and (d) fresh live leaves. Each marker represents one histogram bin (see Figure 6-4).	103
Figure 6-6. Mode temperatures averaged for each leaf group. Average values (solid with markers) are bounded by 95% CIs (dotted).....	104
Figure 6-7. The average distribution of leaf surface temperature is plotted vs. time for each leaf group. Temperature distributions are described by the median (filled circle), middle 50% (inner bar), middle 80% (outer dotted bar) and mode (open circle).	105
Figure 6-8. The average distribution of leaf surface temperature is plotted at various stages of conversion for each leaf group. Temperature distributions are described by the median (filled circle), middle 50% (inner bar), middle 80% (outer dotted bar) and mode (open circle).....	106
Figure 6-9. Average mode temperature vs. normalized mass remaining for each leaf group. Average mass (solid with markers) is bounded by point-wise 95% CIs (dotted). Arrows pointing the x-axis indicate the total mass fraction of moisture starting in the leaves for each group.	107

Figure 6-10. Images of rehydrated dead, dehydrated live and fresh live leaves during heating at 2, 6, 8, 10 and 12 seconds. Zooming is adjusted to include relevant flame behavior.	108
Figure 6-11. Average normalized mass remaining for each leaf group vs. time. Average mass (solid with markers) is bounded by point-wise 95% CIs (dotted).	110
Figure 7-1. Schematic of equal-area leaf sections.	115
Figure 7-2. Schematic of finite difference formulation for conduction into a leaf. Compare to Çengel (2007).	117
Figure 7-3. Derivative of fractional water released versus temperature for diffusion equations with conversion-dependent and temperature-dependent diffusivities.	126
Figure 7-4. Locations of top center, center, and bottom center leaf areas on a 20 row by 10 column leaf. 30 rows and 20 columns were used in calculations.	129
Figure 7-5. Modeled (100 °C release) water mass and node temperature of a top center leaf area of fresh live Run 5. Nodes are labeled from 1 (surface temperature boundary condition) to 5 (symmetry node).	130
Figure 7-6. Modeled (100 °C release) water mass and node temperature of a center leaf area of fresh live Run 5. Nodes 1 (surface temperature boundary condition) and 5 (symmetry node) are labeled.	131
Figure 7-7. Modeled (100 °C release) water mass and node temperature of a bottom center leaf area of fresh live Run 5. Nodes 1 (surface temperature boundary condition) and 5 (symmetry node) are labeled.	132
Figure 7-8. Modeled mass release for CPD dry matter release and 100 °C water release compared to measured mass release for fresh live leaf 5.	132
Figure 7-9. Modeled (conversion-dependent diffusivity) water mass and node temperature of a top center leaf area of fresh live Run 5. Nodes 1 (surface temperature boundary condition) and 5 (symmetry node) are labeled.	134
Figure 7-10. Modeled (conversion-dependent diffusivity) water mass and node temperature of a center leaf area of fresh live Run 5. See figure caption to Figure 7-9 for node locations.	135
Figure 7-11. Modeled (conversion-dependent diffusivity) water mass and node temperature of a bottom center leaf area of fresh live Run 5. See figure caption to Figure 7-9 for node locations.	135
Figure 7-12. Modeled mass release for CPD dry matter release and conversion-dependent diffusivity water release compared to measured mass release for fresh live leaf 5.	136

Figure 7-13. Modeled (temperature-dependent diffusivity) water mass and node temperature of a top center leaf area of fresh live Run 5. See figure caption to Figure 7-9 for node locations.....	138
Figure 7-14. Modeled (temperature-dependent diffusivity) water mass and node temperature of a center leaf area of fresh live Run 5. See figure caption to Figure 7-9 for node locations.....	138
Figure 7-15. Modeled (temperature-dependent diffusivity) water mass and node temperature of a bottom center leaf area of fresh live Run 5. See figure caption to Figure 7-9 for node locations.....	139
Figure 7-16. Modeled mass release for CPD dry matter release and temperature-dependent diffusivity water release compared to measured mass release for fresh live leaf 5.	139
Figure 7-17. Modeled mass release for CPD dry matter release and temperature-dependent diffusivity water release compared to measured mass release for rehydrated dead leaf 5.....	140
Figure 7-18. Modeled mass release for CPD dry matter release and temperature-dependent diffusivity water release compared to measured mass release for dehydrated live leaf 5.	141
Figure 7-19. Predicted temperature of local moisture release for leaf number 5 of each group.....	142
Figure 7-20. Predicted temperature of local component mass release averaged for dry, rehydrated, dehydrated and fresh leaves.....	143
Figure 7-21. Modeled mass release for CPD dry matter release and conversion-dependent diffusivity water release calculated at the arithmetic mean leaf temperature compared to measured mass release for fresh live leaf 5.	144
Figure 7-22. Modeled mass release for CPD dry matter release and conversion-dependent diffusivity water release calculated at the mean kinetic temperature of the leaf compared to measured mass release for fresh live leaf 5.	145
Figure 7-23. Modeled minus measured normalized mass remaining for leaf 8 of each leaf group. (S-a = single-component (a), S-b = single-component (b), M = multicomponent.).....	146
Figure 7-24. Modeled mass release for CPD dry matter release and conversion-dependent water release compared to measured mass release averaged for all leaves in each group.....	148
Figure 7-25. Modeled mass release for CPD dry matter release and temperature-dependent diffusivity water release compared to measured mass release averaged for all	

leaves in each group. Separately-measured moisture data are scaled to the same initial value and shown alongside the moisture model results.	149
Figure 7-26. Derivative of normalized mass determined from CPD and temperature-dependent diffusivity water release models averaged for all leaves in each group.	150
Figure 8-1. Comparison of (a) the base case physics-based submodel to (b) mass release calculated from measured leaf temperatures and (c) mass release measurements. The leaf had a moisture content of 63% and the base case physics-based scaling model is divided into its main constituents.	170
Figure 8-2. Leaf temperature profiles for various moisture contents calculated by the physics-based scaling model compared with the average measured temperature of a burning leaf.	171
Figure 8-3. Leaf normalized mass profiles for various moisture contents calculated by the physics-based scaling model.	172
Figure 8-4. Sensitivity of scaling factors for flame parameters to T_{conv}	174
Figure 8-5. Sensitivity of scaling factors for flame parameters to T_{soot}	175
Figure 8-6. Sensitivity of scaling factors for flame parameters to U	176
Figure 8-7. Sensitivity of scaling factors for flame parameters to vertical flame position.	176
Figure 8-8. $\Delta z_{f,max}$ comparison of improved model simulations (box plots of minimum, first quartile, median, third quartile and maximum) and wind tunnel experiments (dots).	178
Figure 8-9. X_s comparison of model simulations (box plots of minimum, first quartile, median, third quartile and maximum) and wind tunnel experiments (dots).	179
Figure 8-10. Burn time comparison of model simulations (box plots of minimum, first quartile, median, third quartile and maximum) and wind tunnel experiments (dots).	180
Figure 8-11. Run 1 flame path of the wind tunnel experiment (left) and a model simulation (right) viewed from the side. Time is represented by color shading. White contours mark 15 s intervals. The dark patterned area is unburned vegetation while the light patterned area was void.	181
Figure 8-12. Run 2 flame path of the wind tunnel experiment (left) and a model simulation (right) viewed from the side. See figure caption to Figure 8-11.	181
Figure 8-13. Run 3 flame path of the wind tunnel experiment (left) and a model simulation (right) viewed from the side. See figure caption to Figure 8-11.	182

Figure 8-14. Run 4 flame path of the wind tunnel experiment (left) and a model simulation (right) viewed from the side. See figure caption to Figure 8-11.	182
Figure A-1. Top view of the setup of an experiment with manzanita and zero wind speed. Note how the v-shaped bed of excelsior is in contact with the branches.	210
Figure A-2. Measured flame angle (degrees from vertical) vs. wind speed.	213
Figure A-3. Flame angle prediction models compared to observed experiments.....	214
Figure A-4. Illustration of method for measurement of flame length and flame angle.	215
Figure A-5. Measured average flame length vs. wind speed.	216
Figure A-6. Burn time of both species vs. wind speed.	217
Figure A-7. Burnout vs. wind speed for both species.....	218
Figure A-8. Average gas and solid burn temperature vs. wind speed.	220
Figure A-9. IR image showing method to measure solid temperature ahead of the flame.....	221
Figure A-10. Temperature of the solids as a function of distance from the location of maximum temperature. (A) Chamise, and (B) Manzanita.	222
Figure A-11. Change in temperature plotted against change in distance in front of the flame front.....	223
Figure A-12. Maximum solid temperature of each area with respect to time for a manzanita shrub combustion experiment with no wind.....	224
Figure A-13. Rate of fire spread as a function of wind speed. The trend line is the fit of all the points for both species.	225
Figure A-14. Manzanita combustion experiment from December 2009, mixing branches with 10% and 30 % moisture content. The flame shown here burned out shortly after this time, leaving the 10% moisture content side of the bush burned and the 30% moisture content side unburned.	229
Figure C-1. Moisture content of leaves sampled between burns, labeled by leaf number. Moisture content is plotted as a fraction (i.e. 1 = 100% MC).	238
Figure C-2. Flame profiles from average flame parameters for standard and low temperature conditions, showing ignition, maximum flame height, and burn out (straight lines between averaged points).	239
Figure D-1. Parent branch as shipped from Riverside, CA and segments resulting from cutting.	242

Figure D-2. Leaves on manzanita branch dip then recoil. Red lines track movement of two leaves.	243
Figure D-3. Voids between branches of manzanita shrub are narrow.	244
Figure D-4. Manzanita branches at 34% moisture content burned above the FFB. Run 1 (a, b, c) had 6 leaves and run 2 (d, e, f) had 59 leaves. Time is given from the beginning of heating.	245
Figure D-5. Example of foliage location mapping for a manzanita branch, showing views at 0° (left) and 90° (right) and omitting 180° and 270°.	246
Figure D-6. Total merged flame height experiments and model, model coefficients fit to set (a) only.	247
Figure E-1. Horizontally-oriented leaves in a vertical column. Left: prior to flame contact. Center: at start of heating (0 s). Right: at burn out (26 s).	250
Figure E-2. Vertically-oriented leaves in a vertical column. From left to right: prior to flame contact, start of flame contact, 20 s of heating, 40 s of heating (1 s before burn out), and after burn out.	251
Figure E-3. Array of needles emerging from an aluminum foil-covered foam board (left: top view; right: perspective).	252
Figure E-4. Ignition of skewered leaf plane Experiment 1 using an alcohol trough.	253
Figure E-5. Skewered leaf plane Experiment 1 after extinguishing (first panel only).	253
Figure E-6. Skewered leaf Experiment 2 with a 1.5 cm gap prior to ignition.	254
Figure E-7. Skewered leaf Experiment 2 at ignition of the alcohol trough.	254
Figure E-8. Skewered leaf Experiment 2 during early burning.	255
Figure E-9. Skewered leaf Experiment 2 showing flame extension below the leaf surface before fire crosses the 1.5 cm gap.	255
Figure E-10. Skewered leaf Experiment 2 showing flame extension below the leaf surface while fire crosses the 1.5 cm gap.	256
Figure E-11. Skewered leaf Experiment 2 after fire is extinguished.	256

NOMENCLATURE

English letter symbols

A	pre-exponential factor
$A_{c,local}$	cross-sectional area normal to the flame axis affected by heat release
A_c	cross-sectional area
A_{face}	two-sided face area of a leaf
B	experimentally determined flame merging constant
c_{w_1}	concentration of water at location 1
c_{w_2}	concentration of water at location 2
$c_{p,dry}$	specific heat of dry leaf mass
$c_{p,gas}$	specific heat of passing gases
$c_{p,water}$	specific heat of water
c_p	specific heat
d	L-systems step length
d_0	L-systems step length for the first derivation
d_{crown}	crown diameter
d_f	downward flame extension (below leaf)
D	width of porous burner
\mathcal{D}_S	drying diffusivity of water in wood
\dot{e}	volumetric energy generation
E	activation energy
g	gravitational constant
h_1	flame height of a solitary flame
h_f	flame height of a leaf
$h_{f,group}$	collective flame height of a group of flames
$h_{f,max}$	maximum flame height
$h_{f,max,0}$	maximum flame height at base conditions (same value as $h_{f,max}$)
$h_{f,max,F}$	maximum flame height at fire spread scenario
\bar{h}_L	average heat convection coefficient for length L
h_{shrub}	shrub height
i	leaf index
i_b	branch number, numbered from lowest to highest vertical position
j	leaf index
k	thermal conductivity
l	leaf length
l_s	fuel segment length
L_1	flame length of a solitary flame
L_f	merged flame length for some flame configuration
L_m	fully-merged flame length (no separation between flames)
LAI	leaf area index
\bar{m}	average mass

$m_{0,w}$	initial mass of water
m_0	initial total leaf mass
m_{dry}	oven-dried mass of a sample
$m_{cat,i}$	fuel mass expected in each size class
m_{dry}	oven-dry mass
m_i	mass of component or part
m_{tot}	total fuel mass
$m_{w,q}$	moisture mass at time of quenching
m_{water}	mass of water remaining in a leaf
MC	Moisture content (oven-dried basis)
n_F	number of 'F' symbols in an L-systems string
n_L	number of leaves
n_b	number of branches
n_{fuels}	number of fuel elements (i.e. leaves)
n_i	L-systems current derivation number
n_w	molar flux of moisture
N	number of flames
N^*	number of flames meeting meeting distance criterion for merging
\overline{Nu}_L	average Nusselt number over length L
P_s	partial pressure of water at leaf surface
P_{vap}	vapor pressure
Pr	Prandtl number
q_{conv}	convective heat transfer (units of power)
q_{evap}	heat of vaporization of water (units of power)
q_{rad}	radiation heat transfer (units of power)
Q_{max}	maximum heat release rate
r_f	flame radius
R	universal gas constant
R_c	flame overlap multiplier used in volumetric flame coalescence model
R_T	thermal flux ratio
Re_L	Reynolds number
S	separation distance (gap width) between flames
\hat{S}	normalized separation between flames in three dimensions
t	time
t_{bo}	burnout time (from start of heating)
t_{burn}	shrub burn time (from first ignition to last extinction)
$t_{end,0}$	end time determined by physics-based model for base condition
$t_{end,F}$	end time determined by physics-based model for fire spread scenario
t_h	time of maximum flame height (from start of heating)
t_{ig}	time of ignition (from start of heating)
$t_{x,0}$	flame times (e.g. t_{ig} or t_h) at base condition, where x indicates ig , h , or bo
$t_{x,F}$	flame times at fire spread scenario
T	temperature
T_{amb}	ambient temperature (i.e. far away from fire activity)

T_{conv}	bulk convective gas temperature
T_{leaf}	leaf temperature
T_{local}	convective gas temperature near the leaf (considers volatile combustion)
$T_{m,k}$	mean kinetic temperature
T_s	temperature at the leaf surface
T_{soot}	radiation temperature of soot
T_{surr}	radiation temperature of surroundings
U	wind speed local to a leaf
U_{bulk}	bulk wind speed
v	convective gas velocity at the leaf surface
$\bar{v}_{U,\theta}$	mean component of wind speed in the flame axis direction
$\bar{v}_{z,\theta}$	mean component of buoyant velocity in the flame axis direction
V	fraction of initial mass released as volatiles
V_∞	ultimate yield of volatiles as fraction of initial mass
w	leaf width
W	fraction of initial mass released as water
X_s	shrub conversion, or amount burned
x	first Cartesian coordinate
y	second Cartesian coordinate
z	third Cartesian coordinate

Greek letter symbols

α	thermal diffusivity, or parameter in beta distribution
β	parameter in beta distribution
δ	angle of secondary branch from primary branch
ΔF_0	fractional change in dry mass of base case
ΔF_F	fractional change in dry mass of new fire condition
ΔH_{comb}	heat of combustion
$\Delta m_{dry,i}$	change in dry mass over time step Δt of component i
Δm_{dry}	change in dry mass over time step Δt
Δm_{water}	mass released of water during Δt
Δx	leaf (or fuel segment) thickness
Δt	time step
$\Delta z_{f,max}$	maximum flame height above shrub
ε	emissivity
γ	specific gravity
κ	flame opacity
λ	length ratio of a secondary branch to its primary branch
Λ	experimentally determined flame merging constant
μ_θ	mean rotational angle (about z-axis) between consecutive branches
φ	branch tilt angle from vertical
φ_h	physics-based scaling factor for flame height
φ_{dist}	random variation of branching angle
φ_{max}	maximum measured primary branch angle

ρ	density
ρ_{conv}	density of convective gases
σ	Boltzmann constant
τ	mesh Fourier number
θ	flame tilt angle (from vertical)
θ_b	branch angle in x-y plane
θ_T	convection coefficient correction factor for blowing
ν	kinematic viscosity

Subscripts

0	refers to an initial state, base case, or reference value
<i>b</i>	refers to the branch of a plant
<i>c</i>	refers to the cross-section
<i>dry</i>	specifies an oven-dried quantity or a dry-matter component
<i>f</i>	refers to a flame
<i>F</i>	refers to a fire scenario case
<i>i</i>	leaf index
<i>j</i>	leaf index
<i>m</i>	indicates that flames are fully-merged
<i>max</i>	indicates a maximum value
<i>w</i>	refers to moisture (or water) component

(The meanings of other subscripts or symbols should be apparent from the context of their use.)

1. INTRODUCTION

The annual area burned in the U.S. has increased from around 2 million acres in the late 1980s to nearly 10 million acres in the early 2010s. Over the same period, annual suppression costs have increased from around half a billion dollars to nearly two billion dollars (National Interagency Fire Center, 2014), and suppression only accounts for a fraction of the total cost of wildland fires. While wildland fires can renew ecosystems and reduce future fire risk, they may also cause unwanted erosion and other detrimental effects (Keeley and Fotheringham, 2003). More importantly, wildland fires pose a hazard to the lives, homes, and property located in their paths, including lives of firefighters who are deployed to protect the public by regulating fire spread.

Modeling fire behavior involves severe challenges. Fire behavior spans enormous scales in space and time, making fire spread modeling an exercise in tradeoffs. For example, the relevant scales for solid reactions (millimeters and milliseconds) differ greatly from the scales of fire spread over a landscape (hundreds of acres and weeks) or the scale of atmospheric effects (thousands of vertical feet). Furthermore, the uncertainty of weather is complicated by the ability of large fires to alter weather. Finally, models must run quickly (e.g. in half an hour) to provide operational utility to fire managers. Fire behavior models seek to model the most critical features of fire spread while necessarily neglecting other aspects to some degree.

Operational fire behavior models help fire managers make decisions about what assets are in danger and where to devote fire-defense resources. Current operational models are based

on an empirical rate of spread, which is a ratio of the source heat flux to the heat required to ignite potential fuel (Rothermel, 1972; Frandsen, 1973). Fuel models are selected based on vegetation type and provide fuel-specific model parameters. Operational models have been formulated for a variety of uses: BehavePlus, FlamMap, FARSITE and FSPro provide predictive capabilities ranging from fire behavior at a point to probability mapping of fire spread over a specific landscape for a range of likely weather scenarios (Burgan and Rothermel, 1984; Finney, 1998, 2002; Andrews, 2007; Andrews, 2008; Finney et al., 2011).

Research is needed to expand and clarify details about the fire spread process for a next-generation model. This is particularly important for fuel types the Rothermel model was not originally designed to describe, especially live shrub fuels. Fire fronts in live fuels can be sustained at higher moisture contents than observed for dead fuels. These live crown fuels produce unpredictable and sometimes aggressive behavior. Recent observations have indicated that convective heating (i.e. flame-fuel overlap) is a necessary, if not the dominant mode of heat transfer controlling fire spread. For example, fire spreading in still air across a bed of excelsior (shredded aspen wood) did not cross a 1 cm gap in bedding if no fuel bridges the gap (personal observation), and flame-fuel overlap was essential to fire spread between columns of excelsior (Finney et al., 2010). Zhou et al. (2007) performed experiments and modeling which indicated that convection played the dominant role in determining fire spread success. Finney et al. (2010) also discussed supporting observations made over the last fifty years.

A semi-empirical, multi-leaf shrub combustion model in two dimensions was proposed by Pickett (2008), based on the measured combustion behavior of fuel elements (i.e. leaves). Pickett modeled fire spread by flame-fuel overlap, meaning that fire spread occurred when 2-D ignition (or flame) zones extending from burning leaves overlapped and ignited other leaves

located within the 2-D shrub domain. The shrub combustion model was extended to three dimensions for a manzanita (*Arctostaphylos glandulosa*) shrub (Cole et al., 2009), modeling the three-dimensional positions of leaves. Ignited leaves produced flame zones which ignited neighboring, unburned fuel elements upon flame-fuel overlap. Overlapping flames were modeled to coalesce by increasing the height of each flame by a multiple of the volume of flame-flame overlap. Downward flame propagation was modeled empirically as a fraction of the upward-extending flame height. Although wind tunnel fire spread experiments in shrubs had been performed for comparison with model simulations, a thorough comparison had not been made and values for adjustable parameters were not yet chosen. This research project commenced by optimizing adjustable parameters for this shrub combustion model and making comparisons of modeled and measured fire spread behavior in shrubs. The effort to optimize shrub model behavior yielded encouraging but unsatisfactory results.

However, this preliminary work to optimize the adjustable parameters of the shrub fire spread model motivated several research initiatives which were pursued as necessary building blocks for an improved multi-leaf fire spread model. These included: (1) accurately representing the complex fuel matrix of shrubs, (2) describing the effects of moisture in dead versus live foliage, (3) physically modeling heat transfer and mass release from leaves, and (4) modeling the interactions of multiple flames.

2. LITERATURE REVIEW

Wildland fires have been studied for decades. Much of this previous research has been directed at developing useful empirical models for operational fire prediction. As such models have matured, fire researchers have increasingly recognized the need to fundamentally understand fire mechanisms, such as heat transfer, ignition, fuel combustion and fluid dynamics. This literature review has therefore been divided into the following pertinent topics: (1) heat transfer mechanisms in wildland fires and wildland fire modeling; (2) history of wildland fire modeling; (3) wildland fire modeling using ignition zones; (4) shrub fuel structure; (5) fire spread in live vegetation; (6) modeling fire characteristics of live vegetation; (7) pyrolysis behavior and models for biomass; (8) water types and behavior in biomass and (9) merging of multiple flames.

2.1 Heat transfer mechanisms in wildland fires and wildland fire modeling

The literature describing heat transfer in wildland fire spread does not promote a single heat transfer mechanism as universally dominant. Rather, authors have suggested different mechanisms for different fire regimes, or even different mechanisms for the same regime. Van Wagner (1967) summarized three likely mechanisms for heat transfer in forest fires: (1) flame-fuel contact, especially for wind-driven fires (Byram et al., 1964; Countryman, 1964); (2) radiation from burning fuel particles (i.e. embers), especially for crib fires (Thomas et al., 1964), pine needle fires in still air (Anderson and Rothermel, 1965), or other fires with low rates of

advance; and (3) radiation from flames, especially for sloped beds or surface fires driven by moderate winds. Van Wagner found that his model, which exemplified mechanism 3, was descriptive of observed behavior but was inadequate to confirm the dominance of mechanism 3.

Anderson (1969) performed still-air experiments, in which he measured radiation heat flux through the bed (i.e. mechanism 2) and from the flame (i.e. mechanism 3), and performed modeling to determine the role of radiant heat transfer in fire spread. Anderson found that between 15% and 40% of the heat required for fire propagation was supplied by radiation, and reasoned that the remainder was supplied by convection (i.e. mechanism 1). As discussed by Frankman et al. (2010) and Weber (1991a), Pagni and Peterson (1973) concluded that at low wind speeds flame radiation dominated, with contributions from both particle radiation and gas phase conduction, and that at higher wind speeds, convection dominated, with contributions from flame radiation. They also concluded that energy absorbed by pyrolysis was negligible, as was heating by turbulent diffusion of flame eddies. Weber (1991b) performed experiments on single strands of shredded wood and suggested that flame convection was responsible for the fire spread in their results, as well as the spread behavior of fires in beds of pine needles, excelsior, and bush fires.

Albini (1985) derived a rigorous model for the radiation-dominated heat transfer case, arguing that radiation dominates for backing, no-wind and some heading fires; for other heading fires, convection could play a larger role. Morandini et al. (2002) suggested that at high wind speeds convection dominates. In discontinuous fuel under no-wind conditions, ignition and fire spread across a gap only occurred after direct flame contact (Finney et al., 2010).

Rothermel (1972) investigated the relative effects of convection and radiation by performing heading, no wind, and backing burns on fine fuel beds. His temperature-time plots of

fuel element and gas temperatures suggest that radiation dominantly preheats fuel in no wind and backing burns, but for a heading fire at 5 mph (2.2 m/s) the fuel is significantly preheated by convection. The fuel and gas temperature spiked in all three cases at about 200 °C, well under the wood pyrolysis temperature (280 °C) reported by Browne (1958), indicating rapid heating by direct flame contact prior to ignition.

Morandini et al. built a model intended to lead to a fast operational model, using radiation as the basic mechanism of heat transfer, but concluded that neglecting convective heat transfer mechanisms results in underestimated fire spread rates for wind speeds over 3 m/s (Morandini et al., 2001; Morandini et al., 2002). Silvani and Morandini (2009) found that at low wind speeds (up to 10 m/s) preheating occurs predominantly through radiant heating, with convection occurring at the flame front; they also suspected that in high-wind, high-intensity fires convection preheats the fuel.

There appears to be some consensus that convective heat transfer likely plays the major role in ignition and fire spread in fires propagating in high wind conditions and in shrub vegetation. For no-wind and low-wind conditions, there is considerable confusion over the dominant mechanism. However, convection-based modeling seems appropriate to predict fire spread in highly wind-driven fires, such as occur in the California chaparral with its seasonal Santa Ana winds.

2.2 History of wildland fire modeling

Urban sprawl has increased the interface between urban and wildland areas (Theobald, 2005), complicating the task of managing U.S. wildlands and increasing the resources needed to suppress fires near residences (Davis, 1990; Spyrtos et al., 2007; Theobald and Romme, 2007). Research dating back to the 1920s has been performed to understand the factors controlling fire

spread in wildland fuels (Weise and Biging, 1997). The study of wildland fire spread encompasses momentum, energy and species transport, fire chemistry, plant chemistry and physiology, topography, and weather. Factors span large time- and length-scales. The breadth and complexity of wildland fire behavior has led to a wide spectrum of modeling approaches.

Weber (1991a) reviewed fire spread models developed through 1990, and Sullivan reviewed fire spread models from 1990 to 2007 (Sullivan, 2009a, b, c). Experiments performed during the 1930s and 1940s led to the first mathematical model which accounted for conduction, convection and radiation (Fons, 1946; Papadopoulos and Pavlidou, 2011). The head of the fire was visualized as a series of successive ignitions where flame propagation speed or rate of spread (ROS) was dictated primarily by the ignition time of the fuel particles and the distance between them (Fons, 1946). The model's predicted ROS agreed with the experimentally measured ROS in beds of ponderosa pine needles over spread rates of 0.25 m/min to 5 m/min. ROS predictions responded to wind velocity, fuel temperature, fuel compactness, fuel size, fuel density, fuel moisture content and bed slope.

Byram (1959) introduced a definition for "fire intensity" as the rate of heat release per unit time per unit length of fire front, regardless of flame depth. Albini (1981) developed a model of the flame of a wildland fire, and presented several derivations that related flame characteristics to the energy release rate of a fire (which included Byram's fireline intensity). Alexander (1982) explained that Byram's fire intensity is directly related to flame size and is strongly correlated to the environmental impact of a wildland fire. He quoted Van Wagner that "fire intensity thus conceived contains about as much information about a fire's behavior as can be crammed into one number" (Alexander, 1982). Nelson (1993) published the first full derivation of Byram's (1959) energy criterion, a dimensionless number representing the ratio of

rates of horizontal kinetic energy flux (due to wind) to the conversion of thermal to kinetic energy in the convection column, both at some height z . It has been used to distinguish wind-driven and plume-driven wildland fires, for explaining blowup fires and atmospheric wind profiles, and for understanding spotting and the transition to crown fire (Nelson, 1993).

Emmons proposed a mathematical fire spread model in 1964, assuming that heat transfer from the flame front to unburned vegetation was primarily by radiation (Morvan, 2011). Frandsen (1971) evaluated fire spread through porous fuels on an energy flux conservation basis; he omitted conduction and convection. Rothermel (1972) developed a model from Frandsen's "strong theoretical base to make its application as wide as possible." Rothermel indirectly accounted for convective heat transfer, to some extent, by including experimentally determined correction factors for wind and slope.

Rothermel's model is now the basis of the National Fire Danger Rating System and the basis of the fire prediction tool BehavePlus (formerly BEHAVE), which is used operationally to predict and respond to wildland fires (Sullivan, 2009b). Sullivan (2009c) summarized 14 simulation models published from 1990 – 2007, nine of which use Rothermel's spread model. Rothermel's model considers the energy source, the energy sink, and the heat flow between the two. ROS is modeled as the ratio of heat flux received by preheating fuel to the energy necessary for the fuel's ignition. The effects of wind, slope and other fuel characteristics were determined experimentally and are expressed in the model.

Rothermel's model relies on fuel models which provide basic details about the fuel (Burgan and Rothermel, 1984; Keane, 2013; Weise and Wright, 2014). Albini (1976) published the original set of 13 fire behavior fuel models, based on vegetation type, like "Chaparral." Dynamic models for two types of chaparral fuel beds and the palmetto-gallberry fuel complex of

the southeastern U.S. were included to recognize changes as live fuel beds grow over time and change seasonally (Rothermel and Philpot, 1973; Hough and Albin, 1978). Scott and Burgan (2005) created a new set of 40 fuel models based on fuel type, like “Heavy Load, Tall Brush.” The new set provides the option for dynamic moisture content (*MC*) modeling of herbaceous vegetation, which classifies vegetation under 30% *MC* (oven-dry basis) to be cured and over 120% *MC* to be fully green. Intermediate moisture contents are handled by proportionally dividing vegetation between cured and green fuel (Burgan and Rothermel, 1984; Finney, 2002; Scott and Burgan, 2005). Moisture content is defined as:

$$MC = \frac{m_0 - m_{dry}}{m_{dry}} \quad (2-1)$$

where *MC* is the moisture content, m_0 is the original mass of the sample and m_{dry} is the oven-dried mass of the sample (see ASTM standard D4442 - 07 (2003)). Experiments on fuels spanning the full range of natural live moisture content provide an understanding of the functional response of fire behavior to moisture content that goes beyond interpolating between the behaviors of fuels at the extremes of live moisture content.

Field scale operational models are used to plan fire suppression response in real time. Therefore, they must simulate fire spread faster than real time but accurately enough to be insightful. Albin (1976) described several sources of inaccuracies in model prediction, but found that operational models are most often limited primarily by modeling vegetation as a uniform, continuous, homogenous single layer. These errors can be addressed by modeling wildland fuels and fire spread more descriptively.

The USDA Forest Service has produced several operational prediction tools based on Rothermel’s fire spread model. BehavePlus models the effects of fuel and the environment on fire behavior at a point and can be used for basic fire planning. FlamMap is similar to

BehavePlus, but maps the fire spread over a particular landscape for constant ambient conditions and can be used for fuel hazard assessment and fuel treatment projects. FARSITE is similar to FlamMap, but weather and moisture change with time; it is used to predict fire growth for ongoing or hypothetical fires (Rothermel, 1972; Van Wagner, 1977; Rothermel, 1991; Nelson, 2000; Finney, 2002; Andrews, 2007; Andrews, 2008; FireModels.org, 2012). Numerous other implementations of Rothermel's fire spread model, such as FireStation, have been developed but will not be described in detail since they are not in current operational use (Lopes et al., 2002). FIRECAST was developed specifically for use in chaparral fuels and has been operationally tested for the state of California (Cohen, 1986). Flame-fuel overlap is not modeled directly in these models, although for some scenarios—including those with live and discontinuous fuels—fire spread is strongly dependent on this effect.

2.3 Wildland fire modeling using ignition zones

Ignition zone fire spread modeling is a unique approach of incorporating combustion experiments on whole, live wildland fuel samples into a shrub-scale fire spread model (Weise et al., 2005; Fletcher et al., 2007; Pickett, 2008; Pickett et al., 2010; Lozano, 2011). Ignition zone modeling approaches wildland fire spread as a series of ignitions, as initially proposed by Fons (1946), and depends on flame-fuel overlap for modeling convection-dominated heating to ignition. Detailed spatial distributions of fuel elements are easily accommodated since individual leaves are modeled.

Aside from ignition zone modeling, a detailed description of the shrub fuel matrix has not been used in semi-empirical fire spread models. However, by doing so, the ignition-zone approach addresses the fire spread modeling weakness described by Albini (1976), that of overly simplified fuel matrix descriptions. This semi-empirical approach is a step in the direction of

developing a more sophisticated fire behavior model for systems such as FARSITE (Finney, 1998), or as a submodel for landscape-scale computational fluid dynamics calculations.

The ignition zone approach was introduced in two dimensions by Pickett et al. (2009) to utilize experimental data on the burning characteristics of individual leaves (Engstrom et al., 2004; Fletcher et al., 2007; Cole et al., 2011). In his model, the flame heights of ignited leaves were based on experimentally-derived correlations for ignition, maximum flame height and burnout events. Experiments to determine flame behavior were based on the burning behavior of leaves in 1000 °C, 10 mol% O₂ post-flame gases (Engstrom et al., 2004; Fletcher et al., 2007; Cole et al., 2011). Flames (following their correlated flame height profiles) propagated through an arrangement of leaves if they contacted unburned leaves for a sufficient amount of time. Once an unburned leaf was bathed in an ignition zone for its time to ignition, it produced an ignition zone which grew and subsided according to its flame height profile, potentially igniting additional leaves. In this way, fire spread was reduced to a geometric problem, with the physics and chemistry empirically embedded in the experimental correlations. Two-dimensional fire spread from Pickett's model is shown in Figure 2-1 at various times after the initial ignition.

Cole et al. (2009) extended the ignition zone model to three dimensions, and compared the modeled burn path through a theoretical rectangular manzanita shrub and the burn path of a dried Christmas tree. Both were ignited near the bottom edge of the fuel matrix and the fire paths were similar (see Figure 2-2). Although the two fuel matrices had different shapes, the results showed encouraging potential to accurately represent fire spread using ignition zones. In a separate set of simulations, modeled burn extent increased from approximately 0% to 100% in response to an increase in leaf (number) density from 0.005 leaves/cm³ to 0.1 leaves/cm³. Modeled leaves had an average length of 3.2 cm and an average width of 1.8 cm.

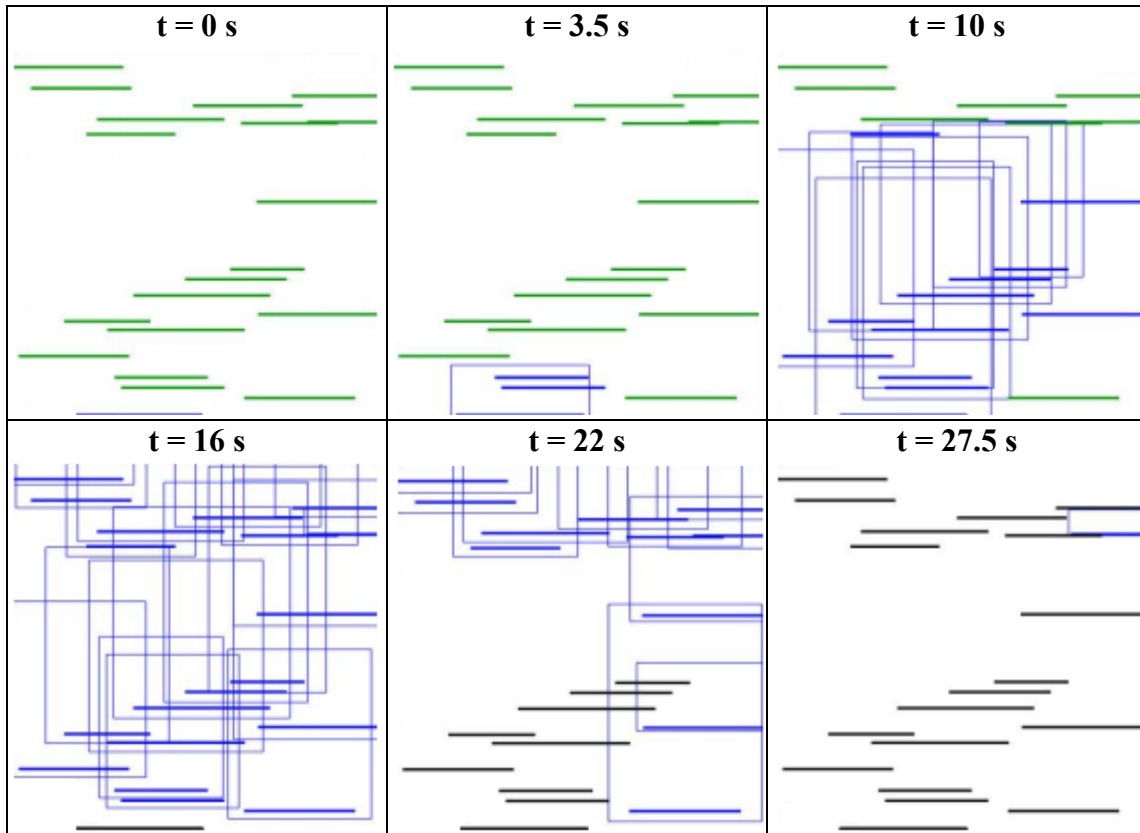


Figure 2-1. Sequence showing the propagation of ignition zones in a multi-leaf shrub model. Horizontal lines are unburned, burning and burned out leaves, indicated by green, blue and black, respectively. Rectangles are ignition zones. (Pickett et al., 2009).

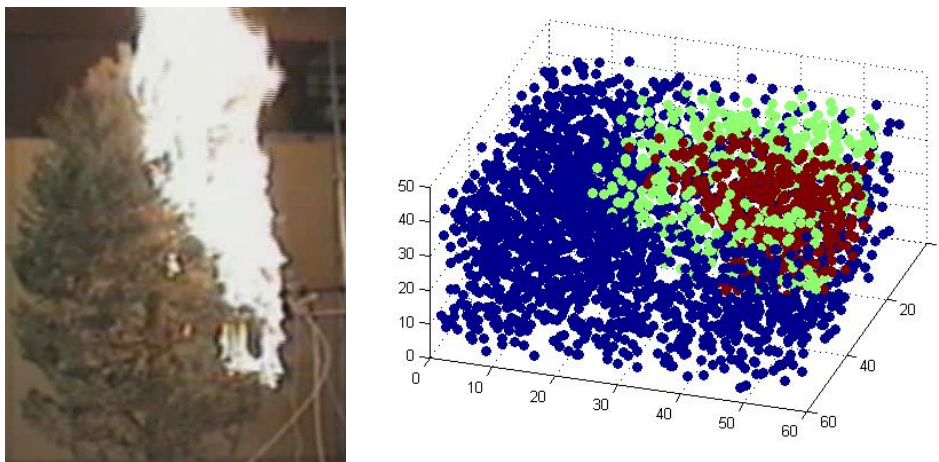


Figure 2-2. Comparison of fire path through a dry Christmas tree (left) and through a modeled manzanita shrub (right). Unburned, burning and extinguished leaves are represented in the model results by blue, green and red dots, respectively (Cole et al., 2009).

The interaction of multiple flames was modeled in three dimensions by augmenting flame heights of overlapping flames by a multiple of the volume of overlap. This creative flame-interaction model relies on calculating the volume of overlapping flames, which is difficult except for rectangular-prism flame shapes, and has limited theoretical basis. Modeling flame interactions based on flame-volume overlap is a natural extension of ignition-zone fire spread modeling, but is incompatible with established methods of estimating flame interactions. These established methods are discussed in a later section, and usually correlate merged flame height with unmerged flame height and fire source proximity.

Ignition zone modeling is well-suited to addressing the fuel complexes of shrubs. Fire spread is modeled in a convection-oriented approach, and fuel geometry can be modeled in detail. Ignition zone modeling presents difficulties associated with calculating the interactions of multiple flame sources, and simplifies the kinetics and heat transfer to a single case (1000 °C and 10 mol% O₂). Ignition zone modeling provides a unique method to examine the effects of three-dimensional fuel placement and convection-dominated ignition. Ignition-zone fire modeling is particularly suited to representing fire spread in live, sparse vegetation. However, model applicability was limited by simplistic fuel location methods, unproven flame merging methods, and single-condition kinetics. Therefore, efforts were pursued to develop fundamental understanding and improved models to describe shrub fuel location, flame merging and the effects of specific fire spread conditions.

2.4 Shrub fuel structure

A portion of wildland fires in the western United States occur in areas with non-continuous groundcover comprised mostly of live shrubs. Current fire spread models used in the United States assume homogeneous fuel (Rothermel, 1972; Finney, 1998; Reinhardt et al., 2003;

Scott and Burgan, 2005; Andrews, 2007) and are based on a semi-empirical surface spread model for dead fuels (Rothermel, 1972) with Van Wagner's crown fire ignition and propagation models (Van Wagner, 1977). However, natural fuel sources are neither completely dead nor homogeneous. Live fuels burn differently than dead fuels (Dimitrakopoulos, 2001; Zhou et al., 2005; Pickett, 2008; Prince and Fletcher, 2013). Heterogeneous fuels have different combustion behavior than homogeneous fuels (Pimont et al., 2009; Parsons et al., 2011), which results in current models consistently underestimating the rate of actual fire spread (Cruz and Alexander, 2010).

Several mechanistic physics-based computational fluid dynamics (CFD) models have been developed (Linn, 1997; Morvan and Dupuy, 2001; Linn et al., 2002; Dupuy and Morvan, 2005; Linn et al., 2005; Mell et al., 2007; Mell et al., 2009) which address fuel heterogeneity. These models have been used to simulate fires at scales as small as single-tree level, (Mell et al., 2009) thereby evaluating the effect of heterogeneity within a single tree (Parsons et al., 2011).

Since CFD models require excessive computational power and time, simpler approaches to describe shrub combustion have been developed. For example, fire spread has been modeled using a semi-empirical, multi-leaf shrub combustion model based on ignition zones in two dimensions (Pickett, 2008) and three dimensions (Cole et al., 2009). In these models, leaves were assigned physical parameters (length, width, thickness, mass and moisture content) to which flame characteristics (ignition time, flame height, time of maximum flame height, and burnout time) were correlated. Physical parameters were drawn from randomly from measured distributions, and leaf placement was randomized. Flame width and flame interactions were also modeled. These characteristics define the flame location of a burning leaf over time. After exposure to another flame for their entire ignition time, leaves were ignited, and then followed a

flame height profile to burn out. Fire propagated when flames from burning leaves overlapped unburned leaves, which ignited, and so on.

These first ignition zone models, while intrinsically possessing the model framework to represent realistic shrub shapes, only distributed leaves within basic rectangular shapes. However, more accurate shrub geometries are needed to take advantage of the capabilities of ignition zone fire spread modeling.

For branching species, such as chamise (*Adenostoma fasciculatum*) and Utah juniper (*Juniperus osteosperma*), fuel is highly concentrated along the branching structure, so matching the stem structure is necessary for accurate modeling. Furthermore, the complexity of spatial distribution within plants (Busing and Mailly, 2004) warrants the use of methods that provide more detail of the branching structure. There are many ways to simulate plant architecture (Godin, 2000), but fractal theory is particularly useful due to its simplicity and applicability. A branching shrub defined by fractal theory provides locations and some physical description for fuel segments, which can be used with correlations for the flame characteristics to model fire spread in, for example, an ignition zone fire spread model.

Plants have been shown to follow fractal patterns (Alados et al., 1999; Godin et al., 2004), and fractals have been used to represent several aspects of plant geometry, including tree crowns (Berezovskaya et al., 1997), leaf and branch properties (van Noordwijk and Mulia, 2002), roots (Fitter and Stickland, 1992; Ozier-Lafontaine et al., 1999; Richardson and Dohna, 2003), and entire plants (Yang and Midmore, 2009). Lindenmayer-systems (L-systems), one method of applying fractals to plant structures, provides a simple way to generate and visualize a self-similar plant (Prusinkiewicz and Lindenmayer, 1990). L-systems are simple enough that they can be used to simulate plant structure effectively without requiring an extensive

background in plant physiology (Renton et al., 2005). The versatility of the approach enables it to be used for many different processes (Prusinkiewicz, 1997, 1998) such as modeling biomechanics in plant structure (Jirasek et al., 2000), simulating carbohydrates and carbon-allocation within trees (Allen et al., 2005), and transforming hand-drawn sketches into computer-simulated plants (Sun et al., 2008; Anastacio et al., 2009). Several models use L-systems along with other methods to model plant architecture (Salemaa and Sievänen, 2002; Renton et al., 2005; Pradal et al., 2009).

L-systems models of shrubs are promising to improve fuel element locations in ignition zone modeling (Pickett, 2008; Cole et al., 2009), but custom models for shrub species have not previously been developed and integrated into the ignition zone fire spread model, though similar fuel-placement models have been integrated into CFD models (Parsons, 2007; Parsons et al., 2011).

2.5 Fire spread in live vegetation

The burning behavior of live fuels clearly differs from that of dead fuels. Fire spread is sustainable at higher fuel moisture contents in live fuels than in dead fuels, but the fundamental reasons for this are not well understood (Finney et al., 2012). Studies have examined the ignition times, rates of fire spread, moistures of extinction, and the fuel temperature histories of both dead and live fuels in a variety of conditions (Catchpole et al., 1998; Dimitrakopoulos and Papaioannou, 2001; Weise et al., 2005; Fletcher et al., 2007; Pickett, 2008; Dimitrakopoulos et al., 2010; Pickett et al., 2010). However, a detailed study of the temperature distribution and mass history of single live and dead leaves near the same moisture content in a wildland fire condition has not previously been performed.

Live fuel moisture content in chaparral fuels has a strong influence on fire behavior (Countryman and Dean, 1979), though the exact mechanism by which moisture affects fire behavior is not well understood. Finney et al. (2012) proposed several ways that fire spread in live vegetation is not explained by current modeling and theory, including: (a) the ability of live fuels to sustain fire spread at higher moisture contents than is possible in dead fuel beds and (b) upon preheating, water is released from live fuels due to structural failure, rather than by diffusion as in dead fuels. Although the moisture of extinction (i.e. the moisture content at which a fire will not spread continuously) is usually between 12% and 30% MC (dry basis) for dead fuels (Burgan and Rothermel, 1984), Dimitrakopoulos and Papaioannou (2001) have measured moistures of extinction as high as 140% moisture content in live foliage.

The existence of an optimal porosity for maximum burning rate and tallest flames has been noted by Anderson (Anderson, 1969), and may contribute to the phenomenon of fire spread in live fuels at high moisture contents. The porosity of forest litter is well below optimum, but live shrubs, which have a much higher porosity, may burn more easily due to more efficient oxygen penetration and heat transfer.

While many experiments have been performed on dead vegetation, experiments on live vegetation have been comparatively less extensive. The fiber saturation point is about 35 wt% moisture content for most dead plant fuels (Cheney, 1981). Moisture contents higher than the fiber saturation point in dead fuels only occur when water condenses inside cells (Dimitrakopoulos et al., 2010). Dead fuel moisture content responds quickly (e.g. hours) and predictably to environmental factors while live fuel moisture content is actively regulated by the plant and is frequently discussed on a seasonal timeframe (Nelson, 2001).

Catchpole et al. (1998) performed 357 packed-bed experimental fires (with moisture content between 2% and 33%) in a large wind tunnel under a wide range of conditions to determine rate of spread dependency on fuel parameters. They found that the rate of fire spread decreased with the square root of the packing ratio. They concluded that more theoretical and experimental work would be required to model live fuel and fuel with mixed size classes in a structured bed (Catchpole et al., 1998) as is the case for live sparse shrubs.

Cheney and Gould (1995) found that grass fires in the open field and in forest understory required a wide fire head width to reach a quasi-steady rate of spread. In grass fires, the head width required to reach quasi-steady state varied with wind speed: 150 m of fire head was required at a wind speed of 5.8 m/s; 75 m for 3.9 m/s; and 14 m for 1.9 m/s (Finney and McAllister, 2011). The width needed to achieve landscape-scale spread rates is not likely achieved in wind tunnels or laboratory conditions, especially the larger widths required at higher wind speeds (Cheney and Gould, 1995). Wildland fires are expected to require an adequate burn path to reach a quasi-steady spread rate as demonstrated in wind tunnel experiments, which share common trends with wildland fires (Marino et al., 2008). Though these and other data provide important insight to fire spread in general, the burning behavior of live fuels differs from that of dead fuels and requires dedicated study.

Live fuel moisture content strongly influences the extent of wildland fire spread. Historical data from the Los Angeles region indicate that the area burned per fire dramatically increases once the live fuel moisture falls under 79% (Dennison and Moritz, 2009). In the Santa Monica Mountains of southern California, Dennison et al. (2008) found that large fires only occur when the live moisture content is below 77%, that most fires occur when the moisture

content is under 71%, and that rainfall timing significantly affects when these thresholds are reached.

The contribution of large diameter woody matter to the ROS of shrub fires is small since foliage is more ignitable and often carries the fire forward. Small diameter twigs (diameter less than a quarter inch, or 6.4 mm) may contribute significantly to fire spread. Costa et al. (1991) measured trunk temperature profiles during ground fires, providing an understanding of heat transfer to woody biomass. Dietenberger (2002) measured the net heat of combustion and derived a kinetic mechanism for Douglas-fir wood volatilization. For different plant species, including chamise, Mardini and Lavine (1993-1994) measured how time to ignition and weight loss of the wood varied with time of year. These properties are important in determining which parts of a plant contribute to fire spread.

Further experimental and theoretical work is needed to understand the burning behavior of live fuels. The role of moisture in fire spread is of particular interest in live fuels, especially with regards to how it may influence fire behavior differently than would be expected based on fire behavior measurements made in dead fuels. Modeling and experiments at a variety of scales are important to understanding fire spread (Weise, 2004) and are needed to build a more fundamental understanding of fire spread in live shrubs.

2.6 Modeling fire characteristics of live vegetation

The burning characteristics of live vegetation differ from those of cured vegetation, and result in modeling complexities which are not encountered in modeling cured vegetation. The “interaction among landscape structure, fuels, and moisture limits the ability of models to predict fire spread, and the fine-grain nature of fuels leads to potentially large errors” (Keeley and Fotheringham, 2003).

Buoyant diffusion flames from beds of oven-dried fuels validated the two-fifths power law, $h_{f,max} = 0.2 Q_{max}^{2/5}$, where $h_{f,max}$ (m) is the maximum flame height and Q_{max} (kW) is the maximum heat release rate (Sun et al., 2006). Q_{max} is usually calculated as the product of the maximum mass loss rate and the heat of combustion. For live fuels, however, the two-fifths power law only holds if the maximum heat release rate was determined from the mass loss rate at maximum flame height rather than from the maximum mass loss rate (Sun et al., 2006).

BehavePlus is a fire modeling system commonly used to predict the spread of wildland fire; it is an extension and improvement of its predecessor, BEHAVE, which incorporates the Rothermel surface fire spread model (Andrews, 2007). When compared to several prescribed fires, five different fuel models all underestimated the ROS (Stephens et al., 2008). Stephens et al. (2008) also found that the chaparral was especially sensitive to varying wind speed and that flame lengths were underestimated by the models by 50% or more. Discrepancies were attributed “to both the difficulties in estimating fire behavior and inadequacy of the models to predict the dynamic nature of fire in live fuels” (Stephens et al., 2008). BEHAVE, as well as two other models, were used in Europe to model prescribed burns and all three underestimated the actual fire spread behavior (Fernandes et al., 2002).

Dimitrakopoulos and Papaioannou (2001) regressed linear models to relate time-to-ignition and moisture content for 24 Mediterranean species. Dimitrakopoulos et al. (2010) and Marino et al. (2011) fit models relating ignition probability and moisture content. FARSITE has produced reasonable simulations of fire spread in drought-season live brush but only after extensive calibration of a custom fuel model (Arca et al., 2007). Procedures for calibrating fire behavior predictions were described by Rothermel and Rinehart (1983).

A classification tree analysis indicated that wind speed has an effect on ignition probability for grass fuels only at moisture contents above 30 wt% (Dimitrakopoulos et al., 2010). High wind increases the effect of convective heat transfer, which helps fire to spread at higher moisture content (Zhou et al., 2005). Weise and Biging (1997) also demonstrated this in stick fuel beds with 35% MC. Directly modeling convective heat transfer may be essential to capture these effects and to correctly predict fire spread in live vegetation.

Wildland fire modeling can be improved by understanding how the composition of vegetation and burning rate impact flame characteristics. Burning crushed vegetation demonstrated that mass burning rate mainly controls flame height, although the composition of the pyrolysis gases can shift the reaction zone and change the flame height (Tihay et al., 2009). The steps and products for the pyrolysis of cellulose, beginning at a temperature of 475 K, have been measured (accounting for nearly 90% of the cellulosic carbon) and the reaction has been fit to two kinetic models (Lin et al., 2009). Lin *et al.* (2009) concluded that the intrinsic kinetics for cellulose pyrolysis did not depend on heating rate. Browne (1958) gave the steps and products of the pyrolysis of cellulose, hemicellulose and lignin and the effects of heating rate on pyrolysis gas composition. Work to understand pyrolysis products as a function of temperature, heating rate, and fuel type can be combined with modeling work to predict flaming or glowing ignition (Mardini et al., 1989).

2.7 Devolatilization behavior and models for biomass

Primary pyrolysis is the process by which solid fuel, upon heating, thermally degrades and releases combustible gases. This occurs as bonds break and volatile fragments are freed from the bulk molecular matrix. Though this process encompasses innumerable unique reactions,

kinetic models summarize the reactions with simplified mechanisms, which may be as simple as a first order Arrhenius expression.

Kinetic models for primary pyrolysis have been used sparsely in fire spread modeling. More frequently, studies on the kinetic behavior of forest fuels are limited to the determination of the chemistry and kinetics of drying and thermal degradation (Leoni et al., 2001; Grishin et al., 2003; Leoni et al., 2003; Korobeinicheva et al., 2013). Grishin (1983), however, incorporated first order Arrhenius kinetics for pyrolysis and combustion, coupled with an energy balance and a model for turbulent eddy diffusivity, in order to model wind-blown forest fire. Pagni and Peterson (1973) considered the thermal effects of pyrolysis but assumed infinitely fast kinetics. In addition, Weber (1991a) noted the potential of kinetic models in wildland fire modeling (to determine fire build-up, the extinction of fire spread, etc.) and encouraged their development. The option to model primary pyrolysis kinetics has been provided in at least one CFD fire spread model, the Fire Dynamics Simulator (FDS) (McGrattan et al., 2010), but is not common in simpler fire spread models such as are used operationally for fire suppression planning.

The energy and fuels community has extensively modeled the devolatilization of industrial fuels, and biomass has experienced a growing focus as an industrial fuel. Kinetic primary pyrolysis models of wood include one-component mechanisms, multi-component mechanisms, and distributed activation energy (DAE) models (Di Blasi, 2008). For large particles, mass and energy transport models have been demonstrated (Miller and Bellan, 1996; Di Blasi, 2008). Most models for wood and biomass consider wood either as a single material or as a combination of cellulose, hemicellulose and lignin. Extractive content, if considered at all, is typically included with hemicellulose, although it has also been treated independently (Biagini and Tognotti, 2014).

Decomposition temperatures for the major constituents of wood are: 598-648 K (cellulose), 498-598 K (hemicellulose), and 523-773 K (lignin) (Di Blasi, 2008). Although independent studies may result in slightly different ranges, they are usually similar, for example: 567-664 K (cellulose), 517-597 K (hemicellulose), and 470-926 K (lignin) (Biagini and Tognotti, 2014). Thermogravimetric analysis (TGA) is a technique frequently used to determine biomass pyrolysis kinetics, but is typically limited to slower heating rates than are experienced in wildland fires or industrial boilers. Because the reactions occur at higher temperatures for faster heating rates (e.g., wood degradation begins at 573 K instead of 500 K at faster heating rates), attempts have been made to derive kinetic parameters at more industrially applicable heating rates (Di Blasi and Branca, 2001). For this purpose, other reactors than TGA have occasionally been used to collect kinetic data for industrial application. Heating rates ranging from 18 K/s to 720 K/s have been measured in crown fires (Butler et al., 2004).

In structure-based devolatilization models, fuel structure is modeled and used to determine when fragments are freed from the macromolecular network. The Chemical Percolation Devolatilization (CPD) model is an advanced devolatilization model which (1) uses kinetic expressions to describe bond breakage and formation, (2) models molecular connectivity and break up, and (3) uses flash vaporization to determine when finite molecular segments freed from the macromolecular network enter the gas phase. CPD parameters have been determined for biomass constituents based on high heating rate experiments (Fletcher et al., 1992; Fletcher et al., 2012; Lewis and Fletcher, 2013).

Anderson (1969) measured and averaged the temperature of the combustion zone of burning fuel beds of ponderosa pine (867 °C), western white pine (779 °C) and lodgepole pine (811 °C). He also found that from 3% MC to 22% MC, the combustion zone temperature fell by

an average of 211°C. Ferguson et al. (2013) modeled the effect of moisture fraction on the combustion of pyrolysis gases, indicating that within the flammable range, moisture caused a decrease in flame temperature of up to several hundred degrees Celsius and a reduction in flame speed of several times. Grishin (1997) reported crown fire temperatures of approximately 800 °C (Butler et al., 2004). Cruz et al. (2011) reported peak flame temperature measurements of 927 °C to 1027 °C for shrubland burn experiments with flame heights higher than 3 m, and of 477 °C to 727 °C for burn experiments with flame heights lower than 2 m.

Although the ignition zone modeling was introduced with a fixed wildland fire condition of 1000 °C and 10 mol% O₂, a reliable fire model clearly must be able to respond to a variety of heating scenarios. Ignition zone modeling must incorporate a dependence on the kinetic behavior of burning fuels in order to represent more than the narrow range of experimental conditions which form the basis for combustion behavior in the ignition zone model.

2.8 Role of water in biomass and wildland fire

Fine wildland fuels are critical to fire spread and consist of foliage and fine branches. Moisture can account for a major portion of biomass in live fuels (up to two-thirds the total mass of foliage). Moisture slows heating and lowers flame temperature (Anderson, 1969). Water relations in wood have been studied in detail, owing mostly to the importance of wood as a building material. Plant foliage has been studied in less detail, but knowledge of water relations in wood provides a first estimate for water relations in foliage where direct study of foliage is lacking.

The living portion of a plant cell, the protoplast, is enclosed in a cell wall, which provides structure and protection from bursting (Wiedenhoft, 2010). Cell walls are composed of cellulose, hemicellulose, lignin and adsorbed moisture. In most mature wood cells, the

protoplasts are removed, leaving behind void spaces, called lumina, which conduct liquid or are simply filled with gas (Wiedenhoef, 2010). No mention of cellular voiding in leaves (i.e. protoplast removal during maturation) has been found in the literature. Indeed, leaves are composed of cells which are engaged in photosynthesis and gas exchange and therefore require the special function provided by living cells. A thorough review of water relations in forest fuels was presented by Nelson (2001).

While burning live fuels, Pickett (2008) observed temperature plateaus indicative of evaporation at mean leaf temperatures of 140 °C and 200 °C, and suggested the elevated boiling point of water solutions as a possible explanation for the plateau at 140 °C. This is supported by a measured elevated boiling point of 140 °C for 95% concentrated sucrose-water solutions at 100 kPa (Ozdemir and Pehlivan, 2008). An alternate explanation for the temperature plateaus in live leaves observed by Pickett at 200 °C may be related to elevated internal pressures. Carpita (1985) used a gas decompression technique to pressurize cells and then measured the fractions of intact cells at various pressures, observing that plant cells burst at elevated pressures. Under the high heat flux conditions of a fire, live leaves may close stoma, which would inhibit mass transfer of moisture, which could increase internal pressure and allow water to reach temperatures above its normal boiling point without evaporating.

In dead fuels, water is bound in cell walls to the hygroscopic constituents: cellulose and hemicellulose. Moisture content in cured biomass responds quickly to relative humidity. At 100% relative humidity, biomass approaches its fiber saturation point, which is usually between 30% to 35% MC. Moisture contents higher than 35% occur in dead biomass only when liquid water on the leaf surface is absorbed into cell cavities (e.g. from rain or dew) (Viney, 1991; Catchpole et al., 2001). Lignocellulosic materials have been described as a composite, forming a

transient microcapillary network in which water can occur as either monolayer water (closely associated with OH groups) or polylayer water (more loosely associated with OH groups) (Hill et al., 2009; Hill et al., 2010; Hill et al., 2012). Though moisture in dead fuels is typically adsorbed to cell walls rather than being held within a cell membrane, elevated pressures may still develop during heating as moisture diffuses through cell walls.

The behavior of water during the heating of live and dead leaves may depend on how the water is held within the leaves. Experiments and modeling are needed to better understand the role of water during heating, how it is released, and how its presence affects combustion behavior.

2.9 Merging of multiple flames

Fire spread models lack adequate models to describe how distinct wildland fires merge into mass fire; and ignition zone wildland fire models lack an adequate model to describe how flames from individual leaves combine. On the landscape scale, flame merging science supports firefighter safety by finding conditions when multiple fires may blow up and merge into a large and dangerous fire. CFD and experiments of flame merging between grids of fire sources show that flame merging and whirling occur resulting from the size of the array, separation distance between fire sources, heat release rate and wind speed (Sato et al., 2007).

Fires arranged in two-dimensional grids follow reproducible trends. Merged flame heights are a function of separation distance (i.e. gap between fire sources), with fully merged flames reaching heights up to 41% higher than unmerged flames (Baldwin, 1968). Kamikawa *et al.* (2005) studied the effects of heat release rate and separation distance on flame height for arrays of porous propane burners and wood cribs, finding that within a certain separation distance the merged flame height was the same as if there were no separation between fire

sources. Sugawa and Takahashi (1993) did similar work with circular pool fires and showed that a fire placed next to an adiabatic wall responds as if it was next to a self-identical fire. Dahm (2007) determined scaling relations for flare fields (both for individual flames and planar merged flames), providing insight into the merging behavior of turbulent flames. Thomas (1963) provided scaling relations and a dimensional analysis to determine conditions for mass merged fires. The Fire Dynamics Simulator (FDS), a CFD program, was used to simulate several flame merging experiments for square fuel arrays and asymmetrical fuel arrangements at a variety of separation distances, and accurately predicted the flame merging behavior (Weng et al., 2004). Fully physical models have been used to model the interactions between two converging fire fronts (one heading and one backing) with reasonable results, though further work was desired to investigate the accuracy of the predictions (Morvan et al., 2011).

Little has been done to examine the merging of vertically-spaced, solid fuel sources. Pickett (2008) performed experiments using a two-leaf arrangement with one leaf at 4 cm and another at 6.5 cm above a flat-flame burner. The higher leaf tended to show a delayed ignition time and shortened flame duration, although the reasons for this behavior were only speculated.

Finney and McAllister (2011) discussed the mechanisms at work in various merging regimes and reviewed the literature on fire merging, but found no unifying method to describe flame merging behavior or the conditions needed to produce a fire with mass fire characteristics. Although flame merging in two-dimensional arrays has been studied, flame merging in 3-D arrangements requires further study in order to be of use in a heterogeneous fuel structure, such as in a shrub.

2.10 Summary

Radiation and convection are complementary heat transfer mechanisms in wildland fires, but the relative importance of each mechanism in fire spread has been debated for decades. However, fire spread models have generally taken a radiation-oriented form and use fuel descriptors which are most suitable for simple fuel structures such as grasses and ground litter. Crown fire spread in shrubs and trees has remained a danger to firefighters and a challenge to fire modelers. Accompanying the complexity of crown fuel matrices is a heightened complexity of fire behavior. This project develops and demonstrates a fire spread model for live, sparse vegetation, including detailed models of fuel placement. Flame behavior is treated on a fuel element basis and includes modeling that governs flame coalescence, the effect of heating conditions, and the effects of moisture. Convection by flame-fuel overlap is a major heat transfer mechanism in destructive wildland fires and is modeled directly in the multi-leaf semi-empirical shrub-scale fire spread model. The results of this work include expanded understanding of fuel structure, fuel behavior, and an improved fire behavior model for eventual integration into operational fire models or as a sub-grid model for landscape-scale computational fluid dynamics (CFD) models.

3. OBJECTIVES AND TASKS

3.1 Objective

The objective of this research was to increase the understanding of fire spread in live, sparse shrubs by the measurement and modeling of fire behavior.

Much of this research has stemmed from initial work to characterize a novel shrub fire spread model which treated propagation as a series of ignitions through distinct fuel elements, driven by flame-fuel overlap. Specific aspects of fire behavior were then addressed, and finally, applicable results were integrated into an improved shrub fire spread model.

3.2 Tasks

This objective was reached by completing the following tasks. For convenience, the chapter number is listed in parenthesis to indicate where each task is discussed.

- Evaluate the semi-empirical shrub fire spread model performance (4).
- Develop detailed fuel placement models for sparse shrubs (5).
- Measure the effects of moisture on the combustion behavior of dead and live foliage (6).
- Kinetically model mass release from burning dead and live foliage (7).
- Improve and evaluate the semi-empirical shrub fire spread model (8).

The work leading up to and presented in Chapter 4 on a novel fire spread model motivated the subsequent chapters. The models developed in Chapter 5 for select plant species provided fuel placement submodels for the semi-empirical fire spread model. The measurements

and modeling of mass release from dead and live leaves discussed in Chapters 6 and 7 provided a foundation for a physics-based submodel which accounted for the effects of heating condition (see Chapter 8). Finally, Chapter 8 discusses the improved shrub fire spread model, including a new flame merging submodel.

4. EVALUATION OF A SEMI-EMPIRICAL MULTI-LEAF FIRE SPREAD MODEL AND COMPARISON TO WIND TUNNEL EXPERIMENTS

Wildland fire models serve many purposes, such as providing insights about fire behavior and decision support for firefighters. Models range in complexity from highly empirical operational models to complex physical models. The spatial distribution of live fuels is typically complex, and although leaf-scale fuel placement potentially impacts bulk fire behavior, a detailed treatment of fuel structure is typically considered outside the scope of empirical and semi-empirical models. Physical and semi-physical models often provide some detail about the fuel, especially related to fluid dynamics. However, the behavior of leaf-scale fuel elements—including their locations, flaming behavior, and the interactions between flames—has generally been neglected by both classes of models.

The semi-empirical fire spread model presented in this chapter describes leaf-scale fuel elements, following an approach first described by Pickett (2008). For the manzanita shrub, each fuel element represents a single manzanita leaf, and specific leaf locations are defined to represent a manzanita shrub. Fuel element physical parameters are assigned to represent the distribution of leaf measurements collected for manzanita. Flame behavior is correlated to physical parameters, based on fundamental whole-leaf combustion experiments performed on hundreds of manzanita leaves of varying freshness and moisture content. A fire spread simulation begins when one or more fuel elements are ignited, producing flames. The fire propagates through the shrub when the flames of burning leaves engulf neighboring leaves,

which in turn ignite according to their experimentally correlated ignition times. Neighboring flames interact synergistically. Convective heat transfer mechanisms are assumed and embedded in the model due to the nature of the experiments and the representation of flames and fuel in the model.

This modeling approach provides a novel framework to study the effects of fuel placement, heat transfer mechanism, ignition mechanism, flame coalescence, moisture content, wind, and kinetic behavior for shrub-scale fuel arrangements. Sensitivity to moisture content, bulk density, fuel placement and wind is presented in this chapter. Model behavior is compared to fire spread experiments which were performed with several shrubs reconstructed in a wind tunnel from cut branches. Inadequacies in model behavior motivated investigations which are presented in the following chapters, and ultimately resulted in a revised version of the fire spread model which is presented in Chapter 8.

4.1 Methods

Combustion experiments on individual leaves in a well-characterized burner were used to determine leaf and flame characteristics. A regression analysis yielded equations that model the physical parameters and flame behavior of individual leaves. Fire spread through shrubs ignited in a wind tunnel was measured for model comparison.

4.1.1 Single-leaf experiments

The semi-empirical, multi-leaf model was developed using leaves from Eastwood's manzanita (*Arctostaphylos glandulosa*) (see Figure 4-1). Manzanita is common in the chaparral of California and is a major fuel in wildland fires. Depending on time of year and amount of

rainfall, manzanita moisture content MC (oven dry basis) ranges from 45% to over 100% (Fletcher et al., 2007).



Figure 4-1. Leaves of a Manzanita shrub – Beatrice F. Howitt © California Academy of Sciences (Howitt, 2008).

The experimental apparatus used to collect data for this model has previously been described by Fletcher et al. (2007), Smith (2005), and Pickett (2008). The fuel sample (i.e. the manzanita leaf) was suspended horizontally in the air by attaching it to a horizontal rod that connects to a mass balance (see Figure 4-2). A flat-flame burner (FFB) on a cart was pulled by a motor and pulley, coming to a stop directly under the leaf. The distance between the FFB (in its stationary position) and the leaf is 5 cm, at which distance the gas temperature is 987 ± 12 °C, with 10 mol% O_2 in the post-flame gases. The hot gases heated the leaf convectively with negligible radiative heating. Radiation from the burner was minimized because the FFB gases burned without producing soot and the FFB remained relatively cool.



Figure 4-2. The experimental apparatus is shown configured for no wind (left) and wind-blown (right) experiments. A mass balance (A), leaf (B), video camera (C), IR camera (D), flat-flame burner on movable cart (E), square duct with fan and honeycomb mesh (F), and an alligator clip for holding fuel samples (G) are identified.

Video images were recorded at 18 Hz by a Sony CCD-TRV138 camcorder. Temperature data were collected by a FLIR A20M IR camera at 7.5 Hz. Mass data were collected by a Mettler Toledo XS204 analytical mass balance, also at 18 Hz. All video, IR, and mass data were time-stamped in order to synchronize the data. Moisture content was determined by a CompuTrac MAX1000 moisture analyzer and was reported on a dry mass basis. Moisture contents of representative unburned leaves were determined at the beginning and end of each experiment, and the two values were averaged together to provide the moisture content for the run.

Physical and combustion characteristics of each leaf were measured. Measured physical characteristics were width (w , in cm), length (l , in cm) and thickness (Δx , in mm). Measured combustion characteristics were (a) time to ignition (t_{ig} , the time between when the FFB stopped under the leaf and when the first visible flame occurred, in s), (b) time to maximum flame height (t_h , time between ignition and maximum flame height, in s), (c) burnout time (t_{bo} , time between start of heating and burnout, in s), (d) maximum flame height ($h_{f,max}$, in cm), and (e) flame tilt angle (θ , the angle that a flame deviates from its otherwise vertical position, in degrees).

4.1.2 Shrub-scale wind tunnel experiments

Manzanita branches with attached foliage were burned in the wind tunnel at the fire laboratory of the USDA Forest Service PSW Research Station facility in Riverside, CA on December 10-11, 2009. The wind tunnel is open-roofed and the doors on one side were usually left open. The tunnel is housed in a well-ventilated burn building which was neither temperature nor humidity controlled. The facility was also described by Lozano et al. (2010). Wind tunnel dimensions are shown in Figure 4-3. Photos and a schematic of burn experiments performed in the wind tunnel are presented as part of upcoming discussions (see Figure 4-4 and Figure 4-9).

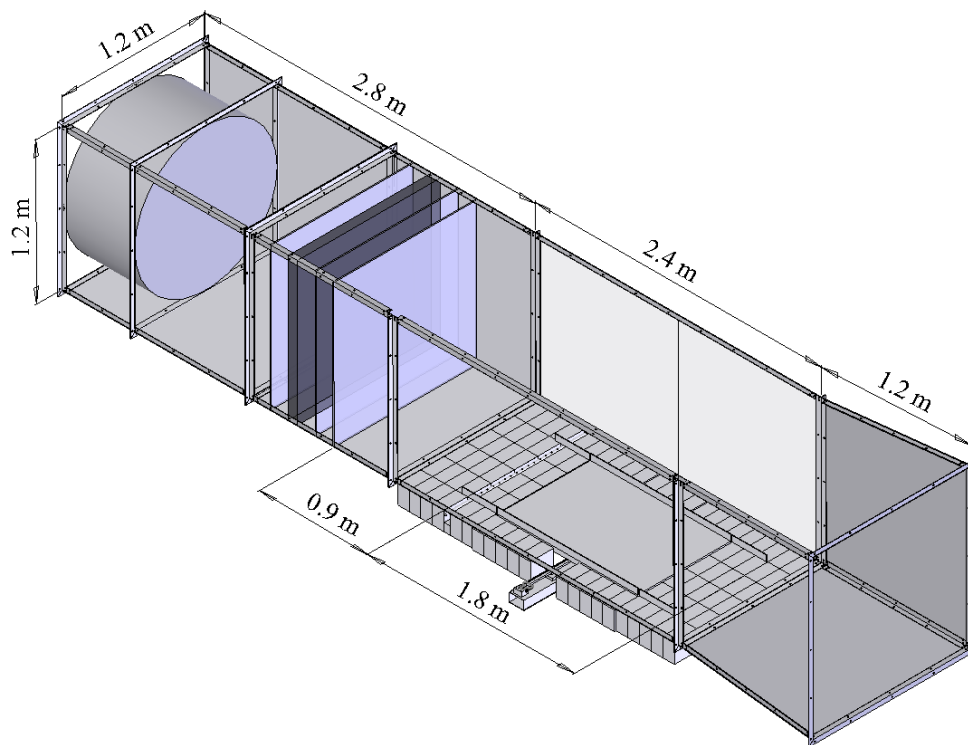


Figure 4-3. Design and dimensions of wind tunnel. Sections, beginning on the left, are: (a) fan; (b) flow conditioner; (c) open-roofed test section with load cell floor panels and fire bricks; and (d) exit Lozano et al. (2010).

Small manzanita shrubs were formed by setting vertically-oriented branches in a wire mesh which was centered on the load cell of the wind tunnel. Dry excelsior (shredded *Populus*

tremuloides wood) was placed on top of the wire mesh just upwind of the branches and served as a starter fuel (see Figure 4-4). Four burn experiments were performed on manzanita shrubs. The first was performed in the absence of wind and burned very little. The second was performed on the mostly intact shrub remaining from the first burn. New shrubs were assembled for Runs 3 and 4. Images at ignition of all four runs are shown in Figure 4-4.



Figure 4-4. Shrubs just after excelsior ignition but before starting the fan for Riverside 2009 manzanita Runs 1 (top left), 2 (top right), 3 (bottom left), and 4 (bottom right). The striped stick at the left of each image marks 25 cm intervals. Viewed through open doors from the same perspective as Figure 4-9.

The total shrub material, m_{shrub} , was weighed before ignition of each shrub and a correlation was developed to estimate the number of leaves n_L from m_{shrub} (Equation 4-1). The

leaves are of interest because in the model they were considered the combustible fuel, while branches were ignored.

Measurements were taken of three manzanita branches and their leaves (Table 4-1) to create a correlation to estimate the number of leaves (n_L) of other manzanita shrubs based on their mass and foliar MC . The branch mass including leaves (m_{branch}) (see Table 4-1), dry branch mass ($m_{branch,dry}$), moisture contents of foliar material (MC) and wood material (MC_{wood}), total leaf mass ($\sum m_{leaf}$), total dry leaf mass ($\sum m_{leaf,dry}$), total wood dry mass ($m_{wood,dry}$) and leaf counts (n_L) are listed. These measurements were used to correlate n_L to m_{shrub} (Equation 4-1). Values for Equation 4-1 were determined from the sum of all three branches.

Table 4-1. Summary of wind tunnel fire spread experiments through simulated manzanita shrubs.

Branch	MC_{leaf}	MC_{wood}	m_{branch}	$m_{branch,dry}$	$\sum m_{leaf}$	$\sum m_{leaf,dry}$	$m_{wood,dry}$	n_L
1	30.2%	11.5%	618 g	510 g	346 g	266 g	244 g	1739
2	30.2%	11.5%	651 g	536 g	376 g	289 g	247 g	1890
3	30.2%	11.5%	301 g	248 g	174 g	134 g	114 g	875
Total	30.2%	11.5%	1570 g	1294 g	896	689	605	4504

$$n_L = \frac{m_{shrub} / \bar{m}_{leaf,dry}}{\left[\frac{m_{branch,dry}}{\sum m_{leaf,dry}} \right] (MC_{wood} + 1) + MC_{leaf} - MC_{wood}} \quad (4-1)$$

The average dry mass of a manzanita leaf, $\bar{m}_{leaf,dry}$ was 0.153 g. The ratio of dry shrub mass to total leaf mass $\left[\frac{m_{shrub,dry}}{\sum m_{leaf,dry}} \right]$ was 1.87. The leaf moisture content MC_{leaf} was determined from the shrub of interest and the wood moisture content MC_{wood} was assumed to match the value listed in Table 4-1. Equation 4-1 was used to estimate the values of n_L listed in Table 4-2 by inserting m_{shrub} and MC from Table 4-2 into Equation 4-1.

Experimental conditions and measurements for the wind tunnel burns are described in Table 4-2. These fire spread experiments were used for model comparison. The span of the shrub in each dimension was measured prior to burning. Dimensions are defined such that x is in the wind direction, y is in the cross-wind direction, and z points up from the wind tunnel floor. Wind speed U describes the air velocity entering the open-roofed section of the wind tunnel. The fraction of each shrub burned X_s was determined visually from video images of the burn experiments. The maximum vertical flame extension above the top of the shrub $\Delta z_{f,max}$ was likewise determined from image analysis, as was total burn time t_{burn} .

Table 4-2. Summary of wind tunnel fire spread experiments through simulated manzanita shrubs.

Run	Dimensions x, y, z (cm)	m_{shrub} (g)	n_L	MC	U (m/s)	Temp (°C)	Relative Humidity	X_s	$\Delta z_{f,max}$ (cm)	t_{burn} (s)
1	66, 50, 65	780	2348	20%	0	10	74%	0.12	11	79
2	66, 50, 65	~780*	1996	20%	0.45/0	10	74%	0.75	35	168
3	57, 52, 81	697	2098	20%	1.08	10	74%	0.77	41	75
4	70, 65, 81	1111	3239	27%	0.69	10	74%	0.87	42	163

*Same shrub as weighed for Run 1, but with a small portion of the leaves already burned.

4.2 Multi-leaf fire spread simulator

The multi-leaf fire spread simulator models fire spread using ignition zones. The model can be described in terms of its submodels which define: (1) fuel element locations; (2) fuel element physical parameters; (3) fuel element flame behavior; (4) fluid flow; and (5) flame-flame interactions.

4.2.1 Fuel element location models

Simple shrub shapes, such as a box (i.e. rectangular prism) or hollow box (no foliar fuel where trunk would be) were formed by randomly distributing leaves within the specified shape. Leaves were oriented with their length dimension parallel to the x-axis and their width dimension

parallel to the y -axis. The randomly-filled box algorithm was used in this chapter to study bulk density.

A second algorithm was developed for creating shrub geometries from a single image of a shrub. This method consisted of several steps. First, the shrub shape was identified from a side view (x - z) image of the experiment. Foliage locations in the image were randomly sampled in the x - z plane to provide x - z pixel coordinates for the estimated number of leaves in the shrub.

Without images from other perspectives, a method was devised to simulate reasonable y -coordinates. For every x - z coordinate previously identified, a second x coordinate was randomly selected based on the z -coordinate from the foliage locations in the x - z image. The second x -coordinate was then converted to a y -coordinate by scaling by the ratio of the y to x total shrub dimensions. Coordinates were converted from pixel-space to meters using the ratio of known lengths to pixels in the image. While the shrub shape determined for the y - z plane was not based on an image from that perspective, it was based on a realistic shrub shape which, at a minimum, provides a reasonable grouping of leaves. The shrub ignited in wind tunnel Run 2, shown in Figure 4-4, was modeled using this approach (see Figure 4-5). Leaves on the right side of the shrub were ignited to begin the fire spread simulation.

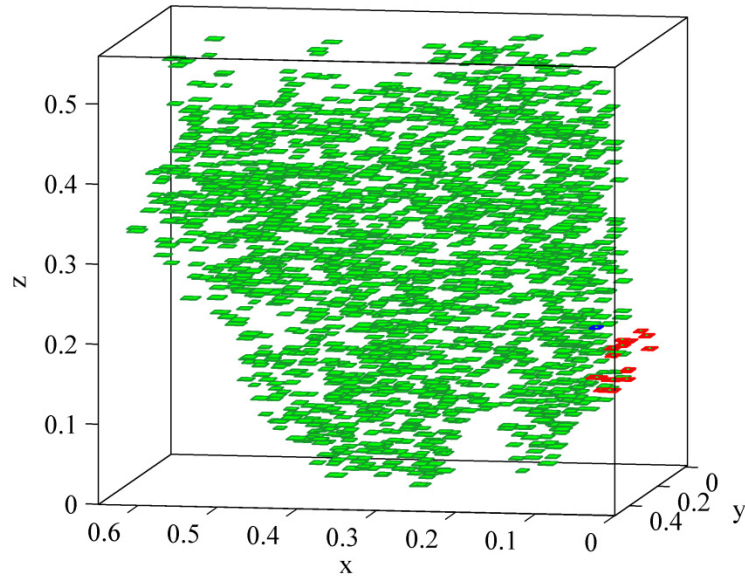


Figure 4-5. Leaves distributed based on an image of the second shrub shown in Figure 4-4. Each rectangle is a single leaf with a unique length, width and thickness.

Shrub geometries were developed for non-broadleaf (e.g. needle-like or scale-like leaves) species using Lindenmayer systems (L-systems) and are described in chapter 5.

4.2.2 Fuel element physical parameters model

Physical properties of manzanita leaves were measured. The mean and standard deviation of those properties served as a basis for defining model leaf parameters. Parameter regression was performed by minimizing the sum squared error between predicted and measured values. Leaf dry mass (m_{dry}) was selected as the best indicator for estimating other parameters. Manzanita m_{dry} measurements approximately followed a beta distribution (Equation 4-2, Figure 4-6). The beta probability density function parameter best estimates were $\alpha = 3.873$ and $\beta = 9.283$, and resulted in a good fit of the distribution of measured leaf masses ($R^2 = 0.93$). The dry masses of leaves in modeled shrubs were determined from Equation 4-2; for each leaf, a random value from a uniform distribution between zero and one was selected for x and input

with α and β to determine m_{dry} . The total mass m_0 was then a simple function of m_{dry} and the desired MC (see Equation 4-3).

$$m_{dry} = \frac{x^{\alpha-1}(1-x)^{\beta-1}}{\int_0^1 u^{\alpha-1}(1-u)^{\beta-1} du} \quad (4-2)$$

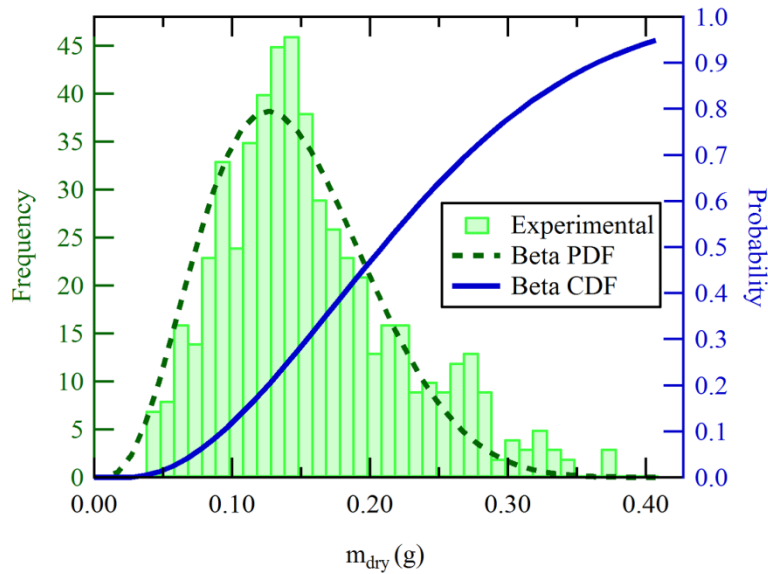


Figure 4-6. Histogram of the experimental leaf masses (dry) compared to the best-fit beta probability density function (PDF) and its cumulative distribution function (CDF).

$$m_0 = m_{dry}(MC + 1) \quad (4-3)$$

Mean values for other physical leaf dimensions (width w , thickness Δx , and length l) were then assigned using regressions to measured values (Equations 4-4, 4-5, and 4-6).

$$w = 1.318 + 2.801m_0 \quad (4-4)$$

$$R^2 = 0.61$$

$$\Delta x = 0.643 + 1.160m_0 - 0.214w \quad (4-5)$$

$$R^2 = 0.58$$

$$l = 3.357 + 3.864m_0 - 0.165w - 1.071\Delta x \quad (4-6)$$

$$R^2 = 0.47$$

The low R^2 values reflect the inherent variability of natural fuels. The standard error of each regression fit to the physical dimensions was used to estimate the standard deviation of that parameter. Physical dimensions were then assigned for each leaf by drawing a random value from a normal distribution based on the mean value indicated by the regression and the standard error of its fit. This incorporated the natural variability of each leaf parameter into the modeled shrub description. The shrub shown in Figure 4-5 displays leaves dimensioned using this approach.

4.2.3 Fuel element flame behavior model

Fuel element combustion characteristics were based on single-leaf experiments performed at conditions chosen to approximate wildland fire conditions. Linear regression analysis related key flame characteristics—ignition time t_{ig} , maximum flame height time t_h , burnout time t_{bo} , and maximum flame height $h_{f,max}$ —to leaf physical characteristics (Δx , m_0 , m_{dry} and MC) and wind speed U , resulting in Equations 4-7, 4-8, 4-9, and 4-10.

$$t_{ig} = -3.32 + 4.26MC + 7.37\Delta x + 3.69m_0 \quad (4-7)$$

$$R^2 = 0.68$$

$$t_h = -3.32 + t_{ig} + 8.11MC + 11.06\Delta x + 4.71m_0 \quad (4-8)$$

$$R^2 = 0.86$$

$$t_{bo} = 3.77 + t_{ig} + 12.24\Delta x + 15.0m_0 + 1.307\ln(MC) \quad (4-9)$$

$$R^2 = 0.76$$

$$h_{f,max} = 8.22 - 2.12U + 26.38m_{dry} - 2.74\Delta x - 8.59m_0 \quad (4-10)$$

$$R^2 = 0.77$$

By linearly interpolating, flame height h_f is modeled from the start of heating to burnout (see Figure 4-7). Once heated to t_{ig} , the remaining flame height profile is assumed to proceed spontaneously.

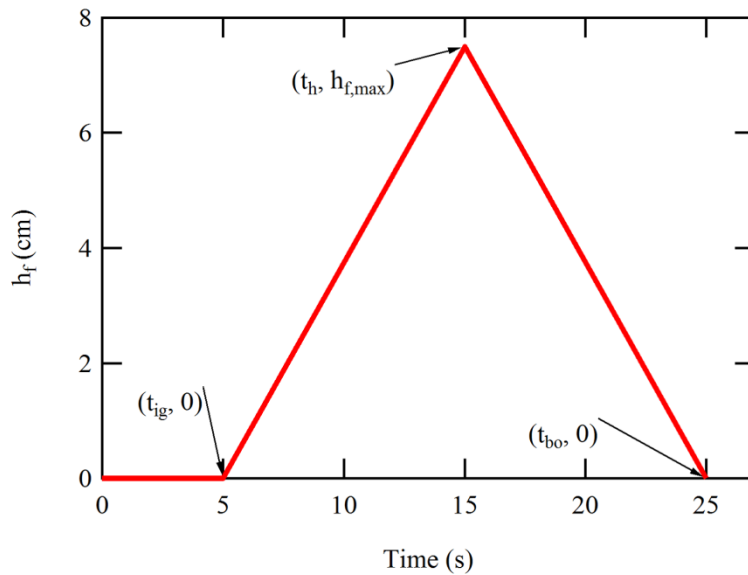


Figure 4-7. Sample modeled flame height profile for a manzanita leaf.

Modeled flame angle θ was based on Albin's (1981) Froude number correlation involving U and h_f (Equation 4-11). Flame angle was assigned as a leaf property, meaning that flame angle was determined on a leaf-to-leaf basis depending on the local wind speed and the height of the flame of the burning leaf.

$$\theta = \tan^{-1} \left[1.22 \left(\frac{U^2}{g \cdot h_f} \right)^{0.5} \right] \quad (4-11)$$

$$R^2 = 0.75$$

As a flame approached $h_{f,max}$, the flame width extended beyond the leaf width. Side flame boundaries were defined to extend beyond the leaf width and length by 11% of the flame height according to an analysis of a subset of the experimental data. In addition, it was observed that a flame originating from a single leaf often dipped below the original location of the leaf. The flame boundary was therefore estimated to extend below the leaf by 15% of h_f . A parallelepiped-shaped flame for every actively burning fuel element is defined by h_f, θ , and the flame boundary relationships (Figure 4-8). This parallelepiped shape was chosen to make the calculation of overlapping flame volume less complicated, since it was a factor in the flame interaction model.

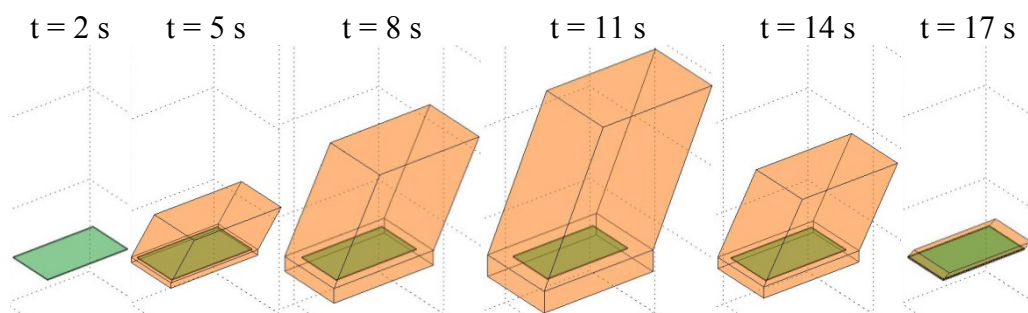


Figure 4-8. Frames showing a single-leaf combustion sequence, including the leaf and flame. At 2 s, the leaf is still preheating, the maximum flame height is reached at about 11 s, and burnout occurs just after 17 s.

4.2.4 Fluid flow model

Wind velocity affects modeled angle and height of the parallelepiped flame. Early versions of the fire spread model assumed that the wind speed was the same at every leaf. This section describes the development of a quadratic fluid flow model (Equation 4-12) based on wind speed measurements (see Table 4-3) taken in a wind tunnel with shrub branches in place but before ignition (Figure 4-9). Equation 4-12 provides an alternative to assuming a uniform velocity for all leaves. The doors on the near side of the open-topped wind tunnel were left open

for infrared imaging. Measurements were collected during a 2010 trip to the Pacific Southwest Research Station, USDA Forest Service, Riverside, CA (see Appendix A for related results).

$$\frac{U}{U_{bulk}} = \left[0.38 \left(\frac{z_{leaf}}{h_{shrub}} \right)^2 + 0.29 \frac{z_{leaf}}{h_{shrub}} + 0.33 \right] \quad (4-12)$$

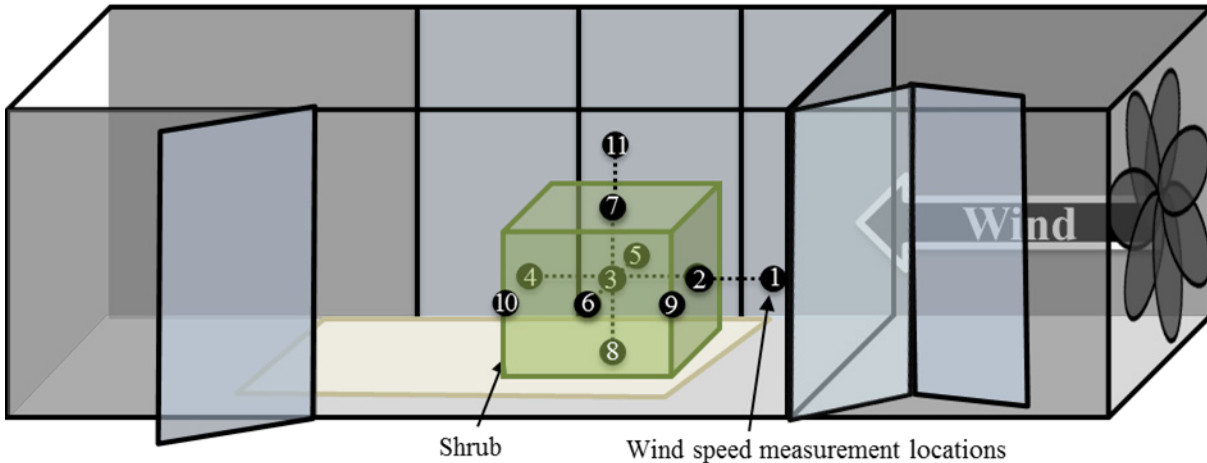


Figure 4-9. Schematic of wind tunnel indicating wind measurement locations relative to shrub location. Also see Figure 4-4.

Table 4-3. Wind tunnel stream-wise velocity (m/s) measured using a Kestrel 3000. Values in parentheses were estimated. Species are chamise (Ch.) and manzanita (Ma.). Location number correspond to Figure 4-9.

	Species	Ch.	Ch.	Ch.	Ma.	Ma.	Ma.	Ma.	Ma.	Ma.	Ch.	Ch.	Ma.
Location Run no.	3	4	5	6	7	8	9	10	11	12	13	14	
Nominal	1.5	2	1	2	2	1	1.5	2	1.5	1.5	1	1	
(1) 1 foot ahead	(1)	1.4	0.4	1.2	1.2	0.5	1	1.4	0.9	1	(0.3)	(0.2)	
(2) Front	1	1.2	0	1	0.7	0	0.5	0.4	0.7	0.9	0.3	0.2	
(3) Middle	0.8	0.7	0	0	0	0	0	0.4	0	0	0	0	
(4) Back	0.3	0	0	0	0	0	0	0	0	0	0	0	
(5) Far side	1.2	1	0.3	0.6	0.8	0	0	0	0.8	1.3	0	0	
(6) Near side	1.1	1	0.6	0.7	0.7	0	0	0.7	0.8	0.7	0	0	
(7) Top		1.3	0.5	1.3	1.2	0	0	1	1.1		0	0	
(8) Bottom		0.8	0	0.4	0.4	0					0	0	
(9) Front corner				1.3									
(10) Back corner				0.4									
(11) 1 foot above						1	1.2	1.5	1.1				

U is the local wind speed, U_{bulk} the bulk wind speed, z_{leaf} the local vertical position from the bottom of the shrub and h_{shrub} the height of the shrub. Equation 4-12 was determined by selecting the “1 foot ahead” measurement as U_{bulk} . “Front,” “Far side,” “Near side,” “Front corner,” and “Back corner” were averaged as local mid-height measurements; “Middle” and “Back” were not used since they were shielded by the front of the shrub, but would be exposed by the time they were burning. The average of the “Top” position was used for full-height measurements (excluding zeroes). For “Bottom” measurements, zeroes were neglected since they may have resulted from the insensitivity of the Kestrel 3000 at low wind speeds, and Run 4 was also excluded to compensate for neglecting the dubious zero measurements. The resulting average velocities at these three heights, normalized by the bulk wind velocity, were fit to a quadratic to give the coefficients appearing in Equation 4-12.

The bulk wind speed can be set to change partway through a simulation, and either a flat or quadratic velocity profile (in space) may be used. This demonstrates, if only in primitive form, the ability to consider fluid flow in the multi-leaf fire spread simulator.

4.2.5 Flame-flame interactions model

The synergistic interaction between flames was modeled by multiplying the overlapping volume of overlapping flames by a flame coalescence parameter, R_c . (estimated to be at least 50%). The resulting volume was then added to the top of both flames. The parameter R_c essentially determines how flame height responds to flame overlap. Side and bottom flame boundaries and flame angle were then recalculated based on the new height. This approach is depicted in Figure 4-10. Physically, an R_c value of 0.5 means that overlapping flame volume is merely displaced and evenly split between the tops of the two overlapping flames. That is why $R_c = 0.5$ was chosen as a minimum value. The subsequent side and bottom adjustments slightly

increase the merging effect. A value of R_c greater than 0.5 can be used to create a stronger merging effect. For example, an R_c value of 2 physically means that overlapping flame volume is multiplied by 2 before being added to the flame tops.

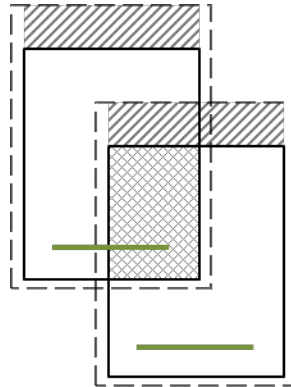


Figure 4-10. Schematic of the flame coalescence model. Horizontal bars are burning leaves, their original flames are solid-lined rectangles and their overlapping volume is cross-hatched. The added volume is striped and the final adjusted flame boundaries are dashed. Not to scale.

4.3 Model evaluation methods

To examine the fire behavior predicted by the multi-leaf fire spread simulator, several studies were performed. These included: (1) the modeled effect of bulk density on amount of shrub consumption, X_s ; (2) a full-factorial sensitivity analysis of model response to n_L , U , MC , and R_c ; and (3) model simulations for comparison to measurements of fire spread through shrubs ignited in a wind tunnel. These studies benchmarked the performance of the model and provide direction for improvements.

4.3.1 Bulk density

A set of model simulations was performed to study the effect of bulk density on X_s . Seventeen levels of bulk density were chosen and each level was simulated 24 times. The box shrub shape was chosen with dimensions of $(x, y, z) = (30 \times 30 \times 50)$ cm. Other factors were held

constant: $MC = 45\%$; $R_c = 1.2$; and $U_{bulk} = 0$ m/s. The bulk density ranged from 0.81 kg/m^3 to 9.9 kg/m^3 , or in terms of the leaf area index (LAI), from 1.3 to 15.7. Levels were selected to match significant LAI values from Law and Waring with additional levels added to illustrate transitions. LAI is calculated as the total one-sided leaf surface area divided by the shrub's plot area (900 cm^2 in these simulations). Typical LAI values for manzanita shrubs range from 3.1 to 9.5 (Law and Waring, 1994). Fire spread for each simulation was initiated by igniting leaves included in an ignition volume along a bottom edge of the shrub domain for each simulation. The ignition volume included any leaves with an x coordinate less than 3 cm and a z coordinate less than 5 cm.

4.3.2 Modeling shrub-scale wind tunnel experiments

Shrubs were ignited in a wind tunnel and the resulting fire spread was modeled. The values of n_L , MC and U in Table 4-2 were used directly in the model. Leaves were placed within the shrub shape specified by the measured y -dimension and the imaged side (x - z) perspective of the shrub. The flame coalescence parameter was set to a low level ($R_c = 0.5$) based on several pilot simulations which indicated overly aggressive fire spread above this value compared to wind tunnel measurements. The quadratic fluid flow equation was used to determine local wind speed.

Other customizations were included in the model to reflect details of the wind tunnel experiments. The area ignited by excelsior in the experiments was approximated in the model. The ignition region was defined from the bottom right corner to a top bound (z -dimension) and left bound (x -dimension), creating a rectangular ignition area which spanned the entire y -dimension (Figure 4-11, Table 4-4).

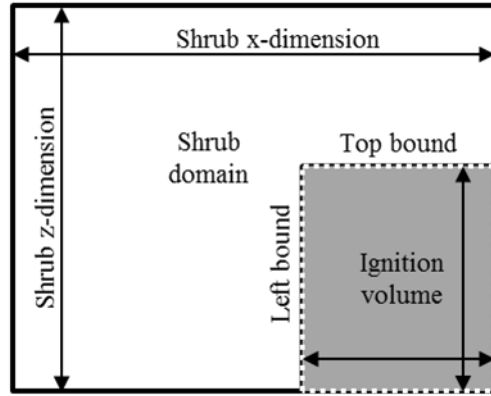


Figure 4-11. Ignition volume defined by left and top bounds. The ignition volume spans the entire y-dimension.

Table 4-4. Ignition volume left and top bounds.

Run	Left bound	Top bound
1	5%	100%
2	40%	40%
3	40%	40%
4	55%	20%

The excelsior flame in Run 2 was observed to advance as a nearly vertical sheet, causing a prolonged, slowly advancing ignition effect. This was modeled by advancing a zone which heated any unburned fuel to ignition, beginning at the ignition side of the shrub and proceeding 25 cm in the x -dimension at a rate of 1.25 cm/s. The wind tunnel fan in Run 2 stopped after 141 s of fire spread, after most of the shrub was burned. This was modeled by changing the wind speed from 0.45 m/s to 0 m/s once leaves positioned beyond $x = 55$ cm were ignited.

Criteria were developed to measure the behavior of the fire spread model and to compare it to shrub-scale burn experiments performed in a wind tunnel. The criteria used to determine values for the model and for wind tunnel experiments are given in Table 4-5. The response of X_s , $\Delta z_{f,max}$, and t_{burn} were determined numerically. The burn path was determined through image analysis of video images and model images. The time of first flame arrival to any pixel on the x - z

projection of the shrub was recorded. The flame arrival times associated with each pixel in the shrub area were then used to create a burn path by mapping times to colors (presented in results).

Table 4-5. Criteria for fire spread evaluation.

Measurement	Criteria	
	Fire spread model	Wind tunnel experiment
X_s	Count of burned leaves.	Visual inspection.
$\Delta z_{f,max}$ (see Figure 4-12)	Model output (exact).	From video images, excluding flames from excelsior.
t_{burn}	Ignition of the first leaf to extinction of the last.	First leaf to reach 280 °C (and contribute to the ignition of other leaves) to extinction of last (including branches).
Burn path	Time of flame arrival at shrub locations from video images.	Time of flame arrival at shrub locations from model images.

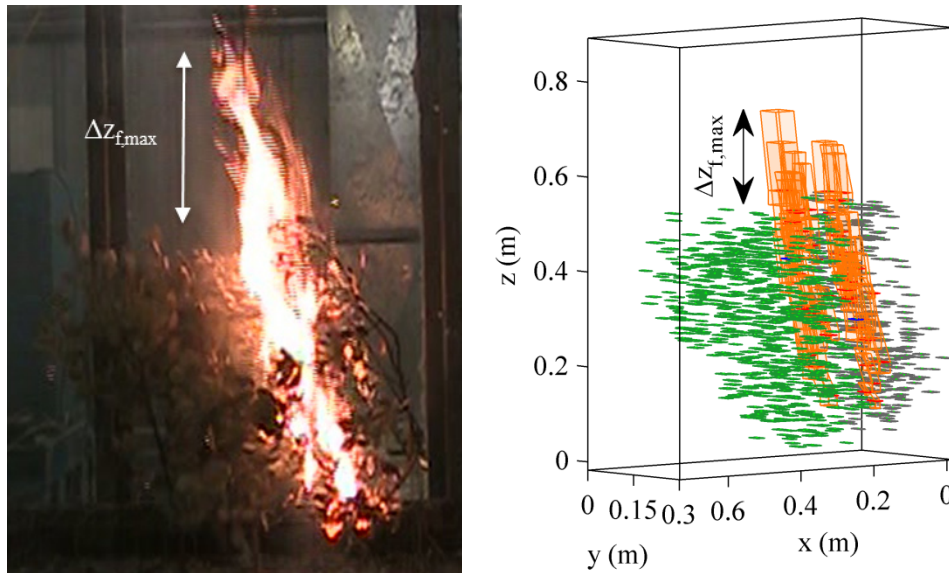


Figure 4-12. Illustration of $\Delta z_{f,max}$ for experiments (left) and the model (right). The shrub area is highlighted with a box in both cases and the flame height is indicated. The largest value of Δz_f for each simulation or experiment was reported as $\Delta z_{f,max}$.

4.3.3 Full factorial sensitivity analysis

Model sensitivity to four factors (n_L , MC , U and R_c) was studied with a 3^4 full factorial design, including low, medium and high levels for each factor. Simulations were repeated 36 times at each of the 81 unique factor-level combinations for a total of 2916 simulations. Leaves were positioned randomly within a shrub shape defined by the x - z view from wind tunnel burn one, but with a y -dimension of 0.25 m. Values for low, medium and high levels of each factor are given in Table 4-6. The medium level of leaves provides a similar density of leaves as the shrub burned in wind tunnel experiment number one since it has half the y -dimension and approximately half the number of leaves. The leaves in the bottom 40%, right (upwind) 20% and the entire y -dimension were ignited to commence fire spread.

Table 4-6. Factors and coded values used in the full factorial design.

Factor	Level		
	Low	Medium	High
Leaf count (n_L)	600	1200	1800
Moisture content (MC)	5%	40%	75%
Wind speed (U)	0 m/s	1 m/s	2 m/s
Flame overlap multiplier (R_c)	0.5	0.7	0.9

4.4 Results and discussion

Fire spread simulations are presented in three parts: (1) effect of bulk density; (2) full factorial study; and (3) wind tunnel comparison.

4.4.1 Effect of bulk density

Increases in modeled bulk density increase the modeled burn fraction X_s . Interestingly, the steepest change in X_s occurred over the natural LAI range (i.e. 3.1 to 9.5) reported for manzanita shrubs (Law and Waring, 1994). From an LAI of 3.1 to 9.5, the average value of X_s increased from less than 5% to 47% (see Figure 4-13). The variance of X_s increased with bulk

density to a maximum at 4.4 kg/m^3 (LAI = 6.9), and then declined. This trend was statistically significant at a 95% confidence level, as measured with F-tests between the largest variance level (990 leaves, LAI = 6.9) and low (495 leaves, LAI = 3.4, $P = 0.0002$) and high (1800 leaves, LAI = 12.6, $P = 0.01$) bulk density levels. The source of variation is the leaf properties and the randomized leaf placement, which on a coarse scale, did not vary. However, X_s was highly sensitive to fine-scale variation in fuel placement and fuel properties, especially in the natural LAI range. These details are entirely overlooked in typical fire spread models. Simulations with bulk densities greater than 9.9 kg/m^3 were not included since there was little increase in X_s above this value.

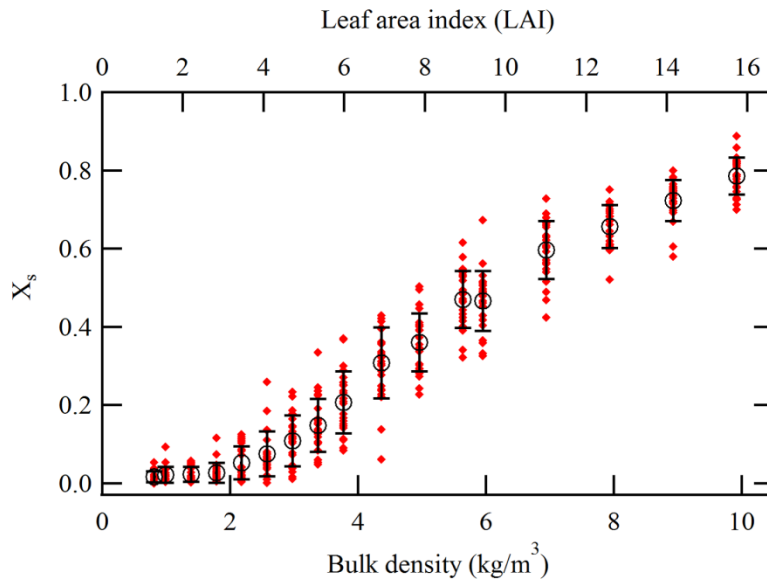


Figure 4-13. Model predictions of fraction of fuel (leaves) burned versus bulk density at 45% MC (dry basis) and 0 m/s wind for a 30 x 30 x 50 cm shrub. Small dots are individual simulations and open circles are mean values with ± 1 standard deviation error bars.

This simulated behavior helps to explain reasons why fire spread in sparse shrubs is difficult to predict: (a) the natural range of LAI for manzanita shrubs includes more heavily-loaded shrubs which propagate fire spread and lightly-loaded shrubs which quickly extinguish fire spread (in these simulations); and (b) the highest standard deviation of X_s was found in the

natural LAI range and was due to leaf-scale variation in fuel placement. At other combinations of wind speed and moisture content, similar fire spread sensitivity is possible. Parsons (2007) noted a related sensitivity to fine-scale fuel placement in detailed CFD calculations, concluding that within-stand spatial variability of fuel locations significantly influenced the magnitude and nature of variability in rate of fire spread.

Wind speed and moisture content have opposite impacts on fire spread. Therefore, fire spread sensitivity to bulk density and fine scale spatial variability of fuel placement is likely at other combinations of wind speed and moisture content, especially at the transition between sustained fire spread and fire spread extinction.

4.4.2 Model comparison to shrub-scale wind tunnel experiments

The multi-leaf shrub model simulates fire spread which can be analyzed in terms of X_s , t_{burn} , $\Delta z_{f,max}$ and burn path. Measurements for these indicators were compared between wind tunnel experiments and the model simulations.

4.4.2.1 Maximum flame height above shrub, $\Delta z_{f,max}$

Flame heights from each wind tunnel run (see Table 4-2) were measured as a function of time using a video camera and image analysis. Figure 4-14 compares the maximum measured and simulated flame heights above the shrub ($\Delta z_{f,max}$) for each wind tunnel configuration. For the set of simulations performed at each configuration, the results of 30 replicate runs are represented with box plots which indicate the minimum, 25% quartile, median, 75% quartile and maximum model values. Experiments 1-4 were performed at wind speeds of 0 m/s, 0.45 m/s, 1.08 m/s and 0.69 m/s, respectively.

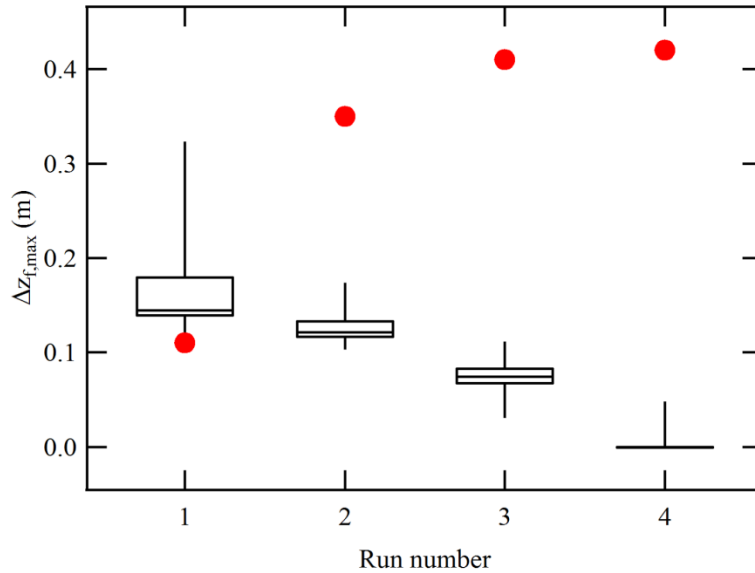


Figure 4-14. $\Delta z_{f,max}$ comparison of model simulations (box plots of minimum, first quartile, median, third quartile and maximum) and wind tunnel experiments (dots).

Flame height is difficult to quantify in shrubs since the vertical depth of the fuel bed is not negligible. $\Delta z_{f,max}$, measured from the top of the shrub to the top of the flame, remains a somewhat inadequate measure of flame height. The experimental and modeled $\Delta z_{f,max}$ diverge with increasing run number. The wind speeds of Runs 1 to 4 were 0 m/s, 0.45 m/s, 1.08 m/s and 0.69 m/s, so the diverging trend roughly follows wind speed. In fact, the cause of the divergence in flame height behavior can be explained by how the model handles wind and flame merging.

In no-wind situations, model flames stand vertically and maximize their flame overlap. At higher wind speeds, model flames do not overlap as much, which means the model does not predict as much synergy between neighboring flames at higher wind speeds. Physically, flame tilt indicates the balance between the vertical buoyancy of hot flames and the horizontal force of wind. More heat release results in more vertically-oriented flames, while stronger wind pushes flames more horizontally. Flame angle correlations use flame height (or length) as an indicator for heat release. Flames in a vertical column coalesce easily since buoyant forces add vertically, and oxygen consumption between flames pulls them together. However, in the model, flames in

a vertical column only interact if they first overlap, which is unlikely at higher wind speeds. Although the flame angle of multiple interacting flames actually depends on their collective buoyancy (and merged flame height), model flame angles are determined from the flame heights of the individual flames, which underestimates the collective effect of buoyancy on the combined flame angle. The final result in the model is that flames at high wind speeds have exaggerated flame angles, underestimated flame interactions and merging, and reduced potential to spread fire to other fuels.

Furthermore, heat release is a function of the rate of fuel heating, which increases in some wind-blown fires. Heating rate and kinetic effects, however, are not addressed in this model. So although buoyancy and flame height increased in the wind-blown wind tunnel measurements, this was hardly reflected by the model.

The experimental relationship between $\Delta z_{f,max}$ and wind speed was positive. The only exception was an artifact of shrub shape and the criterion for determining $\Delta z_{f,max}$: the measured $\Delta z_{f,max}$ of Run 4 was higher than that of Run 3 (even though Run 3 had a higher wind speed) because the shrub for Run 3 had an especially tall branch (see Figure 4-4) which did not burn significantly (see Figure 4-19) and therefore suppressed the $\Delta z_{f,max}$ values of flames emanating from other parts of the shrub. In the model runs, this branch frequently did burn, resulting in the observed model behavior for Run 3.

In summary, the flame-flame interaction and flame angle models did not satisfactorily describe flame behavior in wind-conditions. These results indicate a particular need for improved modeling of flame-flame interactions, flame angles, and kinetic effects.

4.4.2.2 Fraction of shrub consumed, X_s

The model and wind tunnel behavior agreed very well in terms of X_s . Burns one and four were respectively over and under predicted by the model, but two and three fell near the median model predictions (Figure 4-15). The model predictions for X_s in the first configuration are concerning because it was a rather simple scenario, and adjustments to make the model run less aggressively were already made (i.e. $R_c = 0.5$). In this no wind condition, the fire burned relatively calmly and the preheating of nearby fuels was slow. This indicates lower heat flux to preheating fuels at these conditions and lower fuel temperatures during combustion. To represent such behavior in the model, a submodel to describe the kinetic response of the fuel to varying heating conditions would be needed. In burn four, the wind-facing side of the shrub was not initially burned. Fire burning downwind burned back into the wind to consume much of the initially missed upwind side of the shrub. This was aided by the wind-shielding provided by the unburned foliage. The fluid flow model has not yet been prepared to handle such situations and did not burn as far upwind as measured for the wind tunnel burn.

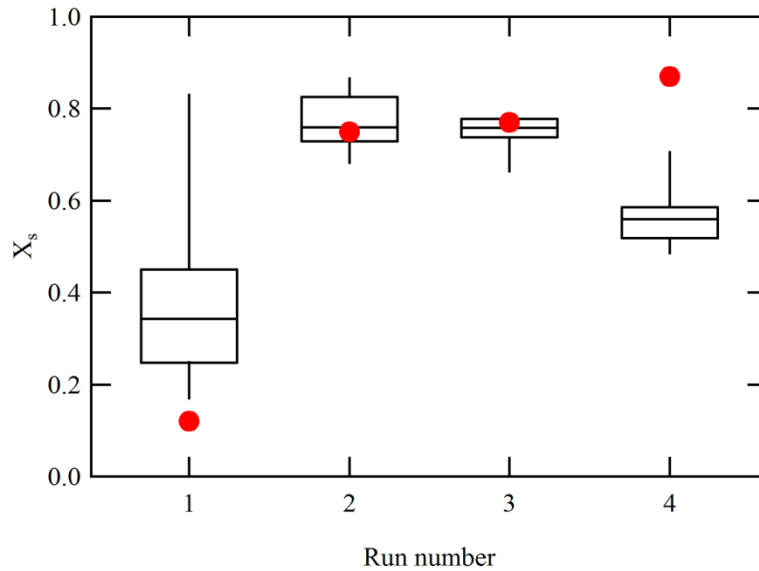


Figure 4-15. X_s comparison of model simulations (box plots of minimum, first quartile, median, third quartile and maximum) and wind tunnel experiments (dots).

4.4.2.3 Burn time, t_{burn}

The t_{burn} of the physical shrubs was erratic (Figure 4-16). The physical shrubs included branches as well as foliage. The ignition of thicker fuels can contribute to extended burn times, though thicker fuels are less important to fire spread since fine fuels typically carry the fire front. However, it is unclear from video footage whether branches or leaves are the source of lingering flames. The modeled t_{burn} had a fairly wide range of values, and only included foliage. The first and third experiments were well-represented by the model simulations, while the second and fourth were typically underestimated.

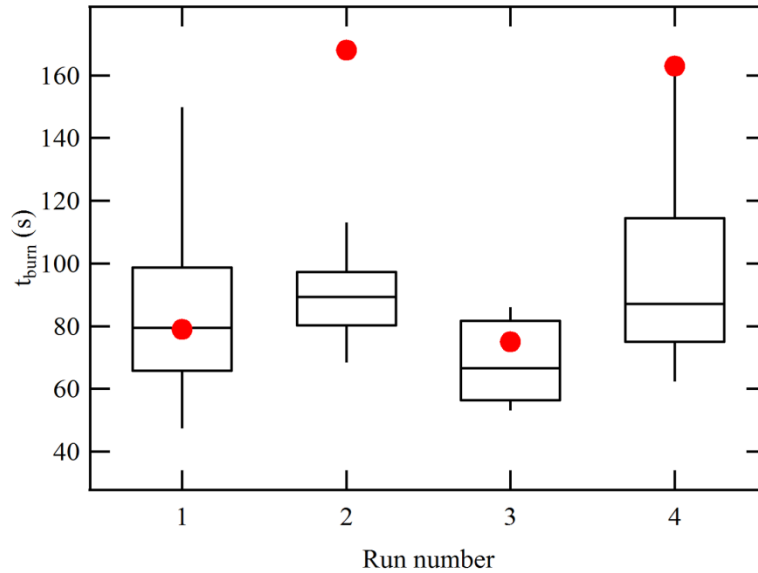


Figure 4-16. Burn time comparison of model simulations (box plots of minimum, first quartile, median, third quartile and maximum) and wind tunnel experiments (dots).

4.4.2.4 Flame path

The flame path of the four experiments and a representative model simulation for each one were represented using contour maps, with colored contours representing time, and solid white lines marking 15-second increments (Figure 4-17, Figure 4-18, Figure 4-19 and Figure 4-20). The dark patterned area represents unburned shrub area while the light patterned area represents void space.

In the first experiment (0 m/s) a vertical flame sheet burned partway across the shrub before extinguishing (Figure 4-17). The simulation showed a more extensive burn path than the experiment, but both self-extinguished (see Figure 4-17). In this way, the go-no-go behavior was correctly modeled. The model for fuel element flame behavior was based on experiments mimicking wildfire-like conditions, while the actual heating conditions in the wind tunnel experiments were milder, particularly in still air. However, this model does not account for differences in energy output or heating rates, which if considered, would potentially help to resolve the difference in burn paths.

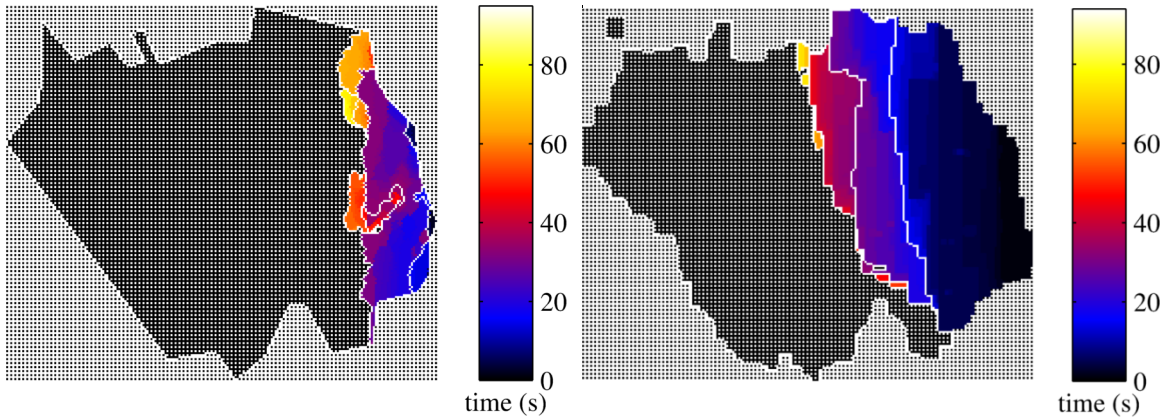


Figure 4-17. Run 1 flame path of the wind tunnel experiment (left) and a model simulation (right) viewed from the side (x-z perspective). Time is represented by color shading. White contours mark 15 s intervals. The dark patterned area is unburned vegetation while the light patterned area was void.

The second experiment provided an especially interesting case since the wind tunnel fan stopped before the entire shrub was consumed, dropping the wind speed from 0.45 m/s to 0 m/s. (Figure 4-18). Fire spread in both the experiment and model simulation was quickly reduced when the wind stopped, and in neither case did fire completely consume the shrub. However, fire spread occurred more slowly in the physical burn. This recalls the discussion that the measured burn was not as intense as a typical wildland fire, and that the model burn times are based on wildfire-like heating rates which yield shorter burn times. In addition to the effects of heating rate, many other factors may also contribute to the difference in fire spread rates.

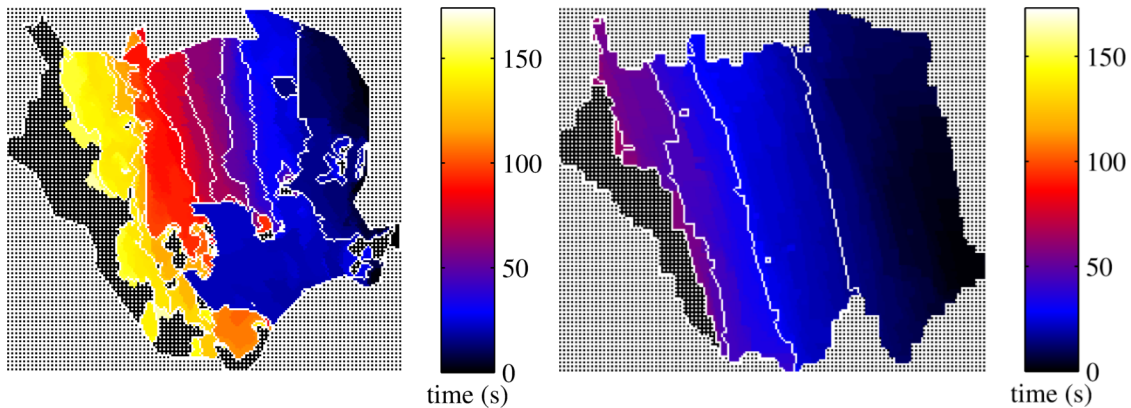


Figure 4-18. Run 2 flame path of the wind tunnel experiment (left) and a model simulation (right) viewed from the side. See figure caption to Figure 4-17.

The third experiment (at 1.08 m/s) exhibited unusual fluid flow patterns which caused the flame to skirt around the sides and bottom of the shrub and immediately burn the far side (Figure 4-19). This left a diagonal burn strip from which fire split and back-burned towards the top right (upwind) corner as well as spreading down to the far bottom corner. The top right corner largely remained unburned. The shrub model predicted some similar burn features. The fire quickly cut through the shrub, but at a less inclined angle. The fire then split and back-burned towards the top right corner and the bottom left. However, a larger section of the bottom left corner remained unburned while nearly all of the top right section burned (see Figure 4-19). The differences between the physical and simulated fire spread behavior seem to stem from complex fluid dynamics which the model did not capture. It is interesting to note that though the burn paths were somewhat different, the burn times were similar. Referring back to the discussion on fire intensity, this third burn had the highest wind speed and what may have been the fire intensity most similar to field wildland fires. This supports the conclusion that fire intensity accounts for slower wind tunnel fire spread and that kinetic modeling could improve model agreement.

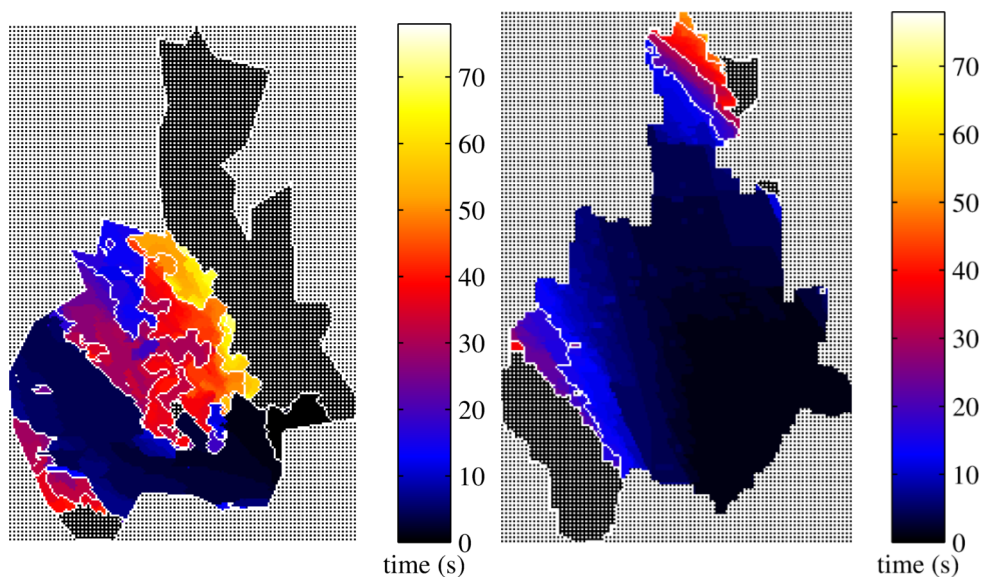


Figure 4-19. Run 3 flame path of the wind tunnel experiment (left) and a model simulation (right) viewed from the side. See figure caption to Figure 4-17.

The experimental and modeled burn paths for the fourth wind tunnel arrangement ($U = 0.69$ m/s) were similar to those observed for experiment three. However, in this case, the top right (upwind) corner did not burn in either the experimental or modeled burns. Similar to experiment two ($U = 0.45$ m/s), the burn was completed more quickly by the model. This supports the previous argument regarding fire intensity and kinetics. Although the difference may be due to larger fuel classes present in the physical shrub, new portions of the physical shrub were overlapped by the flame after 100 seconds, indicating that the burn time wasn't only a result of lingering flames on branches (see Figure 4-20). Nevertheless, the modeled burn time was only off by a factor of two.

In both the model and physical experiment, most of the fire spread occurred in the first half of the burn time. This was also characteristic of the experiments and models for the other three burns.

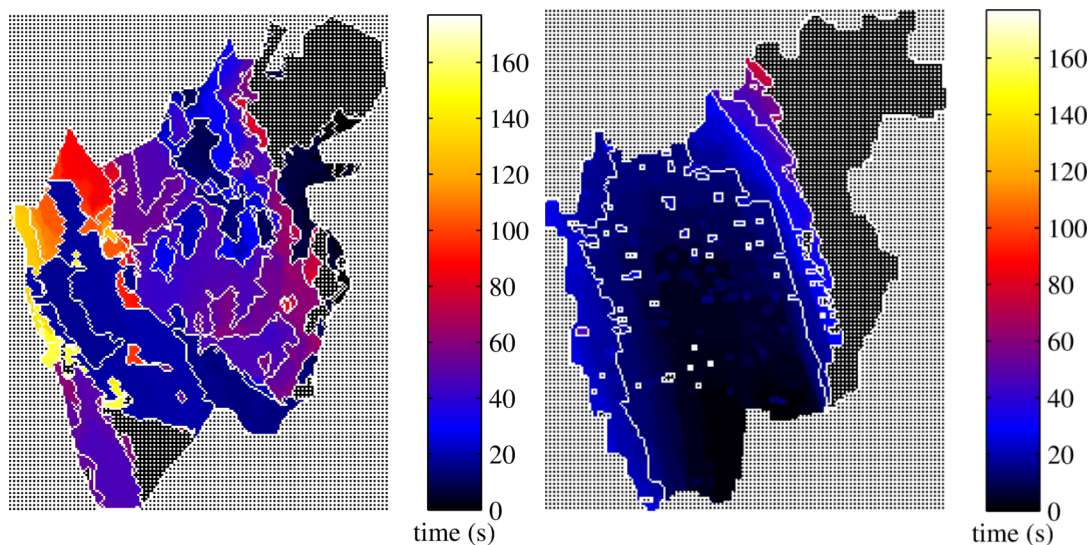


Figure 4-20. Run 4 flame path of the wind tunnel experiment (left) and a model simulation (right) viewed from the side. See figure caption to Figure 4-17.

4.4.1 Full factorial sensitivity analysis

The four-factor three-level full factorial test (81 combinations) with 36 replicates provided insight into the effects of n_L , MC , U and R_c on simulated burn behavior. Levels for each factor were given in Table 4-6. Fire behavior was summarized with three principal fire behavior measurements: (a) the maximum flame height above the shrub $\Delta z_{f,max}$, (b) the fraction of the shrub that burned X_s , and (c) the total burn time t_{burn} . The average model behavior (i.e. $\Delta z_{f,max}$, X_s , and t_{burn}) at each of the 81 configurations is graphed in Figure 4-21 (a-i). Due to the randomized leaf placement algorithm and distribution of leaf properties, burn behavior varied between runs of the same input configuration. However, for graphical clarity, error bars indicating this distribution were not included in Figure 4-21, but the average, minimum and maximum values of standard deviation are provided in Table 4-7. If plotted, one-standard-deviation error bars for each point would fall in the range described by Table 4-7. Relative standard deviation, or the standard deviation divided by the mean, is also included in the table.

Table 4-7. Average, minimum and maximum standard deviation (and relative standard deviation) of t_{burn} , X_s , and $\Delta z_{f,max}$ for each model configuration.

	Standard Deviation			Relative Standard Deviation		
	t_{burn}	X_s	$\Delta z_{f,max}$	t_{burn}	X_s	$\Delta z_{f,max}$
Minimum	2	0.001	0.000	7%	0%	15%
Average	14	0.054	0.038	19%	14%	93%
Maximum	34	0.167	0.128	33%	31%	600%

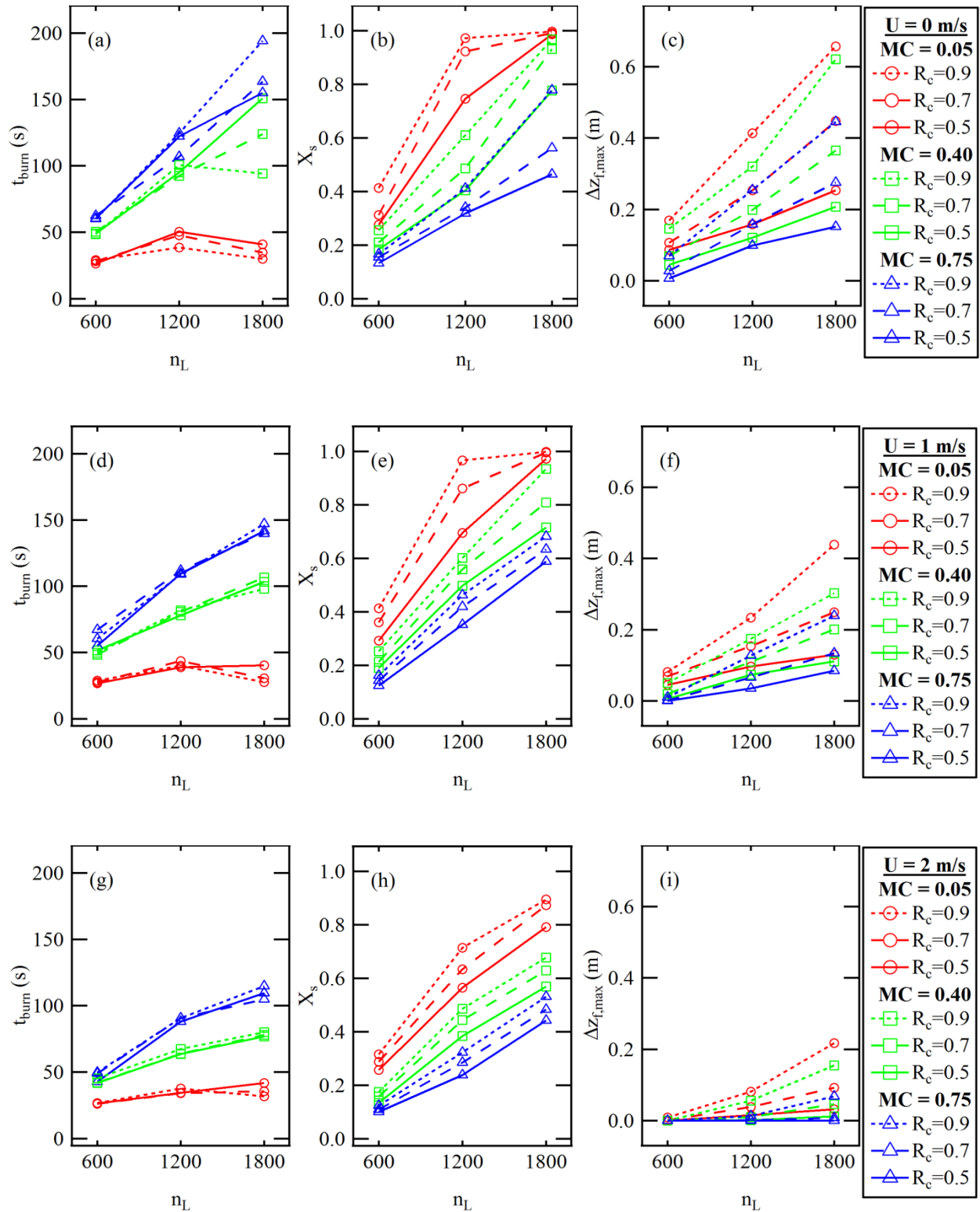


Figure 4-21. Response of t_{burn} , X_s , and $\Delta z_{f,max}$ to n_L , R_c , MC , and U . Each point represents the average of 36 runs. Each legend applies to its entire row.

Trends in t_{burn} demonstrated an expected and realistic response (Figure 4-21, a, d and g). The value of t_{burn} decreased with increasing wind speed. This coincides with faster fire propagation driven by wind. Between $U = 1$ m/s and $U = 2$ m/s, less of the shrub burned, also contributing to the decrease in t_{burn} . Increases in MC generally caused increases in t_{burn} , in spite of decreases in X_s with increasing MC . This reflects the longer t_{ig} and t_{bo} of the moist fuel elements. R_c had only a small impact on t_{burn} . For the most part, increases in n_L caused increases in t_{burn} . However, between $U = 0-1$ m/s and at low MC , the change of n_L from a medium to high level had a mostly negative impact on t_{burn} . Increases in n_L most frequently impacted t_{burn} by facilitating more extensive fire spread, which resulted in longer burn times. However, at low MC and medium and low U , X_s was approaching its maximum at the medium level of n_L , such that increasing n_L to its high level resulted in larger flames and faster fire spread, but less substantial gains in X_s and a decrease in t_{burn} .

The values of X_s responded as expected to n_L , MC , and R_c without exception (see Figure 4-21, b, e and h). The response of X_s to U was somewhat unexpected, though still plausible. As in Figure 4-19 showing the burn path of wind tunnel experiment three, an ignition in the bottom upwind corner can easily miss the upper upwind corner as it propagates through the shrub. So, the burn path may largely be responsible for the response of X_s to U . However, for simulations at high wind and medium or high MC , X_s is low enough to suggest extinction without burning even the leaves that would lie directly in the expected fire path. Perhaps this behavior is reasonable, but wind is generally regarded to enhance wildland fire spread, not extinguish it, as this model predicts for higher MC . The cause of the current model behavior is best attributed to the flame merging and flame angle models, which appear to behave poorly in wind-driven conditions.

Values of $\Delta z_{f,max}$ from the full factorial of model simulations are plotted in Figure 4-21 (c, f and i). The flame height decreased with increases in MC and U , but increased with increases in R_c and n_L . The trend in moisture content reflects the single-leaf behavior measured in experiments, which is captured in the model. Decreasing flame height with increasing wind speed goes contrary to expectations, and signals a model deficiency. This deficiency can be traced to several likely causes. Firstly, the singular flame height was used with the flame angle correlation. The flame angle correlation balances the effect of buoyant forces (using flame height as a measure of heat release) and wind momentum. Because the collective heat release of neighboring flames was not accounted for in the flame angle correlation, heat release was understated, causing overly tilted flame angle predictions. Second, wind drives more intense fires which burn at a different temperature than fires in still air. This increases heat release and upward buoyancy, which counters the horizontal momentum of the wind to yield more upright and taller flames. These two considerations—choosing a flame angle that reflects the actual local heat release, and adjusting the kinetic response of burning fuels to different burn conditions—appear important to improving this model.

The increase of $\Delta z_{f,max}$ with n_L and R_c occurs since both of these factors affect flame coalescence. Increased n_L increased the bulk density of leaves and decreased the space between leaves, thereby increasing the overlap of flames from adjacent leaves. Increases in the flame coalescence parameter R_c increased the amount of flame height added in consequence to flame overlap. Increasing $\Delta z_{f,max}$ depends on increasing flame overlap to add extra height to the flames, which also results in more upright flames which reach higher. It also depends on the fire propagating to the top of the shrub.

4.5 Conclusions

A novel semi-empirical approach detailing the properties and location of distinct fuel elements (manzanita leaves) was developed to model fire spread through a shrub. In the spectrum of wildland fire models, this approach strikes a unique balance between modeling detail and computational speed. For example, in the bulk density simulations, the average computational time on a personal computer was one to two times less than the model time for shrubs with less than or equal to 855 leaves (3.8 kg/m^3). For the heaviest shrub in the bulk density simulations (2250 leaves, 9.9 kg/m^3) computational time was 6.5 times that of the model time.

The model responded well to wind speed, moisture content and leaf count. Wind tunnel experiments showed some agreement compared to simulations, but also highlighted model deficiencies. Several needs were identified, such as improved flame merging, and flame angle models. The importance of fine-scale fuel placement was also identified. The benefits of incorporating kinetics into the flame behavior of the fuel elements may resolve many differences between modeled and measured fire spread behavior in terms of X_s and t_{burn} .

Progress on these suggested improvements and on extending the model to additional species is detailed in the following chapters. The multi-leaf fire spread simulator is intended to provide a submodel for landscape scale computational fluid dynamics calculations and to provide an alternative fire behavior model for operational fire spread predictions.

5. DETAILED FUEL PLACEMENT MODELS FOR SPARSE SHRUBS

Fine-scale fuel placement was an important factor in the fire spread model described in Chapter 4. For shrub species that have concentrated fuel placement near branches, the branching structure must be modeled to determine appropriate locations of readily-burned fuels. Models were developed to simulate the branching structure of chamise (*Adenostoma fasciculatum*) and Utah juniper (*Juniperus osteosperma*). Physical measurements of Utah juniper morphology were performed by Shen (2013). The branching structure was based on a form of fractal theory called Lindenmayer systems (i.e., L-systems) (Prusinkiewicz and Lindenmayer, 1990). The structure model was designed to match the specific characteristics of each species, such as branching angles, the number of stems exiting at ground level, and the fuel element length. Correlations to predict branch number from crown diameter were made based on data from the literature, to ensure that the modeled shrubs would have the same bulk density as live shrubs. These models generate shrub geometries and fuel element placement information which can be directly used in the semi-empirical fire spread models discussed in Chapters 4 and 8.¹

¹ Marianne Fletcher helped with a major portion of the L-systems modeling, especially for chamise. The results presented have been published: Prince, D. R., M. E. Fletcher, C. Shen and T. H. Fletcher, "Application of L-Systems to Geometrical Construction of Chamise and Juniper Shrubs," *Ecological Modelling*, **273**, 86-95 (2014).

5.1 Methods

Physical characteristics of live chamise and Utah juniper were measured and observed. Relevant data were collected from the literature, where available. These data were used to develop correlations, and guided the development of L-systems-based models.

Fractal theory is the concept of taking something simple and replacing it with something that makes it more complex. L-systems is a type of fractal theory in which an initial string (i.e. one or more symbols) is rewritten by replacing certain symbols in the string with a more complex string. This concept is shown in Figure 5-1, where the symbol 'X' was repeatedly replaced with the string 'F+X-XFX.' Each successively rewritten string is referred to as a derivation. In the example, three derivations were performed. Each symbol was associated with a geometric interpretation, such as a forward step or a turn angle (see Figure 5-1). For the starting symbol (n = 0) and first derivation (n = 1), the interpretation of each symbol was labeled. After the second derivation, two 'F' symbols and two turn symbols ('+' and '-') remained from the first derivation. The step of each successive derivation was scaled to preserve the original size.

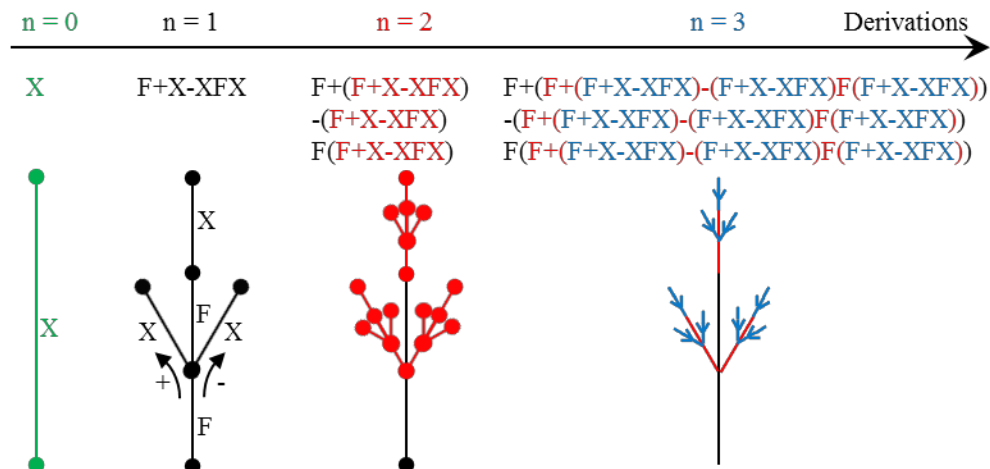


Figure 5-1. An example of the strings resulting from three derivations and the interpreted geometry. In each derivation, 'X' was replaced with 'F+X-XFX.' The commands replaced in each derivation are shown in a different color. Where included, dots mark the ends of a step.

This method is particularly suited to create self-similar geometries, such as are common in plants. An L-systems program consists of two main parts: (1) string rewriting using replacement rules; and (2) string interpretation to create geometries in space. The strings that result from rewriting are instructions for the interpreter. Because the L-systems models developed here were used to provide fuel element descriptions, other characteristics were also assigned, such as the mass of a segment, and ultimately combustion characteristics.

This chapter begins with discussion of measurements which were used to develop L-systems replacement rules. A description of the L-systems models for Chamise and Utah juniper follow. An original L-systems model was written for Chamise, including string rewriting and string interpretation. However, for Utah juniper, an existing L-systems program available from Cornell University (Land, 2006) was used as a starting point. The Cornell program required additional work to correctly interpret commands in three dimensions, but handled a greater number of commands than the interpreter developed for Chamise. The Cornell program was augmented with additional capabilities to suit Utah juniper.

5.2 Measurements, observations and correlations

Geometrical measurements were taken of eight live chamise shrubs in southern California. Twenty-two Utah juniper shrubs were measured in Utah County, Utah. Additional details are described by (Shen, 2013).

5.2.1 Description of chamise

Chamise typically grows with multiple primary branches (or stems) emerging from the ground together (see Figure 5-2). The mean basal circumference (found by the length of string needed to wrap around the emerging stems) was 184 ± 64 cm (95% confidence interval). The

radius, assuming a circular branch placement, provided an estimate of the distance of each stem from the center of the group.



Figure 5-2. A picture of a chamise shrub after the branches have been cut off showing that multiple primary branches emerge from the ground. Arrows point to cut branch ends.

The branch length and branch tip height were used to determine the tilt angle from vertical (ϕ) of two primary branches from each shrub. The maximum measured primary branch angle (ϕ_{max}) was 77° . Secondary branch angles (δ) were determined for two secondary branches on each primary branch by measuring the length of the secondary branch (from its split with the primary branch) and the distance from the secondary tip to the primary branch. The length ratio (λ) of secondary branches to their parent primary branch was determined from the measured lengths of both. A total of 32 measurements were used to determine mean values and 95% confidence intervals for δ ($30^\circ \pm 6^\circ$) and λ (0.45 ± 0.06).

Segments with diameters of less than a quarter-inch were considered as the combustible fuels, so the distribution of thicknesses of segments less than a quarter-inch was studied in detail. Six-centimeter segments were cut from a chamise branch starting at the tips, and the thickness of each segment was recorded. Thicknesses were not uniformly distributed (see Figure 5-3). The

probability distribution for segment thickness is given in Equation 5-1, where Δx is thickness (mm) and x is a random number between 0 and 1 assigned to each segment.

$$\Delta x = \frac{1}{x^{0.383}} \quad (5-1)$$

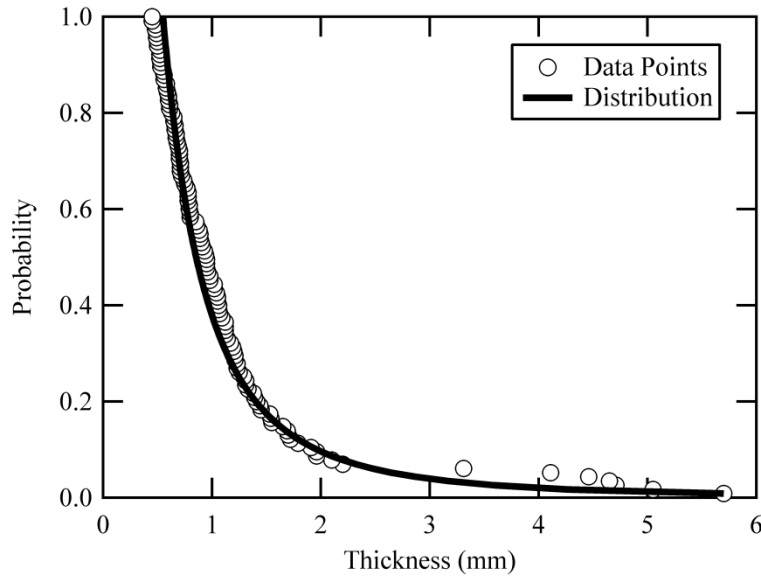


Figure 5-3. Measured and modeled distribution of segment thicknesses for chamise.

Measurements made by Countryman and Philpot (1970) were used to develop a correlation for predicting total mass, m_{tot} , from shrub height (m) (Equation 5-2).

$$m_{tot} = 0.2868 e^{1.201h_{shrub}} \quad (5-2)$$

Using the data of Countryman and Philpot (1970), a correlation was developed to predict the distribution of branch mass into four size classes. A fifth category for foliage (i.e. small needles) was also included in the original data, but in the correlation it was included in the combustible fuel class (quarter-inch or less). The amount of mass expected in each category, or size class, was correlated to the total fuel mass (Equation 5-3 and Table 5-1).

$$m_{cat,i} = a_1 m_{tot} + a_2 \quad (5-3)$$

Table 5-1. The coefficients for each size class (by diameter) used in Equation 3 for Chamise.

Size Class	a ₁	a ₂	R ²
0.25"	0.2456	0.2477	0.92
0.25" – 0.5"	0.2141	-0.0073	0.95
0.5" – 1"	0.3312	-0.0323	0.93
1" – 3"	0.2092	-0.2081	0.81

A correlation for the wet mass of individual segments in the combustible fuel class is shown in Equation 5-4, where Δx is thickness (mm), MC is leaf moisture content (dry basis), and l_s is segment length (cm).

$$m_i = -0.13575 + 0.136 \cdot \Delta x + 0.127 \cdot MC + 0.0178 \cdot l_s \quad (5-4)$$

5.2.2 Description of Utah juniper

Crown diameter (d_{crown}) was determined by choosing the largest crown diameter from three or four different cross-sectional measurements of a shrub. Shrub height (h_{shrub}) was also measured and h_{shrub} was correlated to d_{crown} (Equation 5-5 and Table 5-2). Short-biased and tall-biased correlations were also determined, which fall within the range of measurements but approximately follow the 25% and 75% quartiles of height (also shown in Table 5-2).

$$\frac{h_{shrub}}{cm} = b_1 \left(\frac{d_{crown}}{cm} \right)^{b_2} \quad (5-5)$$

**Table 5-2. The coefficients for h_{shrub} versus d_{crown} (Equation 5-2).
Alternatively, h_{shrub} may be specified directly
in the model.**

Model	b ₁	b ₂	R ²
Short-biased	9.8	0.60	n/a
Average	21.067	0.4786	0.3480
Tall-biased	50	0.35	n/a

Near the base of the juniper trunk, primary branches frequently extended below horizontal but then curved upwards. Minimum primary branch angles typically occurred near the top of the shrub and the smallest measured branch angle (base-to-tip from vertical) was 17°. The top of a juniper extends vertically and if treated as a branch has an angle of approximately 0°.

Secondary branch angles were determined with the same method as was used for chamise and had a mean and 95% confidence interval of $\delta = 36^\circ \pm 4^\circ$. The mean and 95% confidence interval of the length ratio of the highest to lowest primary branch was 0.48 ± 0.17 . Foliage units, or fuel elements, were distributed along the exterior end of branches at a regular interval. The mean distance between fuel elements was 1.5 ± 0.10 cm (95% confidence interval).

Correlations for the dry mass of fuel were determined from measurements. Dry mass was estimated by sampling representative fuel units and then counting the number of units present on the shrub. The samples were oven-dried and weighed, and the dry mass of the entire juniper shrub was estimated. Dry mass was correlated to crown diameter. Data from Mason and Hutchings (1967) was also used. Mason and Hutchings (1967) divided their measurements of Utah juniper shrubs into three different classifications—sparse, medium, and dense—and reported new growth foliage yields (including foliage and fruit). Yield was considered to be 30% of the total foliage and 50% of the total fruit. Therefore, to get the total dry mass of the shrub, their reported yield values were divided by 0.3, assuming that fruit yield was negligible. Correlations for m_{dry} for juniper are given by Equation 5-6 and Table 5-3.

$$\frac{m_{dry}}{kg} = a_1 \left(\frac{d_{crown}}{cm} \right)^2 + a_2 \frac{d_{crown}}{cm} + a_3 \quad (5-6)$$

Table 5-3. The coefficients for correlations by Shen (2013) and Mason and Hutchings (1967) data used in Equation 5-6. The R^2 for Shen's correlation is based on its fit to individual measurements, while the R^2 for Mason and Hutchings is for its fit to average measurements for all loam soil types.

Model	a_1	a_2	a_3	R^2
Shen	0.000	3.005×10^{-2}	-1.764	0.7104
M&H Sparse	2.506×10^{-5}	8.632×10^{-3}	-1.820×10^{-1}	0.9997
M&H Medium	5.478×10^{-5}	7.578×10^{-3}	-2.225×10^{-1}	1.0000
M&H Dense	7.979×10^{-5}	1.079×10^{-2}	-3.229×10^{-1}	1.0000

5.3 Overview of models

Methods were developed to produce plant geometry similar to two branching species—chamise (*Adenostoma fasciculatum*) and Utah juniper (*Juniperus osteosperma*). The models for these species follow the same general algorithm:

1. Crown diameter is specified (and for juniper, models for shrub height and bulk density are also specified);
2. Target mass is determined and used to specify the number of primary branches;
3. Branch angles and starting locations are set;
4. Branch geometry is determined by L-systems;
5. Fuel physical parameters are specified (mass, dimensions, etc.);
6. Shrub is either visualized or exported to a fire spread model.

A model was designed and customized for each species to reflect their unique characteristics.

5.3.1 Chamise model

Symbols used to create strings in the chamise model included:

- 'F' (forward one step of length d),

- ‘+’ (left in x-plane by angle δ),
- ‘-’ (right in x-plane by angle δ),
- ‘*’ (left in y-plane by angle δ),
- ‘!’ (right in y-plane by angle δ), and
- ‘X’ (string replaced with each derivation).

Symbols were compiled and interpreted using an original program. The ‘X’ command was implicitly interpreted as a new branch in the Chamise model. Chamise branches exhibited complex branching behavior making it difficult to identify common patterns for L-systems strings. Consequently, the strings in the chamise model were treated as variables which allowed the user to vary the dry mass and bulk density of the shrub. Strings were chosen that produced a dry mass and bulk density that matched observed values.

There was no single string which could characterize the irregular shape of an entire branch. For this reason a stochastic element was added. An equal probability was assigned for choosing any one of several strings. Each derivation was randomly assigned one string, so branches were similar but not identical. Strings used in the chamise L-systems model were:

1. F+!XF+*X-*XFFF-!XXF;
2. F!X*-XF+*X!-XFFF+XX;
3. F-*X-!XFFF-XFF+*XXFF;
4. F-*XF+XFF+!X!XFF+*XX; and
5. F!X+XFFF*X!-XFFF.

To generate the geometry of an entire shrub, multiple stochastic, three-dimensional branches were combined and became the primary branches of the shrub. The number of primary branches, n_b , in the shrub was based on experimental data. The primary branch lengths and angle

measurements for live shrubs were used in the model. Each branch was assigned angles of rotation about the z-axis (θ_b) and tilt from vertical (φ) so that the primary branches evenly divided the three-dimensional space (see Figure 5-4). An additional variable was also added to non-uniformly specify the radius of a starting branch from the center point of the shrub. The φ values were determined from a normal distribution with a user-specified standard deviation and mean, and the θ_b values were determined from a normal distribution using a mean of:

$$\mu_{\theta} = \frac{360^{\circ}}{n_b} \quad (5-7)$$

The θ_b values were then added together consecutively so that the angles got progressively larger:

$$\theta_{b,i} = \theta_{b,i-1} + \mu_{\theta} \quad (5-8)$$

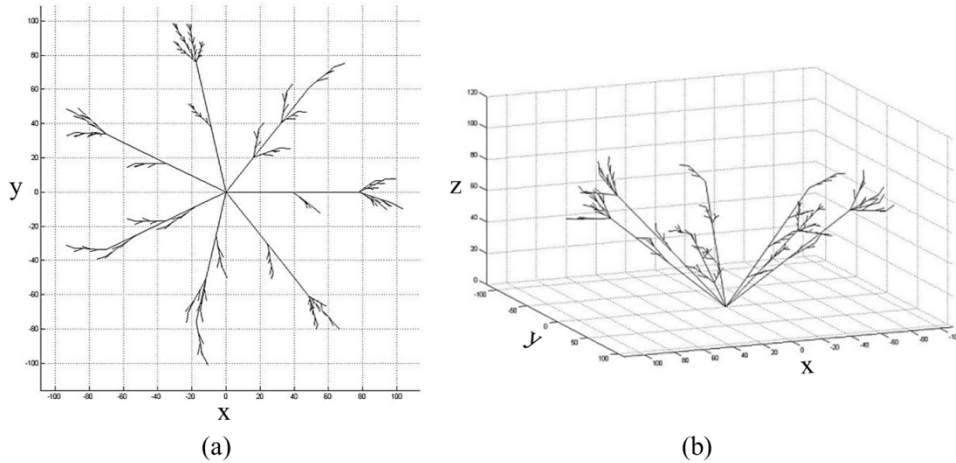


Figure 5-4. An example of a plant with seven primary branches to illustrate how the values of (a) φ and (b) θ evenly divide the three-dimensional space.

In using different strings the length of the branch would be dependent on the number of ‘F’s in the current string instead of on the length of the branch. To avoid this problem, the equation for finding the length of one ‘F’ was normalized according to the total number of ‘F’s

in the current string (n_F) and λ was adjusted for the derivation number (n_i) (Equation 5-9). The length for the first derivation (d_0) and the ratio (λ), which is the ratio of the length of the second derivation to the length of the first derivation, were also specified. An option was included to calculate d_0 using a normal distribution with a user-specified standard deviation. The height of the shrub, h_{shrub} , was calculated using the primary branch length and the scaling factor (Equation 5-10).

$$d = \frac{d_0 \cdot \lambda^{n_i-1}}{n_F} \quad (5-9)$$

$$h_{shrub} = d_0 + \lambda \cdot d_0 \quad (5-10)$$

The chamise model also split the branches into smaller segments with a length (l_s) defined by the user. Using Equation 5-3, based on data from Countryman and Philpot (1970), the number of fuel segments in each fuel thickness class was prescribed. Each branch segment was assigned to a thickness class according to its radius from the origin, where a larger radius corresponds to a smaller segment diameter.

Individual segment thicknesses (within each class) were also assigned based on the distance of the segment from the origin. Segments with a thickness less than a quarter-inch were considered fuel elements or the segments most likely to burn. The individual wet masses of fuel elements were assigned using Equation 5-4. Masses were then assigned to all other segments by calculating their cylindrical volumes and multiplying by the density of wood.

The branch segment masses (for the given l_s and each diameter) and the prescribed mass of each size class were used to determine the number of segments in each class. Based on l_s and the primary branch length, the number of segments required to complete each primary branch was estimated. The number of primary branches was then determined by dividing the total number of segments by the number of segments per primary branch.

5.3.2 Utah juniper model

The diameter, a dry mass correlation, and a height correlation were first selected. Height and dry mass models affect bulk density, which can account for the effect of environmental factors (such as soil quality and sunlight) on foliage production. The resulting m_{dry} was divided by the average dry mass per branch to prescribe n_b .

Branches were evenly spaced along the trunk to reach the shrub height specified by the height correlation and were numbered from bottom to top. To imitate natural primary branching angles in the model φ was set to decrease with increasing branch number (i_b) (see Equation 5-11). This nominally results in a φ of 30° (taken at the trunk) for the top branch, but due to branch curvature, its effective angle (from base-to-tip) was near 0° . The behavior of Equation 5-11 reserved most of the change in angle to the top branches, which had shorter segments without foliage. This helped to distribute foliage more evenly in the shrub. Random variation (φ_{dist}) was included which was a random angle pulled from a normal distribution (estimated standard deviation of 3°).

$$\varphi = 100 - 35 \left(\frac{i_b}{n_b} \right) - 35 \left(\frac{i_b}{n_b} \right)^6 + \varphi_{dist} \quad (5-11)$$

The bend in each primary branch was reduced with increasing i_b , although the curvature in the foliage-laden branches was left unchanged (see Table 5-4). A secondary branch angle of 38.4° was selected from the 95% confidence interval of measurements for live shrubs. To achieve the measured branch length ratio of 0.48 ± 0.17 , the top branch was made about half as long as the bottom branch; the non-foliage-laden section of the branch was scaled from being approximately half the branch at the bottom to nearly zero at the top, while the foliage-laden section remained constant. Fuel elements (i.e. foliage units) were placed at the average measured interval along foliage-laden sections.

Each branch was specified using L-systems. Symbols for the model adapted from Cornell

University included:

- Capital letters (step forward),
- '+' (turn left),
- '-' (turn right),
- '&' (pitch down),
- '^' (pitch up),
- '\ ' (roll left),
- '/' (roll right),
- '[' (start a new branch), and
- ']' (recall last position before branching).

Symbols were compiled and interpreted using a script developed based on an L-systems interpreter available from Cornell University. Five sets of rules were used to govern symbol replacements and were assigned to particular derivations, as detailed in Table 5-5. Where multiple strings were provided for the same replacement, each was given an equal probability of being used. This approach produced stochastic strings which were similar but not identical. Strings were interpreted to reflect the measurements and observations of live juniper shrubs, as detailed in Table 5-4. The 'G' step was a precursor to foliage branch segments 'H' and was therefore not present in a completed branch. The 'F' step was scaled from the length given in the table to achieve the intended shrub diameter and conical shape. The starting seed 'X' was used with a starting direction of $(x, y, z) = (0, 0, 1)$.

Table 5-4. L-systems rules governing symbol interpretation for Utah juniper according to string location. ‘F’ length is scaled from the given value to achieve the specified shrub diameter and conical shape.

Symbol location	Step length (cm)			Turn/pitch/roll angle (degrees)	Application
	F	H	S		
1, 2	22	-	-	-	First primary branch segment
3, 4	11	-	-	$10 - 10i_b/n_b$	Second primary branch segment
>4	-	1.5	3	38.4	All foliage-related branching

Table 5-5. L-systems rules governing symbol replacements for Utah juniper. The derivation(s) when each rule is active and its anatomical result are also summarized.

Before	After (symbol replacement rules)				
	Set A	Set B	Set C	Set D	Set E
F	F	F	F	F	F
G	G	G	HH[/+G]HH[-G]HH[&\G]H or HH[/+G]HHHH[&\G]H	HHHHHHHH	<i>undefined</i>
X	F[&X[G]]	G	<i>undefined</i>	<i>undefined</i>	<i>undefined</i>
H	<i>undefined</i>	<i>undefined</i>	H	H	H[/+S] or H[\/S]
S	<i>undefined</i>	<i>undefined</i>	<i>undefined</i>	<i>undefined</i>	S
Derivation	1, 2	3	4, 5	6	7
Result	Grow primary branches <i>F</i> ; begin foliage-branch starts.	Complete foliage-branch starts <i>G</i> .	Grow foliage branches from starts <i>H</i> .	Complete foliage branches <i>H</i> .	Add foliage segment <i>S</i> to foliage branch segments <i>H</i> .

Each completed branch was (1) rotated to its assigned ϕ (Equation 5-11), (2) translated to its intended height on the juniper trunk, and (3) rotated about the trunk. The rotation about the trunk was somewhat randomized but also favored a non-overlapping radial distribution.

5.4 Results and discussion

5.4.1 Chamise

Visually, the model generated shrubs that look similar to young chamise shrubs (see Figure 5-5). The basic overall shape was a hemisphere, with the distribution of primary branches filling the complete space. Table 5-6 also shows that the physical measurements of both shrubs shown in Figure 5-5 are very similar as well.

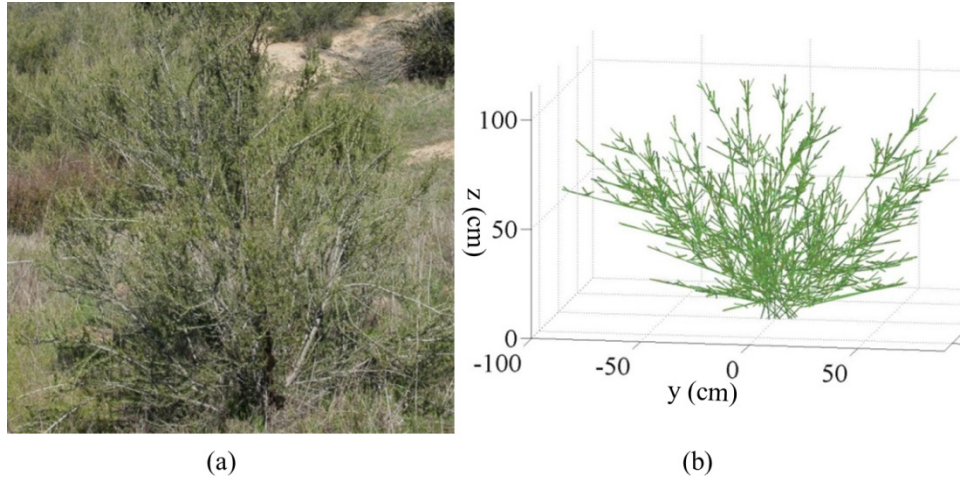


Figure 5-5. A visual comparison of (a) a chamise shrub (b) and an example of a modeled chamise shrub.

Table 5-6. Measurements of the chamise shrub in Figure 5-5(a) versus the modeled shrub in Figure 5-5(b)

Measurement	Measured	Calculated
Crown Diameter (cm)	140	140
Number of Primary Branches	14	12
Dry Mass (g)	494 (predicted*)	482

*Predicted using correlations in Equations 5-2 and 5-3

The crown diameter measured for the shrub in Figure 5-5(a) was input into the model to generate the shrub in Figure 5-5(b). The other two measurements, average primary branch radius from the center of the shrub and number of primary branches, were calculated by the model. The dry mass shown in Table 5-6 in the “measured” column was predicted by the correlations in Equations 5-2 and 5-4.

As mentioned previously, the number of primary branches per shrub was calculated based on the crown diameter of the shrub. This calculation eliminates the necessity of the user having to know how many primary branches should be on the shrub, and ensures that the bulk density of the shrub is in the correct range. Figure 5-6 is a graph illustrating how crown diameter influences the number of primary branches. Figure 5-7 shows a comparison of modeled chamise shrubs with different crown diameters. These diameters extend beyond those presented in Figure 5-6 but

the number of primary branches was calculated in the same way. However, for shrubs that large, it is likely that some of the modeled primary branches would actually be members of the same shoot emerging from the ground, thereby reducing the total count of primary branches (see Figure 5-7).

The dry mass of fuel elements was compared with data from Countryman and Philpot (1970). Figure 5-8 shows the mass of fuel elements versus crown diameter for data from Countryman and Philpot and the results from the model. The model appears consistent with the data, although the model appears slightly low.

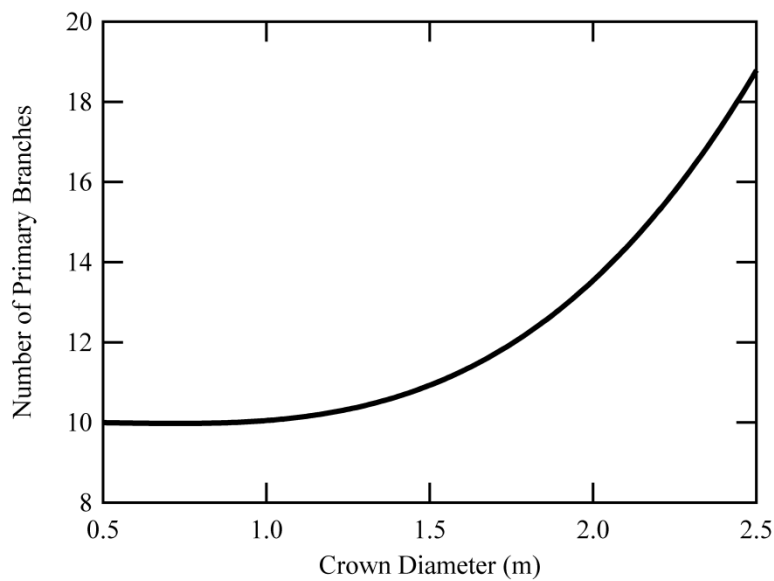


Figure 5-6. This graph shows the relationship between crown diameter and the number of primary branches for a chamise shrub.

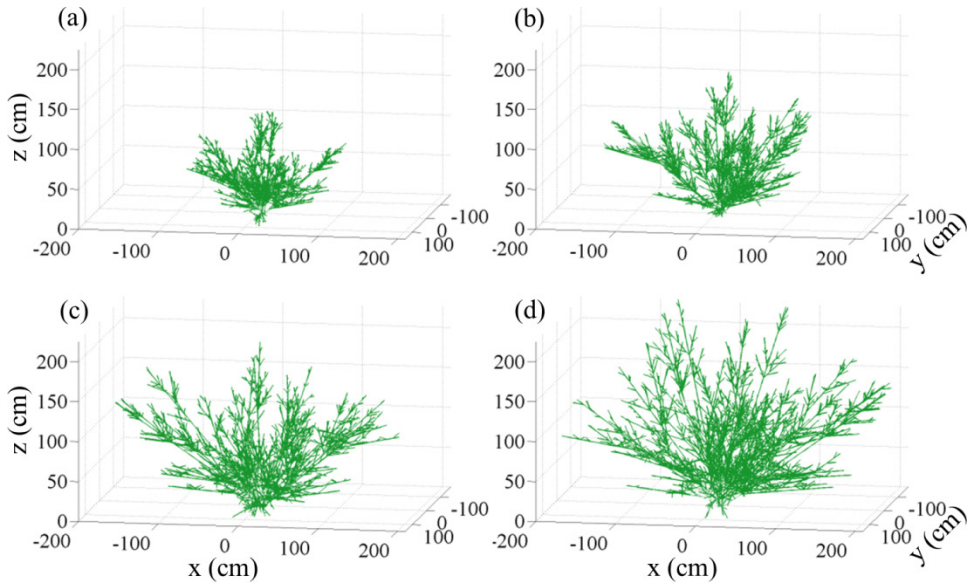


Figure 5-7. Chamise shrubs generated based on crown diameter. (a) 300 cm crown diameter with 98 primary branches, (b) 350 cm crown diameter with 117 branches, (c) 400 cm crown diameter with 139 branches, and (d) 450 cm crown diameter with 166 primary branches.

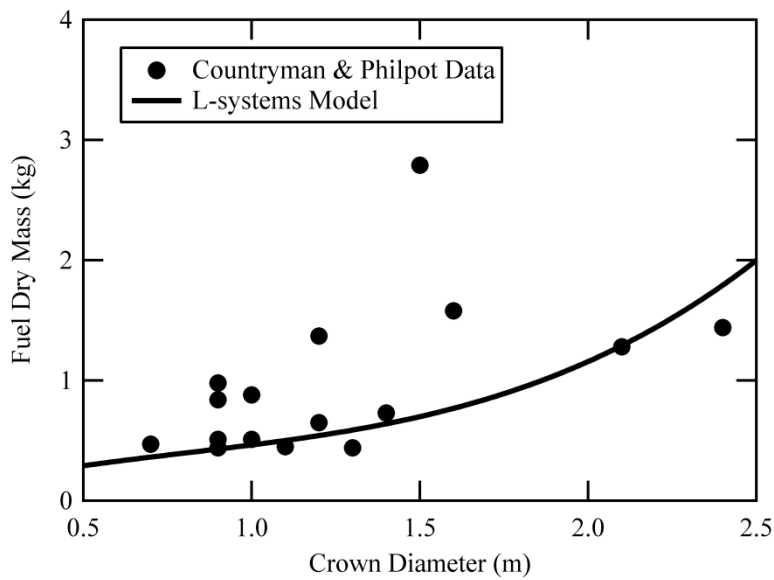


Figure 5-8. Results from the L-systems model compared to the data from Countryman and Philpot for chamise. “Fuel” in the model was defined as all segments with a thickness less than a quarter inch.

The sum of the masses of all segments gave the total shrub mass. The modeled total dry mass versus Countryman and Philpot data are shown in Figure 5-9. Again, the model appears consistent with the data, but slightly low.

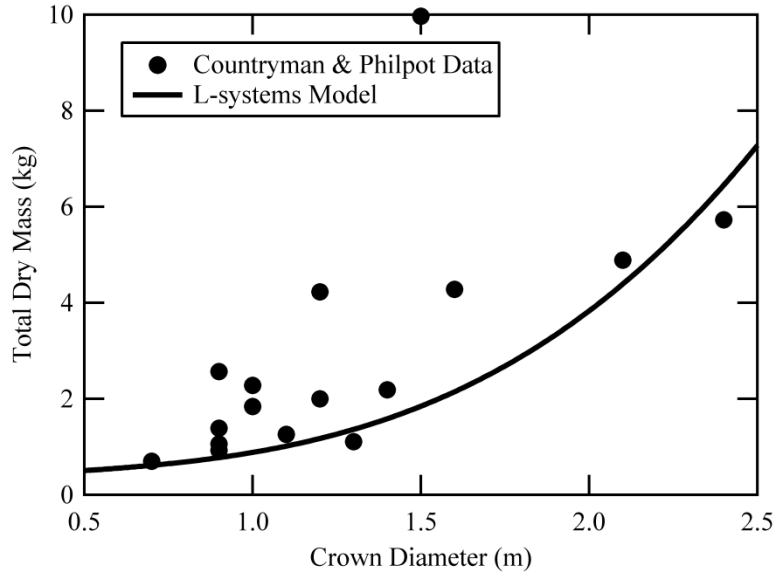


Figure 5-9. Total predicted and measured shrub mass as a function of crown diameter for chamise.

The volume of the shrub was also approximated by dividing the shrub into small, cubic sections and finding the fraction of boxes occupied by fuel. The estimated total volume was the cumulative volume of all boxes with fuel. Then, from the total shrub mass and volume, the bulk density was calculated. The number of segments as well as the volume of the shrub is dependent on the crown diameter, so Figure 5-10 is a graph of the bulk density versus the crown diameter. The model predictions are consistent with the data, but seem slightly lower than the average at any specific crown diameter.

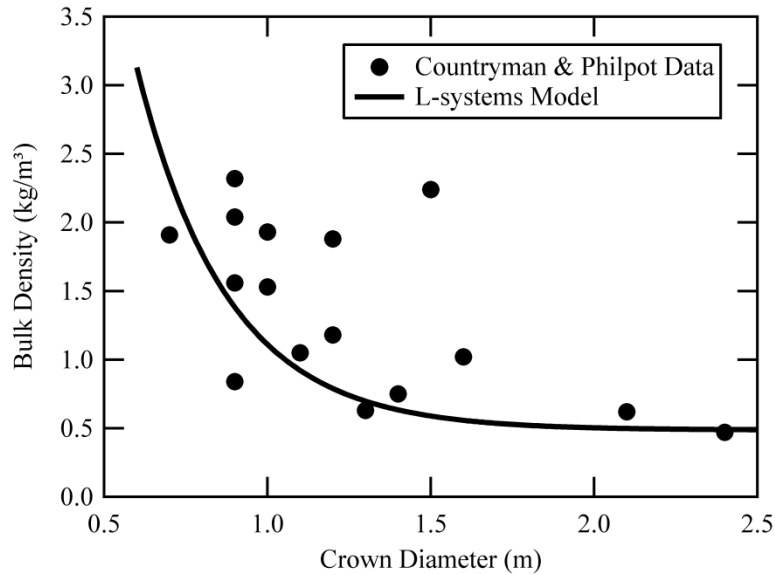


Figure 5-10. Predicted and measured bulk density of chamise as a function of crown diameter for chamise.

5.4.2 Utah juniper

The geometry for modeled Utah juniper is also visually similar to live shrubs. Figure 5-11 shows a picture of a live shrub along with a modeled shrub. The crown diameter of the shrub in the photo was measured, and the model was given the same input. The fuel density of the shrub in the photo was estimated as being between sparse and medium (for model input). The modeled shrub was assigned 35 branches, which falls within this range. Table 5-7 shows a comparison between the dimensions of the shrub and the model in Figure 5-11. The dimensions of the modeled shrub as well as the overall shape are very similar to the live shrub. The predicted height and crown diameter closely match measurements, and the combustible dry mass generated by the model is within 9% of the estimated mass of the shrub in the picture. The dry mass and other dimensions of the shrub were determined by Shen (2013) as described previously.

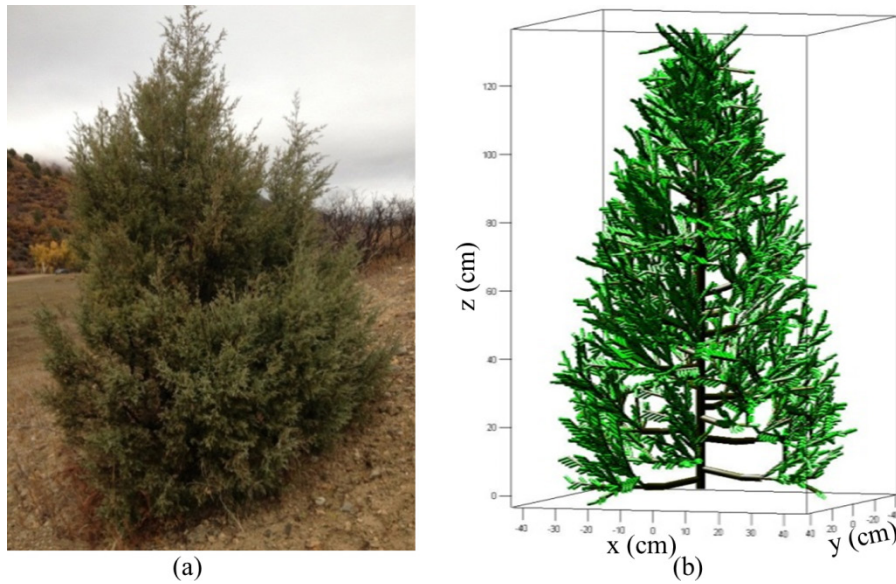


Figure 5-11. Visual comparison of (a) a Utah juniper shrub and (b) a shrub geometry generated by the L-systems approach having 35 branches.

Table 5-7. A comparison of the measurements of the shrub and the modeled shrub shown in Figure 5-11.

Measurement	Measured	Modeled
Height (cm)	140	136
Crown Diameter (cm)	84	90
Dry Mass (g)	664	723

In addition to matching the overall shape of the shrub, another focus of the model was to imitate the placement of fuel elements. Figure 5-12 shows a closer view of one of the branches from the shrub in Figure 5-11 along with examples of branches from the model. The branch curvature and fuel placement are similar. Each terminal cylinder represents one tiny foliage unit (or fuel element) having a mass of 0.102 ± 0.083 g (two standard deviations). The complex branched geometry of the foliage units was not represented.

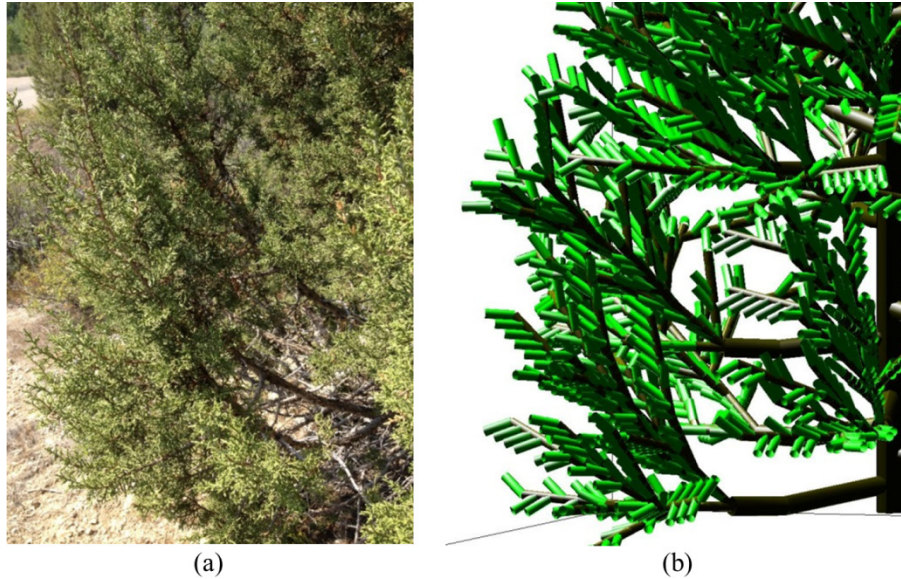


Figure 5-12. (a) A close-up of the Utah juniper shrub and (b) a close-up of a modeled juniper.

The Mason and Hutchings (1967) m_{dry} versus d_{crown} data (collected in Cache County, Utah) with two-standard-deviation error bars is compared to the L-systems model predictions in Figure 5-13. Shen's (2013) data (collected in Utah County, Utah) and its model predictions are also compared. In general the correlation from (Shen, 2013) fell between the medium and dense correlations derived from data reported by Mason and Hutchings. The agreement between the two correlations strengthens the credibility of both. Shrubs using the Mason and Hutchings (1967) three denseness classes are shown in Figure 5-14. The effect of denseness is clearly reflected in the appearance of the shrubs. As with chamise, for larger juniper shrubs some of the modeled primary branches would actually be members of the same branch in a real shrub (Figure 5-14).

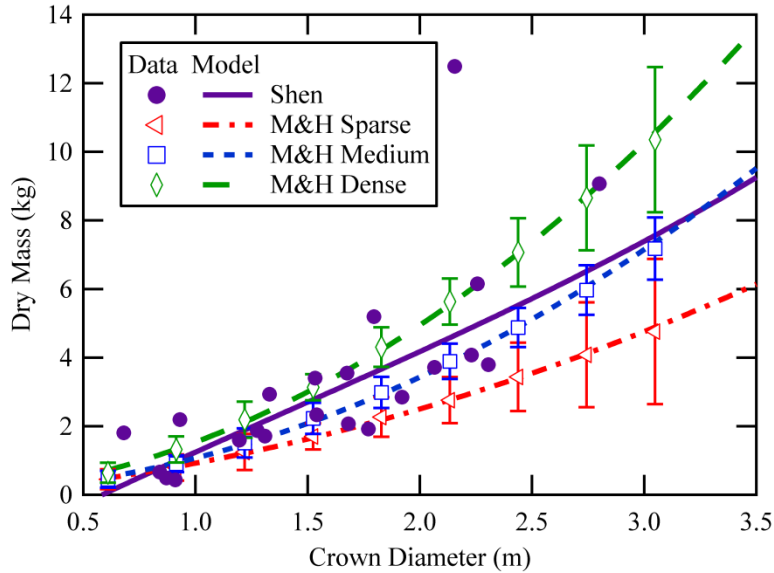


Figure 5-13. Dry mass data (individual measurements from Shen and mean \pm 2 standard deviations for Mason and Hutching) and dry mass of modeled Utah juniper shrubs using each dry mass correlation for various crown diameters.

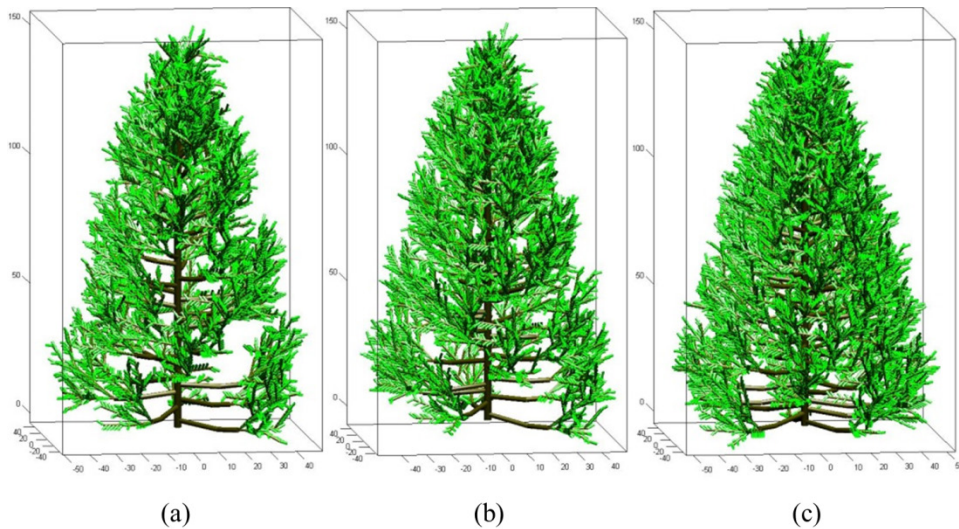


Figure 5-14. Juniper shrubs generated for three classifications of fuel denseness with 1.0 m diameters and 1.6 m heights: (a) sparse with 76 branches; (b), medium with 106 branches; and (c) dense with 152 branches.

The effect of crown diameter on bulk density was also compared between modeled shrubs using the different correlations, seen in Figure 5-15. Bulk density was determined in the model by dividing the total dry mass by the total volume. The total dry mass equaled the sum of the individual masses of all fuel elements. The total volume was determined from the convex

hull of the shrub. In the data presented from Shen (2013), dry mass was determined as previously described and volume was determined based on a cone stacked on a cylinder, with diameters equal to the measurements and respective heights of 75% and 25% the total height.

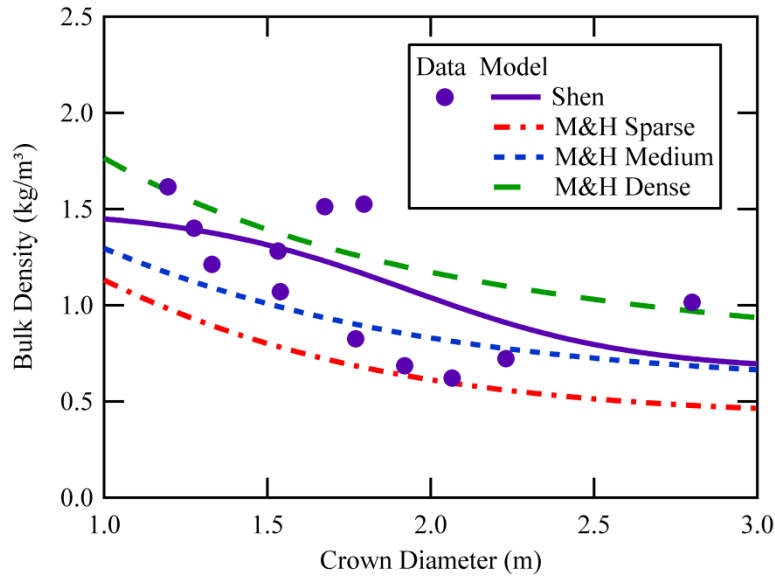


Figure 5-15. Utah juniper bulk density data from Shen and bulk density of modeled juniper shrubs using each dry mass correlation (see Equation 5-6) for various crown diameters.

The influence of crown diameter on bulk density is particularly interesting for the Shen correlation because crown diameter significantly impacts both the mass and the volume of the shrub. Crown diameter directly affects the shrub's dry mass. It also affects volume because it is correlated to the height of the shrub and influences the crown diameter at every height. Hence, as crown diameter increases, both mass and volume also increase. The decrease in bulk density versus crown diameter is due to the fact that the modeled fuel mass is approximately related to the first or second power of diameter (see Equation 5-6) and volume is approximately related to the cube of the diameter. This accounts for the unusual shape of Shen's model.

5.5 Summary and conclusion

Concepts from L-systems theory were incorporated into a model to generate branching shrub geometries specifically for chamise and Utah juniper. L-systems provided the basic framework for individual branch structure, and then several L-systems branches were combined to generate a shrub. The branches were assigned angles so that the overall shape of the shrub would imitate the structure of a real shrub. Additional customizations were added to better match specific characteristics of the individual species. In the chamise model, for example, a variable was added to replicate the characteristic of primary branches exiting the ground close together, but not from one central point. The Utah juniper model also included several customizations, such as having the primary branches emerge from various heights along the trunk of the shrub. Another enhancement to the basic L-system structure in the Utah juniper code included setting the string replacement rules to differ between derivations to simulate the complex structure of juniper branches. Furthermore, lengths and angles were manipulated according to symbol position (in the final string) and branch number (which was a surrogate for vertical position). The juniper customizations resulted in (1) evenly-spaced foliage, (2) primary branches which mimicked the curvature of natural branches and (3) a branching structure reflecting that of real branches.

In order to accurately model the characteristics of each species, geometrical measurements were taken of naturally-growing species and then included in the model. These measurements, including branch lengths and angles, ensured that each model accurately represented its corresponding species.

The chamise and Utah juniper models visually imitate the shrub shapes of their respective species, and also match dry mass data from literature and supplemental measurements. These

characteristics make the chamise and Utah juniper models ideal for generating fuel structures for wildland fire models that require a detailed fuel description.

6. EFFECTS OF MOISTURE ON THE COMBUSTION BEHAVIOR OF DEAD VERSUS LIVE FOLIAGE

The burning behavior of live fuels is different from that of dead fuels. Fire spread is possible at higher moisture contents in live fuels than in dead fuels. Though studies have examined the ignition times, rates of fire spread, moistures of extinction, and the fuel temperature histories of both dead and live fuels in a variety of conditions (Catchpole et al., 1998; Dimitrakopoulos and Papaioannou, 2001; Weise et al., 2005; Fletcher et al., 2007; Pickett, 2008; Dimitrakopoulos et al., 2010; Pickett et al., 2010), a detailed study of the temperature distribution and mass history of single live and dead leaves of similar moisture contents in a wildland fire condition has not previously been performed.

Burning behaviors of individual live and dead manzanita leaves (*Arctostaphylos glandulosa*) were measured in a flat-flame burner. Live and dead manzanita leaves were conditioned to moisture contents above and below the fiber saturation point. Heating patterns and flame behavior were observed in order to determine differences between live and dead heating behavior. Evidence of high internal leaf pressures and moisture retention above 160 °C was found. This chapter describes the measured results while the next describes mass release modeling for the same data set.²

² The results in this chapter have been accepted for publication: Prince, D. R., Fletcher, T. H., "Differences in Burning Behavior of Live and Dead Leaves: 1. Measurements," *Combustion Science and Technology*, **Accepted for publication** (2014).

The objective of this work was to examine the differences in burning behavior of live and dead leaves, especially near the fiber saturation point (this chapter). Furthermore, fundamental models for the mass release of volatiles and water were applied to enable the prediction of mass release at broader conditions (the following chapter).

6.1 Experimental methods

6.1.1 Fuel description

Manzanita (*Arctostaphylos glandulosa*) shrubs are prevalent in California shrublands and their leaves were selected to investigate devolatilization and water release. Manzanita branches were collected in the mountains near Riverside, California and shipped to Brigham Young University in Provo, UT. Four leaf conditions were achieved: (i) fully cured; (ii) rehydrated from a cured state in a humidity chamber; (iii) dried to near the fiber saturation point; and (iv) slightly dried. Leaves given these treatments are hereafter referred to, respectively, as dry dead (4% moisture content, MC, dry basis), rehydrated dead (26% MC), dehydrated live (34% MC), or fresh live (63% MC). Dead and live labels correspond to whether or not the sample had been cured to well below the fiber saturation point (i.e. no water is left in cell lumens and cell walls have contracted). The thickness profile of a sample dry dead leaf is shown in Figure 6-1. The average and standard deviation of leaf thickness of leaves for each group were 0.43 ± 0.05 mm (dry dead), 0.51 ± 0.04 mm (rehydrated dead); 0.52 ± 0.04 mm (dehydrated live); and 0.57 ± 0.05 mm (fresh live).

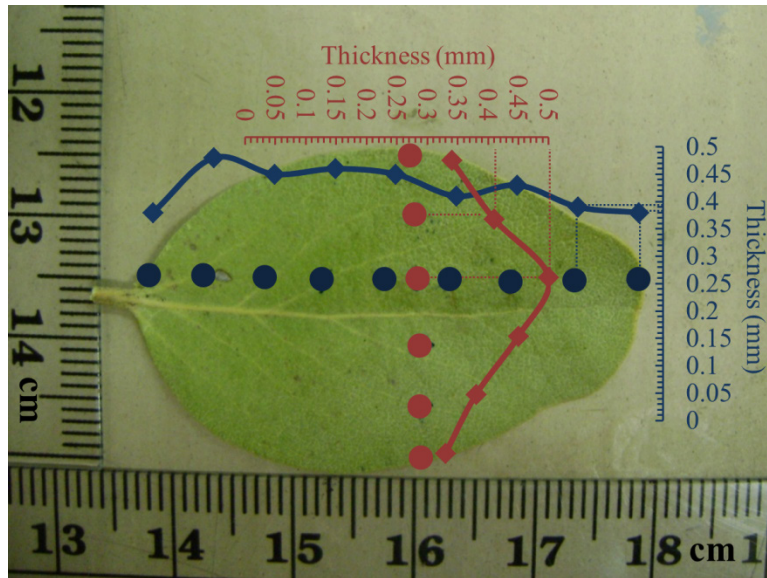


Figure 6-1. Plotted thickness of a dry dead manzanita leaf superimposed on an image of the leaf. The measurement locations are marked and correspond to the plots.

Drying was performed at room temperature with leaves on their branches. Stems were cut at the base of the leaf prior to burning. Several leaves were selected from each group for a moisture content analysis using a Computrac Max 1000 (Arizona Instruments). The moisture content of live (fresh and dehydrated) and dry dead manzanita leaves was stable enough that a single moisture analysis performed during a half-hour sequence of burns was representative of the group. However, additional care was needed for rehydrated dead leaves, which respond quickly to the ambient humidity. Before rehydrating, leaves were individually weighed, and a representative moisture content was measured to determine their dry masses. Each rehydrated leaf was weighed immediately before burning to determine its moisture content. The physical properties of live and dry dead leaves (mass, length, width and height) were also measured just prior to testing. The dimensions of rehydrated dead leaves were measured several hours before burning, and were then replaced in the chamber to maintain their moisture.

6.1.2 Experimental apparatus and instrumentation

Each leaf was suspended in the center of a tempered glass duct by a cantilever mass balance, which was synchronized and time-stamped with video images. A porous 7.5 x 10 inch flat-flame burner (FFB) was quickly rolled into position directly under the leaf and glass cage. The FFB produced a thin hydrogen-methane-air flame (~1 mm thick) with 10 mol% O₂ in the post-flame gas. A K-type thermocouple placed in the post-flame gas at 2 cm, 4 cm and 6 cm above the burner surface measured 997 °C, 985 °C and 962 °C, respectively. Correcting for radiation, the estimated gas temperatures at these heights were 1036 °C, 1023 °C and 997 °C. Details of the radiation correction are included in the appendix. The long dimension of each leaf was oriented vertically with its center at approximately 4 cm and the stem down. A schematic of the experimental setup is shown in Figure 6-2.

Detailed surface temperature of one side of the leaf was recorded with a FLIR camera (Thermovision A20, wavelength 7.5-13 μm). Leaves were estimated to have an emissivity of 0.98 (Lopez et al., 2012). At these wavelengths, the IR camera sees the solid leaf surface but not the soot from the flame. A Matlab script was developed to automatically identify leaf boundaries from IR images, with optional user guidance. In the later portion of a run, leaf folding or twisting sometimes occurred with occasional misidentification of the leaf boundary. These events were monitored but were not observed to significantly impact measured temperature distributions.

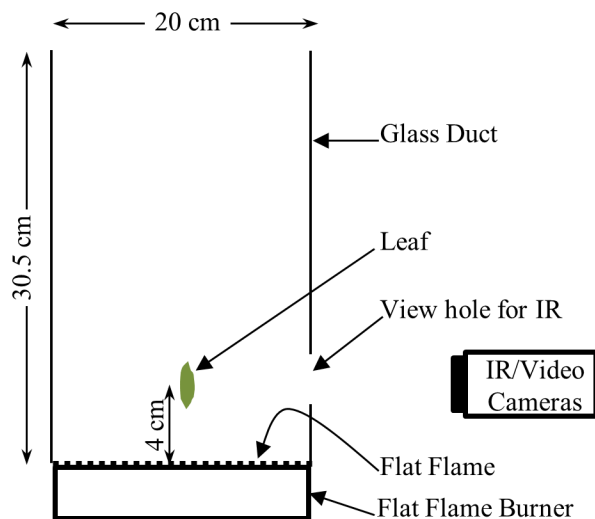


Figure 6-2. Schematic of experimental setup. A leaf is held on the tip of a rod extending from a mass balance through a slot cut in the far glass panel. The FFB is pulled under the glass duct and leaf to begin heating. Temperature and flame behavior are recorded with IR and video cameras. The IR is shot through a 1-inch diameter hole in the glass.

6.2 Results

The dry dead and fresh live groups each consisted of 18 runs. The rehydrated dead and dehydrated live groups each consisted of 19 runs. The following results focus on the average measurements for each group, and when practical, 95% confidence intervals are included.

6.2.1 Heating pattern

Manzanita leaves did not heat isothermally under rapid convective heating conditions. Infrared images show a fresh live leaf heating from the edges in, starting with the bottom (Figure 6-3). Several factors may have contributed to this heating pattern, for example: (a) boundary layer development reduces convective heating along the gas flow path across the leaf, and (b) leaf properties at the edges, such as reduced thickness or moisture content, may accelerate edge heating relative to the rest of the leaf. Large temperature differences were observed between different points of the leaf at the same time. Averaging the runs of each group together, the

largest difference between the 10% and 90% percentile pixel temperatures at any time was 225 K (dry), 332 K (rehydrated), 395 K (dehydrated), and 445 K (fresh). The interval increased with the starting moisture content of the group.

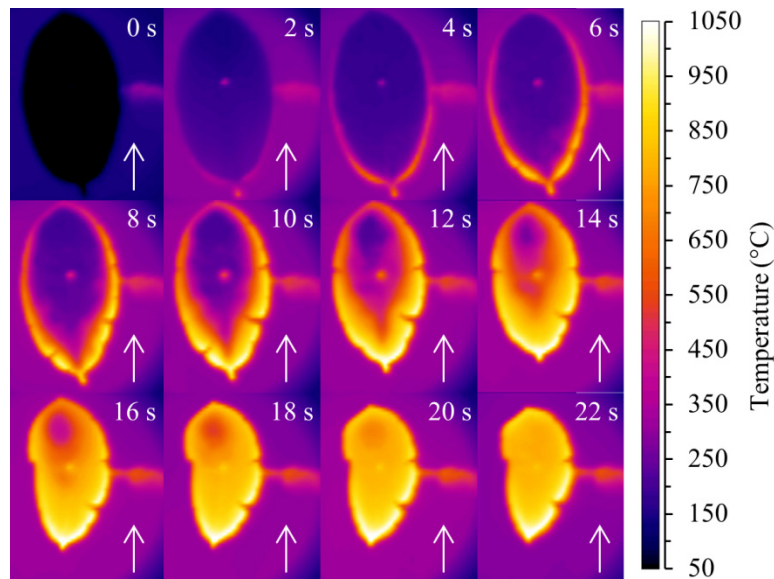


Figure 6-3. IR thermal images of a fresh live manzanita leaf during heating at 2 s intervals. Temperature maps such as these were averaged with other runs to produce the histograms in Figure 6-4 and Figure 6-5. The bright dot in middle is a metal needle skewering the leaf. The arrows show direction of upward gas flow.

6.2.2 Differences in early temperature distribution

Leaf face temperatures were recorded with infrared video for the duration of each burn. This section discusses the temperature distribution at an early residence time (3 s of heating) when water release was expected to be very relevant. Following sections examine leaf temperature over time.

Differences were found in the temperature distributions of live and dead leaves at a residence time of 3 s (see Table 6-1). There were strong similarities between the live groups (i.e. dehydrated and fresh), while the temperature distribution statistics at 3 s for the live groups differed from either of the dead groups (i.e. dry and rehydrated).

Histograms of surface temperature with 20 K bin-widths and a 95% confidence interval (CI) on each bin at a residence time of 3 s are shown in Figure 6-4. Fractions of leaf surface area in each bin were determined by pixel-counting. The statistics listed in Table 6-1 are reflected in Figure 6-4. Particularly, the values of kurtosis (a measure of peakedness) quantify the relative height of the peaks and sharp shoulders observed for live leaves (Figure 6-4, c & d). The kurtosis, coupled with the lower dispersion of live leaves, indicates a high level of temperature uniformity. In contrast, the kurtosis of dead leaves (Figure 6-4, a & b) was closer to three, or that of a normal distribution, indicating a smoother transition from edge temperatures to middle temperatures. Furthermore, the temperatures of dead leaves were distributed over a wider range, as indicated by their high values of dispersion. Live leaves exhibited more temperature uniformity and lower temperatures than dead leaves (even the moist rehydrated leaves) during early residence times.

Table 6-1. Statistics on average leaf temperature distributions after 3 seconds of heating.
 (*Dispersion is represented by the interquartile range, which is appropriate for lognormal distributions (Shoemaker, 1999))

	“Dead” leaves		“Live” leaves	
	Dry	Rehydrated	Dehydrated	Fresh
Mean (°C)	400 ± 17	248 ± 14	190 ± 5	191 ± 8
Dispersion* (K)	80	68	30	23
Skewness	1.5 ± 0.1	2.0 ± 0.2	2.9 ± 0.1	2.6 ± 0.3
Kurtosis	4.7 ± 0.4	6.9 ± 1.3	11.7 ± 1.2	11.3 ± 2.2

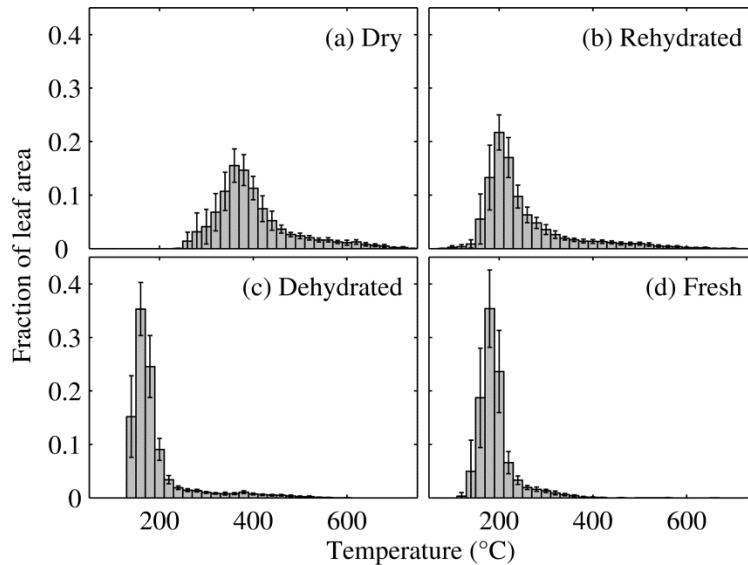


Figure 6-4. Temperature histograms of all the temperature data across the whole leaf face at 3 s of heating, averaging all 18-19 runs for (a) dry dead leaves, (b) rehydrated dead leaves, (c) dehydrated live leaves, and (d) fresh live leaves. Error bars represent 95% CIs on the fraction of leaf area. Fraction of leaf area is determined by pixel counting of the IR images.

6.2.3 Effects of moisture content and moisture history

Average temperature histograms of each leaf group at 2 s intervals are presented in Figure 6-5. Over the 8 s period shown, the temperature rise stalled for all moist groups, but not for the dry group. This suggests that moisture is the cause of the observed temperature stall (e.g. by moisture evaporation or desorption). The temperature stall was least pronounced for the rehydrated dead group, even though its moisture content was similar to that of the dehydrated live group. This further suggests that moisture history (or state) also influences moisture's effect on heating. When previously dried leaves absorb humidity from the air, water binds to cellulose and hemicellulose. Leaves which have not been dried past the fiber saturation point retain some moisture as bulk (or liquid) water. The temperatures stalled above the normal boiling point of water: 170 °C to 210 °C (rehydrated dead), 150 °C to 190 °C (dehydrated live), and 150 °C to 230 °C (fresh live). The likelihood of water accounting for temperature stalls at elevated temperatures is discussed later.

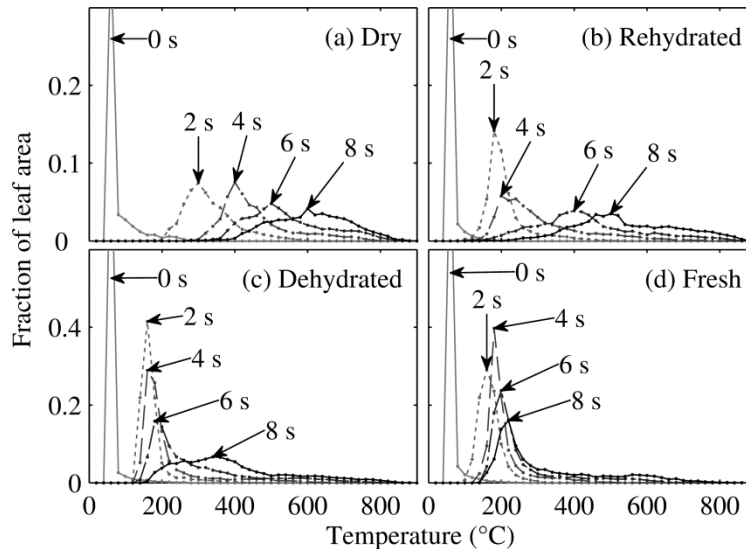


Figure 6-5. Traces of temperature histograms for all temperature data across the whole leaf at 2 s, 4 s, 6 s and 8 s, averaging all 18-19 runs for (a) dry dead leaves, (b) rehydrated dead leaves, (c) dehydrated live leaves, and (d) fresh live leaves. Each marker represents one histogram bin (see Figure 6-4).

6.2.4 Effects of moisture content on temperature plateaus

Moisture held in live leaves had a different effect on the leaf temperature of heating leaves than moisture held by dead leaves. Taking the mode from histograms (20 K bin widths) and plotting over time reveals a temperature plateau for all moist groups (Figure 6-6). The modes are bounded by 95% point-wise confidence bands. The temperature plateau of the rehydrated dead leaves was less flat and at a higher temperature (about 200 °C) than that of the dehydrated or fresh live leaves (both at about 175 °C). Dry dead leaves showed no temperature plateau.

The duration of the temperature plateaus were 2 s (rehydrated), 5 s (dehydrated), and 8 s (fresh). Though the amount of moisture affected the duration of the dehydrated and fresh leaf plateaus, their temperatures and slopes were similar. The temperatures, slopes and durations of the rehydrated and dehydrated leaves differed, demonstrating that moisture held in live leaves had a stronger effect on leaf temperature than did moisture held in dead leaves. Again, this may reflect differences in the behaviors of bulk and adsorbed water.

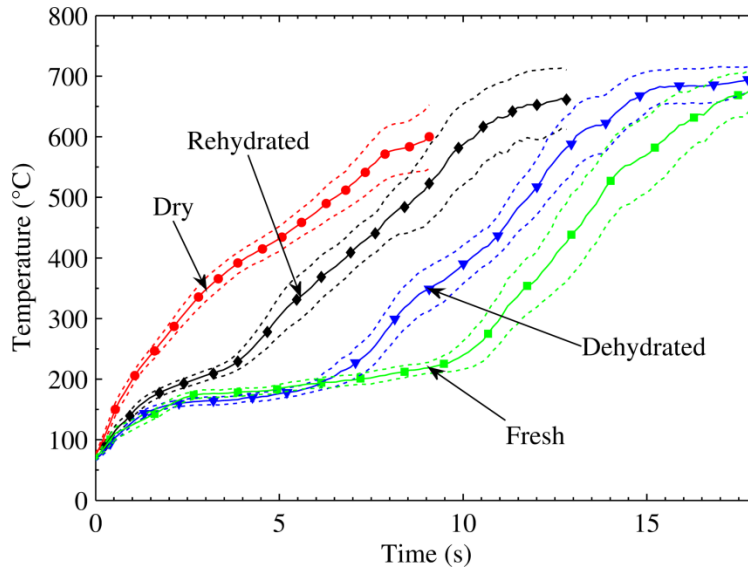


Figure 6-6. Mode temperatures averaged for each leaf group. Average values (solid with markers) are bounded by 95% CIs (dotted).

6.2.5 Use of mode as a moisture marker

The mode temperature, taken from histograms (20 K bin widths), is well-suited to identifying regions where water is being released. The mode is the largest isothermal leaf area. Areas where water evaporates are roughly isothermal because water evaporation is highly endothermic and stabilizes temperature at the boiling point. If this is true, then given the high mode temperature, a high internal pressure is implied (see Figure 6-7). The boiling temperature and diffusion rates of moisture from the leaf are both functions of internal leaf pressure. Pressure and boiling temperature are stabilized when steam diffusion rates equal evaporation rates, and the heat absorbed by evaporation balances heat transfer to the leaf region. A leaf region where water is being lost therefore becomes isothermal compared to the temperature distribution of the remaining leaf. Thus the mode temperature was tracked in order to recognize areas of water release. Convective transport and structural failure were not considered to be important, but may be included as topics for future research.

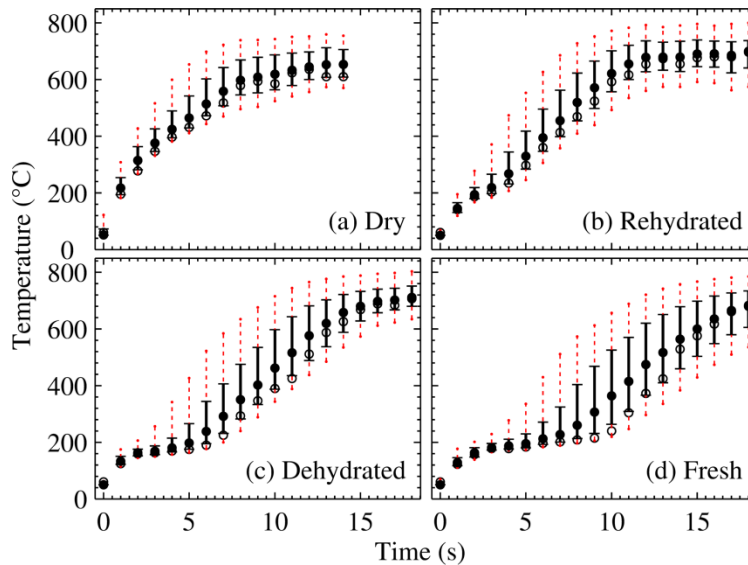


Figure 6-7. The average distribution of leaf surface temperature is plotted vs. time for each leaf group. Temperature distributions are described by the median (filled circle), middle 50% (inner bar), middle 80% (outer dotted bar) and mode (open circle).

The mode temperature (plotted as open circles) is shown in context of the leaf temperature distribution in Figure 6-7 at 1 s intervals. The range from the 25% to 75% percentiles is drawn with solid inner bars, the 10% to 90% range is drawn with dotted outer bars, and the median is plotted as filled circles. While not plotted, the mean temperature closely followed the median temperature. The mode stagnated between 165 °C and 220 °C for dehydrated and fresh leaves while other parts of the leaves increased in temperature. Above these temperatures it is unlikely that pockets of moisture remained, so the mode was no longer regarded as a moisture marker.

6.2.6 Additional evidence of moisture release during the temperature plateau

Little moisture was released before the moist leaves reached temperature plateaus. Figure 6-8 plots the leaf temperature distribution versus normalized mass release at 5% increments for each leaf group. The same markers were used as were described for Figure 6-7. The temperatures plateaued by the time 5% of the mass was released. Depending on the group, at least 76% to 87%

of the starting moisture was retained upon reaching the plateau temperature (based on a moisture mass balance and assuming that water accounts for all of the initial mass release). The remaining moisture was released afterwards, providing cooling to the leaves.

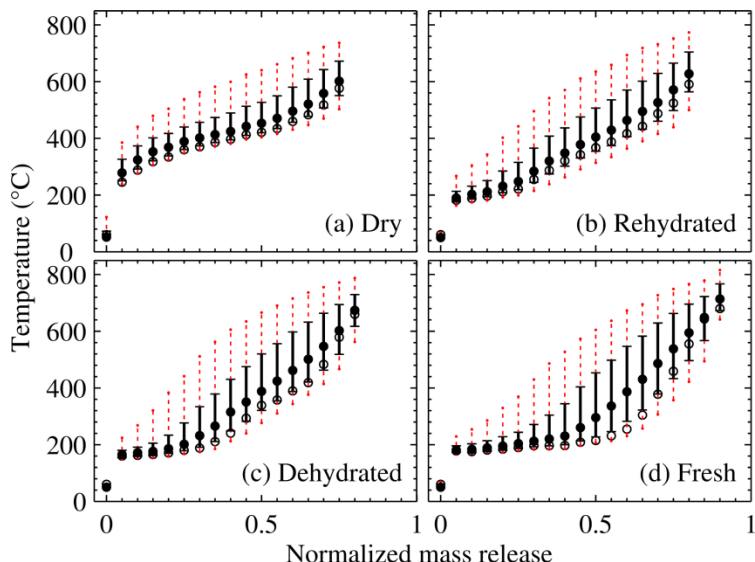


Figure 6-8. The average distribution of leaf surface temperature is plotted at various stages of conversion for each leaf group. Temperature distributions are described by the median (filled circle), middle 50% (inner bar), middle 80% (outer dotted bar) and mode (open circle).

Moisture comprised 21% (rehydrated), 25% (dehydrated) and 39% (fresh) of the starting leaf mass (i.e. dry mass and moisture) for each moist leaf group. Plotting mode temperature (from histograms with 20-K wide bins) for each leaf group shows that the temperature plateaus did not end until the mass release was equal to or greater than the starting moisture mass (Figure 6-9). If the moisture was completely released before any portion of other leaf components, water would persist in the leaves until more than half way (by mass) through the temperature plateaus. However, because the hottest parts of the leaves were above 400 °C by the end of the temperature plateaus (see Figure 6-8), it is more likely that some of the mass release was due to pyrolysis and that water provided cooling until the end of the temperature plateaus. This is not to suggest that lignocellulosic decomposition could account for the temperature plateaus, since the

plateaus began at temperatures below the decomposition temperatures given by Di Blasi (2008) and Biagini and Tognotti (2014).

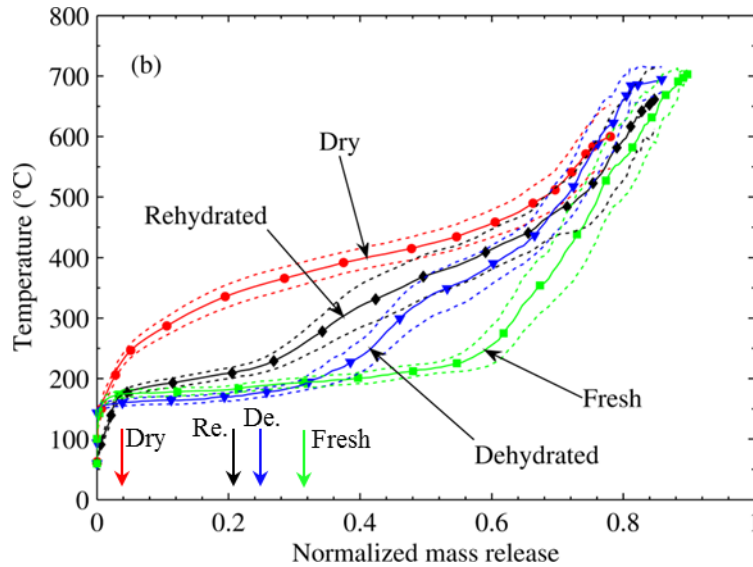


Figure 6-9. Average mode temperature vs. normalized mass remaining for each leaf group Average mass (solid with markers) is bounded by point-wise 95% CIs (dotted). Arrows pointing the x-axis indicate the total mass fraction of moisture starting in the leaves for each group.

The shape and behavior of the flames of moist leaves were consistent with the scenario of moisture release during the temperature plateaus. Substantial pressure would be required to maintain liquid water at the leaf temperatures measured during the temperature plateaus. The flames of dehydrated and fresh live leaves were unsteady and distorted, consistent with the release of high-momentum jetting vapors (Figure 6-10). This momentum was observed disrupting and propelling the flame in downward or outward directions. However, the flames of rehydrated dead leaves were, on average, less erratic than those of live leaves. Images in Figure 6-10 show that the rehydrated leaves frequently had smoother and steadier flames than the live leaves. Since the moisture of rehydrated leaves is in an adsorbed rather than liquid state, it is not surprising that the flames of the rehydrated leaves showed less effect of high-momentum vapor release. Still, effects of high momentum mass release were seen in many rehydrated runs. The

erratic jetting behavior of live leaves seems to be a key difference in flame behavior between live and dead fuels, and is ultimately evidence of pressurized moisture release.

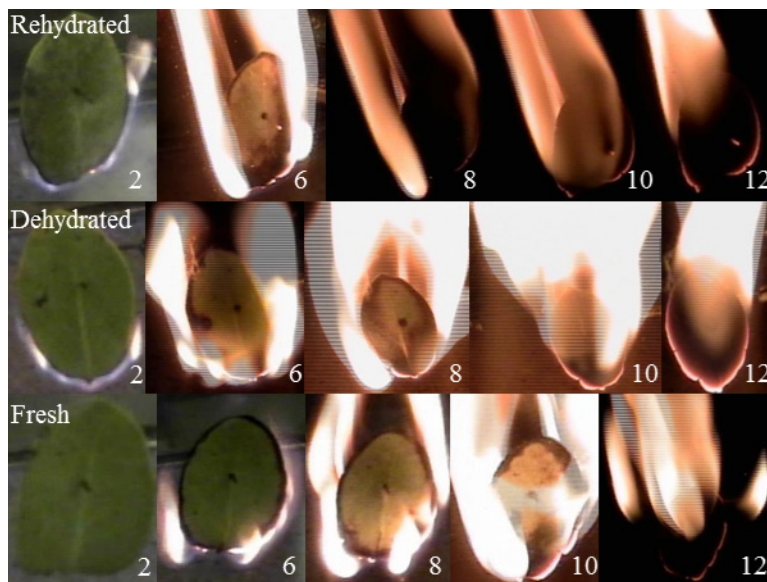


Figure 6-10. Images of rehydrated dead, dehydrated live and fresh live leaves during heating at 2, 6, 8, 10 and 12 seconds. Zooming is adjusted to include relevant flame behavior.

For leaves to withstand the vapor pressure of water at approximately 200 °C, they must tolerate internal pressures approaching 8 atm. This is equivalent to the vapor pressure of water at 170 °C or of a solution with a 30 °C boiling point elevation at 200 °C. Plant cells have been observed to withstand pressures exceeding these levels (Carpita, 1985). Additionally, evidence of high internal pressure (i.e. bursting, bubbling, crackling, hissing and jetting) has been observed for multiple species, including manzanita (Smith, 2005; Fletcher et al., 2007; Shen, 2013). The violent release of moisture (e.g. bursting) is associated with high initial moisture contents (Fletcher et al., 2007).

This study builds on previous work performed using methods described by Pickett (2008). Previously unreported experiments were performed to measure the amount of water remaining in manzanita leaves (47-107% MC) after precisely controlled heating exposures. The

leaves, immediately quenched with nitrogen, were then weighed and their moisture contents evaluated to determine the amount of moisture retained. The exposure time was controlled by a timer and a solenoid valve. Table 6-2 shows the mean moisture mass at each quenching time divided by the initial leaf mass. At 7 s of exposure, moisture was still present. These data provide direct measurements of the longevity of moisture release at similar gas temperatures and O₂ concentrations as in the experiments described earlier in this paper.

Table 6-2. Summary of water content measurements for nitrogen-quenched manzanita leaves of various heating intervals ($m_{w,q}$ = mean mass of moisture at quenching, m_0 = mean initial leaf mass, \pm 95% confidence interval, n = number of measurements).

Quenching time (s)	n	$m_{w,q}/m_0$	Initial MC of leaves
1	20	0.48 ± 0.03	79%
2	20	0.43 ± 0.04	77%
3	69	0.35 ± 0.03	107%, 61%, 47%, 75%
4	20	0.29 ± 0.06	77
5	20	0.24 ± 0.05	70%
6	31	0.17 ± 0.04	80%, 47%, 74%
7	20	0.13 ± 0.07	79%

6.2.7 Differences in mass release

Dead leaves released mass more quickly than did live leaves in these experiments (Figure 6-11). This difference is statistically significant based on the non-overlap of their 95% confidence bands. Moisture content delayed mass release in rehydrated dead leaves. The dehydrated and fresh live leaves had similar mass release profiles and their confidence bands partly overlapped.

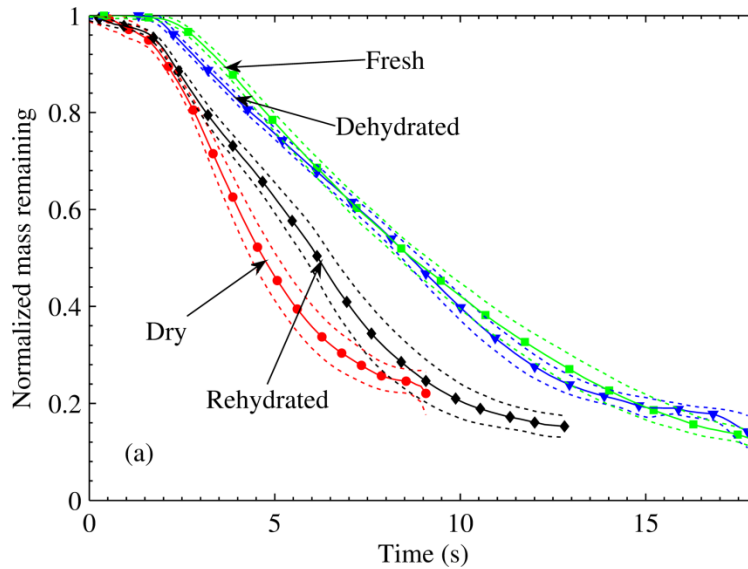


Figure 6-11. Average normalized mass remaining for each leaf group vs. time. Average mass (solid with markers) is bounded by point-wise 95% CIs (dotted).

6.3 Discussion

The measured burning behaviors of live and dead foliage have implications for wildland fire models. Leaf edges reached ignition temperatures first, indicating that ignition and burning does not occur simultaneously across a manzanita leaf, but progresses from the edges towards the center. Moisture content and moisture state impact the duration and flatness of temperature plateaus. Go-no-go predictions for prescribed fires depend on correctly describing heat transfer from burning fuels in the flame zone to neighboring fuels. The temperature distribution, moisture release, and combustion behavior of live and dead leaves are important factors in modeling heating and heat release in a rigorous manner. Thermal modeling of leaves heated in wildland fire conditions can better distinguish between the behavior of live and dead fuels using the results presented here.

6.4 Summary and conclusions

A flat-flame burner was brought under individual live and dead manzanita leaves in a well-controlled, well-instrumented apparatus. The burning behavior of each leaf was measured and analyzed. This is the first set of experiments to determine fundamental differences in the burning behavior of live and dead fuels near the fiber saturation point. First, the temperature plateaus of live leaves were cooler (occurring at approximately 175 °C), flatter, and longer-lasting than the temperature plateau of rehydrated dead leaves (occurring at approximately 200 °C), even though rehydrated leaves had a similar moisture content as dehydrated live leaves. Second, live leaves showed radial and non-uniform flame movement due to high-momentum jetting, indicating high internal leaf pressures. The flames of rehydrated dead leaves were smoother and less erratic than those of live leaves, and high-momentum mass release effects were observed to a lesser extent in rehydrated leaves than live leaves. Third, moisture was retained for all moisture-laden leaves into the 160 °C to 220 °C range, which is above the normal boiling point (100 °C) of water. This finding was supported by direct measurements of moisture content at precise residence times from the quenching study. Concurrent release of pyrolyzates and moisture was identified.

A single temperature does not adequately describe rapidly heated manzanita leaves. Kinetic modeling of leaves or other biomass of similar size should consider their wide temperature distribution during rapid heating, such as in wildland fire conditions. Water release models for these conditions should not assume water release at 100 °C.

7. KINETIC MODELING OF MASS RELEASE FROM DEAD AND LIVE FOLIAGE

Differences in the observed fire behavior of dead and live foliage were described in the previous chapter, including differences between live and dead leaves near the fiber saturation point. Moisture was retained in both dead and live leaves up to leaf surface temperatures between 160 °C and 220 °C. However, questions remained concerning: (1) the local internal leaf temperature during local moisture release; (2) possible mechanisms of moisture release; and (3) whether separate models were needed to model water release from live and dead fuels. Furthermore, fundamental mass release models for both water and dry matter were desired to predict mass release over a range of heating rates.

7.1 Model formulation

The model formulation is discussed in several sections, each of which focuses on a particular aspect of the modeling:

1. Leaf surface temperature (input to mass release models)
2. Internal leaf temperature (modeled by 1-D conduction or set to surface temperature)
3. Composition estimation (of biomass) and component modeling
4. Devolatilization models
5. Moisture release models
6. Internal heat and mass transfer considerations

The release of water from live and dead leaves of similar moisture contents was of particular interest since it may play a role in the different fire spread behaviors observed in live and dead fuels. The modeled mass release was compared to the transient leaf mass measurements. However, the modeled mass was the combination of dry biomass components and water. Therefore, it was important to choose credible devolatilization models to enable accurate conclusions about water release models.

7.1.1 Leaf surface temperature

Manzanita leaves have broad faces but are relatively thin (approximately 0.5 mm). The long dimension of each manzanita leaf was oriented vertically above the flat flame burner surface during heating. Temperature differences in the thickness dimension were expected to be small but could not be directly measured. However, the surface temperature of each leaf face was measured from infrared video recording throughout burning. The variance in surface temperatures motivated dividing the surface into sections for accurate mass release modeling. However, a simpler approach is appealing to reduce computational cost. Therefore, surface temperature was also represented by its: (a) arithmetic mean; and (b) mean kinetic temperature (defined later in Equation 7-1).

7.1.1.1 Temperature in gridded sections

To take advantage of the detailed infrared temperature measurements of the leaf surfaces, each leaf face was subdivided into a grid of 30 rows by 20 columns on each row, resulting in 600 equally-sized areas (Figure 7-1). The temperature of each area was found by averaging the temperature value of all pixels within its boundaries. Mass release for each leaf component was calculated independently for each area based on the local temperature history, and then combined

with the results from all other areas to determine a total mass release profile. Mass release models are discussed in detail later. The grid was adjusted throughout heating to follow the movement and shrinking of the leaf while maintaining equal-area sections. When conduction was modeled, it was calculated through the thickness of each grid area, and for each node mass release for each component was calculated. Conduction is discussed in detail later.

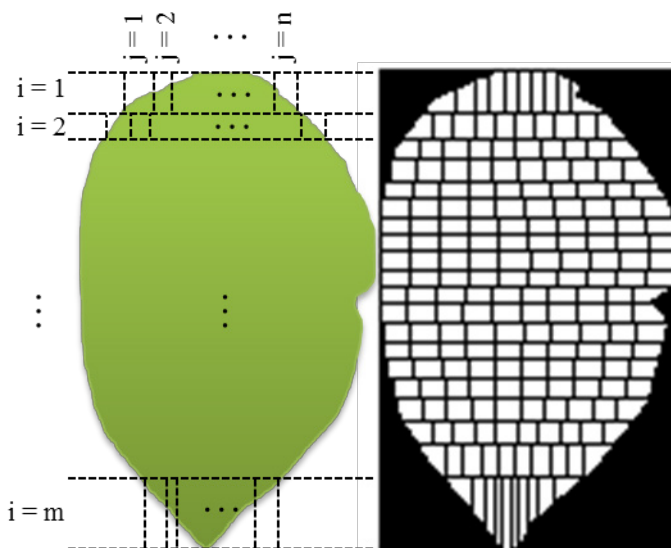


Figure 7-1. Schematic of equal-area leaf sections.

7.1.1.2 Arithmetic Mean Temperature and Mean Kinetic Temperature

Dividing the leaf into hundreds of sections and calculating mass release for each independent section is computationally expensive. Mean temperatures offer a computationally cheap alternative, but reduce the capacity of the model to accurately represent widely dispersed temperatures. The arithmetic mean temperature was the average temperature of all leaf pixels. When used, one value was used to represent the entire leaf temperature for every time step.

Mean kinetic temperature (Equation 7-1) is a single derived temperature which, over some period of time, results in the same amount of chemical degradation of some material as

would result from a range of higher and lower temperatures experienced over the same span of time (ICH - Technical Coordination, 2003). The mean kinetic temperature ($T_{m,k}$) takes into account the nonlinear response of degradation to temperature fluctuations (Haynes, 1971). $T_{m,k}$ uses the Arrhenius equation activation energy E and the gas constant R . A series of time duration t_i and temperature T_i describe the temperature history of the material, where the subscript i denotes the position in the series (see Equation 7-1). As E approaches zero, $T_{m,k}$ approaches the harmonic mean, and as E approaches infinity, $T_{m,k}$ approaches the maximum of T_i . For typical values of E , $T_{m,k}$ is greater than the arithmetic mean.

$$T_{m,k} = \frac{\frac{E}{R}}{-\ln \left[\frac{\sum_i \left(t_i e^{-\frac{E}{RT_i}} \right)}{\sum_i t_i} \right]} \quad (7-1)$$

Although $T_{m,k}$ was developed for temperatures experienced in series (i.e. over time), it was hypothesized that $T_{m,k}$ could be applied to average temperatures experienced concurrently. This was implemented by finding $T_{m,k}$ for the entire leaf at each time step.

The most notable disadvantage of using mean temperatures, as compared to calculating mass release independently for multiple gridded sections, is that there is no way to account for differing levels of mass release in different parts of the leaf: the whole leaf is represented as experiencing a single temperature history.

7.1.2 Internal leaf temperature

Internal leaf temperatures were not measured. Internal leaf temperature was either (a) considered equal to the surface temperature, or (b) modeled using 1-D conduction, including a heat generation term accounting for water vaporization. The 1-D heat equation (Equation 7-2)

was discretized using the explicit form of a finite-difference equation with the heat generation term delayed one step (Equation 7-3) (Çengel, 2007):

$$\frac{\partial T}{\partial t} = \alpha \frac{\partial^2 T}{\partial z^2} + \frac{\dot{e}}{c_p \rho} \quad (7-2)$$

$$T_m^{i+1} = \tau(T_{m-1}^i + T_{m+1}^i) + (1 - 2\tau)T_m^i + \tau \frac{\dot{e}_m^{i-1} \Delta z^2}{k} \quad (7-3)$$

where α is the thermal diffusivity, τ is the mesh Fourier number ($\alpha \Delta t / \Delta z^2$), \dot{e} is the volumetric energy generated, T is the absolute temperature, and z is the coordinate in the leaf thickness direction. Subscripts indicate the node position, spanning from the surface (measured boundary condition) to half way through the thickness of the leaf (symmetry boundary condition) (Figure 7-2).

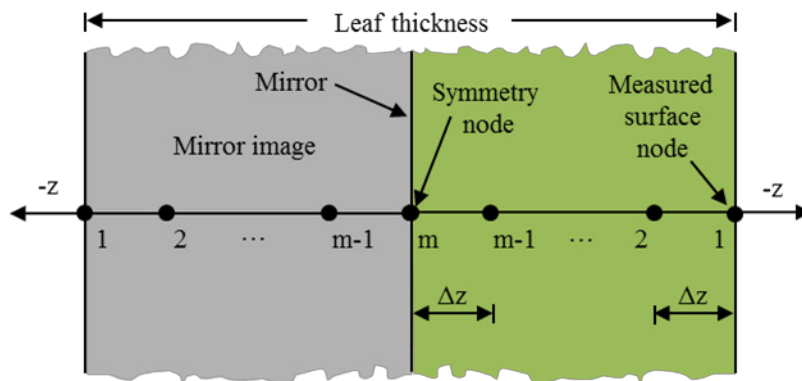


Figure 7-2. Schematic of finite difference formulation for conduction into a leaf. Compare to Çengel (2007).

Superscripts indicate the time step; where i is the previous time, and $i+1$ is the new time. The amount of water evaporated during the previous calculated time step was used to determine the value of \dot{e} , based on the heat of vaporization of water at 100 °C. Equation 7-3, shown for interior nodes, was adjusted at the symmetry surface by replacing T_{m+1}^i with T_{m-1}^i . Several thermophysical properties were needed to calculate τ . Heat capacity was calculated for moisture contents above and below the fiber saturation point using the method described by Glass and

Zelinka (2010). Thermal conductivity was estimated using moisture content-correlated equations for wood (Forest Products Laboratory, 1952), and using an average measured density ρ of dried manzanita leaves of 0.894 g cm^{-3} .

Conduction was used with the gridded treatment based on the leaf surface temperature. For each gridded area, temperatures were calculated using the measured surface temperature as the boundary condition and a symmetry node at the leaf center. Mass release for each component was calculated at each node.

7.1.3 Composition estimation and component modeling

The principal components of lignocellulosic biomass are cellulose, hemicellulose, lignin and water. For modeling the mass release of manzanita leaves, a water release model coupled with a one-component dry matter release model would be appealing for computational simplicity. However, cellulose, hemicellulose and lignin have different mass release behaviors (Di Blasi, 2008), suggesting that a multi-component dry matter model would be more kinetically robust. Both approaches were investigated.

The modeled composition of the dry matter of manzanita leaves was estimated from a correlation by Sheng and Azevedo (2002) using values from an ultimate analysis by Pickett (2008), yielding a composition of 33% cellulose, 32% hemicellulose and 35% lignin. The modeled moisture fraction was determined from leaf measurements. Total mass release during heating was modeled by superimposing each of the individual component mass release models.

7.1.4 Devolatilization models

Four devolatilization models were configured to model dry matter mass release: (1) the Chemical Percolation Devolatilization (CPD) model; (2) a multi-component, one-step model; (3)

a single-component, one-step model configured to match the mass release data; and (4) a single-component, one-step model restricted to more conventional kinetic parameters for biomass.

7.1.4.1 Chemical Percolation Devolatilization

The CPD model (Grant et al., 1988; Fletcher et al., 1989; Grant et al., 1989; Fletcher et al., 1990) was originally developed to describe the devolatilization behavior of rapidly heated coal. CPD was later extended to biomass (cellulose, hemicellulose and lignin), calling it Bio-CPD (Lewis and Fletcher, 2013). Bio-CPD required new ^{13}C NMR (nuclear magnetic resonance) parameters and a new base structural unit definition for each component. The CPD model treats devolatilization on a structural level. The breakdown of the macromolecular structure and consequent release of tar precursors is modeled by percolation lattice statistics. As labile bridges are activated, they are either cleaved to form side chains (which are consumed in a slower reaction) or form stable char bridges, releasing light gas. Molecules freed from the macromolecular structure may either (1) be crosslinked back into the structure, or, (2) are freed from the macromolecular structure. The state of freed fragments is determined by flash vapor-liquid equilibrium, whether the fragments remain associated with the structure as liquid or enter the gas phase as tar or light gas. Fuel-independent kinetic parameters are used as well as fuel-dependent parameters from ^{13}C NMR measurements. There is also only one empirical parameter, which remained constant for these calculations. CPD determines char, tar and gas yields as well as tar and gas composition. The CPD model responds to heating rate, heating history, and ambient pressure.

CPD was adapted for MATLAB (from FORTRAN 77) to interface directly with existing MATLAB data structures. In doing so, a new flash routine was written which followed the Rachford-Rice procedure as described by Seader and Henley (2006). The predictor-corrector

scheme used to solve a system of differential rate equations was replaced with a matrix exponential method, which marginally decreased computational time and permitted larger time steps. A conservation of mass error was discovered which resulted in unstable model calculations for some biomass components at long residence times. This error was caused by correcting negative mass fractions input to the flash routine to zero without preserving the total mass. This was resolved by scaling the remaining positive mass fractions in order to conserve total mass. Other sections of the code were translated without significant modification.

The CPD model was also integrated into an object-oriented class. Object-oriented programming associates data fields and procedures into an object. The specific data fields and procedures possessed by an object are defined by templates called class declarations. The values of the class-defined data fields are persistent and define the state of the object. The CPD class was defined such that the devolatilization calculation could be advanced to any time included in the time-temperature profile and resumed at a later time. Additional time and temperature data could be appended to the existing time-temperature profile whenever desired. Multiple CPD objects could be instantiated (or created) from the same class declaration and exist in the variable workspace at the same time, and each object retained its own state in memory. In MATLAB, arrays of objects can also be formed.

The object-oriented structure allowed any number of CPD objects to be instantiated and manipulated concurrently, allowing mass release calculations for multiple components and leaf locations to run side-by-side. These capabilities were particularly useful when determining 1-D conduction through the leaf, because the temperature of internal nodes at each new time depended on the mass release of the previous time step. Similar structures and capabilities were also prepared for the water release models, which ran alongside CPD.

7.1.4.2 Single-component one-step devolatilization model

A single-component one-step devolatilization model was developed as a fast and simple alternative to other devolatilization models. One-step devolatilization models have the following form (Badzioch and Hawksley, 1970):

$$\frac{dV_i}{dt} = A_i \exp\left(\frac{-E_i}{RT}\right) (V_{\infty i} - V_i) \quad (7-4)$$

where V is the fraction of initial mass released, t is time, A and E are the pre-exponential factor and activation energy, R is the gas constant, T is the absolute temperature, the subscript i indicates which component, and the subscript ∞ identifies V as the ultimate possible value. Two sets of single-component kinetic parameters were found, termed set (a) and set (b) (Table 7-1). Parameter set (a) optimized agreement with the mass release measurements, but was not in the typical range of Arrhenius parameters. Parameter set (b) was tuned for model agreement with measurements, but A and E/R were only allowed values within set ranges. Minimum and maximum limits for A were $3 \cdot 10^{13} \text{ s}^{-1}$ and $5 \cdot 10^{19} \text{ s}^{-1}$, and for E/R , 19,237 K and 34,747 K.

Table 7-1. Parameters of single-component one step devolatilization models.

Model	V_{∞}	$A \text{ (s}^{-1}\text{)}$	$E/R \text{ (K)}$
Single component, set (a)	0.85	100	4,300
Single-component, set (b)	0.85	$3 \cdot 10^{13}$	22,737

Although set (a) provides a better fit with measurements, it severely limits the model to these experimental conditions. Set (b) was confined to reasonable parameter ranges for biomass so that the model would be more reliable outside of these experimental conditions, but sacrificed agreement with experiments. The conflict between experimental agreement and credible parameters exists because a single component model is unable to fully represent the behavior of multiple kinetically-distinct materials.

7.1.4.3 Multi-component one-step devolatilization model

For the multi-component approach, the leaf mass was divided into cellulose, hemicellulose, lignin and water as described above. The cellulose, hemicellulose and lignin components were then each subdivided into side chain and cluster parts, with molecular weights of each part as given by Fletcher et al. (2012). Side chains, clusters and the coordination number ($\sigma + 1$) were discussed for biomass in the context of the CPD model by Fletcher et al. (2012). The coordination number represents the number of side chains for every cluster, and can be used to provide the number fraction of side chains and clusters. The number fractions can be converted to mass fractions using their associated molecular weights (see Table 7-2).

The Arrhenius constants determined by Fletcher et al. (2012) for bridge-breaking and gas formation were assigned as the one-step Arrhenius parameters for side chain and cluster devolatilization, respectively, assigning side chains the more reactive bridge-breaking parameters (see Equation 7-4). Use of these parameters in a one-step model is not consistent with their original definitions; however, they represent bond-breaking reactions, which control the devolatilization rate. Ultimate volatiles yields are given in Table 7-2 and sum to 0.85. The nonvolatile fraction was distributed completely to the cluster portion. One-step models for each part were calculated in parallel then combined.

Table 7-2. Multicomponent one-step devolatilization parameters (m_i = mass of component or part, m_{dry} = mass of dry matter).

Component: Part:	Lignin		Hemicellulose		Cellulose	
	Cluster	Side chain	Cluster	Side chain	Cluster	Side chain
m_i/m_{dry}	0.35		0.32		0.33	
m_i/m_{dry}	0.21	0.14	0.17	0.15	0.18	0.15
V_∞	0.78		0.78		1.0	
V_∞	0.639	1.0	0.585	1.0	1.0	1.0
A (s^{-1})	2.3×10^{19}	7×10^{16}	3×10^{13}	5×10^{19}	3×10^{15}	2×10^{16}
E/R (K)	34,747	27,898	19,237	25,934	30,819	27,898

7.1.5 Moisture release models

Moisture release was modeled with three approaches: (a) by evaporation at a set temperature, usually 100 °C; (b) diffusion with diffusivity based on extent of reaction; or (c) diffusion with diffusivity based on temperature-dependent diffusivity of water in wood. The diffusion models were developed as an alternative to evaporation at 100 °C, because leaf surface temperature measurements and mass release measurements suggested that moisture was retained at elevated temperatures (above 100 °C). Though jetting was observed during the leaf experiments (see Figure 6-10), these moisture release models assume such effects were minimal.

7.1.5.1 Temperature release at a set temperature

In this approach, temperature release was modeled as occurring at a set temperature, usually 100 °C. This is the classical evaporation model for water.

7.1.5.2 Diffusion model, dependent on extent of water release

A diffusion-based approach to modeling water release (Seader and Henley, 2006) was modified by multiplying the original predicted rate of diffusion by the fraction of water remaining. It was hypothesized that the first water to be released was less tightly bound than the last portion of water and that this would result in depressed water release rates as water content became depleted. Thus the rate of diffusion was multiplied by the fraction of water remaining to taper water release as water became depleted.

The rate of water release is given in Equation 7-5, expressed as the time derivative of the fraction of water released (W). Several terms were ultimately gathered to form a single fitting parameter b , where $b = \mathcal{D}AM_w/(m_{0,w}R\Delta z)$. \mathcal{D} is diffusivity of water in leaf matter, A is leaf area, Δz is thickness, M_w is molecular weight of water, $m_{0,w}$ is the original water mass, and R is

the gas constant. The fitting parameter b was given the value of $8 \text{ K atm}^{-1} \text{ s}^{-1}$ to match modeled results (Equation 7-5).

$$\frac{dW}{dt} = b \left[\frac{P_{vap}}{T} - \frac{P_s}{T_s} \right] (1 - W) \quad (7-5)$$

\mathcal{D} was modified based on extent of water release $1 - W$, where W is the fraction of water released. This modification was made so that water released early on was less tightly-bound than water released later. Negative changes in water release were not allowed. The water vapor pressure P_{vap} is a function of the absolute local leaf temperature T , P_s is the partial pressure of water at the surface of the leaf, and T_s is the temperature at the surface of the leaf. P_s was assumed to be 1 atm, and T_s was set to a constant value of 1273 K, which is an upper-bound leaf temperature. Simplifying T_s to a constant value of 1273 K increases the rate of water release by 5% versus using a variable surface temperature at 200 °C. The selection of b compensated for this difference.

7.1.5.3 Diffusion model using the diffusivity of wood

A diffusion model using the diffusivity of moisture in wood was also implemented. An expression for the drying diffusion coefficient of wood \mathcal{D}_S , correlated to its swollen-wood specific gravity γ and temperature, is given in Equation 7-6 (Stamm, 1964; Plumb et al., 1985).

$$\mathcal{D}_S = \exp \left(3.746 - 5.12\gamma - \frac{4317}{T/K} \right) \frac{\text{cm}^2}{\text{s}} \quad (7-6)$$

This equation was originally intended for use with wood, which has a more rigid structure than foliage, although both are biomass materials. The form of the equation, coefficients, and temperature dependence were therefore preserved, but γ was treated as an adjustable parameter rather than as the actual specific gravity of manzanita leaves. The value of γ was ultimately set to

0.05 in order to synchronize moisture release with the local temperature behavior of heating leaves. Typical woods have values of γ well above 0.05.

The molar flow rate of water n_w from the leaf was treated with a steady-state one-dimensional diffusion equation which was updated at every time step:

$$n_w = \mathcal{D}_S A_c \left(\frac{c_{w1} - c_{w2}}{z_2 - z_1} \right) \quad (7-7)$$

where A_c is the cross-sectional leaf area, c is the concentration, the subscript w refers to water vapor, and the subscripts 1 and 2 respectively refer to an interior location of the leaf and the surface of the leaf. Interior water concentration was based on the vapor pressure of water at the local leaf temperature, and water concentration at the surface boundary was set to zero. A value of zero is appropriate for very low rates of water release. At high rates of water release, a higher value of surface water concentration would have been appropriate, but was not calculated. The interior location of one quarter of the total thickness of the leaf was chosen so that $z_2 - z_1$ would be equal to the average distance of moisture to the surface of the leaf. A generic two-sided leaf area of 3 cm by 2 cm times 2 was used for A_c of every leaf.

The molar flow rate n_w was converted to the time derivative of the water release fraction W . This was done by converting concentrations to mass densities and dividing by the initial water mass of the leaf to give Equation 7-8:

$$\frac{\partial W}{\partial t} = \mathcal{D}_S \frac{A_c}{m_{0,w}} \left(\frac{\rho_{w1} - \rho_{w2}}{z_2 - z_1} \right) \quad (7-8)$$

where ρ is mass density and $m_{0,w}$ is the initial mass of water in the leaf.

Equation 7-8 and Equation 7-5 differ due to the temperature dependence of \mathcal{D}_S in Equation 7-8 and the dependence on extent of water release in Equation 7-5. For both diffusion equations, water release was accelerated at higher temperatures due to increased water vapor

pressure. Water vapor pressure was included in Equation 7-5, and was a part of ρ_{w_1} in Equation 7-8. For a 0.2 gm, 50% MC, 0.5 mm thick leaf, Equation 7-5 ($W = 0$ and $W = 0.5$) and Equation 7-8 were plotted versus temperature (Figure 7-3). For temperatures near 100 °C, the conversion-dependent diffusion model (at either value of W) predicts higher rates of water release than the temperature-dependent diffusion model. As the temperature exceeds approximately 150 °C (depending on the value of W), the temperature-dependent diffusion model predicts higher rates of water release. The conversion-dependent term and the temperature-dependent diffusivity have opposite impacts on modeled diffusivity at increasing temperatures (assuming that water release increases with temperature).

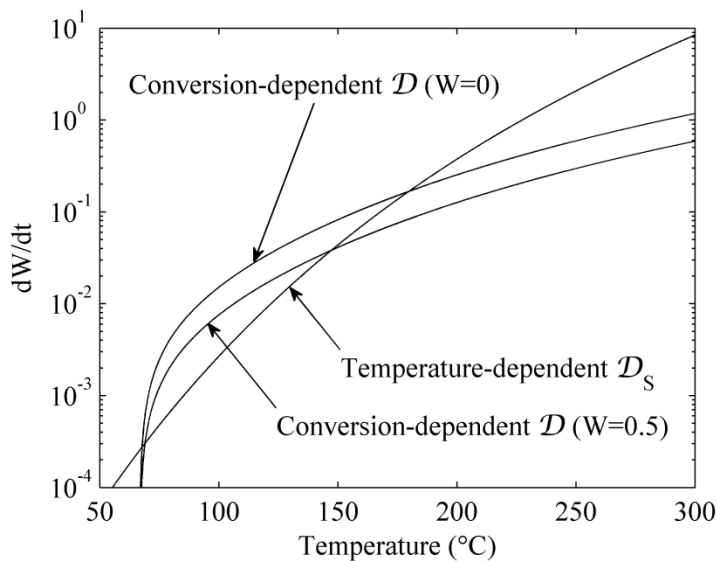


Figure 7-3. Derivative of fractional water released versus temperature for diffusion equations with conversion-dependent and temperature-dependent diffusivities.

7.1.6 Internal heat and mass transfer considerations

At approximately 0.5 mm thick, it was plausible that heat and mass transfer through the thickness of the leaf could be ignored. For biomass spheres with diameters of 0.5 mm or less, Bharadwaj et al. (2004) found that the intraparticle effects of heat and mass transfer could be

neglected in favor of a simpler lumped mass model. To determine whether temperature differences in the thickness dimension could be ignored, conduction through the thickness of the leaf was modeled for one leaf of each of the four moisture content groups. Mass release calculations involving conduction were limited to these four leaves, because they required excessive computational time. The diffusion-limited mass release models were executed for all of the leaves. The diffusion-limited models did not require significantly more computational time than the temperature-release model because moisture diffusion was calculated across a single distance rather than explicitly tracking moisture transport through multiple layers.

7.2 Results and discussion

Several modeling options were discussed in the previous section. Model results are presented here in nine sections and subsections. The modeling discussed in each section is summarized in Table 7-3. The first three sections (7.2.1 to 7.2.3.1) each evaluate a particular water release model for the same arbitrarily-chosen fresh live leaf measurements. The most detailed options were chosen for the other models in order to provide the highest-fidelity results.

The next three sections (7.2.3.2 to 7.2.3.4) expand the results of the temperature-dependent water release model to include one leaf from each of the moisture content groups. The water release models for the rehydrated dead and dehydrated live leaves were evaluated (section 7.2.3.2). Moisture release temperatures were summarized for the three moist leaves (section 7.2.3.3), and biomass release temperatures were averaged for all four groups (section 7.2.3.4).

Sections 7.2.4 and 7.2.5 investigate and compare simplified modeling approaches. In the first, the surface temperature data is simplified, and in the second, simplified mass release models were compared for a second set of arbitrarily-selected leaves.

Section 7.2.6 compares the two diffusion models, without conduction, for all leaves in each moisture content group to provide a broad evaluation of the accuracy of the moisture release models.

Table 7-3. Summary of modeling results by section

Section	Surface temp	Internal temp	Dry release model	Water release model	Leaves discussed
7.2.1	Grid	Conduction (5 nodes)	CPD (3)	Set temperature 100 °C	Fresh live #5
7.2.2	Grid	Conduction (5 nodes)	CPD (3)	Diffusion: conversion-dependent	Fresh live #5
7.2.3.1	Grid	Conduction (5 nodes)	CPD (3)	Diffusion: temp-dependent	Fresh live #5
7.2.3.2	Grid	Conduction (3 nodes)	CPD (3)	Diffusion: temp-dependent	Rehydrated dead #5 Dehydrated live #5 (Dry dead #5)
7.2.3.3	Grid	Conduction (3, 5 nodes)	CPD (3)	Diffusion: temp-dependent	Rehydrated dead #5 Dehydrated live #5 Fresh live #5
7.2.3.4	Grid	Conduction (3, 5 nodes)	CPD (3)	Diffusion: temp-dependent	Dry dead #5 Rehydrated dead #5 Dehydrated live #5 Fresh live #5
7.2.4	Mean, $T_{m,k}$	Measured surface temp	CPD (3)	Diffusion: conversion-dependent	Fresh live #5
7.2.5	Grid	Measured surface temp	Single-comp (a) Single-comp (b) Multi-comp (6) [CPD (3)]	Diffusion: temp-dependent	Dry dead #8 Rehydrated dead #8 Dehydrated live #8 Fresh live #8
7.2.6	Grid	Measured surface temp	CPD (3)	Diffusion: conversion-dependent, temp-dependent	Dry dead (19 runs) Rehydrated (18) Dehydrated (18) Fresh live (19)

7.2.1 Water release at 100 °C

This section presents modeling results of live leaf #5 using gridded surface temperature, 5 conduction nodes, CPD for cellulose, hemicellulose and lignin, and water release at 100 °C. CPD and water release objects were instantiated for each biomass component at every node in every grid section. The measured leaf temperature provided the temperature for the surface node, while conduction and an energy balance determined the temperature of the interior nodes. Water release occurred at 100 °C, and delayed the local temperature rise until the water present in that control volume was spent.

Top center, center, and bottom center locations of the leaf are shown in Figure 7-4. The calculated temperature at each interior node and normalized water mass for the area located at the top center of the leaf (row 1, column 10) is shown in Figure 7-5. Each node is labeled, from node 1, located at the surface, to node 5 located halfway through the thickness of the leaf (see Figure 7-2). Similar plots are presented for leaf areas at the center (row 16, column 10; see Figure 7-6) and bottom center of the leaf (row 30, column 10; see Figure 7-7).

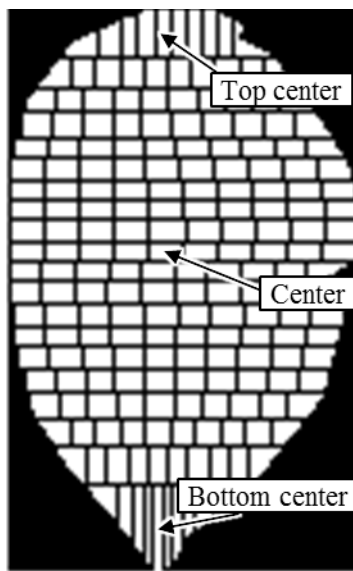


Figure 7-4. Locations of top center, center, and bottom center leaf areas on a 20 row by 10 column leaf. 30 rows and 20 columns were used in calculations.

Water vaporization was expected to be manifest in the leaf temperature by a stop or slowing of temperature rise. For an area at the top of the leaf (Figure 7-5), the modeled water remaining was totally depleted soon after the onset of a period of slowed temperature rise. However, this period of moderate temperature rise lasted 7 s beyond the modeled depletion of moisture content.

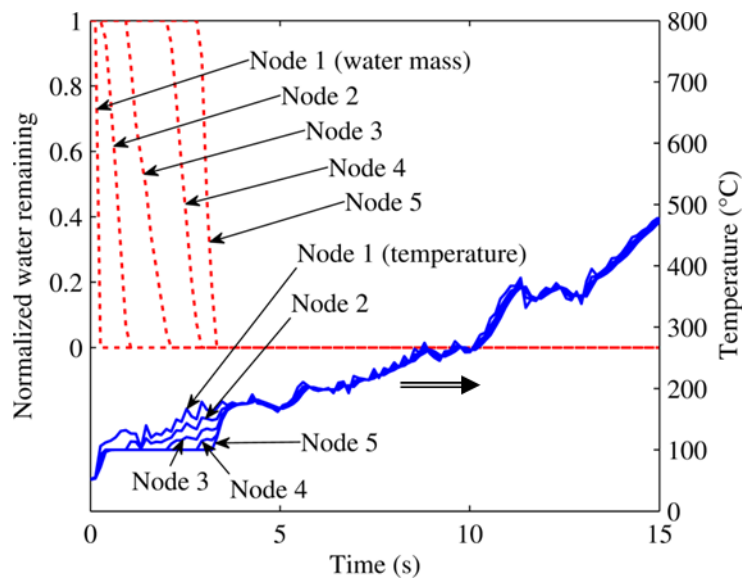


Figure 7-5. Modeled (100 °C release) water mass and node temperature of a top center leaf area of fresh live Run 5. Nodes are labeled from 1 (surface temperature boundary condition) to 5 (symmetry node).

At the center of the leaf, the discrepancy between the period of modeled water release and the period of slowed temperature rise was more obvious (see Figure 7-6). Modeled water was depleted after 3 s of heating though a conspicuous temperature plateau lasted from 3 s to 10 s.

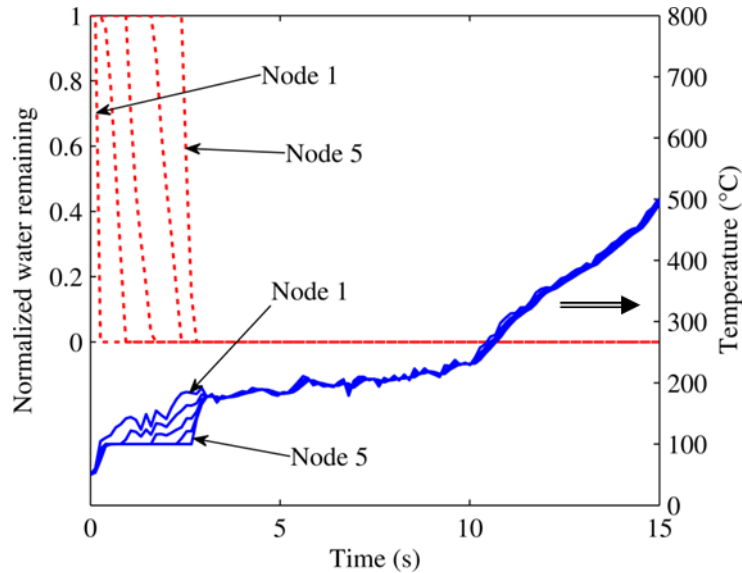


Figure 7-6. Modeled (100 °C release) water mass and node temperature of a center leaf area of fresh live Run 5. Nodes 1 (surface temperature boundary condition) and 5 (symmetry node) are labeled.

For the area selected at the bottom center of the leaf, it is difficult to discern the effect of water release on the leaf surface temperature (node 1). The model predicted complete local water depletion at a residence time of less than 2 s. However, this timing does not coincide with an increase in the rate of temperature rise, but rather a decrease in the rate of temperature rise. Complete water depletion was expected to coincide with an increase in the rate of temperature rise. Therefore, a more likely timing for complete water depletion at the bottom of the leaf at 5 s, when there was a notable increase in the rate of temperature rise (Figure 7-7).

Prediction of early modeled water release caused the total modeled mass of fresh live leaf 5 to drop well below the measured mass (Figure 7-8). This comparison supports the rationale and conclusions determined during the analysis of the local water release and local temperature profiles, i.e. that modeling water release at 100 °C results in premature release of water compared to measurements.

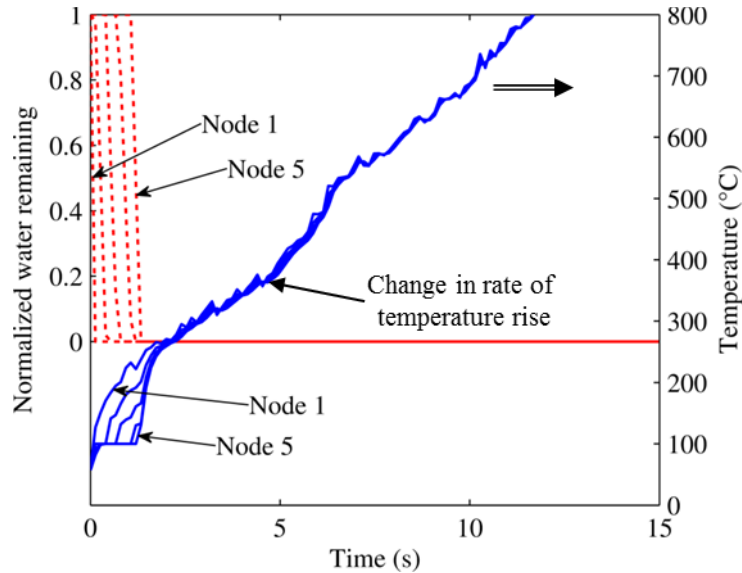


Figure 7-7. Modeled (100 °C release) water mass and node temperature of a bottom center leaf area of fresh live Run 5. Nodes 1 (surface temperature boundary condition) and 5 (symmetry node) are labeled.

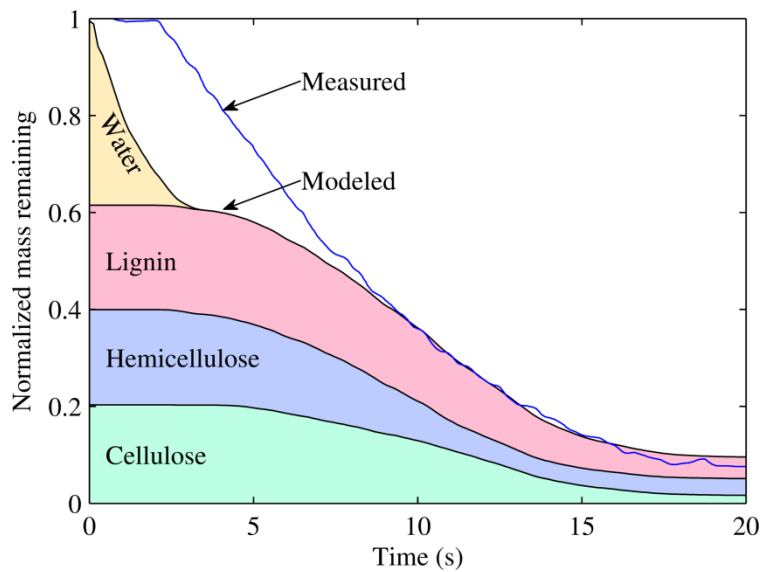


Figure 7-8. Modeled mass release for CPD dry matter release and 100 °C water release compared to measured mass release for fresh live leaf 5.

The differing onsets and durations of the modeled water depletion and temperature plateau (for the classical evaporation model) can be explained by possible behaviors not described by the present modeling, including: (1) mass transfer limitations and pressure buildup; (2) lateral water movement; and (3) the effect of vapor formation on leaf conductivity.

The rate of water release may be limited by the resistance of the leaf structure to water diffusion. In this scenario, leaf temperature and pressure rise when heat transfer to the leaf outpaces the cooling provided by water release. Temperature plateaus occur when internal water vapor pressures and water diffusivity are high enough that heat transfer to the leaf is balanced by cooling by water release.

Water from the fastest-heating part of the leaf (the lower perimeter) could be pushed toward the middle of the leaf. Faster heating around the hotter perimeter of the leaf would raise the local vapor pressure and provide a driving force for water movement. Also, the anisotropic vascular system in leaves may promote water diffusion toward the middle of the leaf rather than transversely through the surface. In wood, Stamm (1964) noted that liquid permeability in the axial direction could be as much as 10 times greater than that of the transverse direction (Seader and Henley, 2006).

The formation of vapor inside the leaf could reduce the conduction of heat to the interior of the leaf and delay internal water release: the conductivity of water vapor is 27 times less than that of liquid water at the normal boiling point, and 8 times less than that of wood (Incropera et al., 2007).

Another potential reason for differing onsets and durations of the modeled water depletion and temperature plateaus could be the estimation of thermophysical properties. Boiling point elevation due to dissolved carbohydrates may contribute to delayed moisture release. The remaining thermophysical properties (such as thermal conductivity and specific heat) were based on correlations to wood. Correlations to the thermophysical properties of wood include dependence on moisture content, specific gravity and temperature. However, these correlated

properties for wood were evaluated and yielded values within the range measured for various leaves reported by Jayalakshmy and Philip (2010).

7.2.2 Diffusion-limited water release: conversion-dependent diffusivity

This section presents modeling results of live leaf #5 using gridded surface temperature, 5 conduction nodes, CPD for cellulose, hemicellulose and lignin, and diffusion-limited water release with a conversion-dependent diffusivity. Water release was compared to temperature for the external boundary condition node and four internal nodes for three selected areas on the leaf: (1) the top, center (Figure 7-9); (2) the center (Figure 7-10); and (3) the bottom, center area (Figure 7-11). These are the same areas selected for the discussion of water release at 100 °C (see Figure 7-4 for locations schematic). However, for this water release model, the predictions of depletion did not occur until after the rate of temperature rise increased.

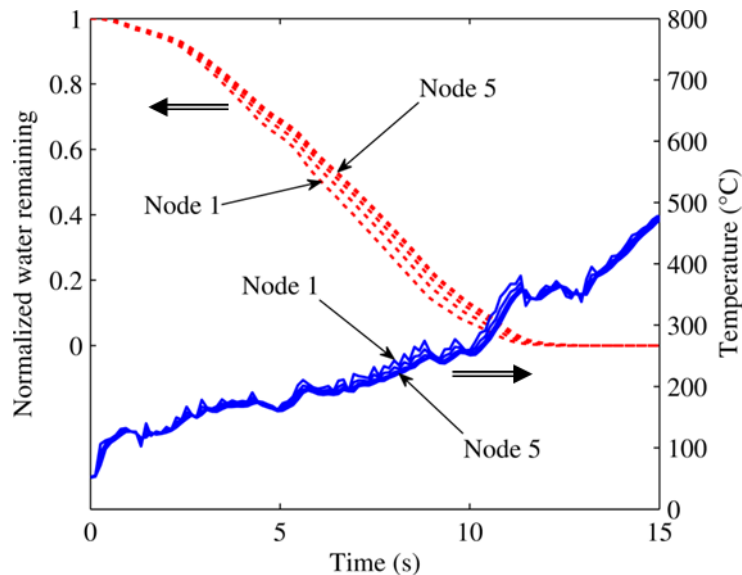


Figure 7-9. Modeled (conversion-dependent diffusivity) water mass and node temperature of a top center leaf area of fresh live Run 5. Nodes 1 (surface temperature boundary condition) and 5 (symmetry node) are labeled.

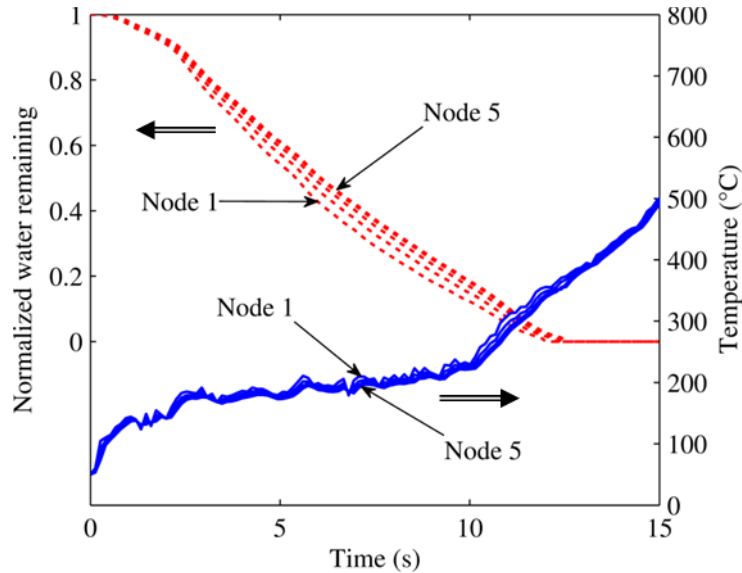


Figure 7-10. Modeled (conversion-dependent diffusivity) water mass and node temperature of a center leaf area of fresh live Run 5. See figure caption to Figure 7-9 for node locations.

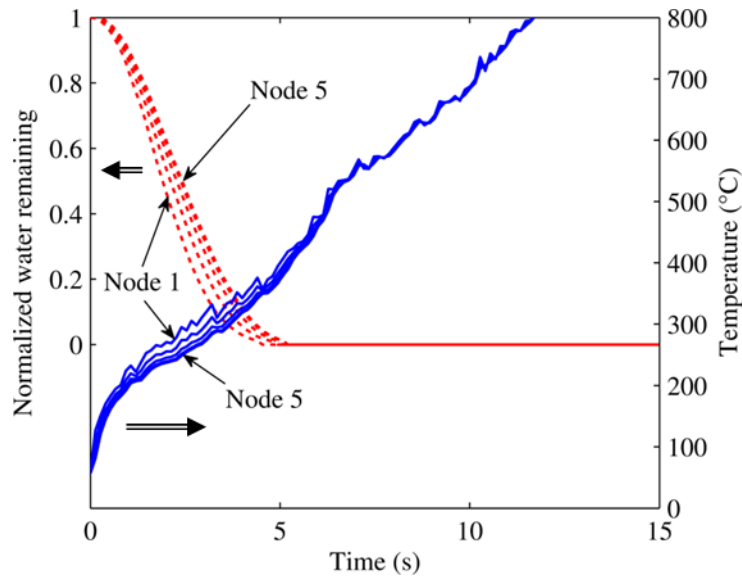


Figure 7-11. Modeled (conversion-dependent diffusivity) water mass and node temperature of a bottom center leaf area of fresh live Run 5. See figure caption to Figure 7-9 for node locations.

At the top (Figure 7-9) and middle (Figure 7-10) of the leaf, the water release persisted to approximately 12 s while the temperature plateaus ended at 10 s. At the bottom of the leaf (Figure 7-11), the moisture profile coincided somewhat with the temperature profile. The temperature rise increased during the same period that moisture release tapered and stopped

(between 4 s and 5 s). Overall, the temperature profiles and moisture release curves exhibited much better qualitative agreement for these arbitrarily selected areas using the conversion-dependent diffusion model than using the 100 °C moisture release model.

The total modeled mass release curve was compared to the measured mass release curve for this leaf with much better agreement (Figure 7-12). The model overshoot the measured values slightly between 4 s and 11 s. This coincided with the long-lasting moisture tails observed for the top and middle leaf areas, but the discrepancy was relatively minor.

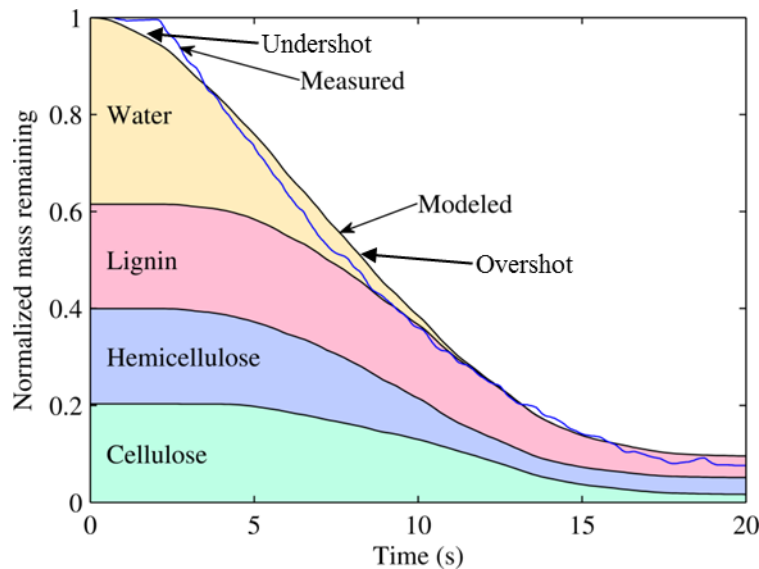


Figure 7-12. Modeled mass release for CPD dry matter release and conversion-dependent diffusivity water release compared to measured mass release for fresh live leaf 5.

The rationale used to relate the rate of temperature rise to moisture release was consistent with this analysis. For the first moisture release model, the local modeled moisture release was premature as compared to the local temperature plateaus, and the comparison of total mass curves reflected this. For the second moisture release model, the local modeled moisture release was slightly too persistent, and the modeled total mass release slightly lagged the measured mass.

7.2.3 Diffusion-limited water release: temperature-dependent diffusivity

This section presents modeling results using gridded surface temperature, internal conduction, CPD for cellulose, hemicellulose and lignin, and diffusion-limited water release with a temperature-dependent diffusivity. Conduction is calculated with 5 nodes for fresh live leaf #5, and with 3 nodes for rehydrated dead leaf #5, dehydrated live leaf #5 and dry dead leaf #5. The first node was the measured surface temperature boundary condition and the others were calculated.

7.2.3.1 Fresh live leaf

Using Stamm's temperature-dependent wood diffusivity correlation (without a conversion-correlated term), mass release and internal temperature were calculated. Leaf areas were again selected at the top, middle and bottom of the leaf. At the top of the leaf (Figure 7-13) local moisture release occurred during a temperature plateau and moisture exhaustion for the various nodes corresponded to increases in the rate of temperature rise. This was followed by a brief plateau, a sharp jump, a plateau, and then another sharp jump in temperature. Such erratic features may reflect actual local temperature changes, or small shifts in the alignment of the sampling area and the leaf: at the edges of the leaf, the temperature gradients were high.

At the center of the face of the leaf (Figure 7-14) the temperature profile was much smoother. Moisture was released during the temperature plateau for each node. Temperature resumed a rapid rate of increase after the moisture content of all nodes was fully depleted.

At the bottom, center of the leaf (Figure 7-15) the start of moisture release coincided with a slowing of the temperature rise, although moisture was depleted at a seemingly insignificant time with regard to the temperature. This position at the bottom of the leaf heated faster than the

other locations and measured and predicted temperatures rose higher before predicted water depletion.

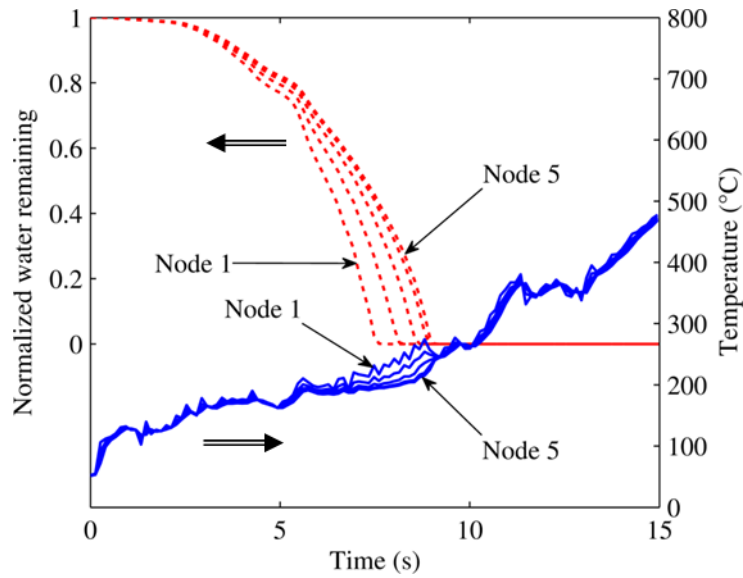


Figure 7-13. Modeled (temperature-dependent diffusivity) water mass and node temperature of a top center leaf area of fresh live Run 5. See figure caption to Figure 7-9 for node locations.

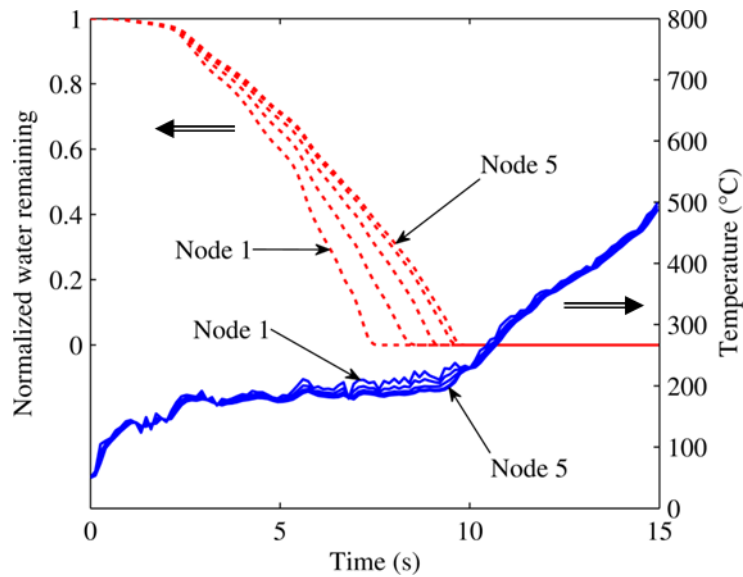


Figure 7-14. Modeled (temperature-dependent diffusivity) water mass and node temperature of a center leaf area of fresh live Run 5. See figure caption to Figure 7-9 for node locations.

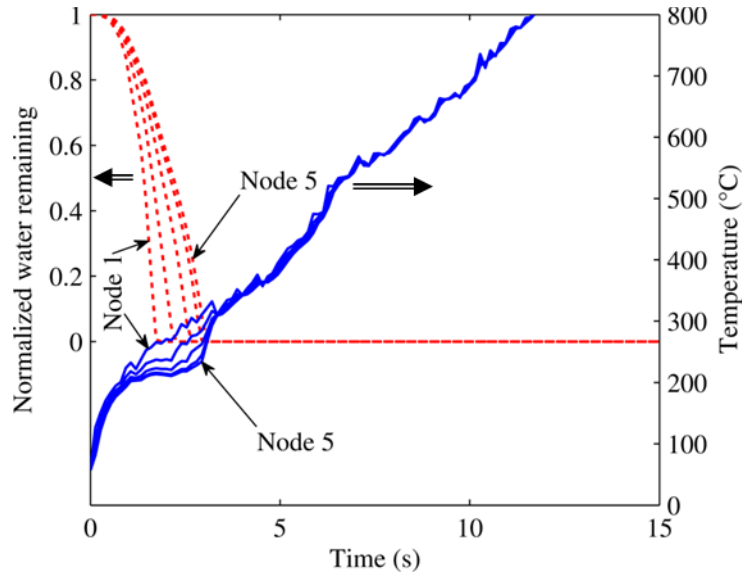


Figure 7-15. Modeled (temperature-dependent diffusivity) water mass and node temperature of a bottom center leaf area of fresh live Run 5. See figure caption to Figure 7-9 for node locations.

The agreement between the measured and modeled mass release (Figure 7-16) improved on that of the previous diffusion-based model. Notably, the modeled mass release left a smaller gap between the modeled and measured mass between 0 s and 3 s and between 5 s and 10 s. This result supports the conclusion that water release from live fresh manzanita leaves in severe heating conditions can be accurately described as a diffusion-controlled process.

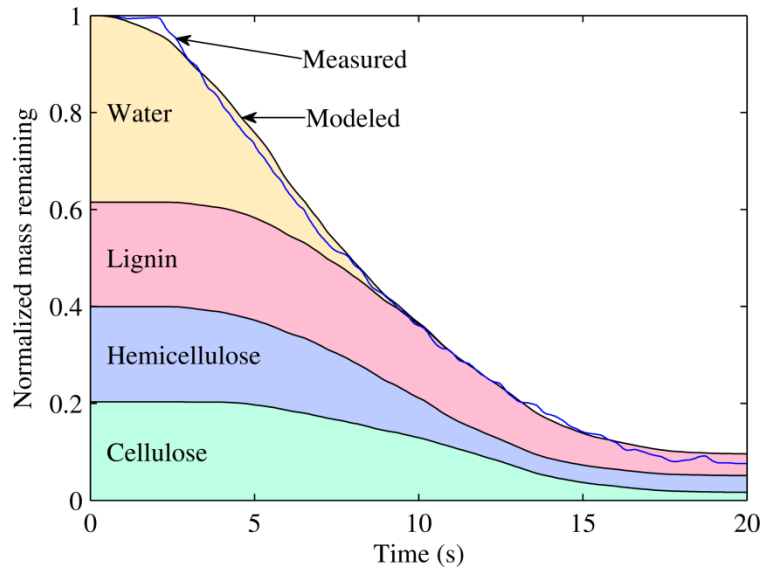


Figure 7-16. Modeled mass release for CPD dry matter release and temperature-dependent diffusivity water release compared to measured mass release for fresh live leaf 5.

7.2.3.2 Rehydrated dead, dehydrated live leaf and dry dead leaves

Similar modeling, using 3 nodes rather than 5 for conduction calculations, was performed for the fifth leaf of each other leaf group (dry dead, rehydrated dead, and dehydrated live). Moisture release from the rehydrated and dehydrated leaves is discussed here, and the devolatilization of the dry dead leaf will be discussed in a following subsection. The rehydrated (Figure 7-17) and dehydrated (Figure 7-18) leaves were modeled to verify that the diffusion moisture release model with temperature-dependent diffusivity was also applicable for a lower moisture content (i.e. the dehydrated leaf), and for a dead but rehydrated leaf. The modeled and measured normalized mass remaining agreed for both the rehydrated and dehydrated leaves.

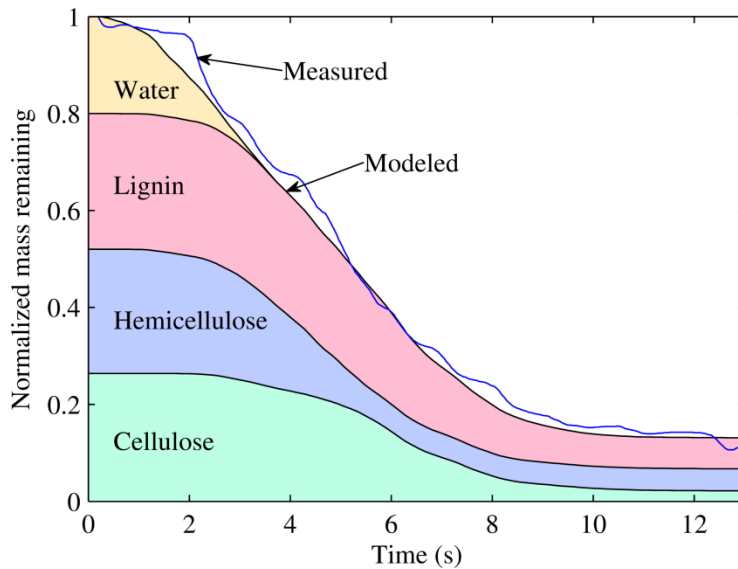


Figure 7-17. Modeled mass release for CPD dry matter release and temperature-dependent diffusivity water release compared to measured mass release for rehydrated dead leaf 5.

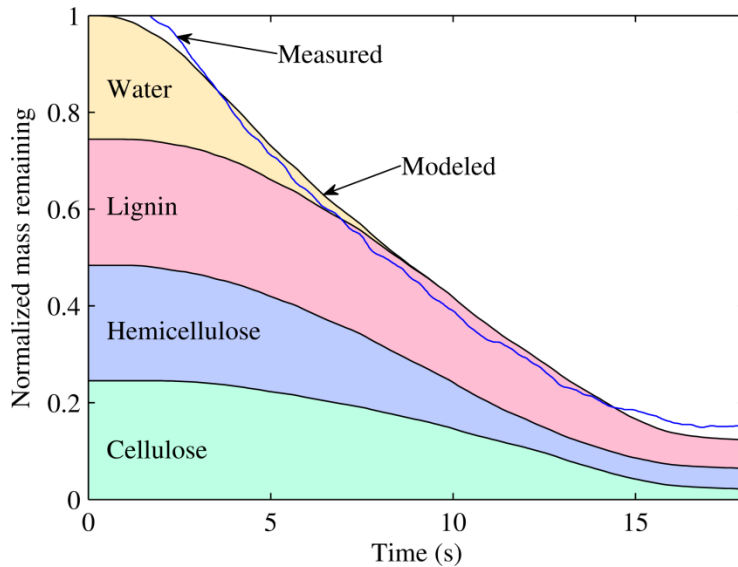


Figure 7-18. Modeled mass release for CPD dry matter release and temperature-dependent diffusivity water release compared to measured mass release for dehydrated live leaf 5.

As with the fresh live leaf, complete local water depletion corresponded with local increases in the rate of temperature rise. This agreement supports the diffusion model and suggests that diffusion is the rate-limiting step of water release for both dead and live manzanita leaves under these heating conditions. However, the time of moisture release was earlier for the dehydrated leaf and much earlier for the rehydrated leaf. These times corresponded with the plateau durations shown in the previous chapter (Figure 6-6). Based on these results, the burning differences in rehydrated dead and dehydrated live leaves is related to the leaf energy balance: water is held longer in live leaves because the drying stage is prolonged by lower temperatures. The cause for the lower temperatures of live leaves is most likely linked to the ways water is held and released in live leaves versus dead leaves (Stamm, 1964).

7.2.3.3 Rehydrated, dehydrated and fresh moisture release temperatures

For each node of each region, the amount of water release versus temperature was tracked. By weighting the temperature of water release by the amount of water released for the

entire temperature history of the leaf, the temperature distribution of modeled water release was determined (Figure 7-19). For the rehydrated leaf and dehydrated leaf, the mean temperatures of modeled water release were respectively 189 °C and 186 °C, and for both leaves over 90% of water release occurred between 150 °C and 225 °C. For the fresh leaf, the mean temperature of modeled water release was 200 °C, and over 90% of water release occurred between 150 °C and 250 °C. The temperature plateaus first identified in Figure 6-5 for each leaf group occupied temperatures which were within the 90% temperature ranges identified here. In Chapter 6 it was hypothesized that moisture was retained in all moisture-laden leaves into the 160 °C to 220 °C range. This modeling supports that claim and quantifies the distribution of moisture release as a function of the local leaf temperature (Figure 7-19).

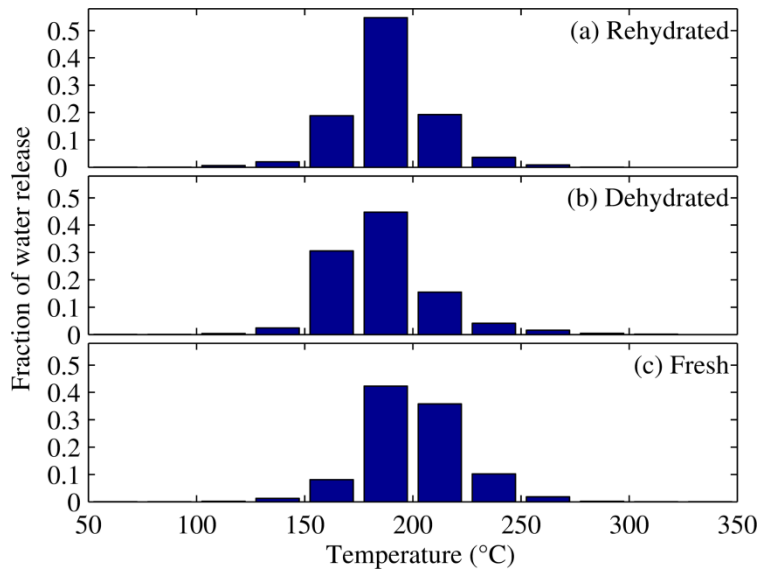


Figure 7-19. Predicted temperature of local moisture release for leaf number 5 of each group.

7.2.3.4 Cellulose, hemicellulose and lignin release temperatures averaged for dry, rehydrated, dehydrated and fresh leaves (#5)

The dry dead leaf (along with each other group) contributed to a temperature distribution of mass release for cellulose, hemicellulose and lignin. The modeled temperatures of devolatilization had little dependence on leaf group and were averaged across the groups (Figure 7-20). The high heating rate of this experiment resulted in higher mean temperatures of component mass release than are often reported (Fletcher et al., 1989; Di Blasi, 2008; Biagini and Tognotti, 2014). The mean local temperatures of cellulose, hemicellulose and lignin release were respectively 481 °C, 334 °C, and 495 °C.

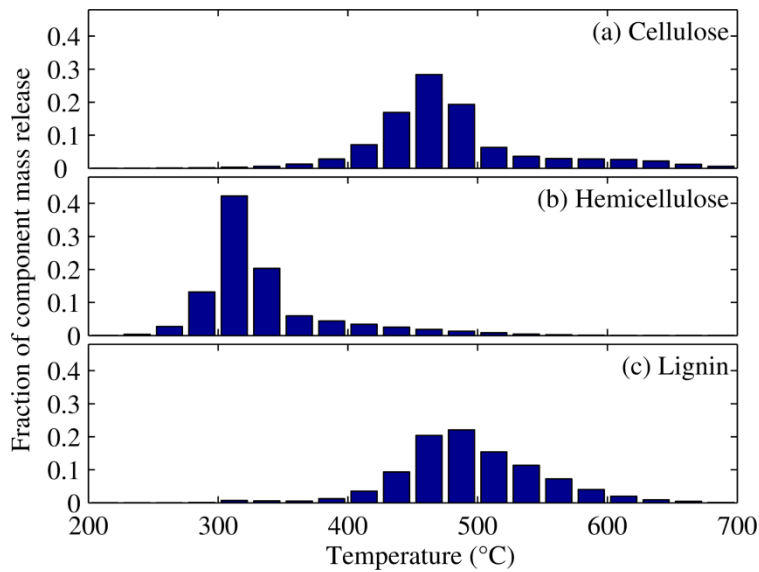


Figure 7-20. Predicted temperature of local component mass release averaged for dry, rehydrated, dehydrated and fresh leaves.

7.2.4 Arithmetic mean temperature and mean kinetic temperature

This section presents modeling results of live leaf #5 using the arithmetic mean surface temperature and the mean kinetic surface temperature. The internal leaf temperature was set to the measured surface temperature of the leaf. Mass release was calculated with CPD for cellulose, hemicellulose and lignin, and with the diffusion-limited, conversion-dependent

diffusion equation for water. Calculating mass release based on a single average leaf temperature profile greatly reduced computational time. When using the arithmetic mean of the leaf surface temperature, the measured and total modeled mass release profiles were similar, but the modeled mass profile showed steps due to the varied timings of mass release for each component (Figure 7-21). Because the average temperature was used, the distribution of temperatures actually experienced by the leaf did not smooth out the mass release curve as occurred when dividing the leaf into many areas for independent mass release modeling.

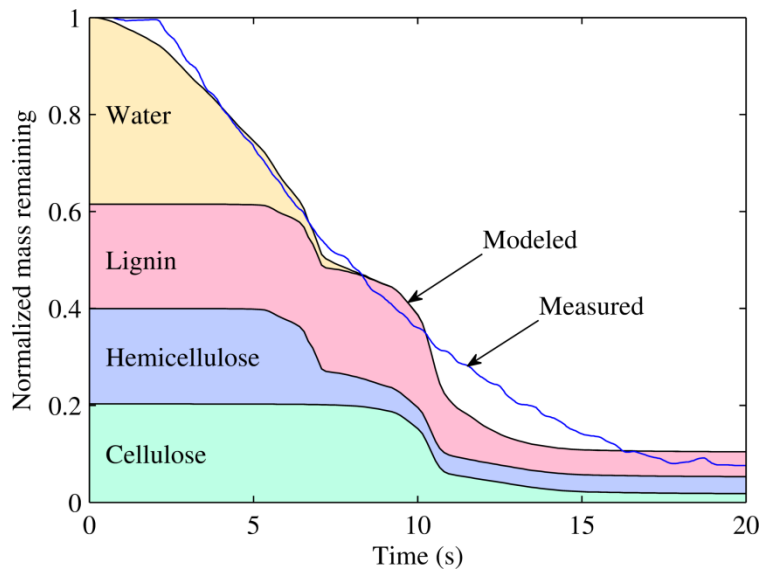


Figure 7-21. Modeled mass release for CPD dry matter release and conversion-dependent diffusivity water release calculated at the arithmetic mean leaf temperature compared to measured mass release for fresh live leaf 5.

Mass release was also modeled using the mean kinetic temperature of the leaf. Values of E/R were used to determine the mean kinetic temperature for each component using Equation 7-1. These were 29,359 K (cellulose), 22,586 K (hemicellulose), 31,323 K (lignin), and 22,586 K (water). As presented in Figure 7-22, mass release occurred quite prematurely using the mean kinetic temperature and is therefore not recommended for this application.

This result is not a reflection of the usefulness of mean kinetic temperature for its originally-intended purpose. However, the mean kinetic temperature is not appropriate to average spatial differences in temperature with the intent of estimating Arrhenius rates at the average temperature. Instead, the use of mean kinetic temperature should be confined to averaging temperature over time in order to determine a theoretical temperature which would result in the same degree of degradation as would be experienced for the actual temperature history (Haynes, 1971).

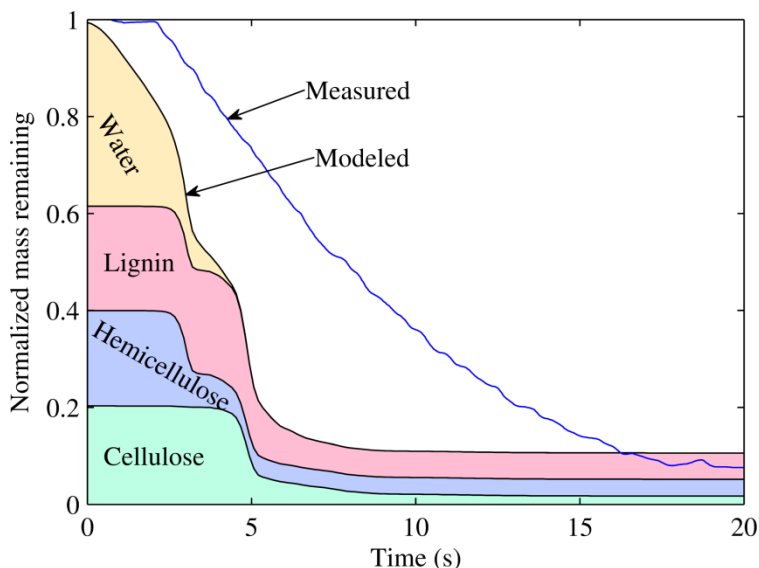


Figure 7-22. Modeled mass release for CPD dry matter release and conversion-dependent diffusivity water release calculated at the mean kinetic temperature of the leaf compared to measured mass release for fresh live leaf 5.

7.2.5 One-step dry matter mass release

This section presents modeling results of live leaf #8 using gridded surface temperature, internal leaf temperature set to the measured surface temperature, and diffusion-limited water release with a conversion-dependent diffusivity. The relative behavior of each one-step devolatilization model (single-component (a), single-component (b), and multi-component) was compared for selected leaves (leaf number 8 of each leaf group). Parameters for the single-

component models (a) and (b) were given in Table 7-1 and multi-component parameters are in Table 7-2. The CPD model was included for reference. Each devolatilization model was coupled with the diffusion water release model that used temperature-dependent diffusivity. Mass release predictions for each model were compared with measured mass for one leaf from each leaf group. Figure 7-23 shows the error between the normalized mass remaining of each modeled leaf and the mass measurements.

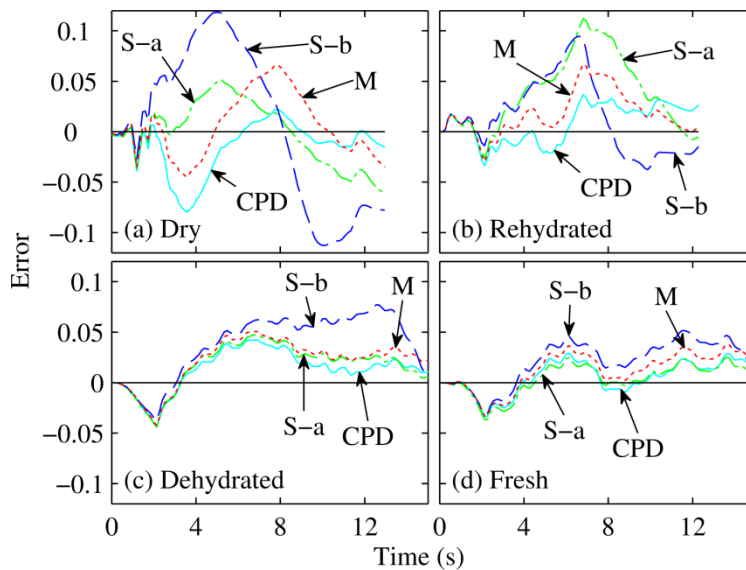


Figure 7-23. Modeled minus measured normalized mass remaining for leaf 8 of each leaf group. (S-a = single-component (a), S-b = single-component (b), M = multi-component.)

The mean absolute error for each leaf (dry, rehydrated, dehydrated and fresh) are listed by model: CPD (1.9%, 1.8%, 1.8%, 1.5%), single-component (a) (2.6%, 4.1%, 2.6%, 1.0%), single-component (b) (6.7%, 3.1%, 4.6%, 2.3%), and multi-component (2.5%, 2.1%, 2.8%, 1.6%). Based on the total mean absolute error for all four runs, the CPD model performed best, followed by the multi-component model, then the single-component (a) model, and finally the single-component (b) model. This is unsurprising since the CPD model was the most sophisticated, followed in complexity by the multi-component model (which was based on the

CPD model). However, though the single-component (a) model performed better than the single-component (b) model, it is not recommended that parameter set (a) be used for any but these very narrow experimental conditions since parameter set (a) is not in a normal range for biomass.

The difference between the single-component parameter sets was illustrated with a simple exercise. A single-component model using parameter set (a) was allowed to calculate mass release over a 25 hour period at a constant temperature of 300 K. Though dry matter does not actually devolatilize at room temperature, 42% of the mass was lost. The same exercise was performed using parameter set (b), and because the parameters were in a more typical range for biomass, no mass was released.

7.2.6 Modeled and measured mass release comparison for all runs

This section presents modeling results of all dry dead runs (total of 19), all rehydrated dead runs (18), all dehydrated runs (18) and all fresh live runs (19). Mass release was modeled using the gridded surface temperature and internal leaf temperature set to the gridded surface temperature. Devolatilization was modeled with CPD for cellulose, hemicellulose and lignin. Water release was modeled with: (1) the diffusion-limited, conversion-dependent model; and then (2) the diffusion-limited, temperature-dependent model. Modeled and measured mass release were averaged across each of the four groups of runs.

The model with the conversion-dependent diffusion model is shown in Figure 7-24. The agreement is good, but it is suspected that the conversion-dependent term is responsible for the slight disagreement between the model and measurements. Devolatilization modeling could also contribute to this behavior.

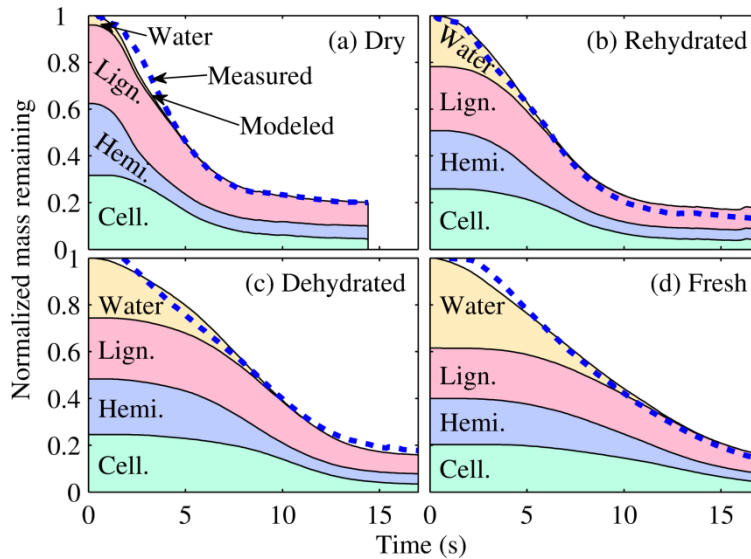


Figure 7-24. Modeled mass release for CPD dry matter release and conversion-dependent water release compared to measured mass release averaged for all leaves in each group.

For the diffusion model with temperature-dependent diffusivity, the agreement between the model and measurements was more consistent (Figure 7-25) than for the first diffusion-based model. These results do not support the hypothesis that a conversion-dependent factor was needed to model decreased mobility of the latter-released water. Rather, they suggest that under these heating conditions, moisture release from manzanita leaves is primarily diffusion-limited, and that other considerations such as bonding energy or normal boiling point are less important. These results support the theory that leaves are highly pressurized during moisture release: the concentration difference driving water diffusion was calculated from the vapor pressure of water, which well exceeded 1 atmosphere. Internal leaf pressures of 8 atmospheres or more can be inferred from the local temperatures of water release presented in Figure 7-19.

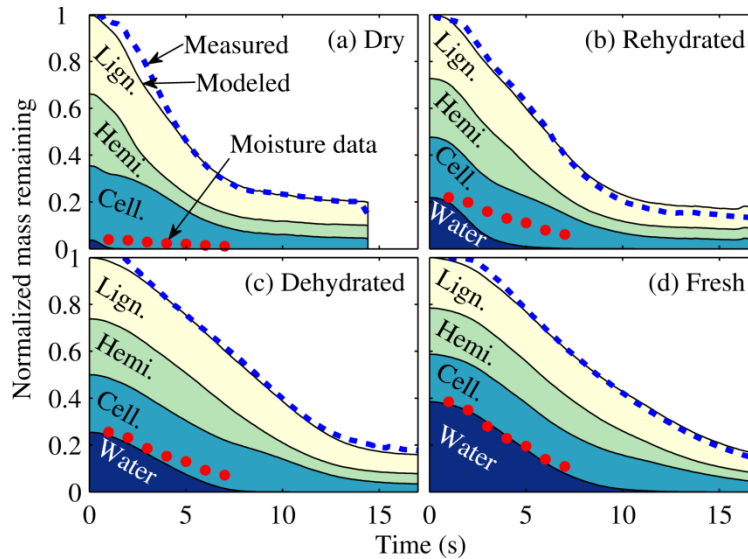


Figure 7-25. Modeled mass release for CPD dry matter release and temperature-dependent diffusivity water release compared to measured mass release averaged for all leaves in each group. Separately-measured moisture data are scaled to the same initial value and shown alongside the moisture model results.

Figure 7-25 also includes the moisture release data listed in Table 6-2, scaled to the initial leaf moisture content and superimposed on the modeled dry matter mass release curves. The initial moisture contents of leaves described in Table 6-2 were mostly in the 70% MC to 80% MC range. The data of Table 6-2 is therefore most applicable for the fresh live leaves, for which the model and measured moisture release data points were very similar. The moisture release data therefore confirms the behavior of the diffusion model and dry matter release models for the fresh live leaves.

The rehydrated and dehydrated leaves had starting moisture contents which were well below the moisture contents of the leaves described in Table 6-2. Therefore the moisture release data points were less applicable to the moisture release behaviors of the dehydrated and rehydrated leaves. The moisture release data points exceeded the model and measured mass release curves of the rehydrated and dehydrated leaves. This was expected because the moisture

release data represented the behavior of leaves that started with higher starting moisture contents than the rehydrated and dehydrated leaves, which leads to slower heating and mass release.

The derivative of the modeled normalized mass release was studied for the average of the entire sets of runs, using the CPD dry matter models and the diffusion (with temperature-dependent diffusivity) model. Components were predicted to release in the order of water, hemicellulose, cellulose and lignin (Figure 7-26). The timing of cellulose and lignin was nearly identical. The predicted release of each component, including water, overlapped significantly. Leaf mass in dead leaves was predicted to release faster than in live leaves. This was especially the case with water, which was predicted to release very quickly for dead leaves.

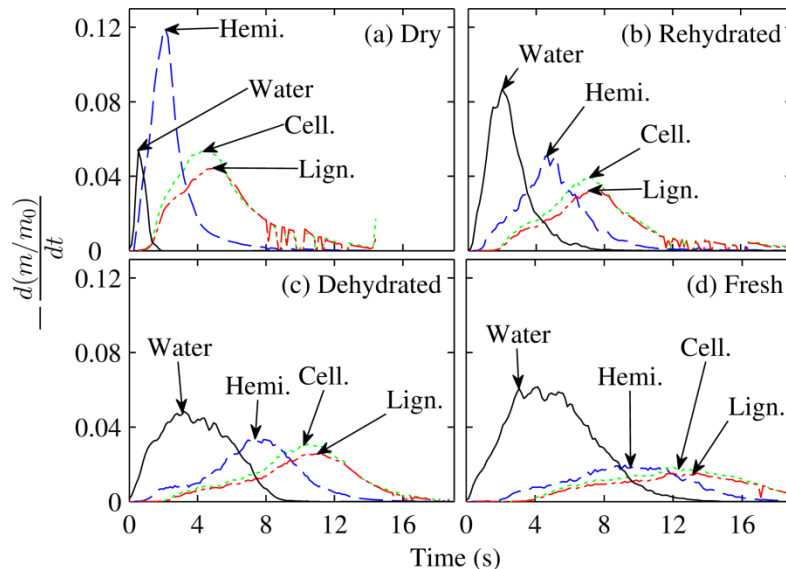


Figure 7-26. Derivative of normalized mass determined from CPD and temperature-dependent diffusivity water release models averaged for all leaves in each group.

7.3 Conclusions

Mass release was best modeled using a detailed description of the leaf surface temperature by dividing the leaf into 600 calculation regions. Modeling mass release with the mean temperature of the leaf resulted in larger errors between modeled and measured behaviors,

but may be sufficiently accurate for some applications. The mean kinetic temperature should not be used as an alternative to the arithmetic mean.

Internal leaf temperatures were calculated based on 1-D conduction and the heat of vaporization of water, but coupling internal heat transfer with mass release calculations was computationally expensive. Internal leaf temperatures were very close to the surface temperatures except during rapid water release, which temporarily caused temperatures at the mid-thickness of the leaf to be as much as 100 °C cooler than at the surface. While modeled and measured mass release agreed very well for arbitrarily selected leaves using 1-D conduction, mass release modeled without including 1-D conduction was also found to agree satisfactorily with measured data.

The CPD model and three one-step devolatilization models were each used to model the dry matter mass release. In combination with a water release model, the CPD model compared most favorably with measured results. The multi-component one-step model also compared well with measured mass. Distinct dry matter components were first modeled separately and then superimposed in the CPD and multi-component models. However, in the single-component devolatilization models, dry matter was treated as a single component. This resulted in a tradeoff between specific modeling accuracy (for these heating conditions) and model applicability (outside these conditions). For applications requiring both accuracy and relevance beyond these heating conditions, single-component mass release models are not recommended for biomass similar to manzanita leaves. The temperatures of mass release identified by the CPD model were higher for these experiments than are often reported for biomass. However, modeled and measured mass release agreed, and local temperatures of mass release increase with increasing heating rate.

Water release was not well-described by classical water evaporation at 100 °C, even when accounting for the cooling effect of water and internal heat transfer. Moisture release was best described by a diffusion model which incorporated an expression for diffusivity originally derived for wood. This model was effective for all leaf groups, suggesting that moisture release at these heating conditions was limited by diffusion. The modeled temperatures of moisture release corroborated measurements that suggested moisture was reaching elevated temperatures before release, and therefore also reaching elevated pressures. Based on these modeling results, 95% of water release occurred between 150 °C and 250 °C, with the highest water release range being from 175 °C and 200 °C for all leaf groups.

The burning differences between rehydrated dead and dehydrated live leaves resulted from relatively low temperatures which were maintained longer by live leaves than by dead rehydrated leaves. The persistence of relatively low temperatures allowed water to remain longer in live leaves than in dead leaves. The difference between the state of water in live and dead leaves, and how that affects the leaf energy balance during heating, is the likely reason for the differing temperature profiles of rehydrated dead and dehydrated live leaves. For example, the heat absorption profiles of liquid water in live leaves and water adsorbed to cell walls in dead leaves could be quite different during rapid heating. Further insight into this matter could be pursued by also modeling heat transfer to the leaf from its surroundings.

8. IMPROVED SEMI-EMPIRICAL SHRUB-SCALE FIRE SPREAD MODEL

The multi-leaf semi-empirical fire spread model discussed earlier in Chapter 4 was developed based on individual leaf experiments conducted at one gas temperature. This chapter discusses how that model was improved to: (1) respond to varying heating conditions; and (2) model flame-merging with more conventional methods. The improved bush model is the integration and culmination of the foregoing chapters. Modeling results are presented for manzanita, though the model can be extended to describe fire spread in other species, such as chamise, by adjusting species-specific parameters and using appropriate fuel placement models, such as those described in Chapter 5.

The reader is referred to Chapter 4 for a detailed overview of the first-generation bush model. The improved bush model was designed on the same framework as the first-generation bush model, but improves aspects of the model which were identified as deficient. The core of the bush model is the correlation of flame parameters (e.g. flame height and ignition time) to the physical parameters of fuel elements (e.g. length and mass). These correlations were developed from combustion measurements which were all performed at the same heating conditions. As a result, there was no experimental basis to determine flame parameters at higher or lower levels of heat flux.

The leaves in the combustion experiments were heated above a flat flame burner which produced 1000 °C, 10 mol% O₂ post-flame gases, which at the height of the leaf was estimated to have a velocity between 0.6 to 1.8 m/s. In later experiments, the flat-flame burner was

surrounded with a glass duct which was measured at temperatures of over 500 K after extended use. These heating conditions are referred to as the base case.

The capability to predict flame parameters for a broad range of heating conditions was achieved in the improved bush model by developing a physics-based submodel to describe leaf heating and mass release. The physics-based submodel predicts how the leaf temperature profile and mass release timing is affected by specific heating factors such as gas temperature and wind speed. The physics-based submodel predictions at both the new heating conditions and the base case provide a basis for scaling the flame parameters to the new conditions. The flame parameters were given previously (see Equations 4-7 to 4-10), and Chapters 6 and 7 provided a foundation for the physics-based submodel.

Fire spread in the bush model occurs when the flame zone of a burning leaf overlaps an unburned leaf long enough to ignite it. The ignited leaf then spontaneously develops a flame according to its flame parameters and has the potential to overlap and ignite neighboring leaves. The first-generation flame merging model was an outgrowth of this geometric description of fire spread. Overlapping flames were expanded based on the volume of flame-flame overlap. This approach did not directly relate to conventional flame-merging methods or measurements nor was it known to scale correctly with fire size. Therefore, a new flame merging model was based on merging measurements and the general approach found in flame merging literature (Weng et al., 2004). However, this new flame merging model goes beyond what is found in the flame merging literature (Thomas, 1963; Baldwin, 1968; Lamorlette and Foster, 2002; Weng et al., 2004; Kamikawa et al., 2005; Dahm, 2007; Satoh et al., 2007; Finney and McAllister, 2011; Maynard, 2013) because fires in shrubs do not conform to horizontal arrangements in some type of grid.

The behavior of the physics-based submodel was evaluated independently of the improved bush model. Next, the behavior of the improved bush model was evaluated as a whole by comparing model predictions to fire spread behavior measured in manzanita shrubs arranged in a wind tunnel (discussed in detail in Chapter 4).

8.1 Model overview

Model execution of the improved bush model was organized into subprocesses, beginning with setting up the fire spread scenario, which included:

1. Specification of simulation details;
2. Definition of physical leaf properties;
3. Definition of flame parameters, with adjustments by the physics-based submodel; and
4. Fire spread initialization.

Fire spread was simulated by stepping through time while calculating:

1. Flame geometry (e.g. flame height, angle, merging effects, radius, etc.); and
2. Leaf status (e.g. preheating, burning or burned out).

Simulation details included the number of fuel elements n_{fuels} , fuel element locations, fuel moisture content, ignition location, bulk wind speed U_{bulk} , and plume convection temperature T_{conv} . A plug flow wind profile based on U_{bulk} was used to set the wind speed at every leaf U . Heat transfer and mass release in the physics-based submodel were affected by U and T_{conv} .

Physical leaf properties included leaf dry mass m_{dry} , moisture content MC (dry basis), total mass m_0 , width w , thickness Δx and length l (see Chapter 4). Flame parameters included ignition time t_{ig} , max flame height time t_h , burnout time t_{bo} and max flame height $h_{f,max}$ (of a solitary flame) (see Figure 4-7 and Equations 4-7 to 4-10).

The physics-based submodel was run for both the base case (which represents the flat-flame burner conditions) and for the new fire spread conditions. Burn time and mass release were then used to scale the flame parameters to the desired conditions. Finally, fire spread was initialized by igniting the leaves in the ignition region.

In the fire spread calculation loop, flame dimensions were determined. Flame dimensions are only introduced in concept here, and will be discussed in detail in the following sections. The unmerged flame height h_l at each time step was found by linearly interpolating between the points defined by the flame parameters (see Figure 4-7). The actual flame heights h_f were determined from h_l by considering flame-flame interactions. Flame radius r_f , flame extension below the leaf d_f , and flame angle θ were all affected by flame merging.

Leaves were ignited based on the duration of flame-fuel overlap and radiation exposure. External heating specifications (such as from excelsior starter fuel) also caused leaves to ignite. The physics-based scaling was revised after any major experimental events such as a change in U_{bulk} .

8.2 Physics-based submodel and flame parameter scaling

The physics-based submodel was developed to scale the flame parameters to a broad range of fire conditions. Flame parameter scaling using the physics-based submodel will be presented here in two parts: (1) the physics-based submodel; and (2) flame parameter scaling.

8.2.1 Physics-based heat transfer and mass release submodel

The physics-based heat transfer and mass release model was used to describe the base case heating conditions and the new fire spread conditions. The submodel coupled:

1. The temperature-dependent mass release;

2. A mechanistic description of heat transfer to the leaf; and
3. The energy balance of the leaf.

Mass release, heat transfer, and the leaf energy balance will be discussed in three subsections.

8.2.1.1 Temperature-dependent mass release

Mass release of the dry matter components was calculated with the multi-component one-step devolatilization model developed in the previous chapter (see section 7.1.4.3). The equation and model parameters were given previously (see Equation 7-4 and Table 7-2). The multi-component model includes two components each for cellulose, hemicellulose and lignin. A diffusion-limited model was used to describe water release. This model was also developed in the previous chapter (see section 7.1.5.3 and Equations 7-6 to 7-8). A temperature-dependent diffusivity was based on drying measurements of wood (Stamm, 1964; Plumb et al., 1985). Both water diffusion and devolatilization depended on the leaf temperature, and leaf temperature depended on the remaining mass of the leaf and the heat of vaporization of water.

8.2.1.2 Convection and radiation heat transfer to the leaf

The value of T_{conv} was set to 1000 °C for the base condition and estimated for the fire spread condition. The temperature in the immediate vicinity of a burning leaf T_{local} was considered to be higher than T_{conv} during pyrolysis and combustion. The increase in temperature was determined from the heat of combustion ΔH_{comb} of the devolatilized dry mass divided by the heat capacity of the gases passing near the leaf (Equation 8-1).

$$T_{local} = T_{conv} + \frac{\Delta H_{comb} \sum_{i=1}^6 \Delta m_{dry,i}}{\rho_{conv} c_{p,gas} v A_{c,local} \Delta t} \quad (8-1)$$

where Δm_{dry} is the change in dry mass, the subscript i specifies the dry matter fraction (of which there were six), and Δt is time step (set to 0.005 s). The gas velocity v at the leaf was estimated as 1.2 m s^{-1} for the base case, which is twice the post-flame gas velocity at the burner surface. This velocity was used to account for buoyant acceleration due to the flame of the leaf and the post-flame gases. For the fire spread case, v was calculated as the sum of the contributions due to wind $\bar{v}_{U,\theta}$ and buoyancy $\bar{v}_{z,\theta}$ (see Equations 8-2 and 8-3). The heat output from the flame of the burning leaf was estimated to affect a cross-sectional area $A_{c,local}$ of 36 cm^2 . The volume of flame-heated air was thus equal to $vA_{c,local}\Delta t$. The gas density ρ_{conv} was determined from the molecular weight of air (28.97 g mol^{-1}) and the ideal gas law at 1 atm and T_{conv} . The heat capacity of the passing gases $c_{p,gas}$ was set to $1.2 \text{ J g}^{-1} \text{ K}^{-1}$ (air, 1100 K to 1600 K (Incropera et al., 2007)). The value of ΔH_{comb} of pyrolysis gases was set to 20 kJ g^{-1} (Jenkins et al., 1998). Temperature-dependent mass release over each time step ($\sum_{i=1}^6 \Delta m_{dry,i}$) was determined from the multi-component devolatilization model.

The component of wind speed in the flame axis direction $\bar{v}_{U,\theta}$ for the fire spread case was calculated by projecting the average local wind velocity onto the flame axis (Equation 8-2), where θ_i is the flame tilt angle (from vertical) of flame i and N is the number of flames.

$$\bar{v}_{U,\theta} = \frac{\sum_{i=1}^{n_{fuels}} U_i}{n_{fuels}} \sin \left(\left| \frac{\sum_{i=1}^N \theta_i}{N} \right| \right) \quad (8-2)$$

The value of θ_i was calculated with the Froude number correlation based on the $h_{f,group}$, which is the collective flame height of a merged group of leaves. The determination of $h_{f,group}$ is discussed later. Unless fire conditions were altered mid-burn, the value of $\bar{v}_{U,\theta}$ was only determined before the simulation was initialized. Therefore, $h_{f,group}$ was initialized to the height of the shrub before finding the initial value of θ for all leaves.

Flame buoyancy generates vertical gas velocity, which was measured and correlated at the centerline as a function of height (McCaffrey, 1979). The centerline velocity was determined at a height of the maximum of: (1) the maximum h_f of all individual flames; and (2) 30% of the mean $h_{f,group}$ of all flames. The average vertical velocity of the buoyant plume was approximated by dividing the centerline velocity by two. The vertical velocity was then projected onto the flame axis to give the buoyant velocity component in the flame direction $\bar{v}_{z,\theta}$ (Equation 8-3).

$$\bar{v}_{z,\theta} = \cos\left(\left|\frac{\sum_{i=1}^N \theta_i}{N}\right|\right) \frac{0.9 \sqrt{\frac{2gT_{conv} \max\left(\max(h_f), 0.3 \frac{\sum_{i=1}^N h_{f,group,i}}{N}\right)}{T_{amb}}}}{2} \quad (8-3)$$

The heat transferred to the leaf by convection q_{conv} was first determined without correcting for blowing (i.e. high rates of mass transfer):

$$q_{conv} = \bar{h}_L A_{face} (T_{local} - T_{leaf}) \quad (8-4)$$

where A_{face} was the two-sided surface area of the leaf calculated as an ellipse with major and minor axes. The mean length and width of the modeled leaves were supplied as the major and minor axes. The leaf was considered to be isothermal at temperature T_{leaf} .

The uncorrected average heat convection coefficient \bar{h}_L was calculated for the average conditions over the entire leaf using a Nusselt number correlation (Incropera et al., 2007) for flat plate geometry under laminar flow conditions and Prandtl numbers Pr greater than 0.6 (Equation 8-5).

$$\overline{Nu}_L \stackrel{\text{def}}{=} \bar{h}_L L / k = 0.664 Re_L^{1/2} Pr^{1/3} \quad (8-5)$$

The Nusselt number averaged for the length of the leaf \overline{Nu}_L was determined for an average leaf boundary layer development length of: $L = 2l/\pi$, where l is the length of the leaf at its maximum. Gas phase properties of conductivity k , and kinematic viscosity ν and Prandtl

numbers were determined at 750 K, which was considered to be a typical film temperature. The Reynolds number was defined as: $Re_L = LV/\nu$. In order to better fit measured results, the final calculated value of \bar{h}_L was scaled by a factor of 1.5. The need for this factor may result from the exothermic process of char oxidation or from flow irregularities which were not modeled.

The convection coefficient \bar{h}_L was corrected by the blowing factor θ_T for high rates of mass transfer (Bird et al., 2002) (Equation 8-6).

$$\theta_T = \frac{\ln(1 + R_T)}{R_T} \quad (8-6)$$

The thermal flux ratio R_T in Equation 8-6 is defined in Equation 8-7:

$$R_T = \frac{[\Delta m_{water} c_{p,water} + \sum_i (\Delta m_{dry,i}) c_{p,dry}] (T_{local} - T_{leaf})}{q_{conv} \Delta t} \quad (8-7)$$

where Δm was mass released and the subscripts *water* and *dry* designate the substance. Values of $2.5 \text{ J g}^{-1} \text{ K}^{-1}$ and $4.2 \text{ J g}^{-1} \text{ K}^{-1}$ were respectively used for $c_{p,dry}$ and $c_{p,water}$. Water release was determined by the diffusion model described in Equations 7-6 to 7-8.

An empirical expression was created to estimate flame opacity κ for radiation of the flame back to the leaf based on the amount of dry mass release (Equation 8-8), where g is grams, s is seconds and c_1 is a coefficient set to 0.5 s g^{-1} .

$$\kappa = \min \left\{ \frac{c_1 \sum_i \Delta m_{dry,i}}{\Delta t}, 1 \right\} \quad (8-8)$$

The calculated κ was then used to balance radiation from the soot in the flame and radiation from the remaining surroundings (Equation 8-9).

$$q_{rad} = \sigma \varepsilon A_{face} [\kappa (T_{soot}^4 - T_{leaf}^4) + (1 - \kappa) (T_{surr}^4 - T_{leaf}^4)] \quad (8-9)$$

A leaf emissivity ε of 0.98 was chosen (Lopez et al., 2012), and σ is the Stefan-Boltzmann constant. A value of 1500 K was chosen for T_{soot} . Higher values were avoided due to numerical

problems. The non-flame surroundings temperature T_{surr} was set to 525 K for the base case and 300 K for fire spread scenarios. In the single leaf base case, the elevated temperature represents the temperature of the glass duct surrounding the burner used in later experiments.

8.2.1.3 Leaf energy balance

The amount of water release was determined by the rate of diffusion through the thickness of the leaf (Equation 7-7) with a total leaf thickness equal to the mean modeled leaf thickness. The cooling due to water evaporation was based on the heat of vaporization of water ΔH_{vap} at 470 K (1951 J g⁻¹) (Equation 8-10).

$$q_{evap} = -\Delta m_{water} \frac{\Delta H_{vap}}{\Delta t} \quad (8-10)$$

Finally, the new leaf temperature T_{leaf}^{i+1} was determined from the previous leaf temperature T_{leaf}^i using the leaf energy balance:

$$T_{leaf}^{i+1} = T_{leaf}^i + \frac{\theta_T q_{conv} + q_{rad} + q_{evap}}{\sum_i (m_{dry,i}) c_{p,dry} + m_{water} c_{p,water}} \Delta t \quad (8-11)$$

where $m_{dry,i}$ is the dry mass remaining in the leaf of each dry component i and m_{water} is the mass of water remaining in the leaf. T_{leaf} was initialized to 300 K.

The final implementation of Equations 8-1 to 8-11 resulted in a model coupling the transient heating of a leaf by convection and radiation, and the mass release of its components. This model was used to determine the ratio of times needed to burn a base case leaf and a leaf in the fire spread scenario as well as the ratio of volatiles released during the burn period in order to scale flame times and flame heights (Equations 8-12 to 8-14).

8.2.2 Flame parameter scaling

The physics-based submodel was run for the base case and the targeted fire spread conditions in order to scale flame parameters (see Equations 4-7 to 4-10) to the targeted fire spread conditions. Flame parameters were scaled based on the duration and amount of mass release. The end of mass release t_{end} was considered to occur when at least 25% of each of the six dry components was released and the total rate of dry matter release was less than 2% of the starting dry mass per second. If these criteria were not met within 50 s, t_{end} was set to 50 s. The ratio of t_{end} for the base case (subscript 0) and new case (subscript F) were then used to scale t_{ig} , t_h , and t_{bo} to the fire spread conditions:

$$t_{x,F} = t_{x,0} \frac{t_{end,F}}{t_{end,0}} \quad (8-12)$$

where the subscript x refers to any of the flame times. The criteria for t_{end} were selected to approximate time at burn out. The fraction $t_{end,F}/t_{end,0}$ is the physics-based scaling factor of flame time.

The flame height was scaled similarly. Flame heights are considered to scale by the two-fifths power of the heat release (Steward, 1970; Sun et al., 2006). Heat release is proportional to the total mass release (excluding water), which is inversely related to the time over which mass is released. Therefore, $h_{f,max}$ was scaled by the physics-based scaling factor φ_h (Equations 8-13 and 8-14):

$$h_{f,max,F} = \varphi_h h_{f,max,0} \quad (8-13)$$

$$\varphi_h = \left[\left(\frac{t_{bo,0} - t_{ig,0}}{t_{bo,F} - t_{ig,F}} \right) \left(\frac{\Delta F_F}{\Delta F_0} \right) \right]^{2/5} \quad (8-14)$$

ΔF_F is the fractional change in dry mass at the new fire condition and ΔF_0 is the fractional change in dry mass at the base condition.

This approach for scaling flame parameters using scaling factors determined with the physics-based submodel compliments the existing model framework while providing model responsiveness to a broad range of fire scenarios. It also provides a convenient foundation for mass release-correlated flame heights as an option for future model iterations. Furthermore, because this approach scales experimental correlations rather than directly calculating flame behavior, the effect of imprecisely estimated values, to some extent, cancels out. With future model development, the experimental correlations for flame behavior may eventually be replaced with direct calculation of flame behavior from an experimentally-validated model, rather than by this intermediate approach.

8.3 Flame-flame interactions model and flame geometry

8.3.1 Flame height

A flame-flame interaction submodel was developed from the experimental measurements of Weng et al. (2004) for 2-D grids of square porous burners, resulting in Equation 8-15 for merged flame height:

$$\frac{L_f}{L_m} = \left(\frac{2\sqrt{N}(\sqrt{N} - 1)S^2 + \Lambda D^2}{\Lambda(2\sqrt{N}(\sqrt{N} - 1)S^2 + D^2)} \right)^B \quad (8-15)$$

This equation describes the effect of burner gap S and burner side length D , where L_f is the flame length at S , L_m is the fully-merged flame length (at $S = 0$), and N is the number of fire sources located in a square configuration. The terms Λ and B were determined from experimental data. Equation 8-15, however, was limited in scope and did not seem to give good results.

In this work, the experimental measurements of Weng et al. (2004) were used as a primary resource for developing a new and more versatile flame merging equation. An equation

was needed for use in flame merging in burning shrubs, which could account for vertical separation, horizontal separation, non-uniform flame heights, non-uniform flame diameters, and arbitrary arrangements of fuel sources. While the new equations were developed to fit the flame merging measurements of Weng et al. (2004), the final selection of coefficients was made with a focus on shrub-scale fire behavior rather than Weng's original flame merging measurements.

Equation 8-16 is proposed to account for the incremental effect of additional flames on the flame height of an array of fully merging flames, where the ratio of L_m to the solitary flame length L_1 is related to N .

$$\left(\frac{L_m}{L_1}\right)_{N_2} - \left(\frac{L_m}{L_1}\right)_{N_1} = c_1 \ln\left(\frac{N_2}{N_1}\right) \quad (8-16)$$

The term N_1 indicates the number of burners in a first array of burners and N_2 refers to the number of burners in a second array of burners. For 1 kW and 0.5 kW flame sources flame merging measurements were fit when c_1 was 0.304 and 0.112, respectively (Weng et al., 2004).

While Equation 8-16 applies to fully merged flame sources in a horizontal array, separation of flame sources in shrub fuel matrices occurs both horizontally and vertically. An equation was determined to describe the separation of flames in a 3-D array, normalized by the relevant flame dimension. Horizontal separation was normalized by the radii ($r_{f,i} + r_{f,j}$) of leaves i and j . Vertical separation of burning leaves i and j was normalized by the flame length ($L_{f,j}$) of leaf j . The value of $L_{f,j}$ was used in Equation 8-17 before being calculated in Equation 8-18. Therefore the value at the previous time step was used, except when the current $h_{1,j}$ was greater. Normalized 3-D separation distance $\hat{S}_{i,j}$ is given in Equation 8-17, where z is vertical leaf position. The first term in Equation 8-17 inside the square root is the normalized horizontal separation, and the second term normalizes the vertical separation.

$$\hat{S}_{i,j} = \sqrt{\left(\frac{S_{i,j}}{r_{f,i} + r_{f,j}}\right)^2 + \left(\frac{z_i - z_j}{L_{f,j}}\right)^2} \quad (8-17)$$

The value of $L_{f,i}$ was then found for each burning leaf in Equation 8-18 using Equation 8-17 for $\hat{S}_{i,j}$. Note that the numerator in the summation term is equivalent to Equation 8-16,

$$\frac{L_{f,i}}{L_{1,i}} = \frac{h_{f,i}}{h_{1,i}} = \left(\frac{v}{v_0}\right)^{c_3} \sum_{j=2}^{N^*} \left(\frac{c_1 \ln\left(\frac{j}{j-1}\right)}{1 + c_2 \hat{S}_{i,j}}\right) + 1 \quad (8-18)$$

where the gas velocity parallel to the flame axis v stretches the flames and v_0 is a reference value of 1.6 m s^{-1} . $\hat{S}_{i,j}$ was ordered from smallest to largest value ($\hat{S}_{i,j-1} \leq \hat{S}_{i,j}$), and N^* is the number of flames j for which a merging criterion was met. The coefficient c_1 was set to 0.7, c_2 was set to 1, and c_3 was set to 2.4. The sorted values of $\hat{S}_{i,j}$ did not exclude comparison of leaf i with itself. However, it was always first in the sorted list and was excluded from flame merging calculations by summing leaves in Equation 8-18 beginning with $j = 2$.

A merging criterion was developed which was loosely based on the relationship between dimensionless separation distance and merged flame height for 2x2 and 4x4 square arrays of burners. For the 2x2 array, no significant change in merging occurred after a normalized separation distance of one and for the 4x4 array the critical distance was two. Therefore, Equation 8-19 was used to relate N and $\hat{S}_{i,j}$ to the number of flames N^* which were substantially merged to the flame of leaf i . This equation means that the maximum index j is selected with the constraint that $\hat{S}_{i,j} < N^{1/2}/2$.

$$N^* = \{\max(j) \mid \hat{S}_{i,j} < N^{1/2}/2\} \quad (8-19)$$

8.3.1 Flame radius and downward extension

In single leaf burn experiments, flame height and flame width were observed to increase as the rate of mass release increased, and decrease as the rate of mass release slowed. This was previously interpreted by setting flame width to increase with flame height, regardless of the cause of the increased flame height.

However, the cause of change in flame height may impact how the flame radius r_f changes. It was postulated that r_f scaled proportionally to changes in flame height related to the rate of mass release, but that r_f was inversely correlated to increases in flame height due flame merging or flame velocity. These hypotheses were used to develop Equation 8-20 for radial extension of the flame from the center of the leaf, with coefficients $c_4 = 2.1$ and $c_5 = 0.32$ yielding favorable fire spread simulations.

$$r_f = \frac{h_1/c_4}{\left(\frac{h_f}{h_1}\right)^{c_5}} \quad (8-20)$$

The solitary flame height h_l was related to the mass release while the fraction h_f/h_1 was equal to the flame height stretching caused by flame merging and fluid velocity. Downward flame extension d_f was assumed to also follow Equation 8-20, and coefficients of $c_4 = 2.1$ and $c_5 = 0.25$ were found to produce reasonable shrub scale fire spread simulations.

Equation 8-20 promoted fire spread stability and brought the model into better agreement with actual fire behavior observed in wind tunnel shrub burns. The magnitude of r_f has a very strong influence on rate and extent of flame propagation while the magnitude of d_f also impacts the extent of flame propagation.

8.3.2 Flame angle

Flames which met the merging criterion were associated into flame groups. Groups with shared members were merged. A small number of groups typically formed during a modeled burn. For each group, the flame height $h_{f,group}$ was determined as the height difference from the lowest burning leaf to the highest flame top. The Froude number correlation used $h_{f,group}$ and U to determine and assign a single preliminary flame angle for all flames in the group (Equation 4-11). The $h_{f,group}$ of flames which were not near enough to other flames to meet the merging criterion were set to h_f .

The preliminary values of $h_{f,group}$ were adjusted to bring the tops of grouped flames closer together, qualitatively mimicking the coalescing behavior of flames. This was done by shifting the x location of each flame top half way to average of the x locations of all flame tops in the group. Pulling flame tops closer together reduces the rate and extent of fire spread.

8.3.3 Flame-fuel overlap and pseudo-radiation

Flame-fuel overlap was determined by first identifying the minimum and maximum x , y and z coordinates occupied by the flame of each leaf. The maxima and minima defined a rectangular prism which circumscribed the cylindrical flame volume and included all leaves potentially overlapped by the flame. Any potentially overlapped leaves within r_f of the flame axis were considered heated by flame overlap. Leaves within a rectangular prism but not overlapped convectively by a flame were considered to preheat by radiation if the overlapping flame was a member of a flame group. Radiant heating was set to 1/20 the rate of heating by flame-fuel overlap. Due to the limited development of this method, the effect of radiant heating was restricted for these small-scale flames. Pseudo-radiant heating was allowed to slowly bring fuels to the point of ignition, but at least momentary flame-fuel overlap was required for ignition.

8.4 Miscellaneous model details

Flame shapes were simulated as cylinders, although they were still rendered as rectangular prisms in model visualizations. Flame intermittency was modeled by multiplying the scaled but pre-merged flame height h_l of each burning leaf by a random number between 0.6 and 1.4. Model speed was increased by recording paired lists of the flame responsible for preheating each leaf during each time step. The paired list was then used to check for flame-fuel overlap on the following time step, reducing the number of preheating leaves requiring exhaustive checks to determine their preheating status. Model speed was also increased by changing the time step from 0.1 s to 0.2 s. The impact of the time step change was not formally tested, but seemed to have no noticeable impact on fire spread predictions. In previous versions of the bush model, leaves heating to ignition were typically set to “cool” if they lost contact with other flames. This was done by subtracting time from their progress to ignition. The leaf cooling assumption was removed from the model in favor of a simple stall in heating if a leaf lost contact with other flames during preheating. Leaves which were intermittently heated were typically near other flames and can be considered to be recipients of their flame radiation, making leaf cooling between flame overlap insignificant.

8.5 Wind tunnel simulation cases

The improved bush model was used to simulate the set of wind tunnel runs described in Table 4-2. Thirty simulations at each condition were performed and the flame height above the shrub $\Delta z_{f,max}$, burn fraction X_s , and burn time t_{burn} were compared.

Values of T_{conv} were set to 810 °C, 830 °C, 840 °C and 830 °C for Runs 1 through 4, respectively. These temperatures were selected to tune the rate of fire spread, but also correspond to the wind speeds of the runs, which in run order were 0 m/s, 0.45 m/s, 1.08 m/s and 0.69 m/s.

The initial ignition volume spanned from x and z equal to zero to specific x and z limits, and included the entire y dimension (see Figure 4-11). Limits were given as a fraction of the total x or z dimension. For burns one through four, described in Table 4-2, the limits were $(x, z) = (0.06, 1), (0.08, 1), (0.35, 0.19),$ and $(0.35, 0.24),$ respectively. To simulate extended heating provided by the excelsior ignition bed in Runs 1 and 2, a y - z ignition plane was advanced across a portion of the x -axis, igniting all leaves in its path. Beginning at $x = 0$, the ignition plane advanced 0.1 m in 20 s in Run 1, and 0.18 m in 30 s in Run 2. In wind tunnel Run 2, the fan stopped at 141 s. This was modeled by changing U_{bulk} in Run 2 to 0 m/s at 141 s and updating flame parameters and physics-based scaling factors. Shrubs were simulated with half the y dimension and consequently half the number of leaves to reduce computational time. Actual shrub dimensions and leaf numbers (before reducing in half) were listed in Table 4-2. The impact of this change was not formally examined, though it was expected to be small. The reduction in shrub width would have a tendency to reduce flame size (due to fewer flame interactions in the y direction) and increase the chance of premature fire extinguishment. Leaf placement was based on the image-based model which was developed for the first-generation shrub model.

8.6 Results and discussion

The physics-based scaling model responded to multiple values affecting convection and radiation. The behavior of the physics-based scaling model was benchmarked and its response to several inputs was demonstrated. Next, the improved fire spread model, which included the physics-based scaling model, was compared to the wind tunnel fire spread measurements. The wind tunnel measurements previously discussed and modeled in Chapter 4 were used so that changes in the fire spread modeling would be easily identifiable.

8.6.1 Physics-based submodel for scaling flame parameters

The physics-based submodel treated the leaf as a lumped capacitance heat reservoir. Modeling mass release based on a single leaf temperature introduces a baseline level error. This was previously shown when using the average of measured leaf temperatures (see Figure 7-21). The physics-based scaling model also calculated leaf temperature based on heat transfer equations rather than from surface temperature leaf measurements, which introduces additional error. Predictions of the physics-based model are shown in Figure 8-1. The physics-based submodel performed similarly to the mass model and measured mass profiles until 7 s of residence time. Between 7 s and 9 s, the physics-based submodel was higher than the other profiles, but by 10 s had dropped below both the measured and mass model curves. The physics-based submodel ends at t_{end} , which occurred near the end of the end of mass release predicted by the CPD mass modeled. Considering the complexity of the physics-based scaling model, the modeled mass release predictions compared favorably with mass release measurements and mass release calculations based on measured leaf temperatures.

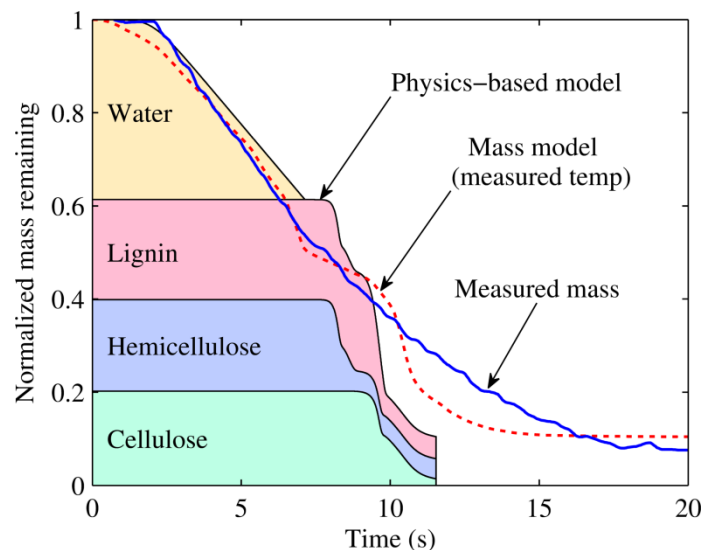


Figure 8-1. Comparison of (a) the base case physics-based submodel to (b) mass release calculated from measured leaf temperatures and (c) mass release measurements. The leaf had a moisture content of 63% and the base case physics-based scaling model is divided into its main constituents.

Because flame parameters were scaled by the ratio of burnout times calculated by the physics-based submodel (see Equations 8-12 to 8-14), some amount of model bias cancels out. The calculated temperature profile of the physics-based scaling model is responsible for nearly the entire difference between the mass release predictions using the physics-based submodel and those based on measured temperatures. For example, temperature profiles generated by the physics-based submodel for the base case are shown for various moisture contents in Figure 8-2. The average measured temperature of the leaf modeled in Figure 8-1 is also plotted for comparison.

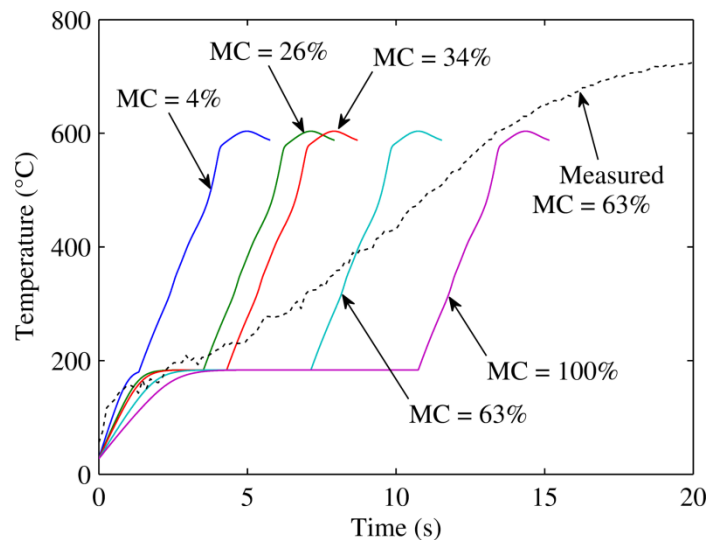


Figure 8-2. Leaf temperature profiles for various moisture contents calculated by the physics-based scaling model compared with the average measured temperature of a burning leaf.

The modeled temperature profiles had better qualitative agreement with the mode temperature profiles plotted in Figure 6-6 than the included mean temperature profile. Further modeling could potentially improve these modeled temperature profiles and provide insights concerning the heat and mass transfer behavior of burning leaves. For the purpose of scaling flame parameters to new fire spread conditions, however, the physics-based submodel was considered acceptable.

The normalized mass release associated with the modeled temperature profiles of Figure 8-2 are shown in Figure 8-3. Each mass release curve ends when the criteria for t_{end} was met. A reasonable end time was achieved for each moisture content. The t_{bo} of a 0.13 g, 3 cm by 2 cm by 0.5 mm leaf ranged from 8.8 s (MC = 4%) to 19.4 s (MC = 100%) based on the flame parameter correlations. For these moisture contents, the value of t_{end} for the physics-based submodel was consistently 63% to 78% of the values of t_{bo} from the flame parameter correlations (see Equations 4-7 to 4-10). Were the physics-based submodel used to scale between two moisture contents, then most of the error would cancel out. However, moisture content is included in the flame parameter correlations, which means that the physics-based submodel is not needed to scale between moisture contents; it is mainly used to scale between heating conditions. However, these results are still relevant because the physics-based submodel must function reasonably well at any moisture content, which these results demonstrate.

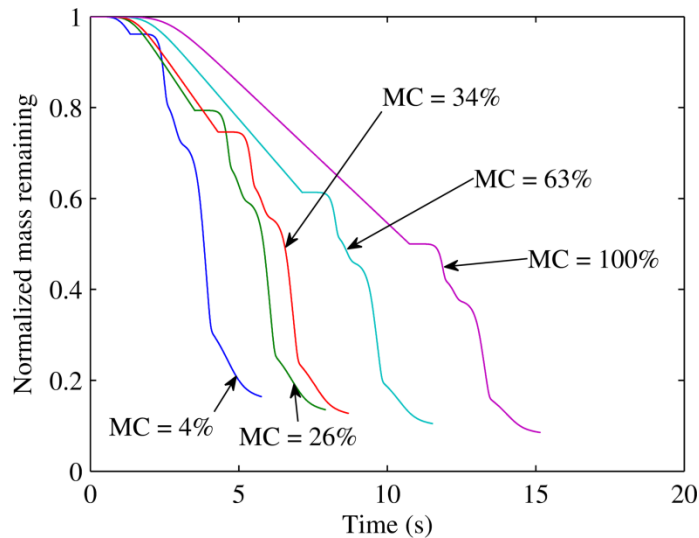


Figure 8-3. Leaf normalized mass profiles for various moisture contents calculated by the physics-based scaling model.

The heating conditions of a fuel element depend on bulk convection temperature, radiation temperature, and convective gas velocity. A sensitivity analysis was made on each of

these effects based on flame parameters of a leaf with $m_{dry} = 0.13$ g, dimensions of 3 cm by 2 cm by 0.5 mm, and a moisture content of 50%, were $t_{ig} = 3.2$ s, $t_h = 10.4$, $t_{bo} = 15.1$ s, and $h_{f,max} = 0.086$ m. The flame angle was based on the Froude number correlation at U and $h_{f,max}$. The variables T_{conv} , vertical flame position, U and T_{soot} were set to respective values of 1000 °C, 0.1 m, 0 m/s and 1500 K. Model response was then demonstrated by changing each variable independently. Both U and vertical flame position affect the convective gas velocity. Physics-based scaling is plotted as defined in Equations 8-12 to 8-14.

8.6.1.1 Sensitivity to T_{conv}

The physics-based scaling of time (Equation 8-12) and flame height (Equation 8-13) versus T_{conv} is shown in Figure 8-4. At temperatures lower than 800 °C, the time scaling was controlled by the 50 s limit on t_{end} . At values of T_{conv} between 500 °C and 800 °C, the flame height scaling increased slightly as more of the leaf was consumed in the 50 s time limit. At higher fire spread scenario temperatures ($T_{conv} > 800$ °C), the time scaling fell as the criteria for t_{end} was met more quickly, and the scaling of flame height increased as the leaf was consumed at a higher rate.

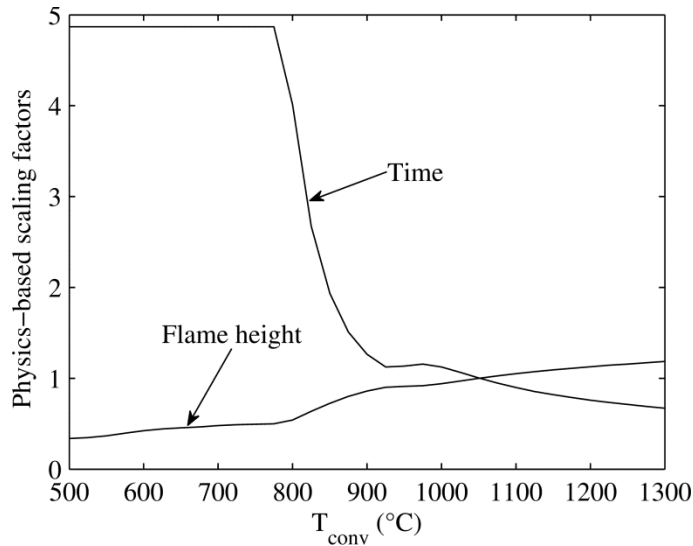


Figure 8-4. Sensitivity of scaling factors for flame parameters to T_{conv} .

8.6.1.2 Sensitivity to T_{soot}

Physics-based scaling due to flame radiation temperature (T_{soot}) was less impactful but more intriguing (see Figure 8-5). Changes in T_{soot} had a relatively low impact on the scaling factors because flame opacity was low due to the value selected for c_1 in Equation 8-8. Time scaling had two prominent changes in slope between T_{soot} of 700 °C and 2000 °C, as did flame height scaling. Negative slopes of the time scaling factor likely result from faster depletion of water and pyrolyzates due to the increased heating. Positive slopes of the time scaling factor presumably result from higher values of T_{soot} increasing the final leaf temperature and prolonging the period before the rate of mass release dropped below $2\% m_{dry} s^{-1}$. These effects, and possibly others, dominate over different temperature ranges, causing the reversals in slope. Flame height scaling mirrors the time scaling because it is based on relative rates of mass release which are affected by the scaled times in Equation 8-14. The flame height scaling is dampened, though, due to the two-fifths power in Equation 8-14.

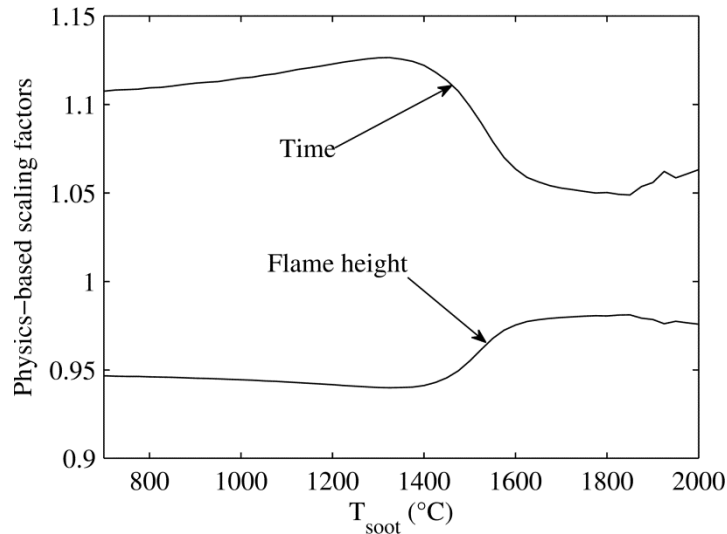


Figure 8-5. Sensitivity of scaling factors for flame parameters to T_{soot} .

8.6.1.3 Sensitivity to wind speed and vertical flame position

The change in the scaling factors due to changes in U (Figure 8-6) were due to the effect of U on the gas velocity in the flame direction v_{θ} (see Equation 8-2). As U increased, convective heat transfer increased, the temperature profile rose more quickly, and less time was required to burn the leaf out. The scaling factors do not meet at 1 as U approaches zero because the base case and the fire spread case have different values for both vertical flame height and T_{surr} in this comparison.

The vertical flame position also affects v_{θ} due to buoyant acceleration of the hot convective gas plume (Figure 8-7, Equation 8-3). As the vertical flame height approaches zero, the physics-based scaling factors diverge because v_{θ} and convective heating approach zero. The flame height scaling due to U and vertical flame position was mostly a function of flame time scaling; the amount of mass release was nearly constant (see Equation 8-12).

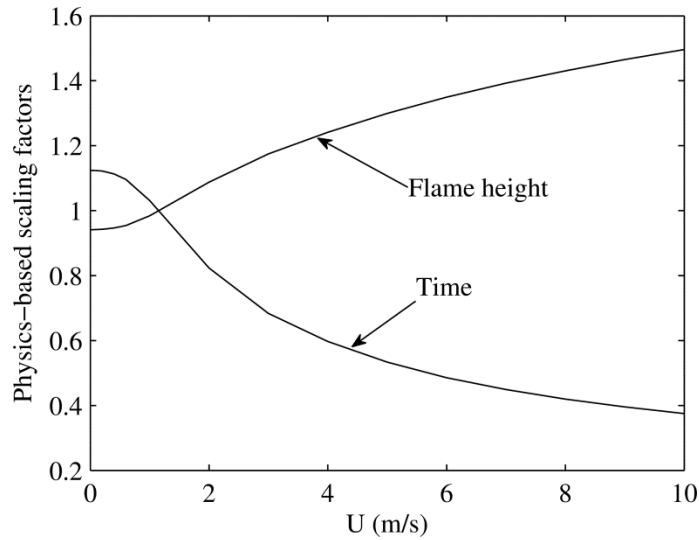


Figure 8-6. Sensitivity of scaling factors for flame parameters to U .

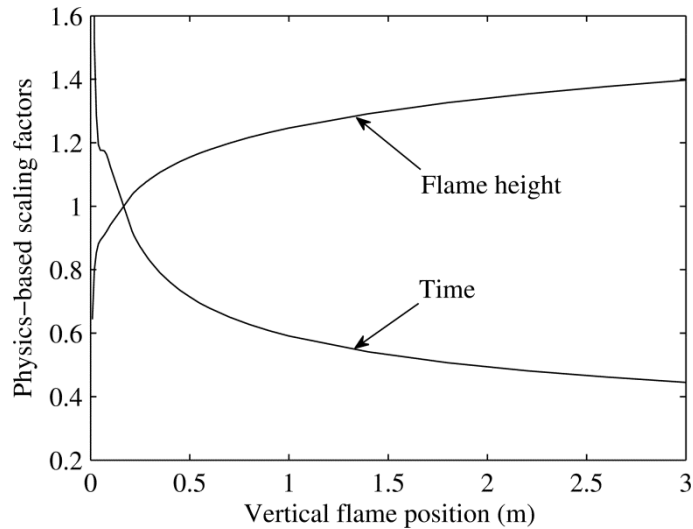


Figure 8-7. Sensitivity of scaling factors for flame parameters to vertical flame position.

Overall, the trends in the physics-based scaling of flame parameters responded as expected to factors affecting wildland fire spread. Developing the ability to respond appropriately to the heat transfer conditions of the fire spread scenario of interest was essential to achieving accurate results for broader fire spread conditions.

True predictive capabilities would also depend on developing methods to predict the fire scenario before a fire had already occurred. Dependence on user-defined heating conditions could be eliminated by periodically feeding back the modeled fire state to a model that would

determine the current heat transfer conditions. The updated heat transfer conditions would then be used to update the physics-based scaling model and flame parameters. A simple feedback model was implemented to do this, but was later removed because it resulted in either runaway or quickly-extinguishing fires. It is suspected that a more carefully-constructed feedback model could provide stable results.

8.6.2 Comparison of improved bush model with wind tunnel experiments

A set of wind tunnel fire spread measurements were described in Table 4-2. The fire spread behavior was modeled with the first-generation bush model in Chapter 4, but the model results did not entirely agree with the fire behavior measurements. Specifically, the flame height above the shrub $\Delta z_{f,max}$ was underestimated by the model and trended down with wind speed rather than up as was observed in the experiments. Furthermore, the burn times measured in the wind tunnel were not well described by the first-generation model. This section describes how the improved model compares with the set of wind tunnel experiments described in Table 4-2.

Box plots (presented below) summarize a set of 30 simulations performed for each wind tunnel configuration. Leaf placement and leaf physical parameters were randomized for each simulation within the boundaries defined by shrub images for each experiment. Flame paths were also compared between a single simulation of each burn and the wind tunnel measurements. Completing 30 simulations along with saving appropriate images required less than one hour on a personal computer.

8.6.2.1 Maximum flame height above shrub, $\Delta z_{f,max}$

The predicted maximum flame height above the shrub $\Delta z_{f,max}$ of the simulations are shown in Figure 8-8 along with the wind tunnel measurements. The predicted $\Delta z_{f,max}$ values had

a similar magnitude to the measurements, which was a major improvement over the first generation model. The measured values of $\Delta z_{f,max}$ increased with run number, which was also the case for the median values of $\Delta z_{f,max}$ for the improved bush model. In the first-generation bush model, $\Delta z_{f,max}$ decreased with run number. Physics-based scaling promoted taller flame heights at higher wind speeds, but flame height scaling based on gas velocity (Equation 8-18) was also needed to achieve this level of agreement with the wind tunnel burns.

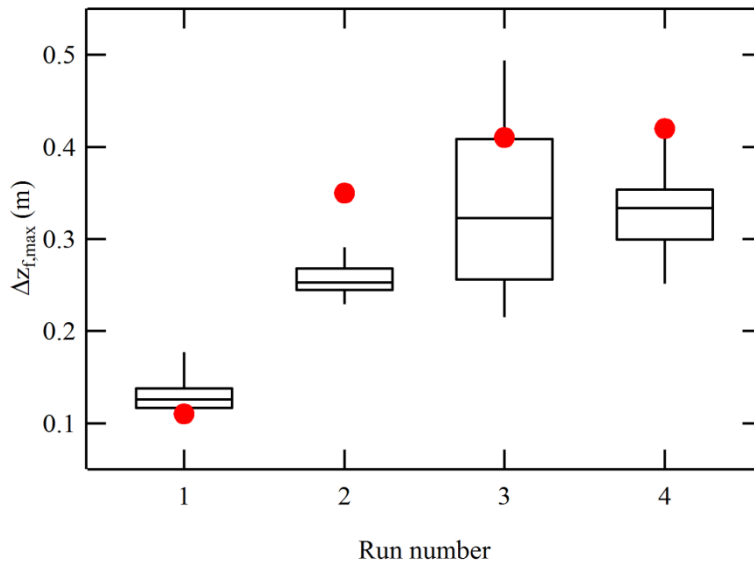


Figure 8-8. $\Delta z_{f,max}$ comparison of improved model simulations (box plots of minimum, first quartile, median, third quartile and maximum) and wind tunnel experiments (dots).

8.6.2.2 Fraction of shrub consumed, X_s

Predictions of the fraction of shrub consumed X_s are shown in Figure 8-9 along with observed values. The first generation fire spread model simulated larger values of X_s for Run 1 than was measured in the wind tunnel. Due to model improvements, predicted fire behavior responded better to wind speed and simulated very little fire spread for Run 1 while predicting high values of X_s for Runs 2 to 4, which had higher wind speeds. Some of the discrepancy between modeled and measured fire behavior is unavoidable without more extensive fluid flow

and ignition models, the former of which would require careful balancing of computational costs. However, the simulations and measured fire behavior were generally similar.

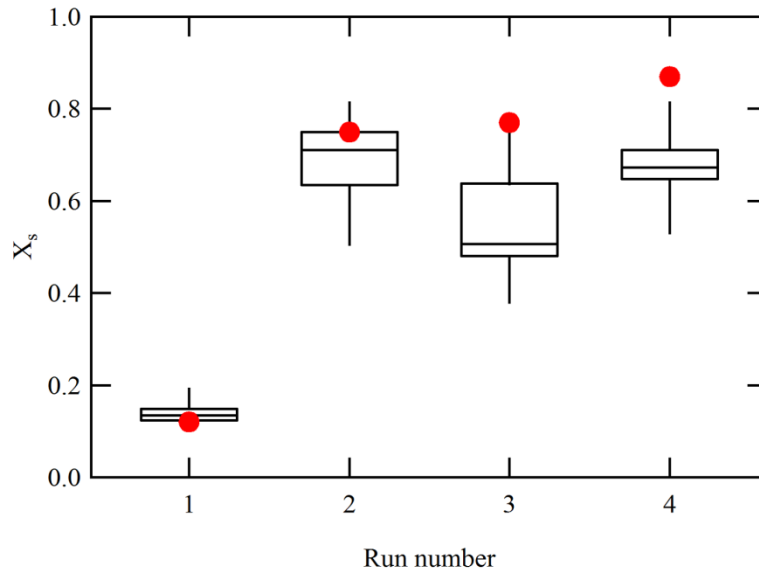


Figure 8-9. X_s comparison of model simulations (box plots of minimum, first quartile, median, third quartile and maximum) and wind tunnel experiments (dots).

8.6.2.3 Burn time, t_{burn}

Predicted burn times t_{burn} by the improved model are shown in Figure 8-10 and agreed quite well with the measured values. Physics-based scaling of flame times was an important factor for achieving agreement between the model and measurements. A small number of the burn simulations were prolonged due to fire spread doubling back on fuel left unburned by the initial fire front. These lingering flames would typically skip from leaf to leaf while only burning a few leaves at a time, which is why the predicted maximum burn times indicated by the vertical lines were so long.

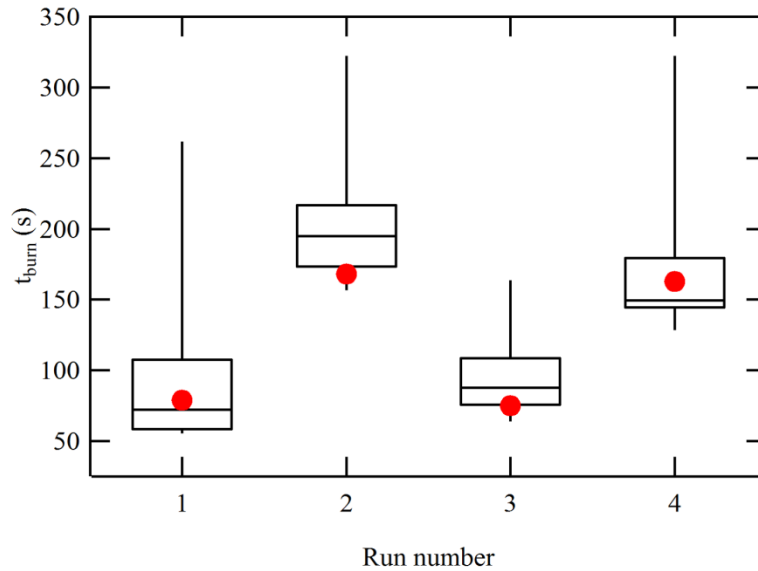


Figure 8-10. Burn time comparison of model simulations (box plots of minimum, first quartile, median, third quartile and maximum) and wind tunnel experiments (dots).

8.6.2.4 Flame path

Measured and modeled flame paths were compared in order to benchmark model behavior. Detailed data from six of the 30 simulations performed for each wind tunnel burn were saved for potential use as flame path runs. Of each set of six, one run was chosen which had values of t_{burn} and X_s which indicated a good match with the measured values of t_{burn} and X_s . These comparisons of flame path are shown in Figure 8-11 to Figure 8-14. A more detailed description of the wind tunnel fire behavior can be found in Chapter 4.

For Run 1, the flame paths measured in the wind tunnel and simulated by the model were very similar (Figure 8-11). Neither the measured nor simulated flame paths extended significantly beyond the area burned while assisted by excelsior starter fuel. The flame paths were nearly identical in timing and extent of burning.

The measured and simulated flame paths of Run 2 were also very similar in timing and extent of burning (Figure 8-12). In both cases, the change of wind speed at 141 s was highly influential in extinguishing the fire spread. The modeled and measured fire behavior of Runs 1

and 2 indicate that a wind speed as low as 0.45 m/s can sustain fire spread that otherwise extinguishes in still air under these laboratory conditions.

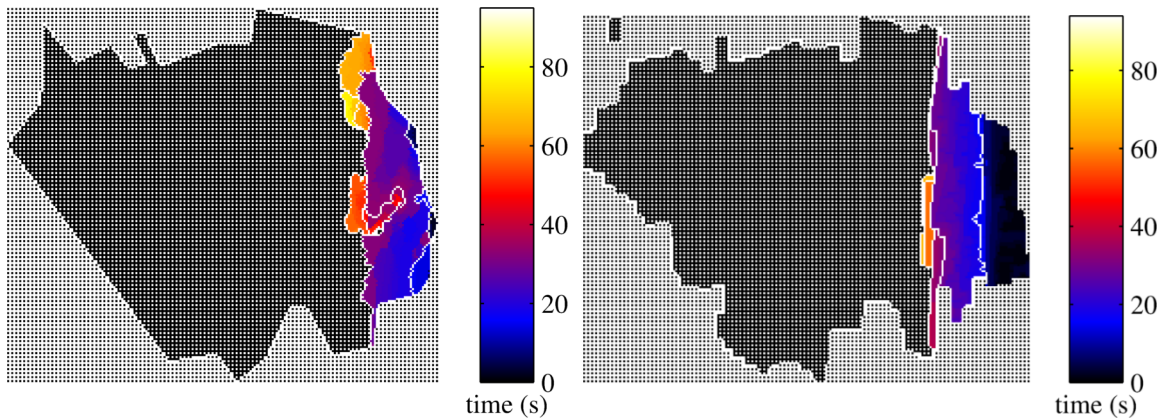


Figure 8-11. Run 1 flame path of the wind tunnel experiment (left) and a model simulation (right) viewed from the side. Time is represented by color shading. White contours mark 15 s intervals. The dark patterned area is unburned vegetation while the light patterned area was void.

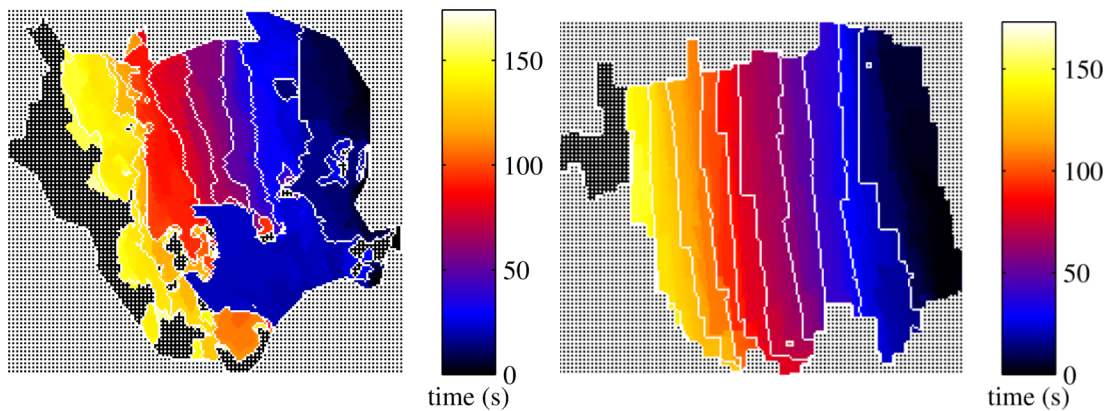


Figure 8-12. Run 2 flame path of the wind tunnel experiment (left) and a model simulation (right) viewed from the side. See figure caption to Figure 8-11.

The wind tunnel burn behaviors of Runs 3 (Figure 8-13) and 4 (Figure 8-14) were influenced by complicated fluid flow patterns which were evident from the flame patterns. These patterns were described in more detail in Chapter 4. Despite aspects of complex fluid flow which were not modeled, the simulations of Runs 3 and 4 displayed similar levels of flame coverage as measured for the wind tunnel runs. The same parts of the shrubs also remained untouched by the flames. However, the measured behavior of Run 3 exhibited significantly more backing fire

spread than was simulated. The measured fire paths of Run 4 was obscured by an early flame which skirted around the near side of the shrub. The burn path is still discernible if the early skirting behavior evident in the lower left of the flame path is ignored. The simulated flame path showed a similar amount and duration of backing fire spread as the measured flame path for Run 4. Overall, The measured burn path and simulated flame path of Run 4 were very similar.

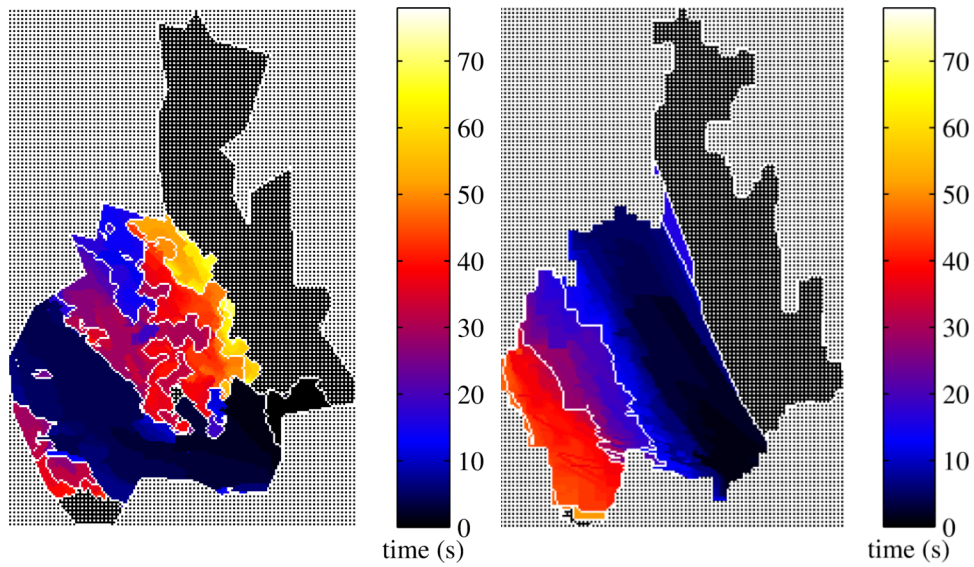


Figure 8-13. Run 3 flame path of the wind tunnel experiment (left) and a model simulation (right) viewed from the side. See figure caption to Figure 8-11.

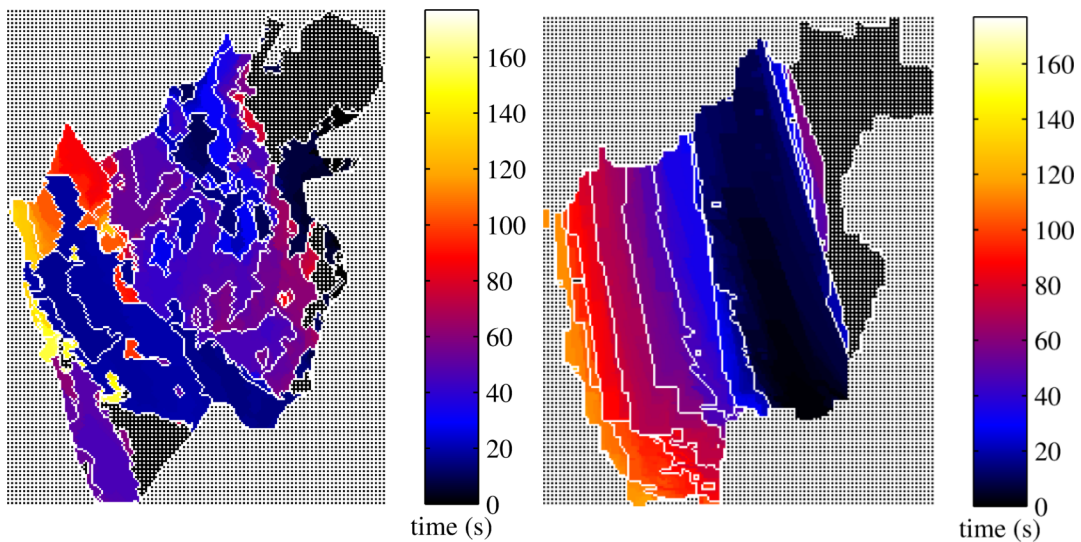


Figure 8-14. Run 4 flame path of the wind tunnel experiment (left) and a model simulation (right) viewed from the side. See figure caption to Figure 8-11.

These results were only achieved through careful selection of model parameters, especially flame radius and downward flame extension parameters, ignition region parameters, and T_{conv} . While these parameters may be broadly applicable, model results are highly sensitive to many of the parameters. This may reflect the inherent sensitivity and nonlinear response of fire spread to small changes in fuel placement, etc. However, to some extent, the sensitivity may also be an artifact of the model rather than a reflection of fire spread physics.

8.7 Discussion and conclusions

Changes were made to the first-generation multi-leaf fire spread model to expand its responsiveness to heat transfer and fire conditions and to bring predicted behavior into better conformity with measured wind tunnel behavior. Physics-based scaling of fire behavior, improved flame merging, and inclusion of the effects of wind and buoyancy on flame dimensions were necessary to obtain realistic predictions of fire behavior. For example, rate of fire spread in the wind tunnel was improved using the physics-based submodel for scaling flame parameters.

The inclusion of distant heating (pseudo-radiation) seemed to improve the overall results. Because flame-fuel proximity is calculated to determine flame-fuel overlap, much of the programmatic structure is already in place to consider radiation between fuel and flames in a more exact manner in the future.

Burn times, flame heights, burn extents and flame paths were improved over the results presented in Chapter 4. The improvements made to achieve better agreement with the wind tunnel results should be equally valuable in applying the fire spread model to other scenarios, including wildland fire spread conditions such as prescribed burns.

Modeling the wind tunnel burns with computational fluid dynamics (CFD), such as with a large eddy simulation (LES) code, would be very difficult. Defining and modeling the shrub geometry, conjugate heat transfer, surface reactions, buoyancy, wind, turbulence, turbulent chemistry, radiation and soot formation would require an extended period to set up and weeks of computational time on parallel computers. While difficult and expensive, the results of an LES simulation could provide many insights and much more information than is available from the wind tunnel experiments. This information could be very useful in improving the bush model. The difficulty and cost of CFD simulations, however, emphasize the distinguishing advantages of the improved bush model. The computational requirements of the improved bush model are only a fraction of the physical burn time, and the model provides fairly accurate and insightful results. The improved bush model balances empiricism with physics to form a model which runs much faster than CFD models, while providing far more insight than the fully-empirical operational models currently used by wildland firefighters.

Recommended future work includes developing a feedback model so that the model is able to adjust its own heat transfer and fire conditions. Modeling the intricate fluid flow patterns of the wind tunnel experiments was not within the scope of this project. However, an improved fluid flow model that at least considers the drag and flow channeling caused by shrubs has potential to benefit the overall model behavior if implemented without imposing a heavy computational burden. Model validation versus other wind tunnel burns or well-described prescribed fires is recommended to further prepare the model for eventual widespread use.

9. SUMMARY AND CONCLUSIONS

9.1 Evaluation of first-generation shrub combustion model

A novel semi-empirical fire spread model developed previously was compared to fire spread measurements of manzanita shrubs in a wind tunnel. This first-generation bush model was appealing due to its balance between modeling detail and computational speed, and responded to wind speed, moisture content and leaf count. However, while the comparison with the wind tunnel experiments demonstrated promise, model deficiencies were evident. Fine-scale leaf placement was found to have a strong impact on predicted fire spread. A new leaf placement method was developed based on shrub images and included in the first-generation model. The need for better flame angle and flame merging models was identified. A physics-based submodel was suggested to adapt flame behavior measured at one temperature in a laboratory to additional fire scenarios. The modeling needs and deficiencies identified by the first-generation bush model motivated the development of new fuel placement models and the detailed study of leaf heating, water release and devolatilization.

9.2 Detailed fuel placement

The improved leaf placement method developed for manzanita, based on shrub images, was not as applicable to species which had concentrated fuel distributions along the branches. Instead, a fuel placement method which included the branching structure was needed to provide a correct fine-scale fuel distribution for species such as chamise and Utah juniper. Concepts from

L-systems theory were incorporated into a model to generate branching shrub geometries for chamise and Utah juniper. The L-systems-based models developed for chamise and Utah juniper were highly customized to imitate the geometry of natural shrubs and measured fuel dry mass data. Effects to randomize shrub geometry and to create shrubs of different sizes were also included.

9.3 Dead versus live leaf combustion measurements

Highly-instrumented single-leaf burn experiments over a flat-flame burner were performed to investigate mass release from dead versus live leaves. Dead and “live” leaves were conditioned to moisture contents near the fiber saturation point. Leaves which had not been dried below the fiber saturation point were called “live.” A dry dead set of leaves (MC = 4%), a rehydrated dead set of leaves (MC = 26%), a dehydrated live set of leaves (MC = 34%), and a fresh live set of leaves (MC = 63%) were examined. The term “fresh” was a comparative distinction. Detailed surface temperatures were measured with an infrared camera. The temperature plateaus of live leaves were cooler (occurring at approximately 175°C), flatter, and longer-lasting than the temperature plateau of rehydrated dead leaves (occurring at approximately 200°C), even though rehydrated leaves had a similar moisture content as dehydrated live leaves. Live leaves showed radial and non-uniform flame movement due to high-momentum jetting, indicating high internal leaf pressures. The flames of rehydrated leaves showed similar behavior, but less consistently. Moisture was retained for all moisture-laden leaves into the 160 °C to 220 °C range, which is above the normal boiling point (100 °C) of water. Concurrent release of pyrolyzates and moisture was identified within the same leaf. The high temperature range of moisture release indicated high diffusion resistance.

9.4 Modeling combustion of live versus dead leaves

Mass release models were developed to model the water release and devolatilization of the dry, rehydrated, dehydrated and fresh leaves. The leaf surface area was divided into gridded sections to model mass release from the differently-heated parts independently. This provided the most accurate results. For a simpler calculation, mass release can be calculated for the mean leaf temperature. This simplified approach was less accurate. Internal leaf temperatures determined with 1-D internal heat conduction and cooling by water release showed little difference between the surface temperature and the internal leaf temperature except during rapid moisture release. The CPD model effectively modeled devolatilization of the dry matter components, and a multi-component one step model was developed to imitate the behavior of CPD for manzanita leaves.

Water release from rapidly-heated manzanita leaves was not well-described by classical water evaporation at 100 °C, even when accounting for the cooling effect of water and internal heat transfer. Moisture release was best described by a diffusion model which used a temperature-dependent diffusivity originally derived for wood drying. This model was effective for all leaf groups, suggesting that moisture release at these heating conditions was limited by diffusion. The modeled temperatures of moisture release corroborated measurements that suggested moisture was reaching elevated temperatures before release, and therefore also reaching elevated pressures. Based on these modeling results, 95% of water release occurred between 150 °C and 250 °C, with the highest water release range being from 175 °C and 200 °C for all leaf groups.

The burning differences between rehydrated dead and dehydrated live leaves resulted from relatively low temperatures which were maintained longer by live leaves than by dead

rehydrated leaves. The persistence of relatively low temperatures allowed water to remain longer in live leaves than in dead leaves. The difference between how live and dead leaves hold water, and how that affects the leaf energy balance during heating, is the likely reason for the differing temperature profiles of rehydrated dead and dehydrated live leaves.

9.5 Improved shrub combustion model

An improved bush fire spread model was developed, which included a physics-based submodel to scale flame parameters. A new flame merging model was also developed that included effects based on vertical as well as horizontal flame spacing. Flame angle calculations were based on the collective flame heights of grouped flames, based on a flame merging criterion. A pseudo-radiation term was added. Flame proximity in the model is calculated in such a way that a more rigorous radiation model could be used for larger fires. Burn times, flame heights, burn extents and flame paths were improved over the results of the first-generation bush model. The improved bush model provided fairly accurate and insightful predictions of wind tunnel fire spread measurements. The model showed high sensitivity to placement of specific fuel elements showing the need for better resolution of fuel placement in wildland fire modeling. The model balances empiricism and physics and is a useful research tool. The improved bush model should be compared to other fire scenarios, including wildland fire spread conditions to determine the need for further improvements. It is hoped that with further development and validation this approach could develop into a very practical tool for fire spread modeling and prediction.

REFERENCES

- "Test Methods for Direct Moisture Content Measurement of Wood and Wood-Base Materials," ASTM International (2003).
- Alados, C. L., J. Escos, J. M. Emlen and D. C. Freeman, "Characterization of Branch Complexity by Fractal Analyses," *International Journal of Plant Sciences*, **160**(6), S147-S155 (1999).
- Albini, F. A., "Estimating Wildfire Behavior and Effects," General Technical Report INT-30, Ogden, UT, USDA Forest Service (1976).
- Albini, F. A., "A Model for the Wind-Blown Flame from a Line Fire," *Combustion and Flame*, **43**, 155-174 (1981).
- Albini, F. A., "A Model for Fire Spread in Wildland Fuels by Radiation," *Combustion Science and Technology*, **42**(5-6), 229-258 (1985).
- Alexander, M. E., "Calculating and Interpreting Forest Fire Intensities," *Canadian Journal of Botany-Revue Canadienne De Botanique*, **60**(4), 349-357 (1982).
- Allen, M. T., P. Prusinkiewicz and T. M. DeJong, "Using L-Systems for Modeling Source-Sink Interactions, Architecture and Physiology of Growing Trees: The L-Peach Model," *New Phytologist*, **166**(3), 869-880 (2005).
- Anastacio, F., P. Prusinkiewicz and M. C. Sousa, "Sketch-Based Parameterization of L-Systems Using Illustration-Inspired Construction Lines and Depth Modulation," *Computers & Graphics*, **33**(4), 440-451 (2009).
- Anderson, H. E. and R. C. Rothermel, "Influence of Moisture and Wind Upon the Characteristics of Free-Burning Fires," *Symposium (International) on Combustion*, **10**(1), 1009-1019 (1965).
- Anderson, H. E., "Heat Transfer and Fire Spread," USDA Forest Service Research Paper INT-69, Intermountain Forest and Range Experiment Station, Forest Service, U.S. Department of Agriculture, Ogden, Utah. (1969).
- Andrews, P. L., "Behaveplus Fire Modeling System: Past, Present, and Future," Proceedings of the 7th Symposium on Fire and Forest Meteorology, Bar Harbor, Maine (2007).

- Andrews, P. L., "Behaveplus Fire Modeling System, Version 4.0: Variable," General Technical Report RMRS-GTR-213WWW, Fort Collins, CO, USDA Forest Service: 107 (2008).
- Arca, B., P. Duce, M. Laconi, G. Pellizzaro, M. Salis and D. Spano, "Evaluation of Farsite Simulator in Mediterranean Maquis," *International Journal of Wildland Fire*, **16**(5), 563-572 (2007).
- Badzioch, S. and P. G. Hawksley, "Kinetics of Thermal Decomposition of Pulverized Coal Particles," *Industrial & Engineering Chemistry Process Design and Development*, **9**(4), 521-& (1970).
- Baeza, M. J., M. De Luis, J. Raventos and A. Escarre, "Factors Influencing Fire Behaviour in Shrublands of Different Stand Ages and the Implications for Using Prescribed Burning to Reduce Wildfire Risk," *Journal of Environmental Management*, **65**(2), 199-208 (2002).
- Baldwin, R., "Flame Merging in Multiple Fires " *Combustion and Flame*, **12**(4), 318-324 (1968).
- Berezovskaya, F. S., G. P. Karev, O. S. Kisliuk, R. G. Khlebopros and Y. L. Tsel'niker, "A Fractal Approach to Computer-Analytical Modelling of Tree Crowns," *Trees*,(11), 323-327 (1997).
- Bharadwaj, A., L. L. Baxter and A. L. Robinson, "Effects of Intraparticle Heat and Mass Transfer on Biomass Devolatilization: Experimental Results and Model Predictions," *Energy & Fuels*, **18**(4), 1021-1031 (2004).
- Biagini, E. and L. Tognotti, "A Generalized Procedure for the Devolatilization of Biomass Fuels Based on the Chemical Components," *Energy & Fuels*, **28**(1), 614-623 (2014).
- Bird, R. B., W. E. Stewart and E. N. Lightfoot, Transport Phenomena, New York, J. Wiley (2002).
- Browne, F. L., "Theories of the Combustion of Wood and Its Control," United States Department of Agriculture Forest Service (1958).
- Burgan, R. E. and R. C. Rothermel, "Behave: Fire Behavior Prediction and Fuel Modeling System - Fuel Subsystem," PMS 439-1 NFES 0275, USDA, USDI, NASF (1984).
- Busing, R. T. and D. Maily, "Advances in Spatial, Individual-Based Modelling of Forest Dynamics," *Journal of Vegetation Sciences*,(15), 831-842 (2004).
- Butler, B. W., J. Cohen, D. J. Latham, R. D. Schuette, P. Sopko, K. S. Shannon, D. Jimenez and L. S. Bradshaw, "Measurements of Radiant Emissive Power and Temperatures in Crown Fires," *Canadian Journal of Forest Research-Revue Canadienne De Recherche Forestiere*, **34**(8), 1577-1587 (2004).
- Byram, G. M., "Combustion of Forest Fuels," Forest Fire: Control and Use, K. P. Davis., New York, McGraw-Hill: 61-89 (1959).

- Byram, G. M., H. B. Clements, E. R. Elliott and P. M. George, "An Experimental Study of Model Fires," Technical Report No. 3, US Forest Service, Southern Forest Fire Laboratory (1964).
- Carpita, N. C., "Tensile-Strength of Cell-Walls of Living Cells," *Plant Physiology*, **79**(2), 485-488 (1985).
- Catchpole, E. A., W. R. Catchpole, N. R. Viney, W. L. McCaw and J. B. Marsden-Smedley, "Estimating Fuel Response Time and Predicting Fuel Moisture Content from Field Data," *International Journal of Wildland Fire*, **10**, 215-222 (2001).
- Catchpole, W. R., E. A. Catchpole, B. W. Butler, R. C. Rothermel, G. A. Morris and D. J. Latham, "Rate of Spread of Free-Burning Fires in Woody Fuels in a Wind Tunnel," *Combustion Science and Technology*, **131**(1-6), 1-37 (1998).
- Çengel, Y. A., Heat and Mass Transfer: A Practical Approach, New York, NY, McGraw-Hill (2007).
- Cheney, N. and J. Gould, "Fire Growth in Grassland Fuels," *International Journal of Wildland Fire*, **5**(4), 237-247 (1995).
- Cheney, N. P., "Fire Behaviour," Fire and the Australian Biota, A. M. Gill, R. H. Groves and I. R. Noble, Australian Academy of Sciences: Canberra: 151–175 (1981).
- Cohen, J. D., "Estimating Fire Behavior with Firecast: User's Manual," Berkeley, Calif., Pacific Southwest Research Station, Forest Service, U.S. Department of Agriculture: 11 (1986).
- Cole, W. J., B. M. Pickett, T. H. Fletcher and D. R. Weise, "A Semi-Empirical Multi-Leaf Model for Fire Spread through a Manzanita Shrub," 6th U.S. National Combustion Meeting, Ann Arbor, Michigan (2009).
- Cole, W. J., M. H. Dennis, T. H. Fletcher and D. R. Weise, "The Effects of Wind on the Flame Characteristics of Individual Leaves," *International Journal of Wildland Fire*, (Submitted for Publication) (2010).
- Cole, W. J., M. H. Dennis, T. H. Fletcher and D. R. Weise, "The Effects of Wind on the Flame Characteristics of Individual Leaves," *International Journal of Wildland Fire*, **2011**(02), 657-667 (2011).
- Costa, J., L. Oliveira, D. Viegas and L. Neto, "On the Temperature Distribution inside a Tree under Fire Conditions," *International Journal of Wildland Fire*, **1**(2), 87-96 (1991).
- Countryman, C. M., "Mass Fires and Fire Behaviour," US Forest Service Research Paper PSW-19, US Forest Service, Pacific Southwest Forest and Range Experiment Station (1964).
- Countryman, C. M. and C. W. Philpot, "Physical Characteristics of Chamise as a Wildland Fuel," Research Paper, Berkeley, CA, USDA Forest Service: 16 (1970).

- Countryman, C. M., "Can Southern California Wildland Conflagrations Be Stopped?," Berkeley, Calif., Pacific Southwest Forest and Range Experiment Station: 11 (1974).
- Countryman, C. M. and W. A. Dean, "Measuring Moisture Content in Living Chaparral: A Field User's Manual," General Technical Report, Berkeley, CA, USDA Forest Service: 28 (1979).
- Cruz, M. G. and M. E. Alexander, "Assessing Crown Fire Potential in Coniferous Forests of Western North America: A Critique of Current Approaches and Recent Simulation Studies," *International Journal of Wildland Fire*, **19**(4), 377-398 (2010).
- Cruz, M. G., B. W. Butler, D. X. Viegas and P. Palheiro, "Characterization of Flame Radiosity in Shrubland Fires," *Combustion and Flame*, **158**(10), 1970-1976 (2011).
- Dahm, W. J. A., "Scaling Relations for Flare Interactions, Flame Lengths, and Crosslighting Requirements in Large Flare Fields," AFRC-JFRC International Symposium, Marriott Waikoloa, Hawaii (2007).
- Davies, G. M., C. J. Legg, A. A. Smith and A. J. MacDonald, "Rate of Spread of Fires in Calluna Vulgaris-Dominated Moorlands," *Journal of Applied Ecology*, **46**(5), 1054-1063 (2009).
- Davis, J. B., "The Wildland-Urban Interface - Paradise or Battleground," *Journal of Forestry*, **88**(1), 26-31 (1990).
- Dennison, P. E., M. A. Moritz and R. S. Taylor, "Evaluating Predictive Models of Critical Live Fuel Moisture in the Santa Monica Mountains, California," *International Journal of Wildland Fire*, **17**(1), 18-27 (2008).
- Dennison, P. E. and M. A. Moritz, "Critical Live Fuel Moisture in Chaparral Ecosystems: A Threshold for Fire Activity and Its Relationship to Antecedent Precipitation," *International Journal of Wildland Fire*, **18**(8), 1021-1027 (2009).
- Di Blasi, C. and C. Branca, "Kinetics of Primary Product Formation from Wood Pyrolysis," *Ind. Eng. Chem. Res.*, **40**, 5547-5556 (2001).
- Di Blasi, C., "Modeling Chemical and Physical Processes of Wood and Biomass Pyrolysis," *Progress in Energy and Combustion Science*, **34**(1), 47-90 (2008).
- Dietenberger, M., "Update for Combustion Properties of Wood Components," *Fire and Materials*, **26**(6), 255-267 (2002).
- Dimitrakopoulos, A. P., "Thermogravimetric Analysis of Mediterranean Plant Species," *Journal of Analytical and Applied Pyrolysis*, **60**(2), 123-130 (2001).
- Dimitrakopoulos, A. P. and K. K. Papaioannou, "Flammability Assessment of Mediterranean Forest Fuels," *Fire Technology*, **37**(2), 143-152 (2001).

- Dimitrakopoulos, A. P., I. D. Mitsopoulos and K. Gatoulas, "Assessing Ignition Probability and Moisture of Extinction in a Mediterranean Grass Fuel," *International Journal of Wildland Fire*, **19**(1), 29-34 (2010).
- Dupuy, J. L. and D. Morvan, "Numerical Study of a Crown Fire Spreading toward a Fuel Break Using a Multiphase Physical Model," *International Journal of Wildland Fire*, **14**(2), 141-151 (2005).
- Engstrom, J. D., J. K. Butler, S. G. Smith, L. L. Baxter, T. H. Fletcher and D. R. Weise, "Ignition Behavior of Live California Chaparral Leaves," *Combustion Science and Technology*, **176**, 1577-1591 (2004).
- Ferguson, S. C., A. Dahale, B. Shotorban, S. Mahalingam and D. R. Weise, "The Role of Moisture on Combustion of Pyrolysis Gases in Wildland Fires," *Combustion Science and Technology*, **185**(3), 435-453 (2013).
- Fernandes, P. M., H. S. Botelho and C. Loureiro, "Models for the Sustained Ignition and Behaviour of Low-to-Moderately Intense Fires in Maritime Pine Stands," Proceedings of the IV International Conference of Forest Fire Research & 2002 Wildland Fire Safety Summit, Coimbra, Portugal (2002).
- Finney, M. A., "Farsite: Fire Area Simulator - Model Development and Evaluation," *Usda Forest Service Rocky Mountain Forest and Range Experiment Station Research Paper*,(Rp-4), 1-+ (1998).
- Finney, M. A., "Fire Growth Using Minimum Travel Time Methods," *Canadian Journal of Forest Research-Revue Canadienne De Recherche Forestiere*, **32**(8), 1420-1424 (2002).
- Finney, M. A., J. D. Cohen, I. C. Grenfell and K. M. Yedinak, "An Examination of Fire Spread Thresholds in Discontinuous Fuel Beds," *International Journal of Wildland Fire*, **19**(2), 163-170 (2010).
- Finney, M. A., I. C. Grenfell, C. W. McHugh, R. C. Seli, D. Trethewey, R. D. Stratton and S. Brittain, "A Method for Ensemble Wildland Fire Simulation," *Environmental Modeling & Assessment*, **16**(2), 153-167 (2011).
- Finney, M. A. and S. S. McAllister, "A Review of Fire Interactions and Mass Fires," *Journal of Combustion*, **2011**, 14 (2011).
- Finney, M. A., J. D. Cohen, S. S. McAllister and W. M. Jolly, "On the Need for a Theory of Wildland Fire Spread," *International Journal of Wildland Fire*, (Special Issue) (2012).
- FireModels.org, "Fire Behavior and Fire Danger Software," Missoula, MO (2012).
- Fitter, A. H. and T. R. Stickland, "Fractal Characterization of Root-System Architecture," *Functional Ecology*, **6**(6), 632-635 (1992).

- Fletcher, T. H., A. R. Kerstein, R. J. Pugmire and D. M. Grant, "A Chemical Percolation Model for Devolatilization .2. Temperature and Heating Rate Effects," *Abstracts of Papers of the American Chemical Society*, **198**, 79-Fuel (1989).
- Fletcher, T. H., A. R. Kerstein, R. J. Pugmire and D. M. Grant, "Chemical Percolation Model for Devolatilization .2. Temperature and Heating Rate Effects on Product Yields," *Energy & Fuels*, **4**(1), 54-60 (1990).
- Fletcher, T. H., A. R. Kerstein, R. J. Pugmire, M. S. Solum and D. M. Grant, "Chemical Percolation Model for Devolatilization .3. Direct Use of C-13 Nmr Data to Predict Effects of Coal Type," *Energy & Fuels*, **6**(4), 414-431 (1992).
- Fletcher, T. H., B. M. Pickett, S. G. Smith, G. S. Spittle, M. M. Woodhouse, E. Haake and D. R. Weise, "Effects of Moisture on Ignition Behavior of Moist California Chaparral and Utah Leaves," *Combustion Science and Technology*, **179**, 1183-1203 (2007).
- Fletcher, T. H., H. R. Pond, J. Webster, J. Wooters and L. L. Baxter, "Prediction of Tar and Light Gas During Pyrolysis of Black Liquor and Biomass," *Energy & Fuels*, **26**(6), 3381-3387 (2012).
- Fons, W. L., "Analysis of Fire Spread in Light Forest Fuels," *Journal of Agricultural Research*, **72**(13), 93-121 (1946).
- Forest Products Laboratory, "Computed Thermal Conductivity of Common Woods," Madison, Wisconsin, USDA Forest Service (1952).
- Frandsen, W. H., "Fire Spread through Porous Fuels from the Conservation of Energy," *Combustion and Flame*, **16**(1), 9-16 (1971).
- Frandsen, W. H., "Effective Heating of Fuel Ahead of Spreading Fire," Research Paper INT-140, Ogden, UT, USDA Forest Service (1973).
- Frankman, D., B. W. Webb, B. W. Butler and D. J. Latham, "Fine Fuel Heating by Radiant Flux," *Combustion Science and Technology*, **182**(2), 215-230 (2010).
- Glass, S. V. and S. L. Zelinka, "Moisture Relations and Physical Properties of Wood," Wood Handbook : Wood as an Engineering Material, R. J. Ross, USDA Forest Service, Forest Products Laboratory, General Technical Report FPL- GTR-190, 2010: 509 p. 1 v.: 4-1 to 4-20 (2010).
- Godin, C., "Representing and Encoding Plant Architecture: A Review," *Annals of Forest Science*, **57**(5-6), 413-438 (2000).
- Godin, C., O. Puech, F. Boudon and H. Sinoquet, "Space Occupation by Tree Crowns Obeys Fractal Laws: Evidence from 3d Digitized Plants," 4th International Workshop on Functional-Structural Plant Models, C. Godin, Montpellier, France: 79-83 (2004).

- Grant, D. M., R. J. Pugmire, T. H. Fletcher and A. R. Kerstein, "A Chemical-Model of Coal Devolatilization Using Percolation Lattice Statistics," *Abstracts of Papers of the American Chemical Society*, **195**, 100-FUEL (1988).
- Grant, D. M., R. J. Pugmire, T. H. Fletcher and A. R. Kerstein, "Chemical-Model of Coal Devolatilization Using Percolation Lattice Statistics," *Energy & Fuels*, **3**(2), 175-186 (1989).
- Green, L. R., "Burning by Prescription in Chaparral," Albany, CA, U.S. Department of Agriculture, Forest Service, Pacific Southwest Forest and Range Experiment Station: 36 (1981).
- Grishin, A. M., A. D. Gruzin and V. G. Zverev, "Mathematical Modelling of the Preading of High-Level Forest Fires," *Sov. Phys. Dokl.*, **28**, 328-330 (1983).
- Grishin, A. M., "Matematicheskoye Modelirovaniye Lesnykh Pozharov I Novyye Sposoby Bor'by S Nimi [Mathematical Modeling of Forest Fires and New Methods of Fighting Them]. [in Russian.]," Novosibirsk, Russia., Nauka Publishers, Siberian Division (1997).
- Grishin, A. M., A. Y. Kusin and E. M. Alekseenko, "Determination of Kinetic Characteristics of the Process of Drying of Forest Combustibles," *Journal of Engineering Physics and Thermophysics*, **76**(5), 1160-1165 (2003).
- Haynes, J. D., "Worldwide Virtual Temperatures for Product Stability Testing," *Journal of Pharmaceutical Sciences*, **60**(6), 927-& (1971).
- Hill, C. A. S., A. Norton and G. Newman, "The Water Vapor Sorption Behavior of Natural Fibers," *Journal of Applied Polymer Science*, **112**(3), 1524-1537 (2009).
- Hill, C. A. S., A. J. Norton and G. Newman, "The Water Vapour Sorption Properties of Sitka Spruce Determined Using a Dynamic Vapour Sorption Apparatus," *Wood Science and Technology*, **44**(3), 497-514 (2010).
- Hill, C. A. S., B. A. Keating, Z. Jalaludin and E. Mahrtdt, "A Rheological Description of the Water Vapour Sorption Kinetics Behaviour of Wood Invoking a Model Using a Canonical Assembly of Kelvin-Voigt Elements and a Possible Link with Sorption Hysteresis," *Holzforschung*, **66**(1), 35-47 (2012).
- Hough, W. A. and F. A. Albini, "Predicting Fire Behavior in Palmetto-Gallberry Fuel Complexes," U. S. D. o. Agriculture, Asheville, North Carolina, Southeastern Forest Experiment Station (1978).
- Howitt, B. F., "Manzanita Image - Photo Id: 8253-3202-4137-0079 - Accessed 1/30/2008," *California Academy of Sciences*, <http://calphotos.berkeley.edu> (2008).
- ICH - Technical Coordination, E., "Note for Guidance on Stability Testing: Stability Testing of New Drug Substances and Products (Revision 2)," T. E. A. f. t. E. o. M. Products, London, UK (2003).

- Incropera, F. P., D. P. DeWitt, T. L. Bergman and A. S. Lavine, Fundamentals of Heat and Mass Transfer, New York, J. Wiley (2007).
- Jayalakshmy, M. S. and J. Philip, "Thermophysical Properties of Plant Leaves and Their Influence on the Environment Temperature," *International Journal of Thermophysics*, **31**(11-12), 2295-2304 (2010).
- Jenkins, B. M., L. L. Baxter, T. R. Miles and T. R. Miles, "Combustion Properties of Biomass," *Fuel Processing Technology*, **54**(1-3), 17-46 (1998).
- Jirasek, C., P. Prusinkiewicz and B. Moulia, "Integrating Biomechanics into Developmental Plant Models Expressed Using L-Systems," 3rd Plant Biomechanics Conference, Freiburg-Badenweiler (2000).
- Kamikawa, D., W. G. Weng, K. Kagiya, Y. Fukuda, R. Mase and Y. Hasemi, "Experimental Study of Merged Flames from Multifire Sources in Propane and Wood Crib Burners," *Combustion and Flame*, (2005).
- Keane, R. E., "Describing Wildland Surface Fuel Loading for Fire Management: A Review of Approaches, Methods and Systems," *International Journal of Wildland Fire*, **22**(1), 51-62 (2013).
- Keeley, J. and C. Fotheringham, "Impact of Past, Present, and Future Fire Regimes on North American Mediterranean Shrublands," Fire and Climate Change in Temperate Ecosystems of the Western Americas, T. Veblen, W. Baker, G. Montenegro and T. Swetnam, New York, Springer-Verlag, **160**: 218-262 (2003).
- Keeley, J. E., "Chaparral," Borth American Terrestrial Vegetation, M. G. Barbour and W. D. Billings, New York, Cambridge University Press (2000).
- Korobeinicheva, O. P., A. A. Paletskya, M. B. Gonchikzhapova, I. K. Shundrinac, H. Chend and N. Liud, "Combustion Chemistry and Decomposition Kinetics of Forest Fuels," *Procedia Engineering*, **62**, 182-193 (2013).
- Lamorlette, A. and N. Foster, "Structural Modeling of Flames for a Production Environment," *Acm Transactions on Graphics*, **21**(3), 729-735 (2002).
- Land, B., "Computing for Neurobiology: L-Systems in Matlab," Cornell University, **2013** (2006).
- Law, B. E. and R. H. Waring, "Remote-Sensing of Leaf-Area Index and Radiation Intercepted by Understory Vegetation," *Ecological Applications*, **4**(2), 272-279 (1994).
- Leoni, E., P. Tomi, B. Khoumeri, N. Balbi and A. F. Bernardini, "Thermal Degradation of Pinus Pinaster Needles by Dsc. Part 1: Dehydration Kinetics," *Journal of Fire Sciences*, **19**(5), 379-397 (2001).

- Leoni, E., D. Cancellieri, N. Balbi, P. Tomi, A. F. Bernardini, J. Kaloustian and T. Marcelli, "Thermal Degradation of Pinus Pinaster Needles by Dsc, Part 2: Kinetics of Exothermic Phenomena," *Journal of Fire Sciences*, **21**(2), 117-130 (2003).
- Lewis, A. D. and T. H. Fletcher, "Prediction of Sawdust Pyrolysis Yields from a Flat-Flame Burner Using the Cpd Model," *Energy & Fuels*, **27**, 942-953 (2013).
- Lin, Y. C., G. W. Huber, J. Cho, G. A. Tompsett and P. R. Westmoreland, "Kinetics and Mechanism of Cellulose Pyrolysis," *Journal of Physical Chemistry C*, **113**(46), 20097-20107 (2009).
- Linn, R., J. Reisner, J. J. Colman and J. Winterkamp, "Studying Wildfire Behavior Using Firetec," *International Journal of Wildland Fire*, **11**(3-4), 233-246 (2002).
- Linn, R., J. Winterkamp, J. J. Colman, C. Edminster and J. D. Bailey, "Modeling Interactions between Fire and Atmosphere in Discrete Element Fuel Beds," *International Journal of Wildland Fire*, **14**(1), 37-48 (2005).
- Linn, R. R., "A Transport Model for Prediction of Wildfire Behavior," Other Information: DN: Thesis presented to the Dept. of Mechanical Engineering, New Mexico State Univ., Las Cruces, NM (US); TH: Thesis (Ph.D.); PBD: Jul 1997; Medium: ED; Size: 212 p. (1997).
- Lopes, A. M. G., M. G. Cruz and D. X. Viegas, "Firestation -- an Integrated Software System for the Numerical Simulation of Fire Spread on Complex Topography," *Environmental Modelling & Software*, **17**(3), 269-285 (2002).
- Lopez, A., F. D. Molina-Aiz, D. L. Valera and A. Pena, "Determining the Emissivity of the Leaves of Nine Horticultural Crops by Means of Infrared Thermography," *Scientia Horticulturae*, **137**, 49-58 (2012).
- Lozano, J., W. Tachajapong, D. R. Weise, S. Mahalingam and M. Princevac, "Fluid Dynamic Structures in a Fire Environment Observed in Laboratory-Scale Experiments," *Combustion Science and Technology*, **182**(7), 858-878 (2010).
- Lozano, J. S., "An Investigation of Surface and Crown Fire Dynamics in Shrub Fuels," PhD Dissertation, Mechanical Engineering, University of California, Riverside (2011).
- Mardini, J., A. S. Lavine, V. K. Dhir and E. B. Anderson, "Heat and Mass Transfer in Live Fuel During the Process of Drying, Pyrolysis, and Ignition," Proc. of the 1989 National Heat Transfer Conf., HTD-106 (1989).
- Mardini, J. and A. S. Lavine, "Effects of Species and Green Wood Moisture Variation of Its Time to Ignition During Fires," 48-121 Engineering IV, Los Angeles, CA, UCLA (1993-1994).
- Marino, E., M. Guijarro, J. Madrigal, C. Hernando and C. Diez, "Assessing Fire Propagation Empirical Models in Shrub Fuel Complexes Using Wind Tunnel Data," *Modelling, Monitoring and Management of Forest Fires*, **2008**(Section 4), 121-130 (2008).

- Marino, E., M. Guijarro, C. Hernando, J. Madrigal and C. Diez, "Fire Hazard after Prescribed Burning in a Gorse Shrubland: Implications for Fuel Management," *Journal of Environmental Management*, **92**(3), 1003-1011 (2011).
- Martins Fernandes, P. A., "Fire Spread Prediction in Shrub Fuels in Portugal," *Forest Ecology and Management*, **144**(1-3), 67-74 (2001).
- Mason, L. R. and S. S. Hutchings, "Estimating Foliage Yields on Utah Juniper from Measurements of Crown Diameter," *Journal of Range Management*, **20**(3), 161-166 (1967).
- Maynard, T., "Fire Interactions and Pulsation - Theoretical and Physical Modeling," (2013).
- McCaffrey, B. J., "Purely Buoyant Diffusion Flames: Some Experimental Results," Washington, D.C., National Bureau of Standards: 44 (1979).
- McGrattan, K., R. McDermott, S. Hostikka and J. Floyd, "Fire Dynamics Simulator (Version 5): User's Guide," National Institute of Standards and Technology 222 p. (2010).
- Mell, W., M. A. Jenkins, J. Gould and P. Cheney, "A Physics-Based Approach to Modelling Grassland Fires," *International Journal of Wildland Fire*, **16**(1), 1-22 (2007).
- Mell, W., A. Maranghides, R. McDermott and S. L. Manzello, "Numerical Simulation and Experiments of Burning Douglas Fir Trees," *Combustion and Flame*, **156**(10), 2023-2041 (2009).
- Miller, R. S. and J. Bellan, "Tar Yield and Collection from the Pyrolysis of Large Biomass Particles," **JPL TRS 1992+**: <http://hdl.handle.net/2014/26140> (1996).
- Morandini, F., P. A. Santoni and J. H. Balbi, "The Contribution of Radiant Heat Transfer to Laboratory-Scale Fire Spread under the Influences of Wind and Slope," *Fire Safety Journal*, **36**(6), 519-543 (2001).
- Morandini, F., P. A. Santoni, J. H. Balbi, J. M. Ventura and J. M. Mendes-Lopes, "A Two-Dimensional Model of Fire Spread across a Fuel Bed Including Wind Combined with Slope Conditions," *International Journal of Wildland Fire*, **11**(1), 53-63 (2002).
- Morandini, F., X. Silvani, L. Rossi, P.-A. Santoni, A. Simeoni, J.-H. Balbi, J. Louis Rossi and T. Marcelli, "Fire Spread Experiment across Mediterranean Shrub: Influence of Wind on Flame Front Properties," *Fire Safety Journal*, **41**(3), 229-235 (2006).
- Morley, C., "Gaseq Chemical Equilibrium Program," **2014**: A Chemical Equilibrium Program for Windows (2005).
- Morvan, D. and J. L. Dupuy, "Modeling of Fire Spread through a Forest Fuel Bed Using a Multiphase Formulation," *Combustion and Flame*, **127**(1-2), 1981-1994 (2001).

- Morvan, D., "Physical Phenomena and Length Scales Governing the Behaviour of Wildfires: A Case for Physical Modelling," *Fire Technology*, **47**(2), 437-460 (2011).
- Morvan, D., C. Hoffman, F. Rego and W. Mell, "Numerical Simulation of the Interaction between Two Fire Fronts in Grassland and Shrubland," *Fire Safety Journal*, **46**(8), 469-479 (2011).
- National Interagency Fire Center, "National Interagency Fire Center: Fire Information: Statistics: Suppression Costs (1985-2913)," Boise, ID, National Interagency Fire Center (2014).
- Nelson, J., Ralph M., "Forest Fires : Behavior and Ecological Effects," San Diego, Calif., Academic Press, Inc.: xvii, 594 p., 4 p. of plates (2001).
- Nelson, R., "Byram Derivation of the Energy Criterion for Forest and Wildland Fires," *International Journal of Wildland Fire*, **3**(3), 131-138 (1993).
- Nelson, R. M. and C. W. Adkins, "Flame Characteristics of Wind-Driven Surface Fires," *Canadian Journal of Forest Research*, **16**(6), 1293-1300 (1986).
- Nelson, R. M., "Prediction of Diurnal Change in 10-H Fuel Stick Moisture Content," *Canadian Journal of Forest Research-Revue Canadienne De Recherche Forestiere*, **30**(7), 1071-1087 (2000).
- Ozdemir, M. and H. Pehlivan, "Prediction of the Boiling Temperature and Heat Flux in Sugar-Water Solutions under Pool-Boiling Conditions," *Heat and Mass Transfer*, **44**(7), 827-833 (2008).
- Ozier-Lafontaine, H., F. Lecompte and J. F. Sillon, "Fractal Analysis of the Root Architecture of *Gliricidia Sepium* for the Spatial Prediction of Root Branching, Size and Mass: Model Development and Evaluation in Agroforestry," *Plant and Soil*, **209**(2), 167-180 (1999).
- Pagni, P. J. and G. Peterson, "Flame Spread through Porous Fuels," 14th Symp. (Int.) Combust., Pittsburgh, Pa, The Combustion Institute: 1099-1107 (1973).
- Papadopoulos, G. D. and F. N. Pavlidou, "A Comparative Review on Wildfire Simulators," *Ieee Systems Journal*, **5**(2), 233-243 (2011).
- Parsons, R. A., "Spatial Variability in Forest Fuels: Simulation Modeling and Effects on Fire Behavior," Dissertation, Forestry, University of Montana (2007).
- Parsons, R. A., W. E. Mell and P. McCauley, "Linking 3d Spatial Models of Fuels and Fire: Effects of Spatial Heterogeneity on Fire Behavior," *Ecological Modelling*, **222**(3), 679-691 (2011).
- Pickett, B. M., "Effects of Moisture on Combustion of Live Wildland Forest Fuels," Ph.D., Chemical Engineering, Brigham Young University (2008).

- Pickett, B. M., T. H. Fletcher, B. W. Butler and D. R. Weise, "Single-Leaf, Two-Leaf, and Multi-Leaf Models for Live Wildland Fire Combustion," (2009).
- Pickett, B. M., C. Isackson, R. Wunder, T. H. Fletcher, B. W. Butler and D. R. Weise, "Experimental Measurements During Combustion of Moist Individual Foliage Samples," *International Journal of Wildland Fire*, **19**, 1-10 (2010).
- Pimont, F., J. L. Dupuy, Y. Caraglio and D. Morvan, "Effect of Vegetation Heterogeneity on Radiative Transfer in Forest Fires," *International Journal of Wildland Fire*, **18**(5), 536-553 (2009).
- Plumb, O. A., G. A. Spolek and B. A. Olmstead, "Heat and Mass Transfer in Wood During Drying," *International Journal of Heat and Mass Transfer*, **28**(9), 1669-1678 (1985).
- Pradal, C., F. Boudon, C. Noguier, J. Chopard and C. Godin, "Plantgl: A Python-Based Geometric Library for 3d Plant Modelling at Different Scales," *Graphical Models*, **71**(1-6), 1-21 (2009).
- Prince, D. R. and T. H. Fletcher, "A Combined Experimental and Theoretical Study of the Combustion of Live Vs. Dead Leaves," 8th US National Combustion Meeting of the Combustion Institute, Park City, Utah (2013).
- Prince, D. R., M. E. Fletcher, C. Shen and T. H. Fletcher, "Application of L-Systems to Geometrical Construction of Chamise and Juniper Shrubs," *Ecological Modelling*, **273**, 86-95 (2014).
- Prince, D. R., Fletcher, T. H., "Differences in Burning Behavior of Live and Dead Leaves: 1. Measurements," *Combustion Science and Technology*, **Accepted for publication** (2014).
- Prusinkiewicz, P. and A. Lindenmayer, The Algorithmic Beauty of Plants, New York, Springer-Verlag (1990).
- Prusinkiewicz, P., "A Look at the Visual Modeling of Plants Using L-Systems Bioinformatics," R. Hofestädt, T. Lengauer, M. Löffler and D. Schomburg, Springer Berlin / Heidelberg, **1278**: 11-29 (1997).
- Prusinkiewicz, P., "Modeling of Spatial Structure and Development of Plants: A Review," *Scientia Horticulturae*, **74**(1-2), 113-149 (1998).
- Putnam, A. A., "A Model Study of Wind-Blown Free-Burning Fires," 10th Symposium (International) on Combustion, Pittsburg, PA (1965).
- Reinhardt, E. D., N. L. Crookston, S. J. Beukema, W. A. Kurz, J. A. Greenough, D. C. E. Robinson and D. C. Lutes, "The Fire and Fuels Extension to the Forest Vegetation Simulator," E. D. Reinhardt and N. L. Crookston, Ogden, UT, U.S. Department of Agriculture, Forest Service, Rocky Mountain Research Station: 209 (2003).

- Renton, M., P. Kaitaniemi and J. Hanan, "Functional-Structural Plant Modelling Using a Combination of Architectural Analysis, L-Systems and a Canonical Model of Function," *Ecological Modelling*, **184**(2-4), 277-298 (2005).
- Richardson, A. D. and H. Z. Dohna, "Predicting Root Biomass from Branching Patterns of Douglas-Fir Root Systems," *Oikos*, **100**(1), 96-104 (2003).
- Rothermel, R. C., "A Mathematical Model for Predicting Fire Spread in Wildland Fuels," Research Paper INT-115, USDA Forest Service (1972).
- Rothermel, R. C. and C. W. Philpot, "Predicting Changes in Chaparral Flammability," *Journal of Forestry*, **71**(10), 640-643 (1973).
- Rothermel, R. C. and G. C. Rinehart, "Field Procedures for Verification and Adjustment of Fire Behavior Predictions," Ogden, UT, U.S. Department of Agriculture, Forest Service, Intermountain Forest and Range Experiment Station: 25 p. (1983).
- Rothermel, R. C., "Predicting Behavior and Size of Crown Fires in the Northern Rocky Mountains," Ogden, UT, U.S. Department of Agriculture, Forest Service, Intermountain Research Station (1991).
- Rowley, R., W. Wilding, J. Oscarson, N. Zundel, T. Marshall, T. Daubert and R. Danner, "Dippr Data Compilation of Pure Compound Properties," *Design Institute for Physical Properties*, (2003).
- Salemaa, M. and R. Sievänen, "The Effect of Apical Dominance on the Branching Architecture of *Arctostaphylos Uva-Ursi* in Four Contrasting Environments," *Flora - Morphology, Distribution, Functional Ecology of Plants*, **197**(6), 429-442 (2002).
- Satoh, K., L. Naian, L. Qiong and K. T. Yang, "Numerical and Experimental Study of Merging Fires in Square Arrays," ASME International Mechanical Engineering Congress and Exposition, Seattle, Washington, USA (2007).
- Scott, J. H. and R. E. Burgan, "Standard Fire Behavior Fuel Models: A Comprehensive Set for Use with Rothermel's Surface Fire Spread Model," F. S. United States Department of Agriculture (2005).
- Seader, J. D. and E. J. Henley, Separation Process Principles, Hoboken, NJ, John Wiley & Sons Inc. (2006).
- Shaddix, C. R., "Correcting Thermocouple Measurements for Radiation Loss: A Critical Review," 33rd National Heat Transfer Conference, Albuquerque, New Mexico (1999).
- Shen, C., "Application of Fuel Element Combustion Properties to a Semi-Empirical Flame Propagation Model for Live Wildland Utah Shrubs," M.S. Thesis, Chemical Engineering Department, Brigham Young University (2013).

- Shoemaker, L. H., "Interquantile Tests for Dispersion in Skewed Distributions," *Communications in Statistics-Simulation and Computation*, **28**(1), 189-205 (1999).
- Silvani, X. and F. Morandini, "Fire Spread Experiments in the Field: Temperature and Heat Fluxes Measurements," *Fire Safety Journal*, **44**(2), 279-285 (2009).
- Smith, S. G., "Effects of Moisture on Combustion Characteristics of Live California Chaparral and Utah Foliage," M.S., Chemical Engineering, Brigham Young University (2005).
- Spyratos, V., P. S. Bourgeron and M. Ghil, "Development at the Wildland-Urban Interface and the Mitigation of Forest-Fire Risk," *Proceedings of the National Academy of Sciences of the United States of America*, **104**(36), 14272-14276 (2007).
- Stamm, A. J., Wood and Cellulose Science, New York,, Ronald Press Co. (1964).
- Stephens, S. L., D. Weise, D. L. Fry, R. J. Keiffer, J. Dawson, E. Koo, J. Potts and P. J. Pagni, "Measuring the Rate of Spread of Chaparral Prescribed Fires in Northern California," *Fire Ecology*, **4**(1), 74-86 (2008).
- Steward, F. R., "Prediction of Height of Turbulent Diffusion Buoyant Flames," *Combustion Science and Technology*, **2**(4), 203-& (1970).
- Sugawa, O. and W. Takahashi, "Flame Height Behavior from Multi-Fire Sources," *Fire and Materials*, **17**, 111-117 (1993).
- Sullivan, A. L., "Wildland Surface Fire Spread Modelling, 1990-2007. 1: Physical and Quasi-Physical Models," *International Journal of Wildland Fire*, **18**(4), 349-368 (2009a).
- Sullivan, A. L., "Wildland Surface Fire Spread Modelling, 1990-2007. 2: Empirical and Quasi-Empirical Models," *International Journal of Wildland Fire*, **18**(4), 369-386 (2009b).
- Sullivan, A. L., "Wildland Surface Fire Spread Modelling, 1990-2007. 3: Simulation and Mathematical Analogue Models," *International Journal of Wildland Fire*, **18**(4), 387-403 (2009c).
- Sun, B., L. Jiang, B. Sun and S. Jiang, "Research of Plant Growth Model Based on the Combination of L-System and Sketch," 9th International Conference for Young Computer Scientists, ICYCS 2008, November 18, 2008 - November 21, 2008, Zhang Jia Jie, Hunan, China (2008).
- Sun, L., X. Zhou, S. Mahalingam and D. R. Weise, "Comparison of Burning Characteristics of Live and Dead Chaparral Fuels," *Combustion and Flame*, **144**(1-2), 349-359 (2006).
- Theobald, D. M., "Landscape Patterns of Exurban Growth in the USA from 1980 to 2020," *Ecology and Society*, **10**(1), - (2005).
- Theobald, D. M. and W. H. Romme, "Expansion of the Us Wildland-Urban Interface," *Landscape and Urban Planning*, **83**(4), 340-354 (2007).

- Thomas, P. H., "The Size of Flames from Natural Fires," Ninth Symposium (International) on Combustion, Pittsburgh, PA (1963).
- Thomas, P. H., D. L. Simms and H. G. H. Wraight, "Fire Spread in Wooden Cribs," Joint Fire Research Organization Fire Research Note No. 537, Joint Fire Research Organization (1964).
- Tihay, V., A. Simeoni, P.-A. Santoni, L. Rossi, J.-P. Garo and J.-P. Vantelon, "Experimental Study of Laminar Flames Obtained by the Homogenization of Three Forest Fuels," *International Journal of Thermal Sciences*, **48**(3), 488-501 (2009).
- van Noordwijk, M. and R. Mulia, "Functional Branch Analysis as Tool for Fractal Scaling above- and Belowground Trees for Their Additive and Non-Additive Properties," *Ecological Modelling*, **149**(1-2), 41-51 (2002).
- Van Wagner, C. E., "Calculations on Forest Fire Spread by Flame Radiation," Special Paper for the 6th World Forestry Conference, Madrid, Spain (1967).
- Van Wagner, C. E., "Conditions for the Start and Spread of Crown Fire," *Canadian Journal of Forest Research*, **7**, 23-24 (1977).
- Viney, N. R., "A Review of Fine Fuel Moisture Modelling," *International Journal of Wildland Fire*, **1**(4), 20 (1991).
- Weber, R. O., "Modelling Fire Spread through Fuel Beds," *Progress in Energy and Combustion Science*, **17**(1), 67-82 (1991a).
- Weber, R. O., "Buoyant Convection: A Physical Process as the Basis for Fire Modelling," 10 (1991b).
- Weise, D. R. and G. S. Biging, "Effects of Wind Velocity and Slope on Flame Properties," *Canadian Journal of Forest Research*, **26**, 1849-1858 (1996).
- Weise, D. R. and G. S. Biging, "A Qualitative Comparison of Fire Spread Models Incorporating Wind and Slope Effects," *Forest Science*, **43**(2), 170-180 (1997).
- Weise, D. R., X. Zhou, L. Sun and S. Mahalingam, "Fire Spread in Chaparral - "Go or No-Go?," *International Journal of Wildland Fire*, **14**(1), 99-106 (2005).
- Weise, D. R. and C. S. Wright, "Wildland Fire Emissions, Carbon and Climate: Characterizing Wildland Fuels," *Forest Ecology and Management*, **317**(0), 26-40 (2014).
- Weise, D. R., T. H. Fletcher, L. L. Baxter, S. Mahalingam, X. Zhou, P. Pagni, R. Linn, B. Butler, "A Fundamental Look at Fire Spread in California Chaparral," 11th Annual AFAC Conference and Inaugural Bushfire CRC Conference, Perth, Western Australia: 186-193 (2004).

Weng, W. G., D. Kamikawa, Y. Fukuda, Y. Hasemi and K. Kagiya, "Study on Flame Height of Merged Flame from Multiple Fire Sources," *Combustion Science and Technology*, **176**(12), 2105-2123 (2004).

Wiedenhoeft, A., "Wood Handbook : Wood as an Engineering Material, Chapter 3: Structure and Function of Wood," USDA Forest Service, Forest Products Laboratory, General Technical Report FPL- GTR-190, 2010: 509 p. 1 v. (2010).

Wilding, W. V., R. L. Rowley and J. L. Oscarson, "Dippr® Project 801 Evaluated Process Design Data," *Fluid Phase Equilibria*, **150–151**(0), 413-420 (1998).

Yang, Z. J. and D. J. Midmore, "Self-Organisation at the Whole-Plant Level: A Modelling Study," *Functional Plant Biology*, **36**(1), 56-65 (2009).

Zhou, X., S. Mahalingam and D. Weise, "Modeling of Marginal Burning State of Fire Spread in Live Chaparral Shrub Fuel Bed," *Combustion and Flame*, **143**(3), 183-198 (2005).

Zhou, X. Y., S. Mahalingam and D. Weise, "Experimental Study and Large Eddy Simulation of Effect of Terrain Slope on Marginal Burning in Shrub Fuel Beds," *Proceedings of the Combustion Institute*, **31**, 2547-2555 (2007).

APPENDIX

- A. Fire behavior of shrub-like fuel arrangements in a wind tunnel
- B. Radiation correction of thermocouple measurements
- C. Manzanita single-leaf experiments at two temperatures
- D. Leaf clump experiments
- E. Multi-leaf column and plane fire propagation experiments
- F. Improved bush model (MATLAB)
- G. L-systems fuel placement code for Utah juniper
- H. L-systems fuel placement code for chamise

A. FIRE BEHAVIOR OF SHRUB-LIKE FUEL ARRANGEMENTS IN A WIND TUNNEL

Fire spread through beds of dead grass and forest litter has been studied extensively, resulting in many fire models. This work was part of an attempt to understand flame spread through live vegetation.³ Live cuttings of manzanita and chamise shrubs were arranged in a simplified natural geometry and held by a wire mesh in a wind tunnel. The shrubs were ignited using a bed of excelsior, i.e., shredded aspen wood. Wind speeds were varied from 0 to 2.0 m/s. Data on flame angle, flame length, rate of spread, burn time, change in mass and burn temperature were gathered from each experiment. For every wind speed increase of 1.0 m/s the observed average flame angle from vertical also increased 20 degrees. A rise in manzanita burn percentage was observed with increasing wind speed. Chamise, on average, burned hotter than manzanita when measuring the temperature of the combustion gases and temperature of the ignited solids. Rate of spread increased linearly with wind speed. Preheating of the shrubs was amplified in higher wind speed experiments.

³ The analysis and writing in this chapter is primarily the work of Kelsey Wooley.

A.1 Methods

A.1.1 Fuel selection and arrangement

Fire behavior was studied in a wind tunnel for Eastwood's manzanita (*Arctostaphylos grandulosa*) and chamise (*Adenostoma fasciculatum*), which are both common species found in the chaparral ecosystem of California (Keeley, 2000). Experiments were performed on July 19-20, 2010 on samples collected near Riverside, California three days prior to the first day of testing. The three-day delay allowed the samples to dry out to more flammable moisture contents (such that fire spread would be more likely in wind tunnel conditions). In previous experiments performed in December 2009, high moisture content branches did not burn well in this apparatus until they were first dried in large ovens. In wildland fires, higher moisture contents can be tolerated due to larger, more intense flame fronts. A Computrac MAX1000 Moisture Analyzer (Chandler, AZ, USA) was used to measure the moisture content of each species. The moisture contents of manzanita (41%, dry basis) and chamise (12%) remained stable between both days of testing.

A two-layered wire mesh was prepared to hold cut branches in simplified shrub geometries. The mesh size was 5.1 cm by 7.6 cm with layers at approximately 7.6 cm and 15.2 cm above the floor of the wind tunnel. The front end of the mesh was positioned 1.5 m from the end of the wind tunnel fan box. Branch stems were trimmed so that branches had similar lengths. Those with stem diameters greater than 2 cm were discarded. The prepared branches were oriented vertically and stems were inserted through the two layers of wire mesh to hold them in place. The cuttings were placed in two rows, parallel with the length of the wind tunnel, at 13-15 cm intervals. While live stems > 1.3 cm do not typically burn under severe conditions (Green, 1981), woody stems up to 2 cm in diameter were retained to maintain some structural integrity

of the fuel bed. Larger stems were removed so the effects of the woody branches were not studied. The rows of branches were about 60-80 cm long. The average bulk fuel density in these experiments was 5 kg m^{-3} (± 1.2) for manzanita and 2.5 kg m^{-3} (± 0.5) for chamise. By comparison, packing ratios of chamise in natural conditions were measured at 0.0007 to 0.0037 (m^3 of solid/ m^3 of shrub) (Davies et al., 2009), corresponding to bulk densities of 0.50 to 2.8 kg m^{-3} assuming a solid density of 737 kg m^{-3} (Morandini et al., 2006). Bulk densities of manzanita shrubs in natural conditions are not available.

A.1.2 Experimental apparatus

The wind tunnel experiments were performed at the USDA Forest Service PSW Research Station fire laboratory in Riverside, California. The shrubs were ignited by forming a triangle-shaped horizontal bed of aspen (*Populus tremuloides* Michx.) excelsior starting at a point upwind on the floor of the wind tunnel and widening to the width of the base of the bush. The distance between the excelsior fuel bed and the bush was varied according to the wind speed for each run. At high wind speeds the flame tip of the ignition source would contact shrub before the base of the flame contacted the shrub, due to the flame angle. The excelsior was arranged so that it would burn out shortly after the ignition of the front side of the bush in order to minimize interaction between the flames of the ignition source and the shrub. At the highest wind speed, (2.0 m/s) the excelsior bed was situated 20 cm from the wire mesh holding the branches. With no wind, the bed was placed directly beneath the first row of branches as shown in Figure A-1. The bed of excelsior was approximately 5 cm thick.



Figure A-1. Top view of the setup of an experiment with manzanita and zero wind speed. Note how the v-shaped bed of excelsior is in contact with the branches.

Three video cameras were used to collect the majority of information. The main video data were taken by an analog Sony Handicam (CCD-TRV138 Video Hi8, San Diego, CA, USA) stationed on a tripod 3 meters away from the wind tunnel at an angle perpendicular to the flow. Flame angle, flame propagation speed, and flame length were all deduced from the images taken with this camera. Recording began with the ignition of the Excelsior and stopped when the last flame died out.

A FLIR thermal imaging camera (Model A20M, Boston, MA, USA), was placed adjacent to the Sony Handicam on the same tripod and was used to obtain burn temperature data and observe possible effects of preheating. Images were collected at 30 Hz and analyzed using ThermoCAM Researcher Pro 2.8. The infrared camera collected images in the 7.5-13 μm wavelength range. An emissivity of 0.8 was estimated for temperature calculation from the infrared camera. A second handheld digital video camera was positioned on a tripod above the wind tunnel directly above the fan with a view parallel to the flow. This view was used to obtain burn duration data and provided an alternate angle to see clearly how the flames behaved.

Before igniting each experiment a hand-held anemometer, Kestrel model 3000, was used to get a profile of the wind around the bush. The hand-held device gave values different from the calibrated wind speeds of the fan, but even with the variation, little to no wind was observed to penetrate to the interior of the shrubs. This anemometer also measured the ambient temperature and relative humidity.

Individual branches were weighed before being arranged in the wire mesh. After all the smoldering had ended, the remains of the shrub were also weighed. This gave a rough comparison of the initial and final mass. Four Type K thermocouples were placed within the branches to collect temperature data at different points within the shrub as the flame front moved through the fuel. The height, width and length of the shrub were recorded, with height measured from the bottom of the wire mesh. Digital photos of the cutting arrangement were taken from the front, side and top with a CoolPix S400 digital camera.

A.2 Results and discussion

Combustion experiments were conducted at four different wind settings (2.0 m/s, 1.5m/s, 1.0 m/s and 0.0 m/s). Each of the eight experiments were replicated once. Analysis of variance and Tukey's propagation of error tests were performed to determine the significance (at 95% confidence) of the effects of wind speed and species type on flame angle, flame length, burn time, change in mass, burn temperature and rate of spread.

A.2.1 Flame angle

Increasing the wind speed increased the flame angle (angle θ measured from vertical). The bottom of the flame and flame tip location were identified manually in images at one-second intervals. The analysis of variance table is presented below in Table A-1. The flame angle data

had a strong positive correlation with wind speed when linearly regressed, ($R^2=0.9541$). Table A-2 presents the average flame angle at each wind speed, combining data from both species.

Table A-1. Analysis of variance for flame angle vs. species and wind speed

Source of Variation	SS	df	MS	F	P-value	F crit
Species	16.03179	1	16.03179	1.892729	0.206179	5.317655
Wind Speed	5362.311	3	1787.437	211.0265	5.94E-08	4.066181
Interaction	92.36931	3	30.78977	3.635069	0.064095	4.066181
Within	67.76161	8	8.470201			
Total	5538.474	15				

Table A-2. Average flame angle (θ) vs. wind speed (combining both species).

Wind Speed	Average θ
0.0 m/s	-3°
1.0 m/s	23°
1.5 m/s	35°
2.0 m/s	42°

The two factors in this analysis were wind speed and species type. The response variable was flame angle. Wind speed (p-value = 0.000014) and species type (p-value = 0.029) had significant effects on the flame angle with no significant interaction between the two factors (p=0.199). The strength of effect for wind was 154% greater than the effect for species. Possible reasons that there was a species effect are that the two species had (1) different morphologies, (2) different moisture contents, and (3) different bulk densities.

When the flame angles were analyzed by species, the linear regression model fits were significantly better. The linear fits of flame angle versus wind speed for each species are listed below in Table A-3 and illustrated in Figure A-2.

Table A-3. Flame angle correlations

Manzanita	$\theta = 23.82 v - 3.58$	$R^2 = 0.9680$	95% CI Slope ± 4.323	95% CI Intercept ± 5.821
Chamise	$\theta = 25.62 v - 3.60$	$R^2 = 0.9708$	95% CI Slope ± 4.439	95% CI Intercept ± 5.976

'v' is wind speed in meters per second and "Θ" is flame angle in degrees from vertical.

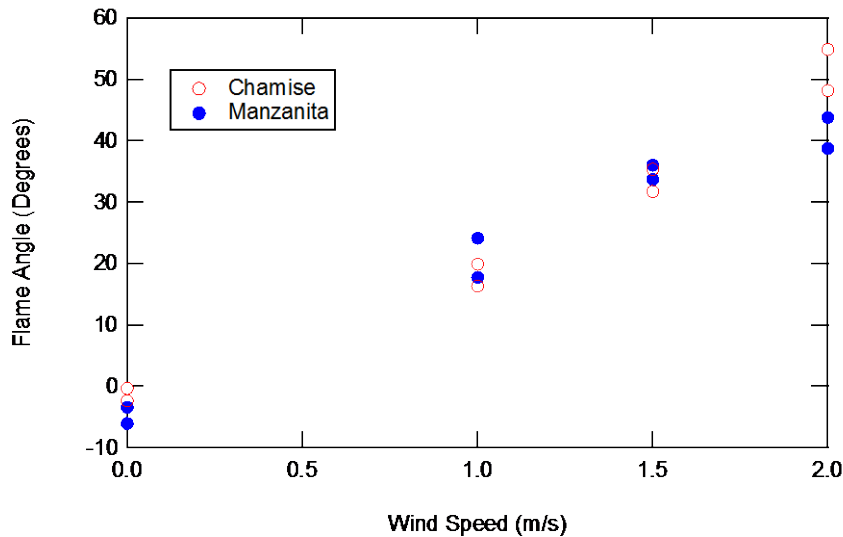


Figure A-2. Measured flame angle (degrees from vertical) vs. wind speed.

The flame angle regression for chamise has a slightly steeper slope than that for manzanita. This variation is not believed to be significant within the error of the experiments with the limited number of replications. The y-intercept of the equations (which indicates flame angle at zero wind) is extremely similar at nearly zero degrees. The likely reason that the intercepts are less than the expected zero degrees is due to one door of the wind tunnel being kept open to allow the infrared camera to gather images of the burn. The open door caused a slight back draft that resulted in the observed flame angle. Even though intuition suggests that the intercepts should be closer to zero, (flame pointing straight up) the observation that they are close to each other suggests the consistency in the information gathered and that the effect of the door was constant over all replicates.

Several flame angle models (Putnam, 1965; Albini, 1981; Nelson and Adkins, 1986; Weise and Biging, 1996) were used to compare calculated flame angle to measured flame angle. Actual flame heights were used in the model calculations, and the average model calculations of multiple experiments are shown in Figure A-3. These models were developed from flat beds of fuel, but the flames here occur inside the shrub as well as above the shrub. However, the calculated flame angles are reasonably close to the measurements.

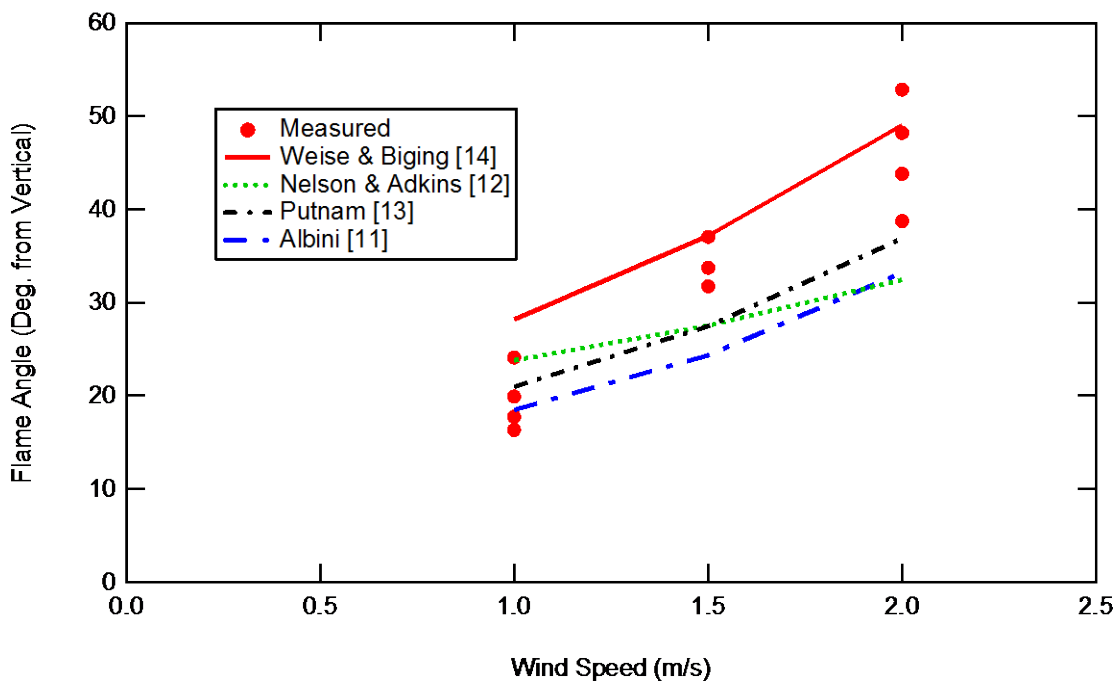


Figure A-3. Flame angle prediction models compared to observed experiments

A.2.2 Flame length

Flame length and angle of tilt were measured using digital video recordings of each experiment which were interpreted with a MatLab code that calculated the number of pixels from the top of the bush to the tip of the continuous flame. A reference length was used to convert number of pixels to length units. After the excelsior flame died away, flame length

measurements were made for every tenth video frame. Flame measurement was stopped when the main body of the flame died off. An average flame length was then computed for each experiment.

Higher wind speeds increased the angle of the flame and therefore the length of the flame (Figure A-4). Flame length here is defined as the distance from the top of the shrub to the tip of the flame, usually following the line of the average flame angle for the frame of video being analyzed, as demonstrated in Figure A-4. The top of the shrub was used as the measurement's starting point to assure that the height of the bush, the flame below the shrub, and the excelsior's flame did not affect the flame length measurement.

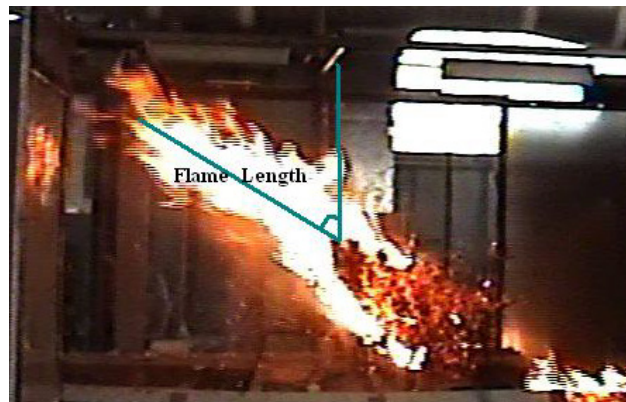


Figure A-4. Illustration of method for measurement of flame length and flame angle.

Flame length increased monotonically with increasing wind speed (see Figure A-5). Wind speed had an effect on flame length ($p= 0.039$), but with 95% confidence, species type and species interaction with wind speed did not influence flame length. The analysis of variance is presented in Table A-4.

Table A-4. Analysis of variance for flame length vs. species and wind speed

Source of Variation	SS	df	MS	F	P-value	F crit
Species	218.4008	1	218.4008	0.047242	0.833375	5.317655
Wind Speed	35882.73	3	11960.91	2.587243	0.12558	4.066181
Interaction	10558.74	3	3519.581	0.761314	0.54668	4.066181
Within	36984.27	8	4623.034			
Total	83644.14	15				

Flame length is a valuable measurement when predicting how a flame front can spread to surrounding fuels. As flames grow buoyancy causes significant air entrainment (Baeza et al., 2002) which can result in decreased flame length. However, large, intense fires lead to taller flames, and wind causes longer flames (Martins Fernandes, 2001).

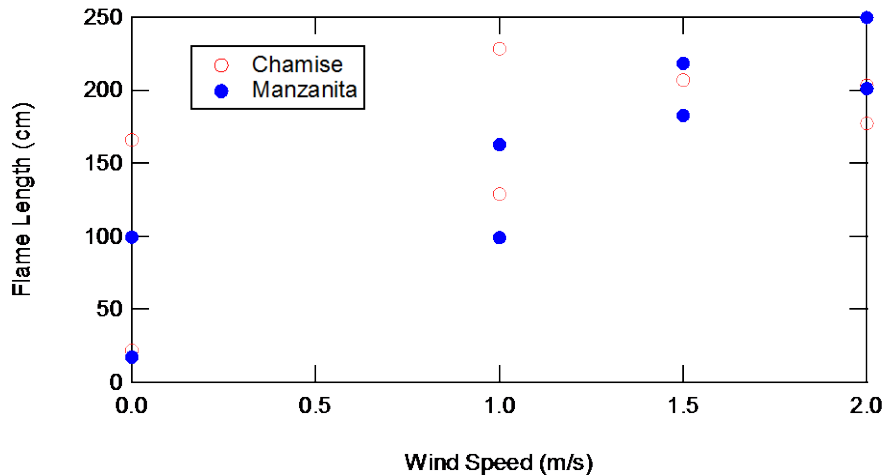


Figure A-5. Measured average flame length vs. wind speed.

A.2.3 Burn time and change in mass

Using the data collected from the camcorder perpendicular to the wind flow, time from ignition of the bush (not the excelsior) to burnout was found to have a significant interaction with wind speed (See Table A-5). Faster wind speeds resulted in shorter burn time with both manzanita and chamise, as shown in Figure A-6. The negative correlation was reported

previously in more detail for single leaves of different fuel types (Cole et al., 2010). In the absence of wind chamise burned almost 100 seconds faster than manzanita. With wind speeds of 1.5 to 2.0 m/s the burn times of the two species were more comparable.

Table A-5. Analysis of variance for burn time vs. species and wind speed

Source of Variation	SS	df	MS	F	P-value	F crit
Species	1849	1	1849	3.086167	0.117025	5.317655
Wind Speed	38214.25	3	12738.08	21.26114	0.000362	4.066181
Interaction	8923.5	3	2974.5	4.96474	0.031119	4.066181
Within	4793	8	599.125			
Total	53779.75	15				

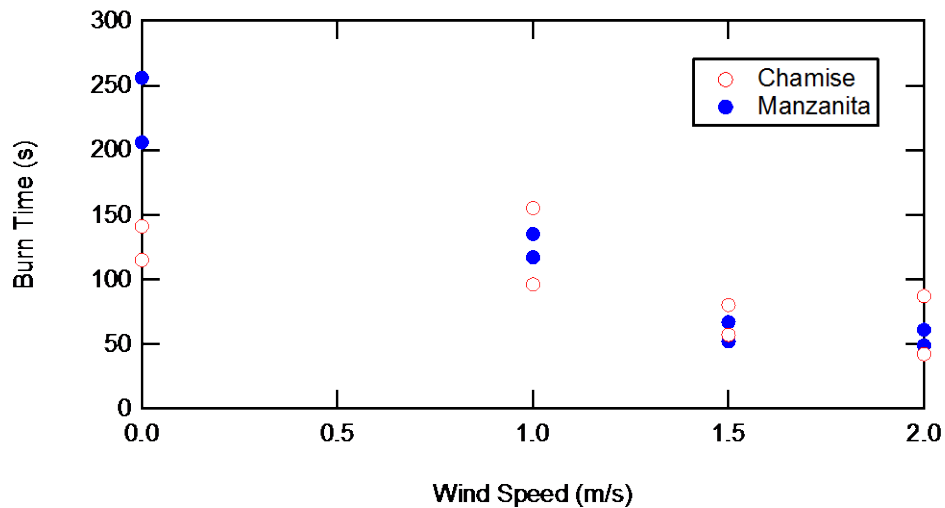


Figure A-6. Burn time of both species vs. wind speed.

This observed difference in species at low wind speeds may be attributed to the moisture content and the physical characteristics of the two different fuels. Chamise has very small needles and thin, dry branches. The average moisture content was 12% for chamise over both days of testing. manzanita is a broad leaf species and able to retain much more water. The average moisture content for the manzanita used was 46%. The manzanita bush burned slower when there was higher moisture content and no wind to accelerate the fire.

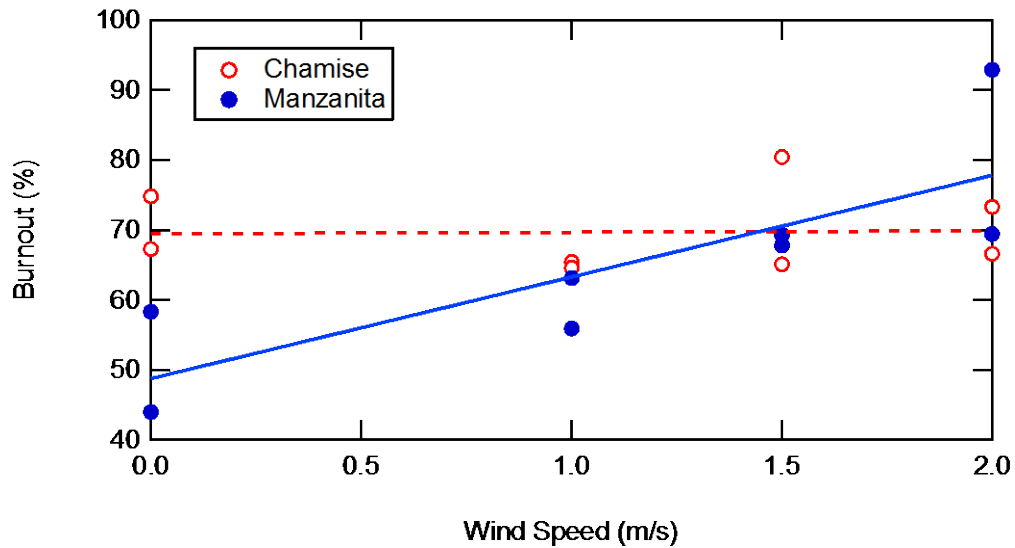


Figure A-7. Burnout vs. wind speed for both species

The difference between the initial mass and the mass after the flames extinguished was normalized by the initial mass for each test and referred to as burnout. Figure A-7 shows the effect of wind speed on burnout (on a wet basis, $(1-m_{\text{Remaining}})/m_{\text{H}_2\text{O}+\text{DrySolids}}$). A weak positive correlation between change in mass and wind speed was observed, but the effect was not statistically significant. However, when the data were correlated by species, the manzanita correlation was somewhat linear ($R^2=0.36$), while chamise exhibited hardly any change at all with wind speed. These behaviors are represented as solid and dashed lines in Figure A-7.

An explanation for this wind-independent behavior possibly is because chamise burned quickly and easily, likely due to naturally lower moisture content, so its branches burned to nearly the same completion on every run. The bulk density of the chamise shrub in these experiments was also about half that of the manzanita shrub.

A.2.4 Burn temperature

The infrared camera and embedded thermocouples were used to measure temperatures in these experiments. The infrared camera measures energy in the 7-13 μm wavelengths and thus estimated radiant temperatures of solids while the thermocouples measured local gas temperatures. After the excelsior flame had extinguished, the maximum solid temperature in the burning shrub was determined for each infrared image over the duration of the experiment. These maximum solid temperatures were then averaged. For each run, the maximum gas temperatures over the duration of the experiment measured by each of the four thermocouples were averaged to obtain a maximum average gas temperature. Temperature change due to radiation was corrected for. The average maximum gas and solid temperature from each replicate are presented in Figure A-8. On average, the combustion gases of chamise were 70°C hotter than for manzanita. Similarly, the temperature of the ignited solids were 100°C hotter for chamise than for manzanita. However, there are no significant interactions with a Student's two-parameter t-test between species and burn temperature. Statistical analysis was hampered somewhat because the data from the infrared camera were not available for last half of the experiments. For example, no IR data were available for manzanita at the 1.5 m/s wind speed, but two sets of data were available for chamise at the 2.0 m/s wind speed. The analysis of variance for the thermocouple temperature data is presented in Table A-6.

Table A-6. Analysis of variance for burn temperature vs. species and wind speed

Source of Variation	SS	df	MS	F	P-value	F crit
Sample	42195.32	1	42195.32	2.284864	0.16909	5.317655
Columns	23213.08	3	7737.695	0.418994	0.744382	4.066181
Interaction	70245.69	3	23415.23	1.267928	0.348959	4.066181
Within	147738.6	8	18467.32			
Total	283392.7	15				

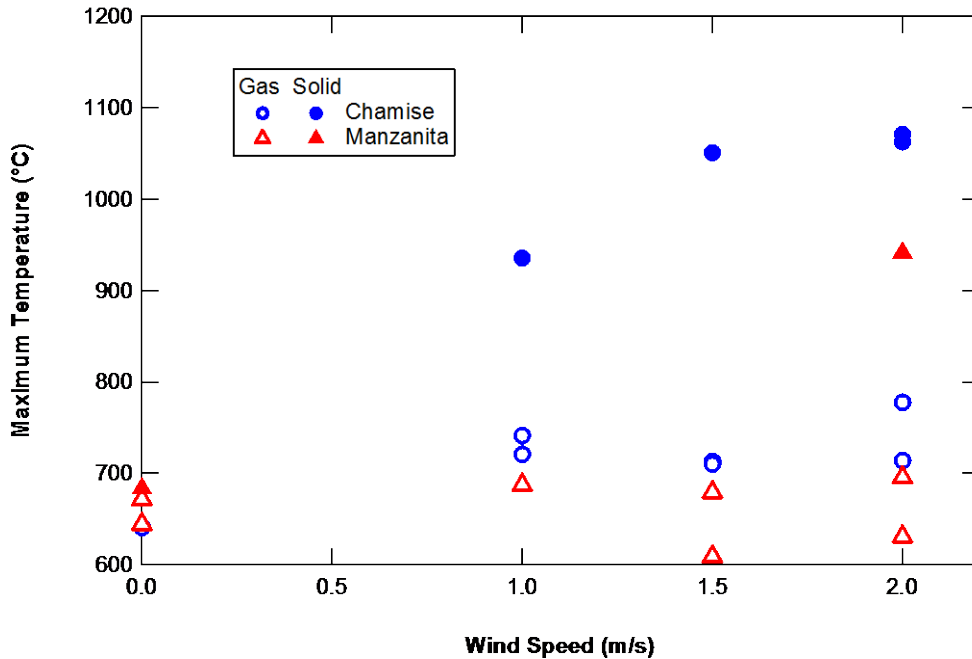


Figure A-8. Average gas and solid burn temperature vs. wind speed.

A.2.5 Preheating effects

The effects of preheating in the burning of live fuels were also analyzed. In each experiment in which infrared data were gathered, a temperature profile in front of the flame front was studied (see Figure A-9). First, a frame from the IR images was selected that had no interactions from an overlapping excelsior flame (around the half-way mark of that experiment's burn time). Then a 40 cm line was drawn on the infrared image starting at the center of the hottest part of the flame and ending ahead of the flame in the unburned portion of the shrub. Each pixel in this line returned a temperature of the solid at that point. This image analysis was performed for each of the eight experiments and is presented below in Figure A-10. The line was made at approximately half the height of the sample. The starting point of the profile on the y-axis is representative of the estimated maximum flame temperature for that frame.

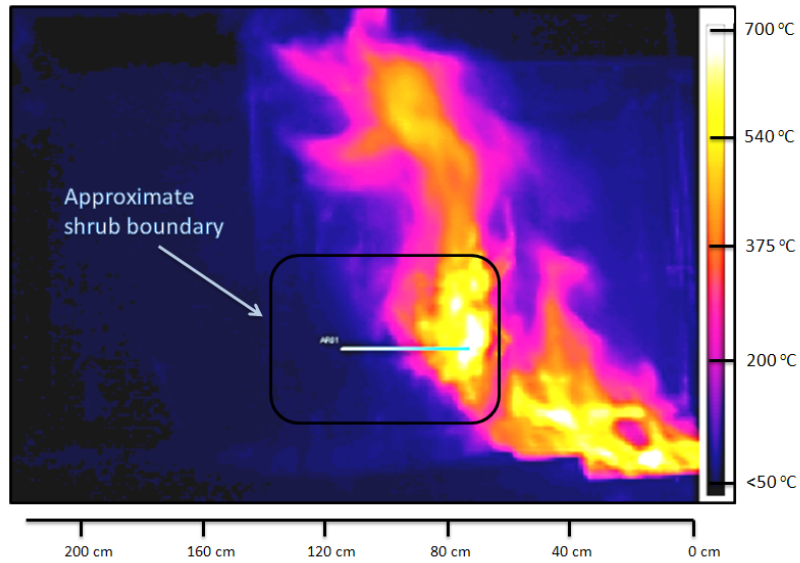


Figure A-9. IR image showing method to measure solid temperature ahead of the flame.

The most apparent pre-heating effects can be seen by the steepness of temperature gradient from the maximum starting temperature near the y-axis of Figure A-10. The experiments where there was little or no wind generally had very steep temperature gradients; the temperature of the solid shrub decreased quickly with distance in front of the flame. The initial temperature gradient was much flatter for experiments with higher wind speeds, indicating more significant convective pre-heating effects with wind present.

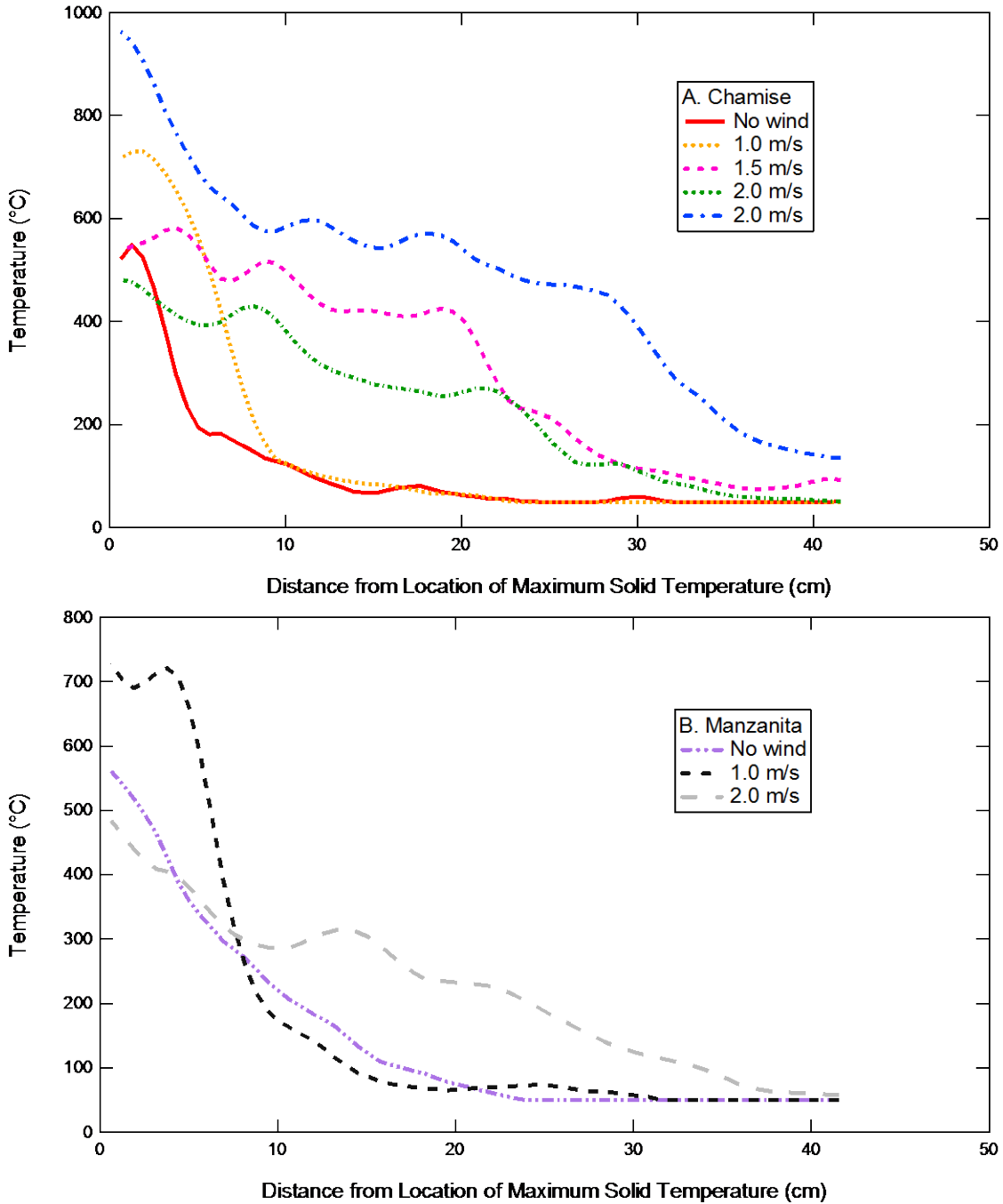


Figure A-10. Temperature of the solids as a function of distance from the location of maximum temperature. (A) Chamise, and (B) Manzanita.

For ease of comparison, Figure A-11 shows the temperature gradient versus distance for each wind speed. The highest temperature gradients occur at the lowest wind speeds, which is consistent with the spreading of the preheat zone for the higher wind speeds. For manzanita,

highest temperature gradient occurred for the 1.0 m/s wind speed condition instead of the no wind condition. This may be due to the noise of this reading, or perhaps related to the different bulk densities of the two species.

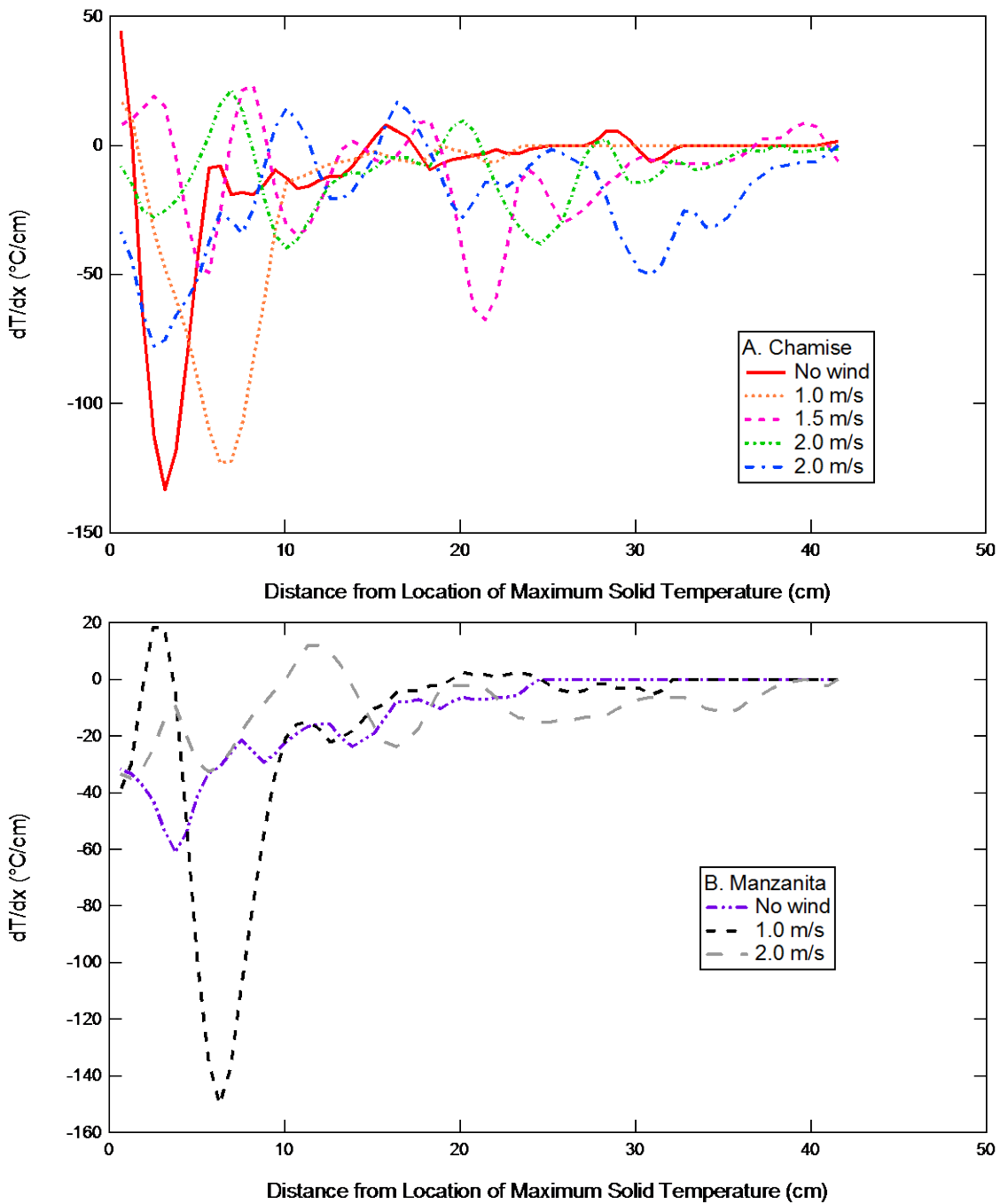


Figure A-11. Change in temperature plotted against change in distance in front of the flame front

Another method to analyze preheating effects was to divide the bush into four equal, vertical sections and record the maximum solid temperature from each frame for each of the four sections. Figure A-12 shows one such graph of the first experiment, manzanita at zero wind speed. A separate line is presented for each of the vertical quarters. Each section has a peak solid temperature at a different time as the flame proceeds through the shrub. Section 1 was the area closest to the ignition source. A steep preheating temperature gradient is observed in Figure A-12, which corresponds to the steep temperature gradient observed for no wind in Figure A-10B. Similar analyses were conducted for experiments with wind and the same results were observed; the steepness of the slope of temperatures decreased with increased wind in a manner similar to the trend shown in Figure A-10.

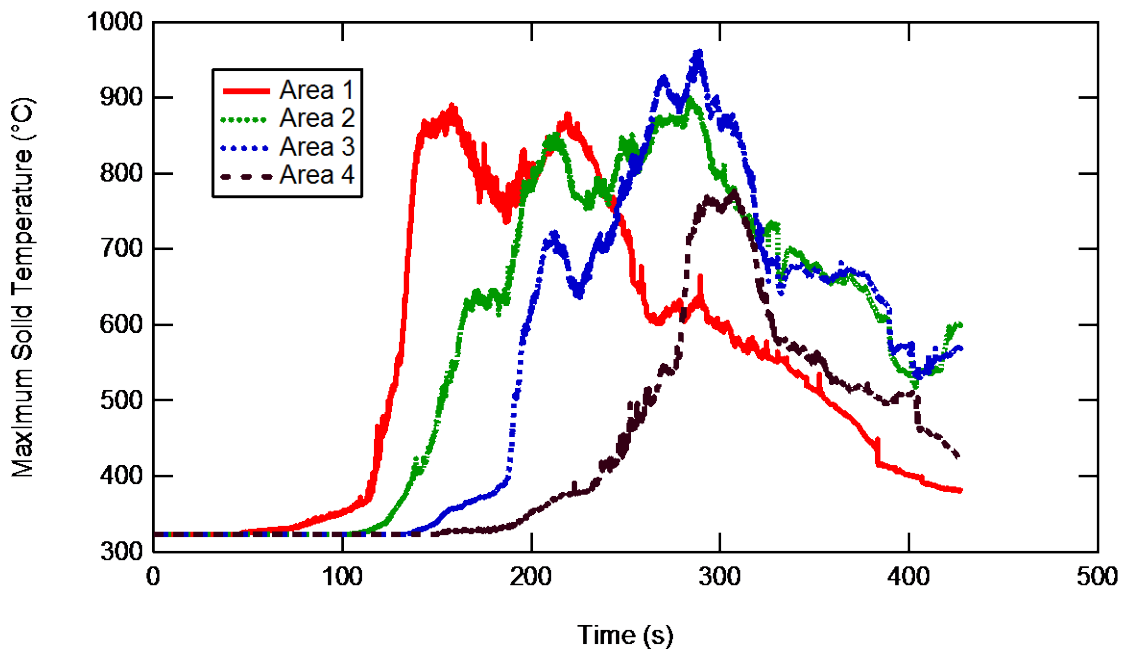


Figure A-12. Maximum solid temperature of each area with respect to time for a manzanita shrub combustion experiment with no wind.

From the temperature measurement alone, it is impossible to differentiate whether radiation, convection or a combination of both heat transfer mechanisms are responsible for

preheating. However, radiation flux to downstream elements would change only through the effects of flame tilting, which effect is thought to be small. Therefore, the changes in the gradients in the downstream solid temperature gradients are thought to be due principally to convective heat transfer from combustion products.

A.2.6 Rate of spread

An average rate of spread (RoS) was determined for each experiment by timing the progression of the flame over a known distance. A rod positioned in the wind tunnel, parallel to the air flow was used as a reference length, and each frame of the visual recording was time stamped. The front of the flame was marked electronically at two different times and the change in distance over the change in time gave an estimate of the RoS. Figure A-13 shows the RoS values determined in these experiments.

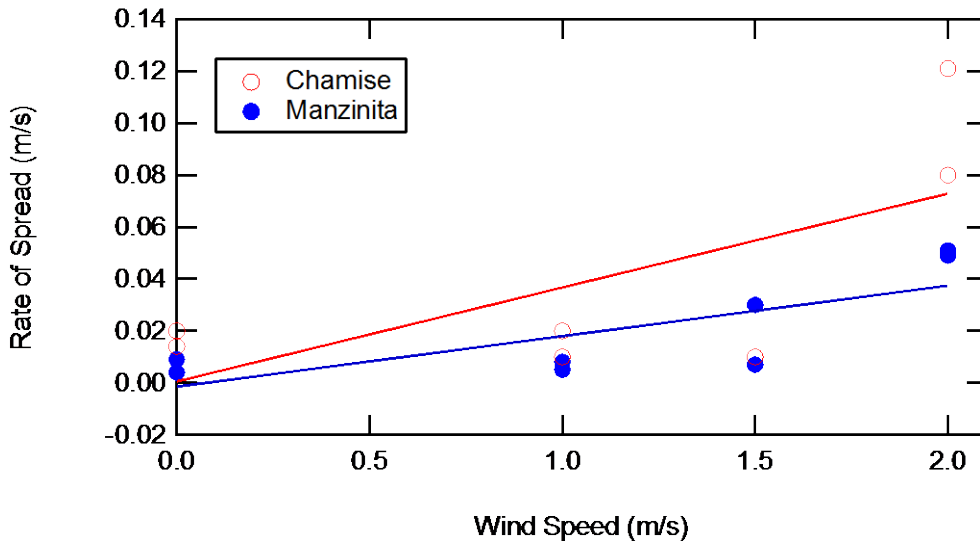


Figure A-13. Rate of fire spread as a function of wind speed. The trend line is the fit of all the points for both species.

Two sources of error with the calculation of the RoS are the line of best fit and human error. In several of the runs, the time to calculate the flame moving through the bush was very short, since the measurement could not be made until the flame from the ignition source had extinguished. In the high-wind tests this may have been a cause of variation. The overall trend appears piecewise linear, as shown in Figure A-13. There may be several causes of this trend. Using a Kestrel 3000 Weather Meter, the wind speed was measured at several designated points within and around the exterior of the bush. Points measured within the shrub were taken to provide a wind velocity profile within the shrub. Points outside the shrub provided a local velocity profile that was slower than the bulk flow upstream. A possibility for why there was no significant RoS increase with wind speeds from 0 to 1 m/s may be due to the wind flow inside the bush boundaries being negligible at such a low bulk air velocity. Further experiments need to be performed with a longer fuel source to make the estimation more accurate.

One data point at 1.5 m/s wind speed was omitted. In this experiment, the excelsior did not burn out before the bush was consumed. This chamise run also had a lower mass density and size than the other runs, making it difficult to compare to the other experiments.

The trend line shown in Figure A-11 was a piece-wise linear fit of the combined data from both species. Manzanita had a very strong $R^2=0.9611$ when linearly regressed by itself. Chamise exhibited the same general linear trend with an $R^2= 0.6780$. Using a Student's t-test, both of the factors tested (wind speed and species type) were found to be statistically significant with p-values of 0.004 and 0.043 respectively with response variable of RoS. These values were calculated using only the extreme wind speeds (0 and 2.0 m/s). The data showing that little change happened between 0 m/s and 1.0 m/s would lower the strength of these effects presented.

Also observed from the video data was that physical flame over lapping with fuel is required for propagation. The samples were arranged with a high enough bulk density that flame spread could occur independent of the ignition source, the excelsior bed. This behavior was present independent of burn temperature.

A.2.7 Moisture in unburned leaves

In three of the manzanita experiments, small clusters of leaves were left unburned, but scorched from the flame. The moisture content of these remaining leaves was measured. Even though the flame had visibly darkened the leaves, the moisture content of the scorched manzanita leaves was still roughly 40%. This finding is consistent with the finding that there is significant moisture in the leaf when ignition occurs, due to mass transfer effects (Pickett et al., 2010).

A.2.8 Seasonal observations

A separate set experiments was conducted earlier in December 2009. Most of the data gathered at the time suggested relationships between parameters, but due to the limited number of replications, no conclusions could be made. It is worth mentioning, however, some comparisons between the winter and the summer experiments.

Both seasons' experiments were conducted with manzanita and chamise and had a similar experimental design. The temperature and relative humidity of the July 2010 experiments were 35°C and 55% respectively. The experiments performed in December 2009 had an average ambient temperature of 10°C and relative humidity of 74%. The dryer, hotter summer season compared to the cooler and wetter winter had a significant effect on the shrubs ability to burn at different wind situations (Anderson and Rothermel, 1965).

An observed phenomenon in the winter experiments was an inability for manzanita branches at 30% moisture content and above to burn. The branches of both species had to be dried in an oven for several hours or set aside to dry for almost a week to obtain roughly 10% moisture content. One experiment demonstrated this moisture content ceiling very well. In this experiment, branches with two different moisture contents were placed in the wire grid in the wind tunnel. The branches closest to the ignition source had leaves at 10% moisture content and the branches furthest away had leaves at 30% moisture content. Upon ignition, the branches with 10% moisture content ignited and burned quickly. Even though the two bunches of branches were touching, the higher moisture content branches did not ignite (See Figure A-14). This same moisture content ceiling was manifest in many other experiments where the burn percentages were very low. This inability to burn was unexpected. Initial explanations were that a shrub with woody parts (thicker stems) required a higher heat flux than obtained by just burning the leaves, or the higher heat flux was needed to dry branches to lower moisture before ignition. After conducting more summer runs, these explanations are likely incorrect. This is supported by the temperature data, which was presented earlier in Figure A-10. It has been recognized for a long time that a greater amount of energy is required to ignite and sustain a fire in live fuel beds (Countryman, 1974). In the present experiment, the excelsior served the role played in natural stands by the dead fuels. While fire will spread in live fuels, it is often a marginal phenomenon (Weise et al., 2005).



Figure A-14. Manzanita combustion experiment from December 2009, mixing branches with 10% and 30 % moisture content. The flame shown here burned out shortly after this time, leaving the 10% moisture content side of the bush burned and the 30% moisture content side unburned.

The moisture contents of all the manzanita branches burned in August were over 30%, which would have not burned well in December, and all experiments had high burnout percentages; manzanita had a burnout percentage of 65.1% and chamise was slightly higher with 69.7%. The average burnout percentage for the December 2009 experiments was only 10% at 0 m/s and 60% at 1 m/s wind speed. Most of the remaining unburned mass from the summer experiments was thicker stems. These percentages are averages over all wind speeds for each species. Even with no wind, the flame in the August experiment would propagate throughout the entire bush and leave little unburned. This result suggests that the maximum moisture content where ignition can is much higher when the ambient temperature is higher. This seasonal effect needs to be examined further to draw a quantitative conclusion.

A.3 Conclusion

A series of combustion experiments were performed on branches of either manzanita or chamise assembled in a wire grid in a wind tunnel. The bulk fuel densities used here were closer to that of actual shrubs than beds or baskets of fuel. Wind speeds were varied from 0 to 2 m/s.

Both visual and infrared videos of the flame were examined to determine flame characteristics and rate of flame spread. Higher wind speeds strongly correlate with a larger flame angle and increased flame length. Higher wind speeds were shown to cause a faster burn time and rate of spread, as expected. In most cases physical flame touching was necessary for ignition to occur. Fuel elements near the flame did not spontaneously catch on fire at the temperatures in these experiments. The observed solid temperatures for chamise were 100°C hotter than observed for manzanita. Similarly, the gas temperatures observed for chamise were 70°C hotter than observed for manzanita. The infrared images were examined to determine the solid temperatures downstream of the flame, which is an indication of preheating effects. Steep temperature gradients in the solid fuel were observed without wind, but more gradual temperature gradients were observed when wind was present. The more gradual temperature gradients observed with wind present are indicative of convective heating from combustion gases. Flames were observed to propagate faster through the chamise bushes than the manzanita bushes.

A comparison was made between shrub combustion experiments performed in the summer and winter in this wind tunnel. The ambient air temperature and humidity was different in the winter than in the summer. The lower air temperature lowered the threshold moisture content where ignition could occur. In other words, shrubs had to be dried to low moisture contents to permit combustion in air temperatures of 10°C.

These observations help form a more accurate model of how species behave during combustion. Chamise, with a lower natural moisture content and lower bulk density than manzanita, burned hotter, faster, and with greater flame angles at various wind speeds. Manzanita burned cooler, slower, and had a flame angle and a change in mass affected by wind speed. The season greatly determines the extent to which a bush will burn and the likelihood of

spreading fire to neighboring fuels. This is due to ambient temperature as well as fuel moisture content.

B. RADIATION CORRECTION OF THERMOCOUPLE MEASUREMENTS

A thermocouple was placed above the flat-flame burner in order to measure the temperature of the convective gases. The thermocouple temperature results from a combination of convection, radiation, conduction through the thermocouple leads, and sometimes catalysis (Shaddix, 1999). The calculations presented here correct the thermocouple bead for radiation.

Bead temperatures at 2, 4 and 6 cm above the flat-flame burner surface were measured as 997 °C, 985 °C and 962 °C, respectively. The bead diameter was measured with a typical value of 0.22 mm. The thermocouple leads had a diameter of 0.127 mm. The viscosity and thermal conductivity of air were determined from temperature-dependent expressions from the DIPPR database (Wilding et al., 1998; Rowley et al., 2003). The actual post-flame gas mixture was not air, so viscosity and thermal conductivity were checked against the actual post-flame gas mixture using GASEQ (Morley, 2005), which were within 2% of the values for air at 1300 K.

To determine the convective heat transfer, the gas velocity was determined. For uncorrected rotameter flow rate settings of 300 L/min air, 35 L/min H₂, and 35 L/min CH₄, the actual (cold) total flow rate was 401 L/min. The cross section of the flow path was measured as 0.049 m² and the hot gas velocity was calculated as the cold velocity times the hot (post-combustion) gas temperature divided by 300 K. Convection and radiation correlations were implemented and an energy balance on the thermocouple bead was calculated to determine its temperature, as presented in the following MathCAD sheet (Table B-1).

Table B-1. MathCAD calculation

Radiation Correction

Thermocouple measurement & properties

measurements: 997°C at 2 cm 985 at 4 cm 962 at 6 cm

$$T_{\text{bead}} := 962^\circ\text{C} \quad T_{\text{bead}} = 1.235 \times 10^3 \text{ K}$$

$$D_{\text{bead}} := .22\text{mm} \quad (\text{from } .21 \text{ to } .25)$$

$$D_{\text{wire}} := 0.127\text{mm}$$

Temperature dependent properties (of air)

DIPPR Equations

$$c_{\mu} := (1.4250\text{E-}06 \quad 5.0390\text{E-}01 \quad 1.0830\text{E+}02 \quad 0)^T$$

$$c_k := (3.1417\text{E-}04 \quad 7.7860\text{E-}01 \quad -7.1160\text{E-}01 \quad 2.1217\text{E+}03)^T$$

$$Y(\text{temp}, \text{co}) := \frac{c_{00} \cdot \left(\frac{\text{temp}}{\text{K}}\right)^{c_{01}}}{1 + \frac{c_{02}}{\left(\frac{\text{temp}}{\text{K}}\right)} + \frac{c_{03}}{\left(\frac{\text{temp}}{\text{K}}\right)^2}}$$

$$\mu_{\text{air}}(\text{temp}) := Y(\text{temp}, c_{\mu}) \text{ Pa}\cdot\text{s} \quad \text{Viscosity} \quad \mu_{\text{air}}(1300\text{K}) = 4.877 \times 10^{-5} \cdot \text{Pa}\cdot\text{s} \quad \text{verified with DIPPR}$$

$$k_{\text{air}}(\text{temp}) := Y(\text{temp}, c_k) \frac{\text{W}}{\text{m}\cdot\text{K}} \quad \text{Thermal conductivity} \quad k_{\text{air}}(1300\text{K}) = 0.083 \cdot \frac{\text{W}}{\text{m}\cdot\text{K}} \quad \text{verified with DIPPR}$$

Comparison with GASEQ

$$k_{\text{gaseq}} := 1.98 \cdot 10^{-2} \frac{\text{cal}}{\text{m}\cdot\text{K}\cdot\text{s}} \quad k_{\text{gaseq}} = 0.083 \cdot \frac{\text{W}}{\text{m}\cdot\text{K}} \quad \frac{k_{\text{gaseq}} - k_{\text{air}}(1300\text{K})}{k_{\text{air}}(1300\text{K})} = -0.649\%$$

$$\mu_{\text{gaseq}} := 4.96 \cdot 10^{-5} \frac{\text{kg}}{\text{m}\cdot\text{s}} \quad \mu_{\text{gaseq}} = 4.96 \times 10^{-5} \cdot \text{Pa}\cdot\text{s} \quad \frac{\mu_{\text{gaseq}} - \mu_{\text{air}}(1300\text{K})}{\mu_{\text{air}}(1300\text{K})} = 1.696\%$$

Burner Velocity

$$\text{Volume} := 400.9 \frac{\text{L}}{\text{min}}$$

Flow rate at rotameter settings of 300-air, 35-h2, 35-ch4. 400.9 calculated using calibration curves in flow rates Excel document.

$$A_{\text{cross}} := 26.9\text{cm} \cdot (20 - 28.7 + 26.9)\text{cm}$$

The second factor is figured out from outer difference and difference glass/frame made on first factor (shield was in the way)

$$A_{\text{cross}} = 0.049\text{m}^2$$

Note: this doe assumes plug flow. However, assuming a centerline velocity of twice this does not change things very much. This does not take into account any change in number of molecules from reactants to products.

$$v_{\text{cold}} := \frac{\text{Volume}}{A_{\text{cross}}} = 0.136 \frac{\text{m}}{\text{s}} \quad v_{\text{hot}}(T_{\text{gas}}) := v_{\text{cold}} \cdot \frac{T_{\text{gas}}}{300\text{K}}$$

Table B-1 continued

Convection correlation

Pr := 0.72 approximate value

$$P_{\text{provo}} := 24.91 \cdot \frac{\text{in}}{\text{mm}} \cdot \text{torr} \quad R_g := 8.314 \frac{\text{J}}{\text{mol} \cdot \text{K}} \quad M_w := 27.29 \frac{\text{gm}}{\text{mol}} \quad (\text{from gaseq})$$

$$\rho(T_{\text{gas}}) := \frac{P_{\text{provo}} \cdot M_w}{R_g \cdot T_{\text{gas}}} \quad \rho(1300\text{K}) = 0.213 \frac{\text{kg}}{\text{m}^3} \quad \text{Big player here is } P_{\text{provo}}, M_w \text{ very similar to air}$$

$$\text{Re}_d(T_{\text{gas}}) := \frac{\rho(T_{\text{gas}}) \cdot D_{\text{bead}} \cdot v_{\text{hot}}(T_{\text{gas}})}{\mu_{\text{air}}(T_{\text{gas}})}$$

Whitaker for sphere, all evaluated at T_{inf} except μ_s at surface temperature. Shaddix has arguments for using cylinder too.

$$\text{Nu}_{\text{dsph}}(T_{\text{gas}}) := 2.0 + \left(0.4 \cdot \text{Re}_d(T_{\text{gas}})^{.5} + 0.06 \text{Re}_d(T_{\text{gas}})^{.6666667} \right) \cdot \text{Pr}^{.4} \cdot \frac{\mu_{\text{air}}(T_{\text{gas}})}{\mu_{\text{air}}(T_{\text{bead}})}$$

$$\text{Nu}_{\text{dsph}}(1300\text{K}) = 2.31$$

$$h_{\text{sph}}(T_{\text{gas}}) := \frac{\text{Nu}_{\text{dsph}}(T_{\text{gas}}) \cdot k_{\text{air}}(T_{\text{gas}})}{D_{\text{bead}}}$$

$$q_{\text{conv}}(T_{\text{gas}}) := h_{\text{sph}}(T_{\text{gas}}) \cdot (T_{\text{gas}} - T_{\text{bead}}) \quad q_{\text{conv}}(1300\text{K}) = 5.681 \times 10^4 \frac{\text{kg}}{\text{s}^3}$$

Radiation values

Shaddix suggested a range of 0.20-0.25 at 1500 K based on measurements that $\epsilon(760\text{K})=0.14$ and rises 0.010-0.015 per 100K. This would be for fresh TC. Emissivity goes up from there. This is somewhat of a shot in the dark, values for similar metals are all over the place. It's also highly dependent on how oxidized it is (which depends on length of use and conditions), how rough it is, etc.

$$\epsilon_{\text{ww}}(\text{temp}) := \left(0.14 + .0125 \cdot \frac{\text{temp} - 760\text{K}}{100\text{K}} \right) \quad \epsilon(1500\text{K}) = 0.233$$

$$\sigma := 5.67 \cdot 10^{-8} \frac{\text{W}}{\text{m}^2 \cdot \text{K}^4} \quad T_{\text{view}} := 50^\circ\text{C}$$

$$q_{\text{rad}}(T_{\text{gas}}) := \sigma \cdot \epsilon(T_{\text{gas}}) \cdot (T_{\text{gas}}^4 - T_{\text{view}}^4)$$

$$q_{\text{rad}}(1300\text{K}) = 3.347 \times 10^4 \cdot \frac{\text{W}}{\text{m}^2}$$

Find corrected gas temperature

$$\text{Given } T_{\text{guess}} := 1900\text{K} \quad q_{\text{rad}}(T_{\text{guess}}) = q_{\text{conv}}(T_{\text{guess}}) \quad T_{\text{gas}} := \text{Find}(T_{\text{guess}})$$

$$T_{\text{correction}} := T_{\text{gas}} - T_{\text{bead}} \quad T_{\text{gas}} = 1.27 \times 10^3 \text{K}$$

Summarize solution

$$\mu_{\text{air}}(T_{\text{gas}}) = 4.811 \times 10^{-5} \frac{\text{kg}}{\text{m} \cdot \text{s}} \quad \mu_{\text{air}}(T_{\text{bead}}) = 4.734 \times 10^{-5} \frac{\text{kg}}{\text{m} \cdot \text{s}} \quad \text{Re}_d(T_{\text{gas}}) = 0.576$$

$$v_{\text{hot}}(T_{\text{gas}}) = 0.578 \frac{\text{m}}{\text{s}} \quad T_{\text{gas}} = 996.821^\circ\text{C} \quad T_{\text{correction}} = 34.821\text{K}$$

Corrected temps at other bead temperatures: 1036 at 2 cm 1023 at 4 cm 997 at 6 cm

C. MANZANITA SINGLE-LEAF EXPERIMENTS AT TWO TEMPERATURES

Eastwood's Manzanita (*Arctostaphylos glandulosa*) leaves were burned at two temperatures to investigate the effect of convection temperature on flame properties. Volumetric flow rates to a porous flat-flame burner were set to the values in Table C-1 for two burn conditions.

Table C-1. Gas flow rate settings for standard and low temperature flat flame burner conditions at 300 K

Condition	Instrument flow rates (L/min)				Actual (adjusted) flow rates (L/min)				Equivalence ratio
	Air	N ₂	H ₂	CH ₄	Air	N ₂	H ₂	CH ₄	
Standard	300	0	35	35	353	0	33	15	0.63
Low temp	200	80	30	20	235	37	27	8	0.61

Uncorrected thermocouple temperatures at approximately 5 cm above the surface of the flat-flame burner were approximately 940 °C for the standard condition and 820 °C for the low temperature condition. Correcting for radiation, values of 972 °C and 841 °C were calculated, respectively (see Appendix B). At the post-flame gas temperature and assuming plug flow, gas velocities were calculated as 0.57 m/s and 0.39 m/s for the standard and low temperature conditions, respectively.

Twenty leaves were selected for each condition. However, every fifth leaf, beginning with the third, was weighed and dried (rather than burned) to track the moisture content throughout the experiment. This left 32 leaves for 16 burns at each condition. The first eight

leaves were burned at the standard condition, followed by 16 leaves at the low temperature condition, and finally eight leaves at the standard condition.

A general description of the experimental methods and setup can be found in Chapter 6 and Figure 6-2. Each leaf was clipped with the long axis oriented vertically above the burner, with the stem pointed down and located approximately 2 cm above the resting position of the burner surface. The burner was then rolled underneath the leaf to commence heating. Leaf mass, gas temperature, and video images were recorded throughout each burn.

Moisture content did not decrease with run number, though it did slightly decrease with thickness. This can be explained by that fact that during the period between sample collection and burning, moisture content was slowly lost. During that time, the shortest route of moisture release was through the thickness of the leaf, making thickness the best predictor of moisture loss. The thinner leaves lost a greater portion of their moisture. In contrast, all 32 leaves were burned within 32 minutes, providing relatively little time for moisture loss between burns.

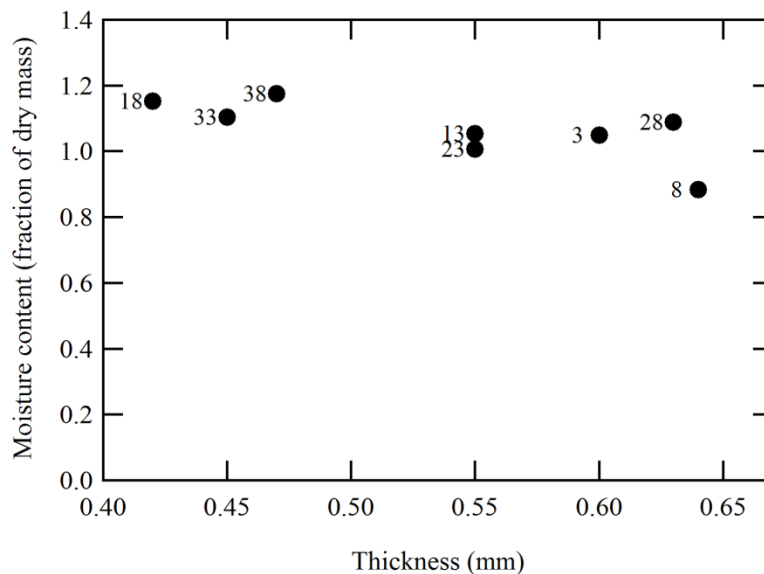


Figure C-1. Moisture content of leaves sampled between burns, labeled by leaf number. Moisture content is plotted as a fraction (i.e. 1 = 100% MC).

Flame parameters were identified for each run, including time of ignition t_{ig} , maximum flame height $h_{f,max}$, time of maximum flame height t_h , and time of burn out t_{bo} . These values were averaged for all runs in each group and are plotted in Figure C-2.

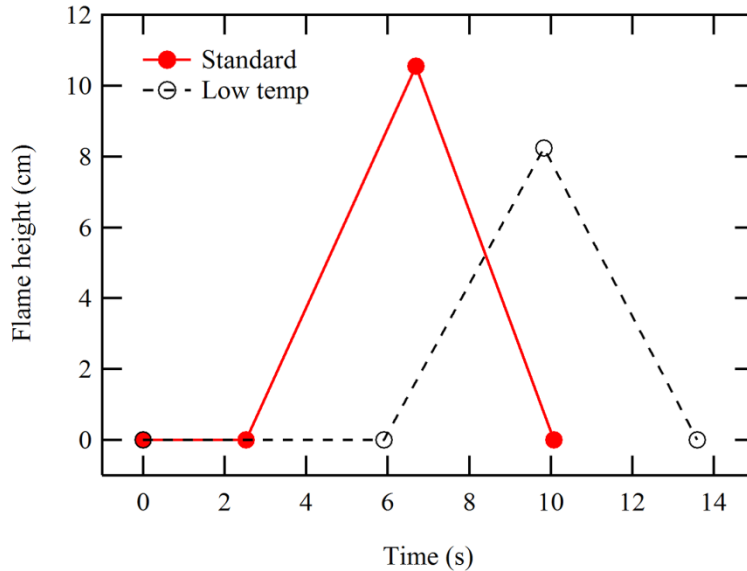


Figure C-2. Flame profiles from average flame parameters for standard and low temperature conditions, showing ignition, maximum flame height, and burn out (straight lines between averaged points).

The expectation was confirmed that the low temperature condition would result in a slower burn and a shorter flame height. A Student's (two-tailed) t-test was used to test the statistical significance of the differences observed in average flame parameters (significance level of 0.1). In each case, the null hypothesis (of no difference) was rejected with 90% confidence: t_{ig} ($P = 4.7 \cdot 10^{-9}$), t_h ($P = 0.001$), t_{bo} ($P = 0.005$) and $h_{f,max}$ ($P = 0.097$).

In summary, based on 32 burns divided between two burn conditions, flame parameters responded as expected to hotter and higher velocity convection. Differences in all flame parameters were statistically significant (with 90% confidence). Similar experiments could be used to further explore the effects of heating conditions on flame properties and to improve and validate physical combustion models such as that presented in Chapter 8.

D. LEAF CLUMP EXPERIMENTS

A total of 32 burn experiments were performed on branches with attached foliage of manzanita (*Arctostaphylos glandulosa*). These results were analyzed to examine the burning behavior of attached foliage.

Whole branches or branch segments were clipped from live manzanita shrubs from the region surrounding Riverside, California by the Pacific Southwest Research Station of the USDA Forest Service and shipped overnight to the burn facility at BYU. Branches were about 16 inches long with intact foliage. These branches were then divided into segments by removing secondary branches at their forks, resulting in approximately 10 segments per shipped branch. Segments with minimal foliage were avoided where possible, but occurred more frequently near the base of the parent branch. Parent branches with a set of subdivided segments are shown in Figure D-1.



Figure D-1. Parent branch as shipped from Riverside, CA and segments resulting from cutting.

Segments were characterized by their mass, branch thickness in middle (in the case of a forking stem, the average of both in the middle was used), branch length and leaf count (excluding budding leaves with a width less than or equal to 5 mm). Each leaf was then characterized by its length, width and thickness. If the number of leaves on a branch became a significant measurement burden, the leaves were visually divided into size classes and a representative leaf was measured for each class and recorded with the number of leaves it represented. Each branch was then clipped into a rotatable stand with a dial marked at 0° , 90° , 180° and 270° and photographed from each angle. A tape measure was placed in view at the same field depth as the sample to determine scale.

D.1 Leaf settling of manzanita leaves connected to branches

Manzanita leaves attached to their branches shift downward during preheating and combustion. Prior to combustion, most manzanita leaves are oriented upwards within 45° of vertical (measuring from the stem to the leaf tip). Before and after ignition, leaves pivot on their stems, extending first horizontally, away from their associated branch, and frequently continue

downward. As the leaves near burn out and afterwards, they typically recoil partway to their original position. The sequence of images shown in Figure D-2 demonstrates this behavior. This behavior is likely to occur because the outward face of the stem is more exposed to the heating, and thus dries, burns and contracts ahead of the shielded, inward face of the stem.



Figure D-2. Leaves on manzanita branch dip then recoil. Red lines track movement of two leaves.

Leaf movement during the combustion of branch segments has important implications for the design and interpretation of single-leaf experiments. Single leaf experiments have traditionally been designed to hold a leaf in a fixed position. Leaves are held either vertically or horizontally. Vertically-oriented leaves best describe the early stages of heating and combustion. Horizontally-oriented leaves are a good representation of the average position of leaves during the majority of the combustion process. An improvement on both orientations can be made by preserving a leaf's stem material and clipping the base of the stem such that the leaf is held at an average natural orientation and is free to move as the leaf and stem heat and contort.

These patterns of leaf movement promote sustained fire spread and should be considered in flame spread models which calculate flame-fuel overlap. As leaves reach out away from their branch during combustion, they are more likely to ignite leaves from neighboring branches, which are often positioned across a narrow fuel gap (see Figure D-3).



Figure D-3. Voids between branches of manzanita shrub are narrow.

As the leaves move downward they are more likely to heat and ignite lower leaves. Furthermore, in single leaf experiments, horizontally-oriented leaves produced flames which extended significantly lower than did vertically-oriented leaves. To accurately model fire spread by flame-fuel overlap, these details must be appropriately considered.

D.2 Heat shielding of upper, interior leaves

Lower and outer leaves on a manzanita branch ignite before upper and central leaves when burned in the FFB. Two examples of this behavior are given in Figure D-4. In run 1, (see Figure D-4 1a to 1c), a small branch with only six leaves was burned. While heating to ignition, the bottom leaves shielded the upper leaves from intense convective heating. The upper leaves were then exposed to the flames of the lower leaves and subsequently ignited (see Figure D-4 1b). These continued burning after the shielding leaves burned out (see Figure D-4 1c). This behavior was nearly identical in the second run with 59 leaves (see Figure D-4 2a to 2c). The shielding leaves for the second run consisted of the leaves along the exterior of the bottom and sides of the branch. In both runs, shielded leaves resisted ignition for over 9 seconds while the

shielding leaves ignited after only five seconds of heating. This behavior should be properly represented in flame spread models which calculate flame-fuel overlap.

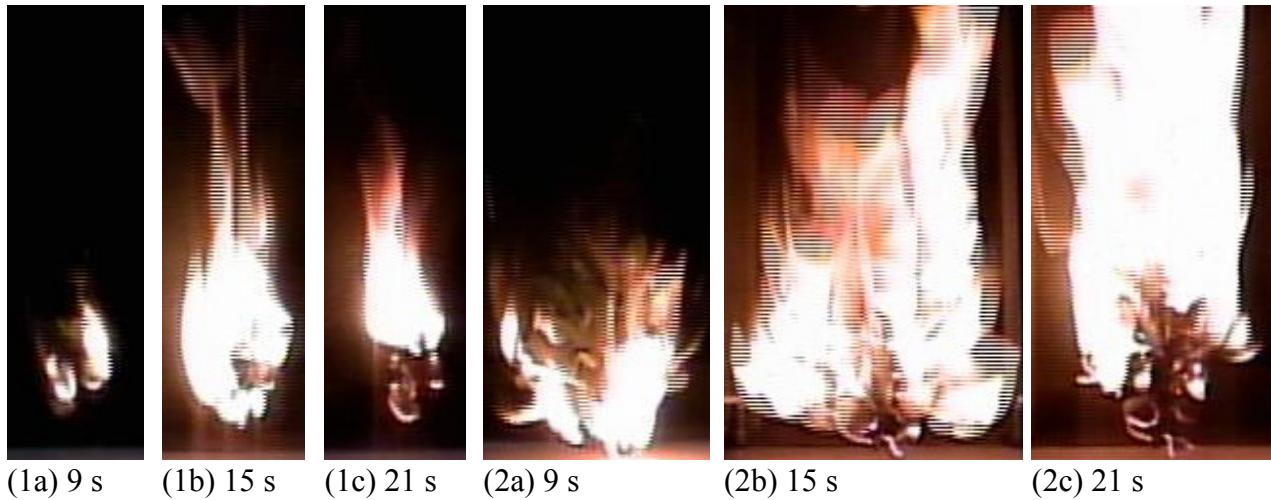


Figure D-4. Manzanita branches at 34% moisture content burned above the FFB. Run 1 (a, b, c) had 6 leaves and run 2 (d, e, f) had 59 leaves. Time is given from the beginning of heating.

D.3 Correlating leaf placement to maximum flame height

Branches with attached foliage were used to quantify the grouping effects of multiple leaves on burn behavior. Several sets of samples were burned at a variety of moisture contents. Photos taken from multiple angles were used to map leaf locations.

A Matlab script was developed to map the location of all visible leaves. Based on the user clicks in all four pictures, the pictures were rotated and scaled so that the physical axis of rotation was vertical and all pictures in a set were at the same pixel to centimeter scaling. A common point on the axis of rotation was selected as an origin. The user then clicked the same leaf from two orthogonal angles, providing its three-dimensional location. This point was then automatically mapped and marked on all images, helping the user to not double-count or miss a leaf. After marking all leaves, leaf locations, in centimeters, were written to a spreadsheet for further analysis. A branch with foliage compared to the identified leaf locations is shown in

Figure D-5. Pictures from two additional angles (180° and 270°) were used to identify leaf locations, reducing the number of leaves blocked from view.

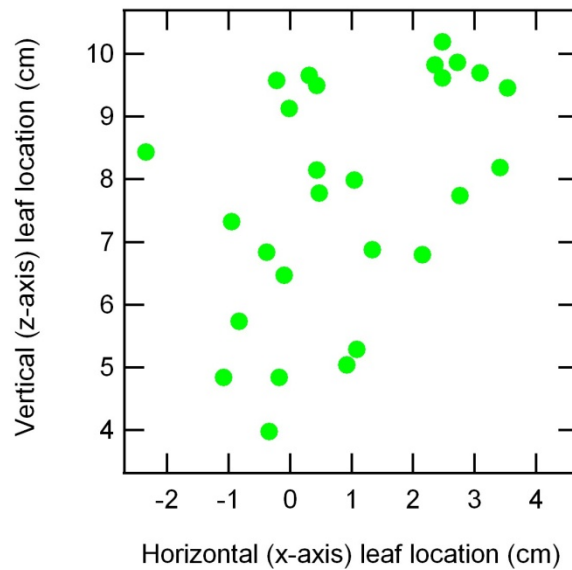
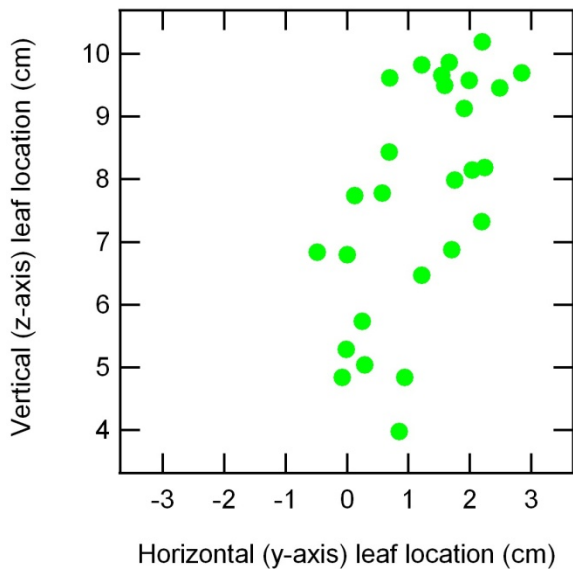


Figure D-5. Example of foliage location mapping for a manzanita branch, showing views at 0° (left) and 90° (right) and omitting 180° and 270°.

Leaf positions were then analyzed to find a correlation between the distribution of their locations and their burn characteristics. Two sets of experiments, each consisting of 11 runs,

were then used to explore the relationship between leaf location and burn characteristics. Preliminarily, only flame height has been analyzed. Using the first set of 11 runs, the parameters for max merged flame height observed $h_{f,max}$ (Equation D-1) were fit:

$$h_{f,max} = a + b \cdot n_L \cdot \log(c \cdot \sigma) \quad (D-1)$$

where a , b and c are fitting parameters, n_L is the number of leaves, and σ is the standard deviation of distances between the center of each leaf and the “origin,” which was selected as a point on the main stem near its base. At the time of writing this dissertation the exact values of a , b , and c , were lost. However, the the comparisons were still available and the form of the equation may still be useful for future research. This first attempt resulted in a good fit of the data ($R^2 = 0.71$ for the fitting set of data and $R^2 = 0.64$ for the second set which was not using for coefficient estimation). The model and the data are shown in Figure D-6. Other combustion characteristics are still being analyzed.

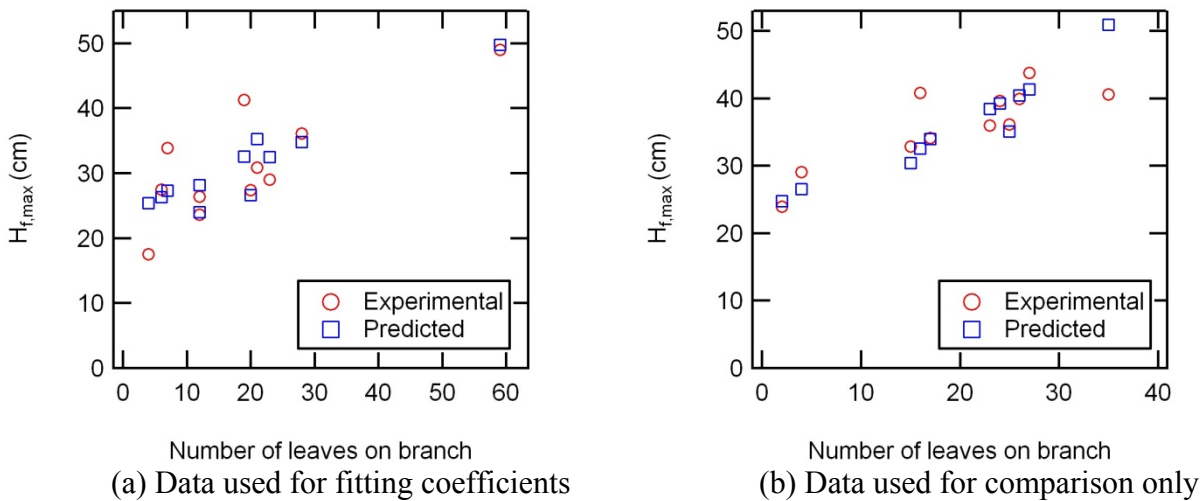


Figure D-6. Total merged flame height experiments and model, model coefficients fit to set (a) only.

E. MULTI-LEAF COLUMN AND PLANE FIRE PROPAGATION EXPERIMENTS

Fire spread experiments were designed to examine fire behavior at a small scale. Manzanita leaves (*Arctostaphylos glandulosa*) were arranged in two ways. In the first, leaves were placed in a vertical column. In the second, a 16 by 20 array of horizontally-oriented leaves were fixed 3.5 cm above an aluminum-covered foam board.

E.1 Single column experiments

A single column of clips were attached at 3 cm intervals to a board. The clips were attached so that they could rotate, allowing both horizontal and vertical orientation of leaves. Leaves were clipped in a vertical column with the width dimension of the leaf always oriented normal to the board.

Four experiments were performed. In the first experiment (see Figure E-1), 30 leaves (11% MC) were placed in a face up orientation. A butane lighter was held below the bottom leaf to ignite it. The bottom leaf burned slowly but did not ignite the leaves above it.

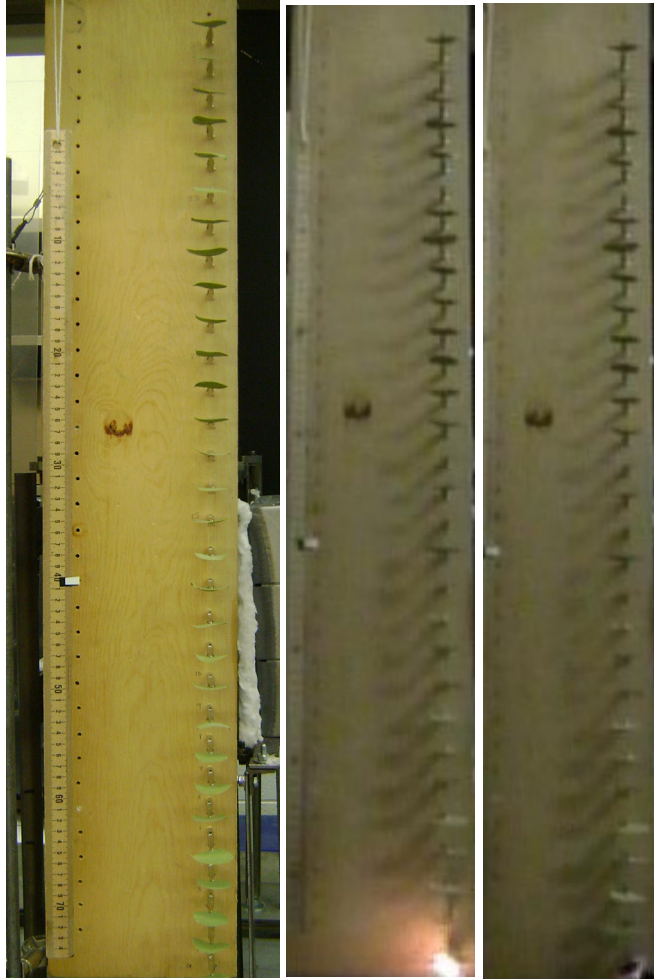


Figure E-1. Horizontally-oriented leaves in a vertical column. Left: prior to flame contact. Center: at start of heating (0 s). Right: at burn out (26 s).

In the second experiment (see Figure E-2), the leaves were oriented with their length direction aligned vertically. The lighter was held under the bottom leaf and the fire spread marginally, scorching the bottom seven leaves. Most of the bottom seven leaves were only partially burned.

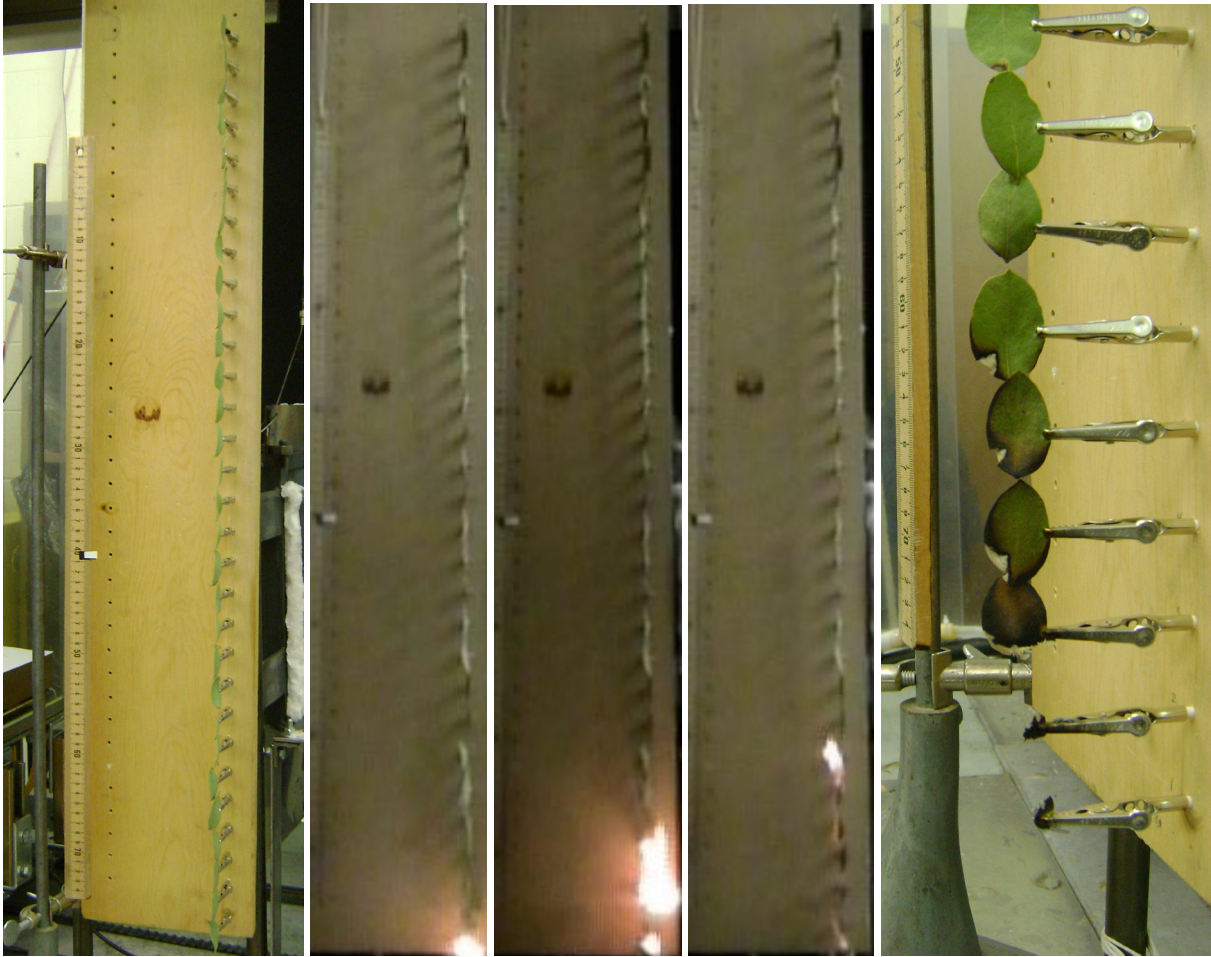


Figure E-2. Vertically-oriented leaves in a vertical column. From left to right: prior to flame contact, start of flame contact, 20 s of heating, 40 s of heating (1 s before burn out), and after burn out.

In the third experiment, the same setup as the second experiment was repeating but with the hood off to reduce air drafts, but the same behavior was repeated. The leaves burned in the fourth experiment were allowed to dry out at room temperature, reaching 3% MC. This experiment was not video recorded. With the same leaf orientation as experiments two and three, the fire propagated from the bottom to the top leaf.

In conclusion, vertically-oriented leaves provided better fire spread up the vertical column than horizontally-oriented leaves, and very low moisture content was required to produce sustainable flame propagation up the column under these laboratory conditions.

E.2 Skewed leaf experiments in a plane

Manzanita leaves were pinned horizontally on an array of vertical needles to make a horizontal plane of leaves. Needles were set in a 16 by 20 grid with 2 cm spacing in both directions. Needles were inserted through an aluminum foil-covered foam board with their tips extending approximately 3.5 cm above the surface of the board (Figure E-3). The aluminum foil was intended to protect the foam from burning or melting. The board and foil in the 20-needle long direction included a break after 10 needles that allowed the two sides to be separated by any spacing in order to investigate the ability of fire to cross a fuel gap.

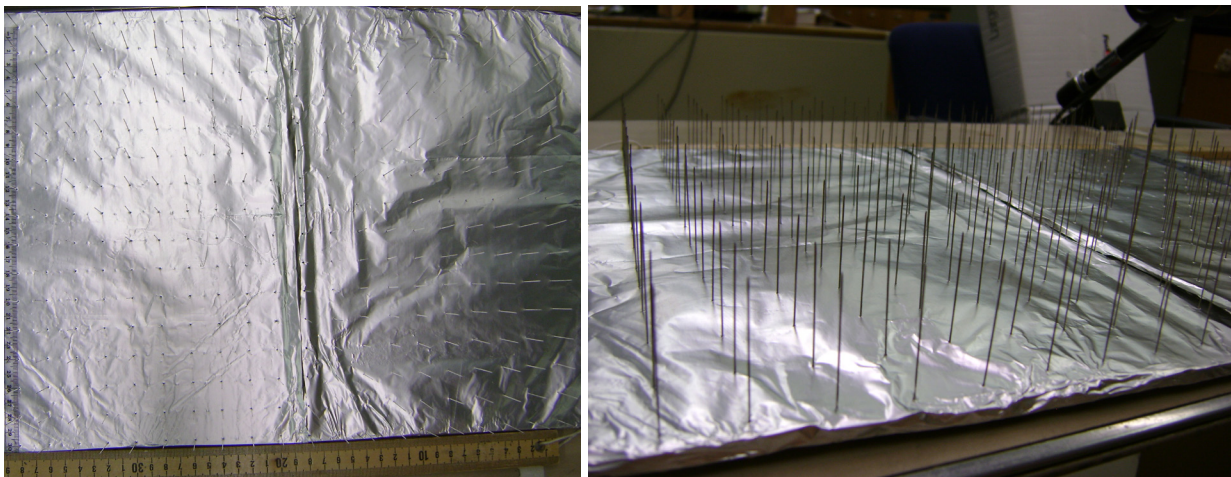


Figure E-3. Array of needles emerging from an aluminum foil-covered foam board (left: top view; right: perspective).

A leaf was pressed onto the top of each needle. An aluminum trough approximately 2 cm wide, 2 cm deep and 34 cm long was made. This trough was placed along the 16 leaf edge of the array, filled with ethanol, and ignited to initiate fire spread (Figure E-4). The first skewered leaf experiment had a moisture content of 60.82% (dry basis) and is shown in at ignition in Figure E-4 and after extinguishing in Figure E-5. Burning extended little beyond the reach of the

alcohol ignition trough. Unburned leaf material near the edge of the burned material showed yellowing due to heat exposure.



Figure E-4. Ignition of skewered leaf plane Experiment 1 using an alcohol trough.

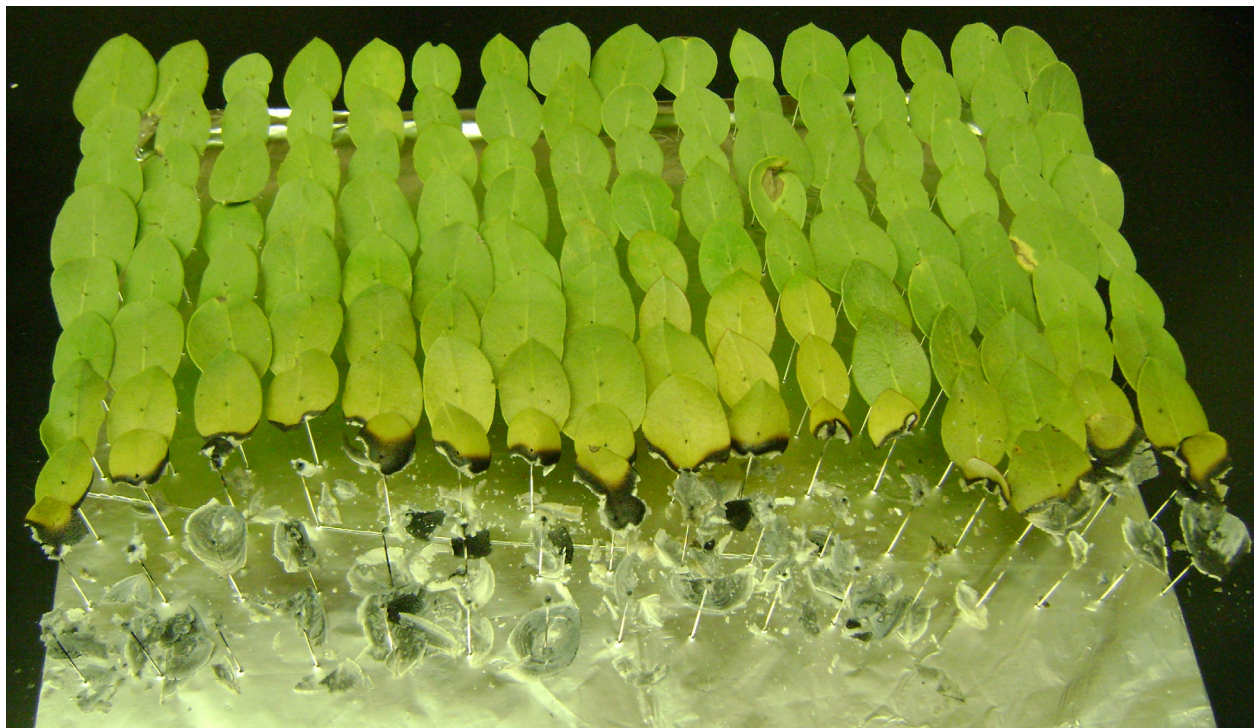


Figure E-5. Skewered leaf plane Experiment 1 after extinguishing (first panel only).

A second experiment was performed with a gap between the two panels of 1.5 cm (or a total spacing between needles at the gap of 3.5 cm). Leaves were dried at room temperature to 3.1 % MC before burning to ensure fire spread. The experimental fuel array is shown in Figure E-6 and ignition with an alcohol trough in Figure E-7. The white hanging marker is 10 cm long.



Figure E-6. Skewered leaf Experiment 2 with a 1.5 cm gap prior to ignition.

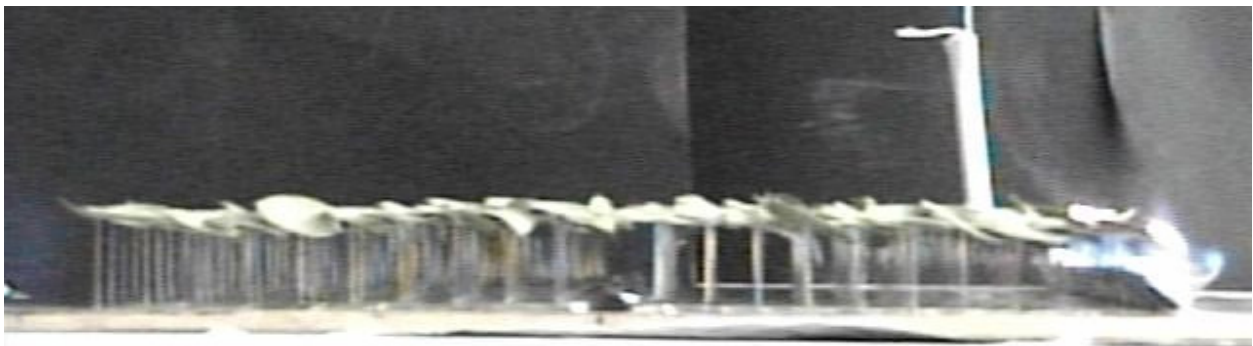


Figure E-7. Skewered leaf Experiment 2 at ignition of the alcohol trough.

The ignition of the first leaves is shown in Figure E-8 followed by burning through the first panel of leaves (the first 16 by 10 leaves) in Figure E-9. Flame extension below the level of the leaves is visible in both Figures. Downward fire extension is an important phenomenon for fire spread.

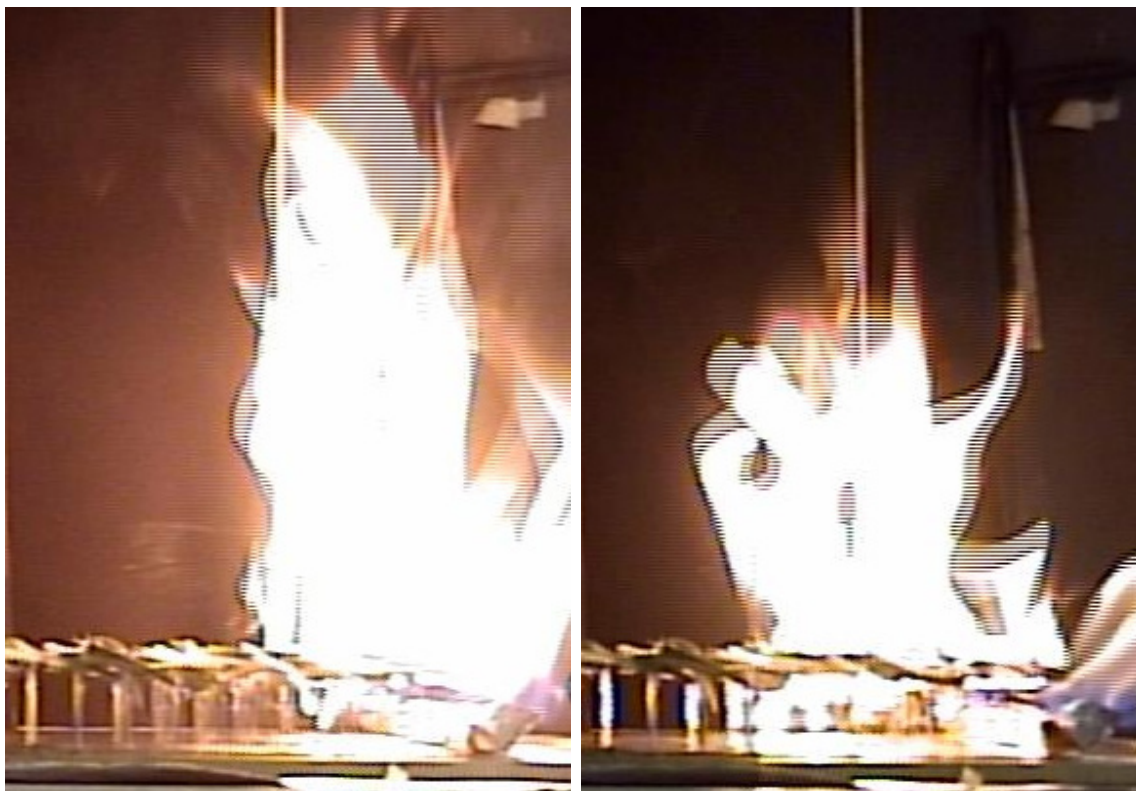


Figure E-8. Skewered leaf Experiment 2 during early burning.



Figure E-9. Skewered leaf Experiment 2 showing flame extension below the leaf surface before fire crosses the 1.5 cm gap.

The fire front is shown crossing the gap in Figure E-10 with additional views of fire extension beneath the level of the leaves. Finally, the burned fuel array is shown in Figure E-11.



Figure E-10. Skewered leaf Experiment 2 showing flame extension below the leaf surface while fire crosses the 1.5 cm gap.

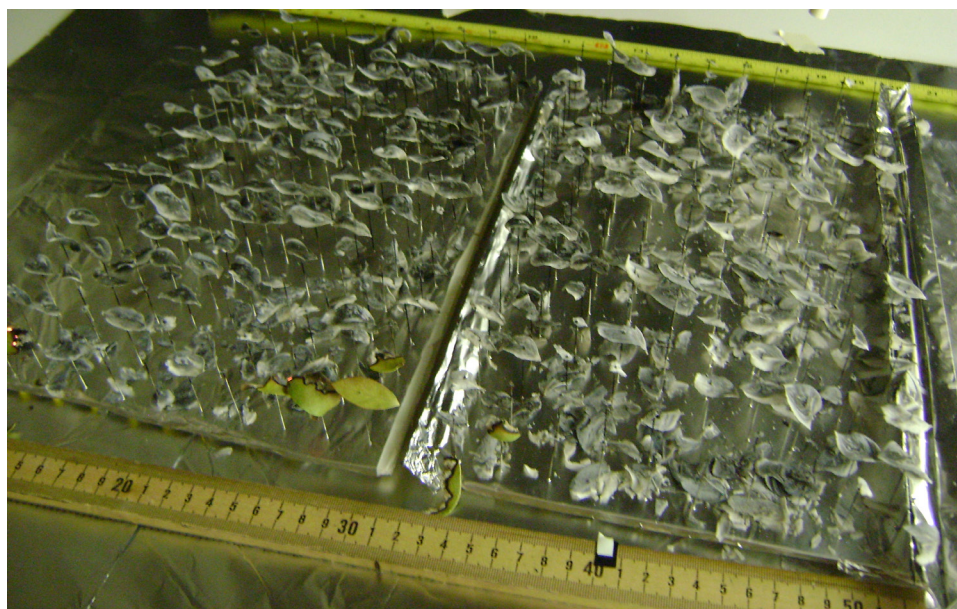


Figure E-11. Skewered leaf Experiment 2 after fire is extinguished.

Experiments performed at this level of complexity provide a rich context for examining fire behavior and for comparing model simulations.

F. IMPROVED BUSH MODEL CODE (MATLAB)

This MATLAB code is the improved bush model discussed in Chapter 8.

```
function BushModel
%NOTE: t_fd has been replace by t_bo in this version to match definitions
% Setup
clear; close all; summary = single([]);
for repetitions = 1:30
    g = 9.81;

% Model settings
    dt = 0.2; % s (time step)
    dt_p = 1; % plot every ith dt (integer)
    save_csv = 0;
    if repetitions >= 25
        plots = 1; % make plots (slower) 1 = yes, 0 = no
        showFlames = 1; % show flames in 3D plot: 1 = yes, 0 = no
        save_figs = 1; % save 3d patch images?: 1= yes, 0 = no
    else
        plots = 0; % make plots (slower) 1 = yes, 0 = no
        showFlames = 0; % show flames in 3D plot: 1 = yes, 0 = no
        save_figs = 0; % save 3d patch images?: 1= yes, 0 = no
    end
    aFr = 1.22; % for Albin Froude number flame angle
correlation (Albin)
    bFr = 0.5; % for Albin Froude number flame angle
correlation
    T_weather = 300; %K temperature away from fire
    T_igzone = single(1273.15); %ignition zone temperature, default--possibly
modified in run_details

% Simulations details
for situation = 1:4
    tic
    rng('shuffle')
    m = single([]);
    U_bulk = m; n_fuels = m; m_dry = m; MC = m; globule = m;
    left_bound = m; top_bound = m; image_name = m;
    x_fuels = m; y_fuels = m; z_fuels = m;
    x_domain = m; y_domain = m; z_domain = m;
    th = m; w = m; l = m; t_ig = m; t_h = m; t_bo = m; h_f = m;
    t_ig_base = m; t_h_base = m; t_bo_base = m; h_max_base = m;
    t_base = m; F_base = m; kin_scale_t = m; kin_scale_H = m;
    h_f_s = m; h_f_group = m; h_max = m; h_scale = m; t_rxn = m; rF = m;
    stage1 = m; stage2 = m; stage3 = m; stage4 = m; n_stage3 = m;
    U = m; x1 = m; x2 = m; x1_fuels = m; x2_fuels = m; %xF1 = m;
    y1 = m; y2 = m; z1 = m; z2 = m; z1_fuels = m; z2_fuels = m;
```

```

theta = m; dF = m; V = m; speed_pairs = m; speed_pairs_temp = m;
t_index = m; t_tab = m; f_burned = m; f_preheating = m; f_burning = m;
h_scale_avg = m; h_f_mean = m; h_f_s_mean = m; h_f_max = m; h_f_p_max =
m;
Dh_f = m; DH_f = m; max_FH = m;

if save_figs == 1; mkdir([pwd '/figs_' num2str(situation) '_'
num2str(repetitions)]); end

run_details % include all run-specific details here, sets
locations, fuel properties
physical_properties % assigns physical, local wind, burn
properties to each fuel element
flame_properties
initialize % initialize burning, other parameters
while burning == true
    flameUpdate3
    stageUpdate
    outputLoop
    t = t + dt;
% % % if mod(round(t*10)/10,10)==0 && t>9
% % % scaleFire
% % % end
burning = (sum(burn_stage==3) + sum(burn_stage==2)) > 0; %stop
condition

end
outputBurn
end %situation
end %repetitions
disp(summary)
if save_csv==1
    csvwrite(['ALL_case_rep.csv'],summary,1,0)
end

%%
function physical_properties
    % fuel properties

    % Mass
    a = single(3.87297342448949);
    b = single(9.28275998422041);
    mMin = single(0);
    mMax = single(0.47);
    m_dry = single((betainv(rand(n_fuels,1),a,b)).*mMax); %gm (dry
mass)
    m = single(m_dry*(MC + 1)); %gm
    (total mass)

    % Width
    mu_w = 1.31751063750442 + 2.80135108631734*m;
    se_w = 0.235879787099019;
    w = single(.01*norminv(rand(n_fuels,1),mu_w,se_w)); %m

    % Thickness
    mu_th = 0.643359449523647 + 1.15956933135836*m -
100*0.214205603653271*w;

```

```

se_th = 0.0657664166567882;
th = single(0.001*norminv(rand(n_fuels,1),mu_th,se_th)); %m

% Length
mu_l = 3.35668230360503 + 3.86425923934776*m -
100*0.164938644004346*w - 1000*1.07122472144737*th;
se_l = 0.323286506334316;
l = single(0.01*norminv(rand(n_fuels,1),mu_l,se_l)); %m
end

function flame_properties
% Fluid flow model
U = U_bulk*ones(n_fuels,1);
% U = U_bulk.*(0.38.*(z_fuels./z_domain).^2 +
0.29.*(z_fuels./z_domain) + 0.33);

% main quantities
t_ig = single((-3.316 + 4.265.*MC + 7.372.*th.*1000 + 3.69.*m));
%ignition time, s (preheat time)
t_h = single(-3.32 + t_ig + 8.11.*MC + 11.06.*th.*1000 + 4.71.*m);
%max flame height time, s
t_bo = single(3.77 + t_ig + 12.24.*th.*1000 + 15.0.*m +
1.307.*log(MC)); %flame duration, s
h_max = single((8.22 - 2.12.*U + 26.38.*m_dry - 2.74.*th*1000 -
8.59.*m)*0.01); %max flame height, m

% adjust main quantities to prevent problems
t_ig(t_ig<0.1) = 0.1;
t_h(t_h<0.2) = 0.2;
t_bo(t_bo<0.3) = 0.3;

% set theta for flame as tall as shrub
if isempty(h_f_group)
h_f_group = max(z_fuels)-min(z_fuels);
end
tan_theta = ((U>=0).^2 - 1).*aFr.*(U.^2./(g.*(h_f_group))).^bFr; %
measured from vertical, run/rise
theta = atan(tan_theta);

% disp([mean(t_ig) mean(t_h) mean(t_bo) mean(h_max)])
scaleFire % kinetically scale fire behavior
% disp([mean(t_ig) mean(t_h) mean(t_bo) mean(h_max)])
end %fuel_properties

%%
function flameUpdate3
% Modular shrub fire sperad model BETA
% Started 9/5/2012 by Dallan Prince
% FUEL ELEMENT FLAME UPDATE script
% for Manzanita

% This versions uses the distances, compare v. 5

% flame height (singular flame height)
h f s = (burn_stage==3).*...

```

```

        ((t_rxn<=t_h).*h_max./(t_h - t_ig).* (t_rxn - t_ig) ...
        + (t_rxn>t_h).*h_max./(t_bo - t_h).* (t_bo -
t_rxn)).*(1+(rand(n_fuels,1)-.5)*.8 ); %single/unmerged flame with 40% +/-
intermittency
        h_f_s(h_f_s<0)=0; % (shouldn't happen but has when flame properties
change midrun, but I'm fixing that by also updating t_rxn)

        % flame radius (h_scale currently based on previous time step or
initialization)
        rF = h_f_s.*((h_scale-1)/1.1 + 1)/2/4.5;
        rF = h_f_s/2/4;
        rF = h_f_s./(1.1+h_scale.^8)*(1.7/V)^.25;
        % % % %
        rF = h_f_s./(.5+h_scale.^1).*kin_scale_H.*(1.7/V)^.9;
        rF =
h_f_s./(2.1)./h_scale.^0.32;%./(h_scale.^1);%.*kin_scale_H.*(1.6/V)^0;

        % flame down (h_scale currently based on previous time step or
initialization)
        dF = h_f_s.*1/2/2.4;
        % %
        dF = h_f_s./(1.1+h_scale.^5)*(1.7/V)^.25.*kin_scale_H;
        % % % %
        dF = h_f_s./(.5+h_scale.^1).*kin_scale_H.*(1.7/V)^.9;
        % dF = h_f_s./(.6+h_scale.^3).*kin_scale_H.*(1.7/V)^1.2;
        %
        dF = rF;
dF = h_f_s./2.1./h_scale.^0.25;
        % flame base location
        % x_shift % shift base of flame based on wind
        x_sh = zeros(n_fuels,1);
        x1 = x_fuels(stage3) + x_sh(stage3); % flame ends WITH wind shift
        y1 = y_fuels(stage3);
        z1 = z_fuels(stage3); % used as flame source, below

        % FLAME INTERACTION SIZE UPDATE, based on Weng, adapted by Dallan
Prince
        globs = zeros(n_stage3,1); %may expand as needed
        Lf_L1 = ones(n_stage3,1);
        ln_inc = (log((2:n_stage3)./(1:n_stage3-1)))';
        for i3 = 1:n_stage3
            % Coalescence (see Weng)
            % flame angle "vertical". But, also consider role of buoyancy
            Dxy = ((x1-x1(i3)).^2 + (y1-y1(i3)).^2).^0.5;
            rr = rF(stage3(i3)) + rF(stage3);
            SxyD = (Dxy-rr)./rr;
            SxyD(SxyD<0)=0;
            Lf_old = max(max(h_f_s(stage3),h_f(stage3)),.0001);
            DzLf = (z1-z1(i3))./Lf_old;
            S3D_hat = (SxyD.^2 + DzLf.^2).^0.5;
            S3D_sort = sort(S3D_hat);
            merge_crit = (n_stage3^0.5)/2; %based on Fig 6, where for 2x2
array, S/RR > 1 didn't add to, and for 4x4, S/RR>2 didn't help. So, that's
(N^0.5)/2
            indj = find(S3D_hat < merge_crit);
            ijlist = stage3(indj);
            if isempty(indj) || length(indj)==1
                Lf_L1(i3) = 1; %flame is essentially solitary
            else
                Lf_L1(i3) = (V/1.6)^2.4*sum(0.7*ln_inc(1:length(indj)-1) ./(1

```

```

+ 1*S3D_sort(2:length(indj))) + 1;
end

% GROUP FLAME HEIGHT (first make the groups)
if length(indj)>1
    looking=1;
else
    looking=0;
end
glob=zeros(n_stage3,1);
glob(indj)=1;
ig0 = 1;
while looking == 1 %form globs
    if sum((globs(:,ig0)==glob).*(globs(:,ig0)==1))>0 ||
sum(globs(:,ig0))==0
        globs(indj,ig0)=1;
        looking = 0;
    elseif size(globs,2)==ig0 %if no next column, drop into new
column
        globs(:,ig0+1)=glob;
        if size(globs,2)>5
            collect_globs
        end
        looking = 0;
    else %check next column
        ig0 = ig0+1;
    end
end

end %i3 = 1:n_stage3
Lf_L1(isnan(Lf_L1)) = 1;
Lf_L1(Lf_L1<1) = 1;
h_scale = ones(n_fuels,1);
h_scale(stage3) = Lf_L1;
h_f = h_scale.*h_f_s; % merged flame height
% GROUP FLAME HEIGHT, for determining flame angle ONLY
collect_globs
function collect_globs
    szg = size(globs,2);
    for ig1 = szg:-1:2
        for ig2 = ig1-1:-1:1
            if sum((globs(:,ig2)+globs(:,ig1))>1)>1
                globs(:,ig2) = globs(:,ig2)+globs(:,ig1);
                globs(:,ig1) = 0;
            end
        end
        globs(globs>1)=1;
    end
    if size(globs,2)>1
        globs(:,sum(globs)==0)=[];
    end
end

% disp(sum(globs)) %check to make sure globs is making groups like
you see them
if sum(sum(globs))>0
    globs = globs(:,sum(globs)>0);
end

```

```

globs = logical(globs);
indvec = cumsum(ones(length(globs),1));

% h_f_group is to be used for flame angle/froude number calculations
only!
h_f_group = h_f; % reset the group flame heights to zero
% h_f_group(stage3) = h_f(stage3); % replace burning leaves flame
heights with their coalesced flame heights
[~,c_g] = size(globs); % how many flame groups there are
for i = 1:c_g % update to be true group flame height from bottom leaf
to top of top flame (exclude flame down)
    globule{i} = stage3(indvec(globs(:,i))); % store a flame height
group as a globule
end
for i = 1:length(globule)
    h_f_group(globule{i}) = max(z_fuels(globule{i}) +
h_f(globule{i})) - min(z_fuels(globule{i})); % replace individual flame
heights with group flame heights where flame is member of globule
end
if max(h_f_group)>10
    keyboard
    disp('20 m high flames, really?')
end

% flame angle by groups
tan_theta = ((U>=0).*2 - 1).*aFr.*(U.^2./(g.*(h_f_group))).^bFr; %
measured from vertical, run/rise
tan_theta(h_f_group==0)=0;
theta = atan(tan_theta);

% shift base of flame based on wind?
% x_shift
x_sh = zeros(n_fuels,1); %no shift ...zeros

% flame ends WITH wind shift
x1 = x_fuels(stage3) + x_sh(stage3);
y1 = y_fuels(stage3);
z1 = z_fuels(stage3) - dF(stage3);
y2 = y_fuels(stage3);
z2_fuels = z_fuels + h_f;
z2 = z2_fuels(stage3);

if U_bulk ~= 0
    x2_fuels = x_fuels + h_f.*tan_theta + x_sh;
else
    x2_fuels = x_fuels;
end

%pinch tops of flames together
for i = 1:c_g
% globule = stage3(indvec(globs(:,i))); % store a flame height
group as a globule
% globule = globule(globule>0); % remove blank (0) entries
x2_fuels(globule{i}) = (mean(x2_fuels(globule{i})) +
1.*x2_fuels(globule{i}))./2;
% refresh flame angle
tan_theta(globule{i}) = (x2_fuels(globule{i}) -

```

```

x_fuels(globule{i})./(z2_fuels(globule{i}) - z_fuels(globule{i}));
    theta(globule{i}) = atan(tan_theta(globule{i}));
end

x2 = x2_fuels(stage3);
x1_fuels = x_fuels + x_sh;
z1_fuels = z_fuels - dF;
X1 = [x1 y1 z1]; % bottom of flame coordinates
X2 = [x2 y2 z2]; % top of flame coordinates
X1_fuels = [x_fuels y_fuels z_fuels];
X2_fuels = [x2_fuels y_fuels z2_fuels];
X = [x_fuels(stage3), x_fuels(stage3) +
h_f(stage3).*tan_theta(stage3)];
Y = [y_fuels(stage3), y_fuels(stage3)];
Z = [z_fuels(stage3), z_fuels(stage3) + h_f(stage3)];
end %flame Update3

%%
function initialize
% ignition
t = 0; %s
burning = true;
t_rxn = zeros(n_fuels,1);

% ignition model
burn_stage = 3.*(x_fuels/x_domain <= left_bound).*(z_fuels/z_domain
<= top_bound); % bottom left corner
burn_stage(burn_stage==0) = 1;

t_rxn(burn_stage==3) = t_ig(burn_stage==3);

stage3 = find(burn_stage==3);
n_stage3 = length(stage3);

% % other quantities
% [theta_h_max, tan_theta_h_max] = flame_angle(U, h_max, g, aFr,
bFr);
% theta_h_max_mean = mean(theta_h_max);
% sideFlame_max = f_side(h_max, frac_side);
%
% % for flame interaction model
% flame_slope_h_max = 1 ./ tan_theta_h_max;
% flame_intercept = z_fuels - flame_slope_h_max .* x_fuels; %
initialize using h_max
% flame_interceptA = z_fuels - flame_slope_h_max .* (x_fuels - w/2 -
sideFlame_max);
% flame_interceptB = z_fuels - flame_slope_h_max .* (x_fuels + w/2 +
sideFlame_max);
%
% % for neighbors
% sideFlame_safe = h_max * 1;
% bottomFlame_safe = h_max * 1;
% flame_interceptA_safe = z_fuels - flame_slope_h_max .* (x_fuels - w
/ 2 - sideFlame_safe);
% flame_interceptB_safe = z_fuels - flame_slope_h_max .* (x_fuels + w
/ 2 + sideFlame_safe);
%

```

```

only!) % % initialize group flame height for (FA (froude #) calculation
h_scale = ones(n_fuels,1);
h_f_group = h_max;
h_f = zeros(n_fuels,1);
x2_fuels = x_fuels;
tan_theta = zeros(n_fuels,1);
speed_pairs = [];
speed_pairs_temp = [];
rng('shuffle');
end %initialize

%%
function stageUpdate
% Modular shrub fire sperad model BETA
% Started 9/12/2012 by Dallan Prince
% FLAME PROFILE REGULATOR: updates burn stage and advances fuel
elemen rxn time
% for Manzanita

%preheating updater
burn_stage(burn_stage == 2) = 1; % reset preheating to 1 then check
if preheating
stage3 = find(burn_stage == 3);
n_stage3 = length(stage3);

for ig = 1:length(globule)+1

if ig>length(globule)
group = setdiff(stage3,cell2mat(globule(:)));
rad_ok = 0; %don't do radiation, random leafs not in groups
else
group = globule{ig};
rad_ok = 1; %radiation okay because these are grouped
end
if ~isempty(group)
x1g = x1_fuels(group);
x2g = x2_fuels(group);
y1g = y_fuels(group);
y2g = y1g;
z1g = z1_fuels(group);
z2g = z2_fuels(group);
% Narrow considerations to flaming region
%these define a rectangular prism circumscribing the flame
% Find/define max/min x,y,z location of each flame
rFx = rF(group).*cos(theta(group));
xF1 = min(x1g,x2g) - rFx;
xF2 = max(x1g,x2g) + rFx;

rFy = rF(group);
yF1 = min(y1g,y2g) - rFy;
yF2 = max(y1g,y2g) + rFy;

dFz =
max(rF(group).*sin(theta(group)),dF(group).*cos(theta(group)));
zF1 = z1g - dFz;
zF2 = z2g + dFz;

```

```

        % n value is the root leaf index of all leaves in the
circumscribing prism
        % by applying max/min, we're looking at all leaves in 1 box
        % containing all flames
        nVal = intersect(find(burn_stage<2), find(x_fuels <
max(xF2)));
        nVal = intersect(nVal, find(x_fuels > min(xF1)));
        nVal = intersect(nVal, find(y_fuels < max(yF2)));
        nVal = intersect(nVal, find(y_fuels > min(yF1)));
        nVal = intersect(nVal, find(z_fuels < max(zF2)));
        nVal = intersect(nVal, find(z_fuels > min(zF1))); % nVal is
the list of fuels that could be ignited, like a temporary neighbors

        % this could be repeated on the level of a particular leaf if
desired in
        % any or all combinations of dimensions (inside loop)

        if isempty(nVal)
            %then nothing is preheating - no other checks necessary
        else
            if ~isempty(speed_pairs)
                [r_sp,~] = size(speed_pairs);
                for i_sp = 1:r_sp
                    i1 = speed_pairs(i_sp,1);
                    j1 = speed_pairs(i_sp,2);
                    AA = [x2_fuels(i1) y_fuels(i1) z2_fuels(i1)] -
[x1_fuels(i1) y_fuels(i1) z1_fuels(i1)];
                    BB = [x1_fuels(j1) y_fuels(j1) z1_fuels(j1)] -
[x_fuels(j1) y_fuels(j1) z_fuels(j1)];
                    dist = norm(cross(AA,BB))/norm(AA); % i is flame,
j is fu_el shortest distance from leaf to flame axis
                    if dist < rF(i1)
                        burn_stage(j1) = 2; % j is root leaf index
(1:n_fuels)
                        speed_pairs_temp = [speed_pairs_temp; i1 j1];
% this is the igniter, ignited list
                    end
                end
                speed_pairs = speed_pairs_temp;
                speed_pairs_temp = [];
                if ~isempty(speed_pairs)
                    nVal = setdiff(nVal,speed_pairs(:,2)); % this
removes the ones that ignited from speed_pairs
                end
            end

            %something might be heating
            for ii = 1:length(group) % i is flame, j is fu_el
                i = group(ii);
                overlap_zone = zeros(length(nVal),1);
                overlap_zone = ...
                    (x2g(ii)>=x1g(ii)).*((xF1(ii) <
x_fuels(nVal)).*(x_fuels(nVal) < xF2(ii))...
                    *(yF1(ii) < y_fuels(nVal)).*(y_fuels(nVal) <
yF2(ii))...
                    *(zF1(ii) < z_fuels(nVal)).*(z_fuels(nVal) <

```

```

zF2(ii)) + ...
                                (x1g(ii)<x2g(ii)).*((xF1(ii) >
x_fuels(nVal)).*(x_fuels(nVal) > xF2(ii))...
                                *(yF1(ii) > y_fuels(nVal)).*(y_fuels(nVal) >
yF2(ii))...
                                *(zF1(ii) > z_fuels(nVal)).*(z_fuels(nVal) >
zF2(ii)));
                                if sum(overlap_zone)>0
                                    for jj = find(overlap_zone)'%1:length(nVal)
                                        j = nVal(jj);
                                        if overlap_zone(jj) > 0
                                            AA = [x2g(ii) y2g(ii) z2g(ii)] - [x1g(ii)
y1g(ii) z1g(ii)];
                                            BB = [x1g(ii) y1g(ii) z1g(ii)] -
[x_fuels(j) y_fuels(j) z_fuels(j)];
                                            dist = norm(cross(AA,BB))/norm(AA); % i
is flame, j is fu_el

                                            if dist < rF(i)
                                                burn_stage(j) = 2; % j is root leaf
index (1:n_fuels)
                                                speed_pairs = [speed_pairs; i j]; %
this is the igniter, ignited list

                                                % remove j from nVal set?
                                            elseif rad_ok
                                                burn_stage(j) = 1.4; %radiation
heating
                                                end
                                            end
                                        end
                                    end
                                end
                                if ~isempty(speed_pairs)
                                    nVal = setdiff(nVal,speed_pairs(:,2)); % this
removes the ones that ignited from speed_pairs
                                end
                            end
                        end
                    end %stage3
                end %globule

                % heating override
                external_heating

                % run surprises, if something changes
                profileCorrector

                %burn_stage(s_ind) = 3;
                stage2 = find(burn_stage==2);
                stage1 = find(burn_stage==1);
                stageR = find(burn_stage==1.4);

                % update rxn time for stages 1, 2, 3, R
                % t_rxn(stage1) = (t_rxn(stage1) > dt).*(t_rxn(stage1) - dt);
                %cooling between flame overlap
                t_rxn(stageR) = (t_rxn(stageR)+dt/20);
                t_rxn(stageR) =
                (t_rxn(stageR)<t_ig(stageR)).*(t_rxn(stageR))+t_ig(stageR)).*

```

```

(t_ig(stageR)-dt/2);
    burn_stage(stageR) = 1;
    t_rxn(stage2) = t_rxn(stage2) + dt;%*(.25 < rand(length(stage2),1));
% intermittency
    t_rxn(stage3) = t_rxn(stage3) + dt;

    % advance stages for 2->3, 3->4
    burn_stage((burn_stage == 2) & (t_rxn > t_ig)) = 3;
    t_rxn((burn_stage == 3) & (t_rxn >= t_bo)) = t_bo((burn_stage == 3) &
(t_rxn >= t_bo));
    burn_stage((burn_stage == 3) & (t_rxn >= t_bo)) = 4;

    % record new burn stages
    stage1 = find(burn_stage==1);
    stage2 = find(burn_stage==2);
    stage3 = find(burn_stage==3);
    stage4 = find(burn_stage==4);
    n_stage3 = sum(burn_stage == 3);

end %stageUpdate

%%
function outputLoop
% Modular shrub fire sperad model BETA
% Started 9/5/2012 by Dallan Prince
% REALTIME OUTPUT

% tabulate data
t_index = round(t/dt) + 1;
t_tab(t_index) = t; % time for plotting tabulated data
f_burned(t_index) = (sum(burn_stage==4))/n_fuels;
f_preheating(t_index) = sum(burn_stage==2)/n_fuels;
f_burning(t_index) = sum(burn_stage==3)/n_fuels;
f_burned(t_index) = sum(burn_stage==4)/n_fuels;
h_scale_avg(t_index) = mean(h_scale(stage3));
if sum(burn_stage==3) > 0
    h_f_mean(t_index) = mean(h_f(burn_stage==3));
    h_f_s_mean(t_index) = mean(h_f_s(burn_stage==3));%% attention
    h_f_max(t_index) = max(h_f(burn_stage==3));
    h_f_p_max(t_index) = max(h_f(burn_stage==3));%% attention
    Dh_f = z_fuels(burn_stage==3) + h_f(burn_stage==3) - z_domain;
    DH_f(t_index) = max(Dh_f);
    max_FH(t_index) = max(z2_fuels - z_fuels + dF);
else
    h_f_mean(t_index) = 0;
    h_f_s_mean(t_index) = 0;
    h_f_max(t_index) = 0;
    h_f_p_max(t_index) = 0;
    DH_f(t_index) = 0;
    max_FH(t_index) = 0;
end

if plots == 1
    dt_p(t_index + 1) = dt_p(t_index) - dt;
    if dt_p(t_index + 1) <= 0

```

```

                % Fuel element flame behavior model
                figure(situation);
% % %
                subplot(2,2,1);
% % %
plot(t_tab,f_preheating,t_tab,f_burning,t_tab,f_burned);
% % %
                ylim([0 Inf]); ylabel('Fraction'); xlabel('Time
(s)')
% % %
legend('Preheat','Burning','Burned','Location','NorthWest')
% % %
                subplot(2,2,3);
% % %
                plot(t_tab,h_scale_avg)
% % %
                ylabel('Flame Scaling (% base)'); xlabel('Time
(s)')
% % %
                subplot(2,2,2);
% % %
                plot(t_tab,h_f_s_mean,'ro-',t_tab,h_f_mean,'bx-')
% % %
                xlabel('Time (s)'); ylabel('Average flame height')
% % %
                legend('Single','Merged','Location','NorthWest')
% % %
                subplot(2,2,4);
                plot3Dburn % burn plot
                subplot(2,2,2);
%
%
plot(t_tab,toc_FU,t_tab,toc_FL,t_tab,toc_FI,t_tab,toc_OL,t_tab,cpuSpeed)
%
                ylim([0 Inf]); ylabel('Computation Stat'); xlabel('Time
(s)')
%
                legend('Flame Update','Flame Licking','Flame
Int','Output Loop','Speed','Location','NorthWest')
                format compact
                disp([t sum(burn_stage == 4)/n_fuels max(DH_f) max(max_FH)
toc]);
                dt_p(t_index + 1) = dt_p(1)-dt;
            end
        end

    end %outputLoop

    function outputBurn
        % Modular shrub fire sperad model BETA
        % Started 9/5/2012 by Dallan Prince
        % OUTPUT BURN, was OUTPUT FINAL

        format compact
%
                cpuSpeed = t/toc
%
                t_calc = toc
%
                t_burn = t
%
                Xs = sum(burn_stage == 4)/n_fuels
%
                DH_f_max = max(DH_f)
%
                max_comp(situation,1) = [max(max_FH)];

                disp('
Case CPUspeed t_calc t_burn Xs DH_f_max')
                disp([situation t/toc toc t sum(burn_stage == 4)/n_fuels max(DH_f)])
                alldata = [t/toc toc t sum(burn_stage == 4)/n_fuels max(DH_f);...
                    1 2 3 4 5;...
                    t_tab' DH_f' f_burned' f_burning'*n_fuels f_preheating'*n_fuels];
                if save_csv == 1
                    csvwrite(['DOE ' num2str(situation) ' rep ' num2str(repetitions)

```

```

'.csv'],alldata,1,0)
    end
    summary((repetitions-1)*4+situation,1:7) = [situation repetitions
t/toc toc t sum(burn_stage == 4)/n_fuels max(DH_f)];
    end %outputBurn was Final
    %%
    function run_details
    % Run details (case/switch structure)
    slice = 2;
    switch situation
    case 1
        n_fuels = 2348/slice;           % number of fuel elements
        MC = .20;                       % moisture content (decimal), dry
basis
        U_bulk = 0.0001;                % m/s
        y_domain = .66/slice; %m
        pix2m_x = 0.0031; % 0.0031 run 1,2,3; 0.0031*154/116 for 4
        pix2m_z = 0.003;
        left_bound = .06;
        top_bound = 1;
        image_name = 'run1crop.jpg';
        T_igzone = 1273.15-190;140;
        locations_image
    case 2
        n_fuels = 1996/slice;           % number of fuel elements
        MC = .20;                       % moisture content (decimal), dry
basis
        U_bulk = 0.45;                  % m/s
        y_domain = .66/slice; %m
        pix2m_x = 0.0031; % 0.0031 run 1,2,3; 0.0031*154/116 for 4
        pix2m_z = 0.003;
        left_bound = .08;
        top_bound = 1;
        image_name = 'run2crop.jpg';
        T_igzone = 1273.15-170;177;135;
        locations_image
    case 3
        n_fuels = 2098/slice;           % number of fuel elements
        MC = .20;                       % moisture content (decimal), dry
basis
        U_bulk = 1.08;                  % m/s
        y_domain = .57/slice; %m
        pix2m_x = 0.0031; % 0.0031 run 1,2,3; 0.0031*154/116 for 4
        pix2m_z = 0.003;
        left_bound = .35;
        top_bound = .19;
        image_name = 'run3crop.jpg';
        T_igzone = 1273.15-160;130;
        locations_image
    case 4
        n_fuels = 3240/slice;           % number of fuel elements
        MC = .27;                       % moisture content (decimal), dry
basis
        U_bulk = 0.69;                  % m/s
        y_domain = .70/slice; %m
        pix2m_x = 0.0031*154/116; % 0.0031 run 1,2,3; 0.0031*154/116
for 4

```

```

pix2m_z = 0.003*154/116;
left_bound = .35;
top_bound = .24;
image_name = 'run4crop.jpg';
T_igzone = 1273.15-170;177;
locations_image
case 5
U_bulk = 1; % m/s
n_fuels = 2348/1; % number of fuel elements
MC = .20; % moisture content (decimal), dry
basis
y_domain = .66/1; %m
pix2m_x = 0.0031; % 0.0031 run 1,2,3; 0.0031*154/116 for 4
pix2m_z = 0.003;
left_bound = .07;
top_bound = 1;
image_name = 'run1crop.jpg'; % for locations_image
locations_image
case 6
U_bulk = 2; % m/s
n_fuels = 7000/4; % number of fuel elements
MC = .30; % moisture content (decimal), dry
basis
y_domain = .15; %m
pix2m_x = 0.0031; % 0.0031 run 1,2,3; 0.0031*154/116 for 4
pix2m_z = 0.003;
left_bound = .15;
top_bound = .15;
image_name = 'box.jpg'; % for locations_image
locations_image
case 7 % clumps 3:1
U_bulk = 0; % m/s
MC = .34; % moisture content (decimal), dry
basis
left_bound = 0;
top_bound = 0;
x_fuels = [-0.0201 0.3038 -0.2144 -1.3009 -0.1352 -
0.6533]*.01;
y_fuels = [1.7286 0.3685 0.0447 1.7299 -0.9902
1.6004]*.01;
z_fuels = [5.1338 9.0197 9.0197 6.2605 6.5195
8.0739]*.01;
x_fuels = x_fuels - min(x_fuels);
y_fuels = y_fuels - min(y_fuels);
z_fuels = z_fuels - min(z_fuels);
x_domain = max(x_fuels);
y_domain = max(y_fuels);
z_domain = max(z_fuels);
n_fuels = length(x_fuels);
case 8 % clumps 3:2
U_bulk = 0; % m/s
MC = .41; % moisture content (decimal), dry
basis (41 for clumps
left_bound = 0;
top_bound = 0;
x_fuels = [-0.11929 -1.6184 0.92871 -0.61448 -0.87903
0.44371 -0.39403 -1.7066 -1.3979 -1.442 -0.6043 -0.085388 0.0027952 -

```

```

0.83494    0.63026 0.32162 -0.25156    0.13507]'.01;
    y_fuels = [-0.11302 0.46016 -0.63653    -1.827    -0.85699    -
1.342    -2.0475 -0.55394    0.10743 0.10743 -0.55394    0.024841    -1.6947 -
0.23971    -1.3476 -1.5239 0.41607 -0.50426]'.01;
    z_fuels = [5.5198    6.578    6.9307 7.9007 6.1811 9.0912
9.5762 8.6503 9.2675 10.017 11.384 11.516 10.282 11.56 10.193
9.7525 11.119 10.723]'.01;
    x_fuels = x_fuels - min(x_fuels);
    y_fuels = y_fuels - min(y_fuels);
    z_fuels = z_fuels - min(z_fuels);
    x_domain = max(x_fuels);
    y_domain = max(y_fuels);
    z_domain = max(z_fuels);
    n_fuels = length(x_fuels);
    case 9 % clumps 3:3
        U_bulk = 0; % m/s
        MC = .41; % moisture content (decimal), dry
basis (41 for clumps
    left_bound = 0;
    top_bound = 0;
    x_fuels = [1.0427    -0.48283    1.0688    -1.2808 0.46187 -
0.95675    -1.4887 -0.48283    -0.70449    -1.2365 0.32888 -0.29177    -
0.15877    -0.69076    -1.0454 -1.0011 -0.66016    -0.38043]'.01;
    y_fuels = [-0.67122 -1.177    -0.91103    -0.64504    -1.6346 -
1.9449 -2.3439 -0.51205    -2.0193 -2.7286 -1.9449 -1.9006 -2.2553 -2.0779 -
2.7872 -2.4769 -3.039    -1.5016]'.01;
    z_fuels = [4.5954    6.7978 7.1081 7.8174 8.2444 9.3971
10.55 10.078 11.674 10.788 9.8847 10.594 11.215 11.88 11.259
11.791 11.32 11.17]'.01;
    x_fuels = x_fuels - min(x_fuels);
    y_fuels = y_fuels - min(y_fuels);
    z_fuels = z_fuels - min(z_fuels);
    x_domain = max(x_fuels);
    y_domain = max(y_fuels);
    z_domain = max(z_fuels);
    n_fuels = length(x_fuels);
    case 10 % clumps 3:5
        U_bulk = 0; % m/s
        MC = .41; % moisture content (decimal), dry
basis (41 for clumps
    left_bound = 0;
    top_bound = 0;
    x_fuels = [-0.63789 1.3044 1.8021]'.01;
    y_fuels = [-0.37117 -0.56479 0.9282]'.01;
    z_fuels = [8.0089 6.2197 6.9385]'.01;
    x_fuels = x_fuels - min(x_fuels);
    y_fuels = y_fuels - min(y_fuels);
    z_fuels = z_fuels - min(z_fuels);
    x_domain = max(x_fuels);
    y_domain = max(y_fuels);
    z_domain = max(z_fuels);
    n_fuels = length(x_fuels);
    case 11 % clumps 3:6
        U_bulk = 0; % m/s
        MC = .41; % moisture content (decimal), dry
basis (41 for clumps
    left_bound = 0;

```

```

        top_bound = 0;
        x_fuels = [-1.2802  0.29681 -1.468  -0.0035797  -1.2865  -
1.6978 -1.5806 -0.52926  -0.9873 -1.1743 -1.4734 -0.72553  -0.87511  -
1.2117 -0.9873 -0.35157  -1.7684]'.*0.01;
        y_fuels = [0.068052 0.70378 1.3395  1.6387  0.41973 1.7135
2.3492  2.8354  1.7313  2.5556  1.7313  1.4315  2.3683  1.9561  2.031  2.743
1.9752]'.*0.01;
        z_fuels = [4.7377  5.8266  5.2634  9.281  6.9028  9.0718
7.6664  8.2297  6.4167  9.0718  6.7907  9.0344  9.2962  9.5206  8.9222
8.6231  8.6427]'.*0.01;
        x_fuels = x_fuels - min(x_fuels);
        y_fuels = y_fuels - min(y_fuels);
        z_fuels = z_fuels - min(z_fuels);
        x_domain = max(x_fuels);
        y_domain = max(y_fuels);
        z_domain = max(z_fuels);
        n_fuels = length(x_fuels);
    case 12 % clumps 3:7
        U_bulk = 0; % m/s
        MC = .41; % moisture content (decimal), dry
basis (41 for clumps
        left_bound = 0;
        top_bound = 0;
        x_fuels = [-0.091116  1.5481  0.78949 1.5491  2.2288
0.94839 2.5886  1.3882  -0.051135  1.1883  1.6691]'.*0.01;
        y_fuels = [0.38685  0.14649 -0.72288  -0.40366  0.63381
0.70733 0.71361 0.42691 0.34679 0.90763 -0.20415]'.*0.01;
        z_fuels = [6.7621  7.3219  5.9378  6.0978  6.7774  6.962
6.8974  7.2419  6.2823  6.7621  6.7774]'.*0.01;
        x_fuels = x_fuels - min(x_fuels);
        y_fuels = y_fuels - min(y_fuels);
        z_fuels = z_fuels - min(z_fuels);
        x_domain = max(x_fuels);
        y_domain = max(y_fuels);
        z_domain = max(z_fuels);
        n_fuels = length(x_fuels);
    case 13 % clumps 3:8
        U_bulk = 0; % m/s
        MC = .41; % moisture content (decimal), dry
basis (41 for clumps
        left_bound = 0;
        top_bound = 0;
        x_fuels = [-1.2725  -0.37212  2.1141  -1.9505 -2.5758
1.6056  0.027173  1.3833  0.70524 1.3268  0.36245 0.8145  1.5491  0.58848
2.6792  -2.7454 -1.4457 -2.9714 -2.4063 0.98402 0.19294 1.6658  -0.033085
1.0443  0.93126 0.87476 -0.54164  -2.3498 -1.9543 -1.4457 1.8316  0.13643
1.323  -3.932  -3.3669 -2.8019 -4.158  1.1535  -0.42487  -1.0464 -2.9676 -
0.99368  0.76175 -0.085838  0.36621 -2.6286 -2.1765]'.*0.01;
        y_fuels = [-0.10227 -0.62946  0.27463 1.0844  -0.23392
1.4612  1.8754  2.4405  2.1015  -0.72383  2.5349  2.1393  2.4218  2.4783  -
1.7596 2.4218  2.5914  1.5177  2.3088  -0.17742  1.1222  4.6442  1.9698
3.3446  4.0226  1.6494  2.4783  0.89619 2.0828  2.7609  1.2352  1.4612
2.3653  1.7438  2.5914  1.2917  1.1787  4.117  1.9884  3.9096  2.61
1.1222  1.4799  1.9319  3.7966  2.949  3.8531]'.*0.01;
        z_fuels = [4.4084  5.586  4.2864  4.6344  4.7385  5.36
13.562 12.884 13.901 10.681 11.858 13.045 12.423 12.423  8.3548
10.106 11.237 10.728 10.785  8.4678  6.0946  9.4374 10.389  9.7199

```

```

10.398  6.1036  9.1459  8.5808  7.3942  6.5466  10.615  8.2418  7.8463
6.9422  7.4507  6.9422  6.3206  7.9028  7.1772  10.172  8.7593  7.9028
10.907  9.2114  9.3809  11.246  9.4374] '*.01;
x_fuels = x_fuels - min(x_fuels);
y_fuels = y_fuels - min(y_fuels);
z_fuels = z_fuels - min(z_fuels);
x_domain = max(x_fuels);
y_domain = max(y_fuels);
z_domain = max(z_fuels);
n_fuels = length(x_fuels);
case 14 % clumps 3:10
U_bulk = 0; % m/s
MC = .41; % moisture content (decimal), dry
basis (41 for clumps
left_bound = 0;
top_bound = 0;
x_fuels = [-1.8204  1.5824  1.4397  0.67829] '*.01;
y_fuels = [-0.71911 -0.56574 -0.08987 -0.75609] '*.01;
z_fuels = [5.6558  7.0323  8.0792  8.0792] '*.01;
x_fuels = x_fuels - min(x_fuels);
y_fuels = y_fuels - min(y_fuels);
z_fuels = z_fuels - min(z_fuels);
x_domain = max(x_fuels);
y_domain = max(y_fuels);
z_domain = max(z_fuels);
n_fuels = length(x_fuels);
case 15 % clumps 3:11
U_bulk = 0; % m/s
MC = .41; % moisture content (decimal), dry
basis (41 for clumps
left_bound = 0;
top_bound = 0;
x_fuels = [0.80097 -0.89782  0.66686 1.8292 -0.49547
0.085692 -0.093128  2.0392 0.95975 2.8488  1.9942  2.9387  1.5163
2.4998  2.399  0.50998 2.768  2.0527] '*.01;
y_fuels = [0.10006 -0.4364 0.14477 1.173  0.23418 0.94946 -
0.79404  0.052594 -0.71202  0.77223 0.27748 1.7617  1.6647  1.173
0.90716 0.45739 0.86005 1.173] '*.01;
z_fuels = [9.6716  4.4858  4.8881  8.2857  6.0952  6.721
5.0669  7.448  6.1886  9.382  11.001  10.371  10.476  10.879  10.461
6.2336  9.1798  10.566] '*.01;
x_fuels = x_fuels - min(x_fuels);
y_fuels = y_fuels - min(y_fuels);
z_fuels = z_fuels - min(z_fuels);
x_domain = max(x_fuels);
y_domain = max(y_fuels);
z_domain = max(z_fuels);
n_fuels = length(x_fuels);
case 16 % clumps 3:12
U_bulk = 0; % m/s
MC = .41; % moisture content (decimal), dry
basis (41 for clumps
left_bound = 0;
top_bound = 0;
x_fuels = [-1.5581 -0.74716  0.77936 0.77936 -0.55564
0.31501 -0.38151  1.0696 -0.67173 -0.091295 -1.2522 1.592  0.31501
2.0563 -0.26543  0.37305 1.5339 1.65  1.0696 1.0696 0.60523] '*.01;

```

```

y_fuels = [0.04036 -0.3072 -0.42446 1.1975 -0.65616
1.2554 0.1548 1.1975 0.27065 0.32858 1.0816 1.8926 0.67614 1.6609
2.4718 1.7767 2.4139 1.9505 1.6609 2.1243 1.1975]'*.01;
z_fuels = [3.5636 4.2008 6.5241 6.5822 7.2787 7.3368
7.685 8.9039 8.9039 10.529 10.471 10.877 12.445 12.851 12.445
13.257 13.431 13.547 13.664 12.967 12.909]'*.01;
x_fuels = x_fuels - min(x_fuels);
y_fuels = y_fuels - min(y_fuels);
z_fuels = z_fuels - min(z_fuels);
x_domain = max(x_fuels);
y_domain = max(y_fuels);
z_domain = max(z_fuels);
n_fuels = length(x_fuels);
case 17 % clumps 3:13
U_bulk = 0; % m/s
MC = .41; % moisture content (decimal), dry
basis (41 for clumps
left_bound = 0;
top_bound = 0;
x_fuels = [-0.34065 -2.3424 -0.17923 -1.078 0.92376 -
0.95343 2.1493 -0.38349 -0.83286 -0.2181 -0.095541 1.3343 2.4761
3.5383 0.43354 1.0463 0.47439 0.43354 2.7621 3.4157 2.4761 -0.013838
3.0909 2.3556 0.31297 1.0892 2.7232]'*.01;
y_fuels = [0.84964 0.68623 0.9422 -0.07495 0.29122
2.1977 0.0064219 -0.48181 0.25054 1.9935 1.2173 1.7075 0.69808
2.4883 2.0407 1.7559 0.57602 1.5932 0.12848 2.2441 2.2035 1.9118
2.8514 1.2173 1.5441 -0.0082449 1.6667]'*.01;
z_fuels = [3.9768 8.4296 4.8383 4.8383 5.0426 7.3267
6.7992 6.8401 5.7371 9.5735 6.4688 6.8773 9.618 9.4546 8.1473
7.9839 7.7797 9.4954 7.7388 8.1882 10.19 9.1241 9.696 9.8186
9.6552 5.2841 9.8595]'*.01;
x_fuels = x_fuels - min(x_fuels);
y_fuels = y_fuels - min(y_fuels);
z_fuels = z_fuels - min(z_fuels);
x_domain = max(x_fuels);
y_domain = max(y_fuels);
z_domain = max(z_fuels);
n_fuels = length(x_fuels);
case 101 % multi-bush run
MC = .20; % moisture content (decimal), dry
basis
U_bulk = 1; % m/s
pix2m_x = 0.0031; % 0.0031 run 1,2,3; 0.0031*154/116 for 4
pix2m_z = 0.003;
left_bound = .08;
top_bound = 1;

y_domain = .66; %m
n_fuels = 2348;
image_name = 'run2crop.jpg';
locations_image
x_fuels_1 = x_fuels;
y_fuels_1 = y_fuels;
z_fuels_1 = z_fuels;

y_domain = .57; %m
n_fuels = 2098;

```

```

        image_name = 'run3crop.jpg';
        locations_image
        x_fuels_2 = x_fuels;
        y_fuels_2 = y_fuels;
        z_fuels_2 = z_fuels;

        y_domain = .69; %m
        n_fuels = 3240;
        image_name = 'run4crop.jpg';
        locations_image
        x_fuels_3 = x_fuels;
        y_fuels_3 = y_fuels;
        z_fuels_3 = z_fuels;
        %merge all fuels
        n_fuels = 2348 + 2098 + 3240;
        x_fuels = [x_fuels_1 + 0.0; x_fuels_2 + 0.7; x_fuels_3 +
1.4];

        y_fuels = [y_fuels_1; y_fuels_2; y_fuels_3];
        z_fuels = [z_fuels_1; z_fuels_2; z_fuels_3];
        x_domain = max(x_fuels);
        y_domain = max(y_fuels);
        z_domain = max(z_fuels);
end
function locations_image
    % Fuel element placement from picture
    % Requires image with white (deleted) background

    im = imread(image_name);

    [r,c,~] = size(im);
    x_domain = pix2m_x*c;
    z_domain = pix2m_z*r;

    % get region of fuel
    % im = im(g_row(1):g_row(2),g_col(1):g_col(2),:);
    img = im(:,:,3);
    img(img < 180) = 0;
    img(img >= 180) = 255;

    % now thin pixels down to x-z locations for fuel elements
    xz_loc = zeros(size(img));
    xz_loc(img==0) = 1;
    n_fuels0 = sum(sum(xz_loc));
    while n_fuels0 ~= n_fuels
        if n_fuels0 > n_fuels
            p_keep = n_fuels/n_fuels0;
            p_test = rand(size(xz_loc));
            xz_loc(p_test>p_keep) = 0;
        elseif n_fuels0 < n_fuels
            places = find(img==0);
            ip = ceil(rand(n_fuels-n_fuels0,1)*length(places));
            xz_loc(places(ip)) = 1;
        end
        n_fuels0 = sum(sum(xz_loc));
    end
    [z_pix, x_pix] = find(xz_loc);
    x_fuels = (single(x_domain - x_pix*pix2m_x));

```

```

z_fuels = (single(z_domain - z_pix*pix2m_z));

y_fuels = y_domain*zeros(n_fuels,1,'single');
for i = 1:n_fuels
    ylower = find(img(z_pix(i),:)==0,1,'first');
    yupper = find(img(z_pix(i),:)==0,1,'last');
    y_fuels(i) = ylower + rand*(yupper-ylower);
end
y_fuels = y_fuels-min(y_fuels);
y_fuels = y_fuels./max(y_fuels).*y_domain;
y_fuels = (single(y_fuels));
end %locations_images
end %run_details

function external_heating
% heating_override
% cases should match run details

switch situation
case {7,8,9,10,11,12,13,14,15,16,17}
    top_bound = .5;
    left_bound = 1;
    if t>=10
        top_bound = 1;
    end
    burn_stage(burn_stage==1) = 1 +
(x_fuels(burn_stage==1)/x_domain <=
left_bound).*(z_fuels(burn_stage==1)/z_domain <= top_bound);
end
end %external_heating

function profileCorrector
switch situation
case 1
    if t<25
        for i = 1:n_fuels
            if burn_stage(i) == 1
                if x_fuels(i) < .1*t/20
                    burn_stage(i) = 2;
                    t_rxn(i) = t_rxn(i) + dt;
                elseif t<30 && t>20 && x_fuels(i) < .1
                    burn_stage(i) = 2;
                    t_rxn(i) = t_rxn(i) + dt;
                end
            end
        end
    end
end
case 2
    % long ignition sequence (18cm of shrub over 30 s) due to
excelsior
    if t<30
        for i = 1:n_fuels
            if burn_stage(i) == 1
                if x_fuels(i) < .18*t/30
                    burn_stage(i) = 2;
                    t_rxn(i) = t_rxn(i) + dt;
                end
            end
        end
    end
end
end

```

```

        end
    end
end
    % wind stopped at 141 s
    if max(burn_stage(x_fuels>0.55)) > 2 && U_bulk>.1
    if t>=141 && U_bulk>.1
        U_bulk = 0.0001;
        T_igzone = 1273.15-150;
        flame_properties
    end
    case 3
    case 4
    if t>=75 && U_bulk<.6901
        U_bulk = 0.6901;
        T_igzone = 1273.15-190;
        flame_properties
    end
end
end
function plot3Dburn
    % Modular shrub fire sperad model BETA
    % Started 9/5/2012 by Dallan Prince
    % 3D BURN VISUALIZATION
    % for Manzanita

    % plotting limits
    H_max = max(2*h_max);
    x_low = 0 - H_max*.11;
    x_high = x_domain + H_max*(U_bulk + .11);
    y_low = 0 - H_max*.11;
    y_high = y_domain;
    z_low = 0 - H_max*.11;
    z_high = 2*H_max+z_domain;

    zbot=z_fuels-th/2;
    ztop=z_fuels+th/2;
    xbot=x_fuels-w/2;
    xtop=x_fuels+w/2;
    ybot=y_fuels-l/2;
    ytop=y_fuels+l/2;

    h3d = scatter3(x_fuels,y_fuels,z_fuels,1,[0 1 0],'filled');

    % vertices
    x1v=x_fuels - rF.*cos(theta);
    x2v=x_fuels + rF.*cos(theta);
    x3v=x2_fuels - rF.*cos(theta);
    x4v=x2_fuels + rF.*cos(theta);
    y1v=y_fuels - rF;
    y2v=y_fuels + rF;
    z1v=z_fuels - rF.*sin(theta) - dF;
    z2v=z_fuels;
    z3v=z2_fuels + rF.*sin(theta);

    %If the leaf is within an ignition zone, this will turn the leaf
    %orange.
    fuel_color(1,:) = [0 1 0];

```

```

fuel_color(2,:) = [.1 .1 .8];
fuel_color(3,:) = [.8 .1 .1];
fuel_color(4,:) = [0.5 0.5 0.5];

fuel_edge_color(1,:) = [.0980 .5922 .1804];
fuel_edge_color(2,:) = [0 0 1];
fuel_edge_color(3,:) = [1 0 0];
fuel_edge_color(4,:) = [0.4 0.4 0.4];

flamecolor=[1 .4588 .0196];

for burn_stage_set = 1:4
    f_color = fuel_color(burn_stage_set,:);
    f_e_color = fuel_edge_color(burn_stage_set,:);
    s_ind = find(burn_stage == burn_stage_set);
    n_set = length(s_ind);

    if n_set > 0

        % fuel elements

xv=[xbot(s_ind);xtop(s_ind);xtop(s_ind);xbot(s_ind);xbot(s_ind);xtop(s_ind);x
top(s_ind);xbot(s_ind)];

yv=[ybot(s_ind);ybot(s_ind);ytop(s_ind);ytop(s_ind);ybot(s_ind);ybot(s_ind);y
top(s_ind);ytop(s_ind)];

zv=[zbot(s_ind);zbot(s_ind);zbot(s_ind);zbot(s_ind);ztop(s_ind);ztop(s_ind);z
top(s_ind);ztop(s_ind)];
        vert=[xv,yv,zv];
        fuelFaces = zeros(6*n_set,4);
        for i_fuels = 1:n_set
            fuelFacesSet = [0*n_set + i_fuels,1*n_set +
i_fuels,5*n_set + i_fuels,4*n_set + i_fuels;1*n_set + i_fuels,2*n_set +
i_fuels,6*n_set + i_fuels,5*n_set + i_fuels;2*n_set + i_fuels,3*n_set +
i_fuels,7*n_set + i_fuels,6*n_set + i_fuels;3*n_set + i_fuels,0*n_set +
i_fuels,4*n_set + i_fuels,7*n_set + i_fuels;0*n_set + i_fuels,1*n_set +
i_fuels,2*n_set + i_fuels,3*n_set + i_fuels;4*n_set + i_fuels,5*n_set +
i_fuels,6*n_set + i_fuels,7*n_set + i_fuels];
            fuelFaces(1 + (i_fuels-1)*6:6 + (i_fuels-1)*6,:) =
fuelFacesSet;
        end
        patchinfo.Vertices = vert;
        patchinfo.Faces = fuelFaces;
        patchinfo.FaceColor = f_color;
        patchinfo.FaceAlpha = 'flat';
        patchinfo.FaceVertexAlphaData = 0.4;
        patchinfo.EdgeColor = f_e_color;
        p = patch(patchinfo);
    end
end

axis equal
xlim([x_low,x_high])
ylim([y_low,y_high])
zlim([z_low,z_high])

```

```

title([num2str(t)])

im_name = ['DOE_' num2str(situation) '_rep_' num2str(repetitions) '_']
sprintf('%03g',t) '_sec'];
view(180,0)
if save_figs == 1;
    saveas(h3d,[pwd '/figs_' num2str(situation) '_']
num2str(repetitions) '/leaves_' im_name '.fig'],'fig');
end
for burn_stage_set = 1:4
    f_color = fuel_color(burn_stage_set,:);
    f_e_color = fuel_edge_color(burn_stage_set,:);
    s_ind = find(burn_stage == burn_stage_set);
    n_set = length(s_ind);

    if n_set > 0
        if burn_stage_set == 3 % flames
            if showFlames == 1

xv=[x1v(s_ind);x2v(s_ind);x2v(s_ind);x1v(s_ind);x1v(s_ind);x2v(s_ind);x2v(s_i
nd);x1v(s_ind);x3v(s_ind);x4v(s_ind);x4v(s_ind);x3v(s_ind)];

yv=[y1v(s_ind);y1v(s_ind);y2v(s_ind);y2v(s_ind);y1v(s_ind);y1v(s_ind);y2v(s_i
nd);y2v(s_ind);y1v(s_ind);y1v(s_ind);y2v(s_ind);y2v(s_ind)];

zv=[z1v(s_ind);z1v(s_ind);z1v(s_ind);z1v(s_ind);z2v(s_ind);z2v(s_ind);z2v(s_i
nd);z2v(s_ind);z3v(s_ind);z3v(s_ind);z3v(s_ind);z3v(s_ind)];
        vert=[xv,yv,zv];
        flameFaces = zeros(10*n_set,4);
        for i_fuels = 1:n_set
            flameFacesSet = [0*n_set + i_fuels,1*n_set +
i_fuels,5*n_set + i_fuels,4*n_set + i_fuels;1*n_set + i_fuels,2*n_set +
i_fuels,6*n_set + i_fuels,5*n_set + i_fuels;2*n_set + i_fuels,3*n_set +
i_fuels,7*n_set + i_fuels,6*n_set + i_fuels;3*n_set + i_fuels,0*n_set +
i_fuels,4*n_set + i_fuels,7*n_set + i_fuels;0*n_set + i_fuels,1*n_set +
i_fuels,2*n_set + i_fuels,3*n_set + i_fuels;4*n_set + i_fuels,5*n_set +
i_fuels,9*n_set + i_fuels,8*n_set + i_fuels;5*n_set + i_fuels,6*n_set +
i_fuels,10*n_set + i_fuels,9*n_set + i_fuels;6*n_set + i_fuels,7*n_set +
i_fuels,11*n_set + i_fuels,10*n_set + i_fuels;7*n_set + i_fuels,4*n_set +
i_fuels,8*n_set + i_fuels,11*n_set + i_fuels;8*n_set + i_fuels,9*n_set +
i_fuels,10*n_set + i_fuels,11*n_set + i_fuels];
            flameFaces(1 + (i_fuels-1)*10:10 + (i_fuels-
1)*10,:) = flameFacesSet;
        end
        patchinfo.Vertices = vert;
        patchinfo.Faces = flameFaces;
        patchinfo.FaceColor = flamecolor;
        patchinfo.FaceAlpha = 'flat';
        patchinfo.FaceVertexAlphaData = 0.06;
        patchinfo.EdgeColor = flamecolor;
        p = patch(patchinfo);
    end
end
end
end
end

```

```

        view(180,0)
        if save_figs == 1;
            saveas(h3d,[pwd '/figs_' num2str(situation) '_'
num2str(repetitions) '/all_' im_name '.fig'],'fig');
        end

    end %plot3Dburn

function scaleFire
%
% My attempt at feeding back flame heat release to determine the
% temperature and kinetics...very unstable. Calculating flame radiation
% would help to stabilize temperature.
    if isempty(stage3)
        h_mid = mean(h_f_group)/3.33;%max(max_FH)-max(max(DH_f),0);
        V_U = mean(U)*cos(pi/2-abs(mean(theta))); %velocity from wind
projected onto flame axis
        V_Z =
cos(abs(mean(theta))).*0.5*0.9*(2*g*h_mid*T_igzone/T_weather)^.5;
%http://fire.nist.gov/bfrlpubs/fire79/PDF/f79001.pdf; estimating at 1/2
height of flame

    else
        h_mid =
max(max(h_f(stage3)),mean(h_f_group(stage3)))/3.33;%max(max_FH)-
max(max(DH_f),0);
        V_U = mean(U)*cos(pi/2-abs(mean(theta(stage3))))); %velocity from
wind projected onto flame axis
        V_Z =
cos(abs(mean(theta(stage3))))).*0.5*0.9*(2*g*h_mid*T_igzone/T_weather)^.5;
%http://fire.nist.gov/bfrlpubs/fire79/PDF/f79001.pdf; estimating at 1/2
height of flame
    end
    V = V_Z+V_U;
% %%%
%
%     dH_comb = 20000; %J/g
%     Mw = 28.97; %gram/mol
%     massRel_g = sum((h_f_s(stage3)*dt)./((t_bo(stage3)-
t_ig(stage3)).*h_max(stage3)/2).*m_dry(stage3));
%     Ac_all = 1.1*(max(x1_fuels(stage3))-
min(x1_fuels(stage3)))*cos(mean(theta))*(max(y_fuels(stage3))-
min(y_fuels(stage3))); %cross-sectional area of flame, normal to flow
direction of flame
%     p_amb = 1.013*10^5; %Pa = J/m3
%     Rg = 8.314; %J/(mol K)
% %
%     T_guess = 1273;
%     cp_air = 1.2; %J/(g K) @1100 - 1600 K I&D
% %%%
%
% %%%
%     for i = 1:3 %let temperature hit equilibrium for mass release and
velocity
% %%%
% %%%
% %%%

```

```

%
%         if massRel_g~=0
%             T_igzone = 300 +
dH_comb*massRel_g/(p_amb/(Rg*T_igzone)*Mw*cp_air*V*Ac_all*dt);
%             end
%         end
%         disp(T_igzone)
% %%%
%         if isempty(t_base)
%             [t_base,F_base] = kinScale(mean(m_dry), MC, mean(l), mean(th),
pi*mean(l)/2*mean(w)/2*2, 1273.15, .6*2, 1500, 525);
%         end
%         [t_new,F_new] = kinScale(mean(m_dry), MC, mean(l), mean(th),
pi*mean(l)/2*mean(w)/2*2, T_igzone, V, 1500, 300);
%         kin_scale_t = t_new/t_base;
%         if isempty(t_ig_base) %reset t_x for new adjustment if necessary
%             t_ig_base = t_ig;
%             t_h_base = t_h;
%             t_bo_base = t_bo;
%             h_max_base = h_max;
%             scale_old = 1;
%         else
%             scale_old = t_bo(1)/t_bo_base(1);
%             t_ig = t_ig_base;
%             t_h = t_h_base;
%             t_bo = t_bo_base;
%             h_max = h_max_base;
%         end
%         t_ig = t_ig_base * kin_scale_t;
%         t_h = t_h_base * kin_scale_t;
%         t_bo = t_bo_base * kin_scale_t;
%         t_rxn = t_rxn*kin_scale_t/scale_old;
%
%         t_bo_avg_base = mean(t_bo_base-t_ig_base);
%         t_bo_avg_new = mean(t_bo-t_ig);
%         kin_scale_H = (t_bo_avg_base/t_bo_avg_new*F_new/F_base)^(2/5); % Hmax
= 0.2 * Qmax^(2/5); Qmax ~ 1/t_bo and t_bo. Also, scaling by the amount of
flammables released
%         h_max = h_max_base * kin_scale_H;
%         disp(['Time scale = ' num2str(kin_scale_t) '; Height scale: '
num2str(kin_scale_H) '; t_base: ' num2str(t_base) '; t_new: '
num2str(t_new)])
%         end
%         %%
%         function [t_stop,F_dry_rel] = kinScale(m_dryAvg, MCAvg, x_Re, thAvg,
faceArea, T_pfg, Vel, T_soot, T_surr)
%             % [t_stop] = kinScale(.13, .62, .03, .0005, 0.03*0.02*2, 1273.15,
.6*2, 3000, 525)
%
%             %% Kinetic
%             % data = []; %uncomment here and below, and add to outputs to get
some data
%
%             % constants
Rg = 8.314; %J/(mol K)
sigma = 5.670373*10^-8; %W/(m2 K4)

```

```

% air
p_amb = 1.013*10^5; %Pa = J/m3
k = 54.9*10^-3; %W/(m K); @750 K - Incropera & DeWitt
Pr = 0.702; %@750 K - Incr.Dewitt
nu = 76.37*10^-6; %m2/s @750 K - Inc&Dewitt
Mw = 28.97; %gram/mol
cp_air = 1.2; %J/(g K) @1100 - 1600 K I&D

% water
dH_vap = 1951; %J/gram @470 K
eff_evap = 1; %evaporation efficiency -- cooling affected/cooling
potential

% flame
A_baseFlame = 0.06^2; %m2 - base area that flame heats up (for
convective flame feedback to heat fuel-how much to dilute heat of combustion)

% % radiation
% T_soot = 2000; %K
% T_surr = 525; %K

% % convection conditions
% Vel = 0.6*2; %m/s - 0.6 is calculated, estimated factor of 2 faster
at centerline
% % calculation: 400.9 L/min / (7.5*10in2) * 1000C/300K = 0.586
m/s
% T_pfg = 1273; %K - post-flame gas temperature (baseline ignition
zone temperature)
rho_amb = p_amb/Rg/T_pfg*Mw; %g/m3 = J(/m3) mol K(/J) (/K) g(/mol)

% leaf
% x_Re = 0.03; %m (3 cm) %Re number length dimension
x_Re = 0.637*x_Re; %This changes the diameter of a circle (or
ellipse?) to the average distance to cross the leaf in the flow direction |
integral(abs(sin(x))dx,0,2pi)/(2pi) = 0.637
Cp_solid = 2.500; %J/(g K)
Cp_water = 4.200; %J/(g K)
% th = 0.0005; %m thick (used in water release diffusion model for
z1-z2)

delH_comb = 20000; %J/gram
% faceArea = 0.03*0.02^2; %m2
eps = 0.98;

% dimesionless numbers & convection
% laminar flow, average, @film Temp, Pr>=0.6 (Incr. Dewitt)
Re_x = x_Re*Vel/nu; %unitless = m m(/s) s(/m2)
fudge = 2;
Nu_avg = 0.664*Re_x^.5 * Pr^.3333;
h = Nu_avg * k/x_Re * fudge; % convection coefficient

% vapor pressure of water (Pa = J/m3)
cof = [7.3649E+01 -7.2582E+03 -7.3037E+00 4.1653E-06 2.0000E+00];
Pvap = @(Temp) exp(cof(1) + cof(2)/Temp + cof(3)*log(Temp) +
cof(4)*Temp^cof(5)); %Pa (checks out with MathCAD)

% diffusion factor for Stamm's diffusion equation (technically

```

```

specific
    % gravity, but used here as fitting factor
    gamma = 0.05;

    %initialize
    th_T = 1; %for blowing factor
    m0 = m_dryAvg*(1+MCAvg); %inital mass (g)
    T_leaf = 300; %initialize leaf temp

    components = {'lignin cluster' 'lignin side' ...
                  'hemicellulose cluster' 'hemicellulose side' ...
                  'cellulose cluster' 'cellulose side'};
    f_frac = [.35*.61 .35*.39 .32*.53 .32*.47 .33*.54 .33*.46]; % six
parallel one-step devol. models (multi-component)
    Am = [2.3*10^19 7*10^16 3*10^13 5*10^19 3*10^15 2*10^16 ]; %A 1/s
    ER = [34747 27898 19237 25934 30819 27898 ]; %E/R (ER)
K
    Vinf = [0.639 1.000 0.585 1.000 1.000 1.000 ]; %Vinf
    f_solid = 1/(MCAvg+1)*f_frac;
    m_solid = m0*f_solid; % grams
    m_water = m0*(1-sum(f_solid)); %grams
    dm_solid = 0.0005*f_solid; %grams
    dm_water = 0;
    relLim=(m0*f_solid.*(1-Vinf));
    t1 = 0;
    dt1 = 0.005; %s time step
    m_stop = (m0*f_solid.*(1-Vinf*.25));
    c_flame = 0.5;
    %loop
    % disp('disp([t1 T_leaf sum(m_solid)/m0 m_water/m0 dq_conv dq_rad
flame_opacity th_T RT])')
    while (sum(m_solid)>m_stop)>0 || sum(dm_solid)/m_dryAvg/dt1>0.02) &&
t1 < 50 %here is the condition for when to consider the leaf burned
    % if isempty(T_flame)
    % delT_comb =
sum(dm_solid)*delH_comb/(cp_air*Vel*A_baseFlame*dt1*rho_amb); % K
    T_local = T_pfg+max(delT_comb,0);%K+K
    % else
    % T_local = T_flame;
    % end
    dq_conv = h*faceArea*(T_local-T_leaf);
    % (J (/s /m /K) /m * m2 * (K-K) = J/s = W
    flame_opacity = min(c_flame*sum(dm_solid)/dt1,1); %s/gm
    %gm/s, but then multiply off units
    dq_rad = faceArea*sigma*eps*(flame_opacity*(T_soot^4-
T_leaf^4)+(1-flame_opacity)*(T_surr^4-T_leaf^4));
    %m2*J(/s /m2 /K4)**(*K4 + *K4) = J/s = W
    RT = (eff_evap*dm_water*Cp_water +
sum(dm_solid*Cp_solid))*(T_local-T_leaf)/dq_conv/dt1; %g
    % (g *J(/g /K)+ g *J(/g /K) )*(K - K) (/J)s (/s) =
unitless
    if RT<=0, RT=.00001; end
    th_T = log(1+RT)/RT; %unitless
    dm_solid = m0.*f_solid.*Am.*exp(-ER./T_leaf).*(Vinf-(
m0.*f_solid-m_solid)./(m0.*f_solid)).*dt1;
    % g* 1/s ** ( unitless - (g* - g) / (g*))s = g
    dm_solid(dm_solid<0)=0;

```

```

    if m_water > 0.00001
        dm_water = exp(3.746-5.12*gamma-
4317/T_leaf).*0.01^2.*faceArea/(thAvg/4)*(Pvap(T_leaf)*Mw/Rg/T_leaf)*dt1;
        % m2/s * m2 /m *J /m3 g /mol    mol K /J    /K    *s = g
    else
        dm_water = m_water;
    end
    dq_evap = -eff_evap*dm_water*dH_vap/dt1;
    % g * J /g /s = J/s = W
    m_solid = m_solid - dm_solid;
    m_solid(m_solid<m0*f_solid.*(1-
Vinf))=relLim(m_solid<m0*f_solid.*(1-Vinf));
    % g - g;
    m_water = m_water - dm_water;
    % g - g;
    mCp = sum(m_solid)*Cp_solid + m_water*Cp_water;
    % g * J /g /K + g * J /g /K = J / K
    T_leaf = T_leaf + (th_T*dq_conv + dq_rad + dq_evap)/mCp*dt1;
    F_dry_rel = 1 - sum(m_solid)/m_dryAvg; %Fraction of mass released
    % K + (J /s + J /s)*K /J * s = K
    % Q = (sum(dm_solid) * delH_comb - dm_water * dH_vap)/dt;
    % g * J /g - g * J /g = J
    % hold on; plot(t1,dm_solid./m0)
    % disp([t1 T_leaf sum(m_solid)/m0 m_water/m0 dq_conv dq_rad
flame_opacity th_T (sum(m_solid)+m_water)/m0 Q])
    % data = [data; t1 T_leaf sum(m_solid)/m0 m_water/m0 dq_conv
dq_rad flame_opacity th_T (sum(m_solid)+m_water)/m0 Q];
    t1 = t1+dt1;
end
t_stop = t1-dt1;
end
end
end

```

G. L-SYSTEMS FUEL PLACEMENT CODE FOR UTAH JUNIPER

This MATLAB code was used to generate Utah juniper geometries discussed in Chapter 5.

```
% L-systems
% 3D
% Utah Juniper
% By Dallan Prince
% Guided and informed by previous work of Marianne Fletcher
% Contributions from Chen Shen, Dr. Tom Fletcher
% Based on L-system string compiler and Turtle interpreter from Cornell
% University, BioNB 441, L-Systems in Matlab (code had an error),
% https://instruct1.cit.cornell.edu/courses/bionb441/LSystem/

%%% Initialize Workspace ----- %%%
clear all; close all;

%%% MAIN INPUTS -- juniper-specific ----- %%%
diameter = 84; %cm 84
Mmodel = 1; %MASS,#Branch: 1-User, 2-Chen, M&H: 3-Sparse, 4-Med, 5-Dense
Hmodel = 2; %HEIGHT: 1-User, 2-shorter, 3-average, 4-taller
           % All height are correlations to Chen Shen's data and
           % fall within range, having zero, high or low bias.

%%% Dry Mass Model --- # of Branches ----- %%%
m_per_br = 21; % g/branch. average based on 300+ L-system-created branches.
           % If you change the strings so that the branches have different average
           % mass, you should update this value by making a shrub with a lot of
           % branches and then insert the value of Mdry/nBranch.
switch Mmodel % select "no.-of-branches/dry mass" method
case 1 % Direct user selection
    nBranch = 35; % <== put in value here
    M_target = nBranch*m_per_br;
otherwise % (quadratic functions of diameter(in cm), output kg)
    if Mmodel==2 %Shen Correlation (coefficients)
        c1 = [0, 3.005E-02, -1.76433 ]; %R^2 to data = 0.7104
    elseif Mmodel==3 % Mason and Hutchings Correlation SPARSE
        c1 = [2.506E-05, 8.632E-03, -1.820E-01]; %R^2 to avg data=1.000
    elseif Mmodel==4 % Mason and Hutchings Correlation MEDIUM
        c1 = [5.478E-05, 7.578E-03, -2.225E-01]; %R^2 to avg data=1.000
    elseif Mmodel==5 % Mason and Hutchings Correlation DENSE
        c1 = [7.979E-05, 1.079E-02, -3.229E-01]; %R^2 to avg data=9.997
    end
    M_target = (c1(1)*diameter^2 + c1(2)*diameter + c1(3))*1000; %g
    nBranch = round(M_target/m_per_br);
```

```

end

%%% Height Model --- Vertical branch spacing along trunk ----- %%%
switch Hmodel % select height model (based Chen's height, diam. measures)
  case 1 %Custom
    height = 140;
  case 2 %Shorter (biased low, ~25% quartile)
    height = 9.8*diameter^0.6; %R2 = 0.33
  case 3 %Average (not biased)
    height = 21.067*diameter^0.4786; %R2 = 0.33 (a lot of scatter)
  case 4 %Taller (biased high, ~75% quartile)
    height = 50*diameter^0.35; %R2 = 0.33
end

spacing = (height-34)/nBranch; %-34? is to deduct the length of the top
% branch before caclulating branch spacing to hit a particular height
% If branch strings are changed, or angle of top branch, you may have
% to change the number subtracted from height to be the branch
% vertical reach at the top of the shrub.

%%% Output setup --- Initializations ----- %%%
mBNames = {'CustomB' 'Shen' 'M&H Sparse' 'M&H Medium' 'M&H Dense'};
mHNames = {'CustomH' 'Short' 'AverageH' 'Tall'};
disp(['mBNames{Mmodel} ', ' mHNames{Hmodel} ', D*=' num2str(diameter) ...
      ' cm, H*=' num2str(round(height)) ' cm, #Branch=' num2str(nBranch) ...
      ', Mdry*=' num2str(M_target) ' g, Spacing=' num2str(spacing) ' cm'])
rot_log = Inf*ones(nBranch,1); rot_ang_old = 0; n_fuels = 0;

%%% Begin branch-making loop ----- %%%
h = waitbar(0,'Defining Axioms');
for iB = 1:nBranch
  clear axiom
  waitbar(iB/nBranch);

  %%% Create axiom ----- %%%
  %angle: (you might want to check these, r/l etc could be swapped)
  % "+" : Turn left by angle Delta, Using rotation matrix R_U(Delta).
  % "-" : Turn right by angle Delta, Using rotation matrix R_U(-Delta).
  % "&" : Pitch down by angle Delta, Using rotation matrix R_L(Delta).
  % "^" : Pitch up by angle Delta, Using rotation matrix R_L(-Delta).
  % "\" : Roll left by angle Delta, Using rotation matrix R_H(Delta).
  % "/" : Roll right by angle Delta, Using rotation matrix R_H(-Delta).
  % "|" : Turn around, Using rotation matrix R_H(180).

  %starting seed
  axiom = 'X';

  %number of repititions (derivations)
  nReps = 7;

  %Rules--Branch Structure (Sets are cycled through as derivations are
  %completed)
  % Set A
  ruleA(1).before = 'F';
  ruleA(1).after = 'F';
  ruleA(1).after2 = 'F';
  ruleA(2).before = 'G';
  ruleA(2).after = 'G';

```

```

ruleA(2).after2 = 'G';
ruleA(3).before = 'X';
ruleA(3).after = 'F[&X[G]]';
ruleA(3).after2 = 'F[&X[G]]';
% Set B
ruleB(1).before = 'F';
ruleB(1).after = 'F';
ruleB(1).after2 = 'F';
ruleB(2).before = 'G';
ruleB(2).after = 'G';
ruleB(2).after2 = 'G';
ruleB(3).before = 'X';
ruleB(3).after = 'G';
ruleB(3).after2 = 'G';
% Set C
ruleC(1).before = 'F';
ruleC(1).after = 'F';
ruleC(1).after2 = 'F';
ruleC(2).before = 'G';
ruleC(2).after = 'HH[/+G]HH[-G]HH[&\G]H';;% 'HH[+HH+HHHHH]HH[-HH-
HHHHHH]H[^/HH^HHHHHH]H[&\HH\&HHHHHH]H';
ruleC(2).after2 = 'HH[/+G]HHHH[&\G]H';
ruleC(3).before = 'H';
ruleC(3).after = 'H';
ruleC(3).after2 = 'H';
% Set D
ruleD(1).before = 'F';
ruleD(1).after = 'F';
ruleD(1).after2 = 'F';
ruleD(2).before = 'G';
ruleD(2).after = 'HHHHHHH';;% 'HH[+HH+HHHHH]HH[-HH-
HHHHHH]H[^/HH^HHHHHH]H[&\HH\&HHHHHH]H';
ruleD(2).after2 = 'HHHHHHH';
ruleD(3).before = 'H';
ruleD(3).after = 'H';
ruleD(3).after2 = 'H';
% Set E
ruleE(1).before = 'F';
ruleE(1).after = 'F';
ruleE(1).after2 = 'F';
ruleE(2).before = 'H';
ruleE(2).after = 'H[/+S]';;% 'HH[+HH+HHHHH]HH[-HH-
HHHHHH]H[^/HH^HHHHHH]H[&\HH\&HHHHHH]H';
ruleE(2).after2 = 'H[\-S]';
ruleE(3).before = 'S';
ruleE(3).after = 'S';
ruleE(3).after2 = 'S';

nRules = length(ruleA); % make sure all the rules have the same length

%make the string
for i=1:nReps
    %one character/cell, with indexes the same as original axiom string
    axiomINcells = cellstr(axiom');
    if sum(i==[1 2])
        rule = ruleA; %Building branches
    elseif i==3

```

```

        rule = ruleB; %finalize foliage branch seeds (i.e. convert X=>G)
    elseif sum(i==[4 5])
        rule = ruleC; %grow fuel seeds (H) from branch seeds (G)
    elseif i==6
        rule = ruleD; %finish off G=>H (replace G with 1.5 cm H segments-
-fuel seeds)
    elseif i==7
        rule = ruleE; %add fuel segment (S) to seach fuel start node (H)
    end

    for j=1:nRules
        %the indexes of each 'before' string
        hit = strfind(axiom, rule(j).before);
        if (length(hit)>=1)
            for k=hit
                switch ceil(rand*2)
                    case 1
                        axiomINcells{k} = rule(j).after;
                    case 2
                        axiomINcells{k} = rule(j).after2;
                end
            end
        end
    end

    %now convert individual cells back to a string
    axiom=[];
    for j=1:length(axiomINcells)
        axiom = [axiom, axiomINcells{j}]; % this is the formula for the
whole branch
    end
end
axioms{iB} = axiom;
n_fuels = n_fuels + sum(((find(axiom=='H')*0+1)));
end

%%% Draw the string (axiom) as turtle graphics ----- %%%
% Upper case (e.g. F or G) causes a line to be drawn in the current
% direction of the turtle
% Lower case causes a move with no draw
h = waitbar(0,'Interpreting Axiom, 3d Coordinates');
for iB = 1:nBranch
    clear verts
    waitbar(iB/nBranch);
    %Init the turtle
    xT = 0;
    yT = 0;
    zT = 0;
    hT = [0 0 1];
    axiom = axioms{iB};

    %init the turtle stack
    stkPtr = 1;

    %set(gca,'xlim', [-5 5], 'ylim', [-5 5]);
    clf
    hold on

```

```

%vertex counter
vN1 = 1;
vN2 = 1;
vN3 = 1;
vN4 = 1;
vN5 = 1;
for i=1:length(axiom)
    %% Customize axiom interpretation (you have to examine the axiom to
    determine where you want the angle/lengths to change)
    ang_dev = randn*3;
    if sum(i==[1 2])
        lenF = 22; %length in cm (may be scaled just below
    elseif sum(i==[3 4])
        lenF = 11;
        a = (10-10*iB/nBranch)*pi/180;
%
        a = (-ang_dev + (35-20*(iB/nBranch)-15*(iB/nBranch).^6));
    else
        lenS = 3; lenH = 1.5;
        a = (38.4)*pi/180; %degrees 22.5
    end
    lenF = lenF*(diameter/2-22)/33; %divide by sum of F's (roughly), -22
    is for estimated length of foliage part when branch is flat
    lenF = lenF*(nBranch-iB+1)/nBranch;%scale lengths for height (growing
    from the bottom up); make to cm

    cmdT = axiom(i); %grab character to execute it's interpretation
    if sum(cmdT==['+' '-' '&' '^' '/' '\' '|'])>0
        %% Raw Turtle Interpretation (the engine)----- %%
        Rhp = [ cos(a) sin(a) 0; -sin(a) cos(a) 0; 0 0 0
1];%turn left-right matrix
        Rhm = [ cos(-a) sin(-a) 0; -sin(-a) cos(-a) 0; 0 0 0
1];
        Rlp = [ cos(a) 0 -sin(a) ;0 1 0; sin(a) 0
cos(a)]; %pitch up-down
        Rlm = [ cos(-a) 0 -sin(-a) ;0 1 0; sin(-a) 0
cos(-a)];
        Rup = [ 1 0 0; 0 cos(a) -sin(a) ; 0 sin(a) cos(a) ]
;%roll left/right
        Rum = [ 1 0 0; 0 cos(-a) -sin(-a) ; 0 sin(-a) cos(-a) ]
;
        Rbk = [ cos(pi) sin(pi) 0; -sin(pi) cos(pi) 0; 0 0 0
1]; %back up
    end

    switch cmdT
    case 'F'
        newxT = xT + lenF*hT(1);
        newyT = yT + lenF*hT(2);
        newzT = zT + lenF*hT(3);
        %
        line([xT newxT],[yT newyT],[zT newzT], 'color',[.5 .4 0],
'linewidth',2);
        verts{vN1,1} = [xT yT zT ; newxT newyT newzT];
        vN1 = vN1 +1;
        xT = newxT;
        yT = newyT;
        zT = newzT;
    case 'G'

```

```

newxT = xT + lenG*hT(1);
newyT = yT + lenG*hT(2);
newzT = zT + lenG*hT(3);
% line([xT newxT],[yT newyT],[zT newzT], 'color',[0 1 0],
'linewidth',2);
verts{vN2,2} = [xT yT zT ; newxT newyT newzT];
vN2 = vN2 +1;
xT = newxT;
yT = newyT;
zT = newzT;
case 'X'
newxT = xT + lenX*hT(1);
newyT = yT + lenX*hT(2);
newzT = zT + lenX*hT(3);
% line([xT newxT],[yT newyT],[zT newzT], 'color',[0 0 1],
'linewidth',2);
verts{vN3,3} = [xT yT zT ; newxT newyT newzT];
vN3 = vN3 +1;
xT = newxT;
yT = newyT;
zT = newzT;
case 'H'
newxT = xT + lenH*hT(1);
newyT = yT + lenH*hT(2);
newzT = zT + lenH*hT(3);
% line([xT newxT],[yT newyT],[zT newzT], 'color',[0 1 1],
'linewidth',2);
verts{vN4,2} = [xT yT zT ; newxT newyT newzT];
vN4 = vN4 +1;
xT = newxT;
yT = newyT;
zT = newzT;
case 'S'
newxT = xT + lenS*hT(1);
newyT = yT + lenS*hT(2);
newzT = zT + lenS*hT(3);
% line([xT newxT],[yT newyT],[zT newzT], 'color',[0 1 1],
'linewidth',2);
verts{vN5,3} = [xT yT zT ; newxT newyT newzT];
vN5 = vN5 +1;
xT = newxT;
yT = newyT;
zT = newzT;
case '+'
hT = hT * Rup;
case '-'
hT = hT * Rum;
case '&'
hT = hT * Rlp;
case '^'
hT = hT * Rlm;
case '\'
hT = hT * Rhp;
case '/'
hT = hT * Rhm;
case '|'
hT = hT * Rbk;

```

```

    case '[' %push the stack
        stack(stkPtr).xT = xT ;
        stack(stkPtr).yT = yT ;
        stack(stkPtr).zT = zT ;
        stack(stkPtr).hT = hT ;
        stkPtr = stkPtr +1 ;
    case ']' %pop the stack
        stkPtr = stkPtr -1 ;
        xT = stack(stkPtr).xT ;
        yT = stack(stkPtr).yT ;
        zT = stack(stkPtr).zT ;
        hT = stack(stkPtr).hT ;
    otherwise
        disp(['ERROR: unable to interpret string: ' cmdT])
    return
end
%drawnow
end
figure(1)
daspect([1 1 1])
view(-7,7)
box on
rotate3d on

%% swing and shift "branches" to final position ----- %%
rot_ang = rot_ang_old + (138 + rand*44 - 22)*pi/180;
rot_ang(rot_ang>2*pi) = rot_ang-2*pi;
count = 0;
ncheck = 9;
while min(abs(rot_log(max(1,iB-ncheck):max(1,iB-1))-
rot_ang))<180/min(iB,ncheck)*pi/180 && count<100
    rot_ang = rot_ang+rand*pi/2;
    rot_ang(rot_ang>2*pi) = rot_ang-2*pi;
    count = count + 1;
end
rot_log(iB) = rot_ang;
rot_ang_old = rot_ang;
% disp(num2str(count)) %find out how many retries
tilt_ang = (ang_dev + (100-35*(iB/nBranch)-35*(iB/nBranch).^6))*pi/180;
for i_col = 1:nRules
    branch_vector = reshape([verts{:,i_col}]',3,[]);
    branch_vector =
RotateVector(branch_vector,quaternion.angleaxis(tilt_ang,[0;-1;0])); %fold
down from vertical (angledown,vectoraround)
    branch_vector =
RotateVector(branch_vector,quaternion.angleaxis(rot_ang,[0;0;1])); %swing
around vertical axis [0;0;1] by some angle
    branch_vector(3,:) = branch_vector(3,:) + iB*spacing; % shift
"branch" up
    new_vector = reshape(branch_vector,[],2)';
    for iv = 1:length(new_vector)/3
        verts2{iv,i_col} = new_vector(:,3*iv-2:3*iv);
        vertsAll{iv,i_col,iB} = new_vector(:,3*iv-2:3*iv);
    end
end
end

```

```

end

%%% Plot in 3D with pipes ----- %%%
h = waitbar(0,'Plotting');
figure(2)
clf
daspect([1 1 1])
Nsides=8;
view(3);
box on
rotate3d on
for iB=1:nBranch
    waitbar(iB/nBranch,h)
    verts2 = vertsAll(:, :, iB);
    hs1=streamtube(verts2(:,1),2,[1,Nsides]); %primary branch
    set(hs1,'cdata',cat(3,.07*ones(2,Nsides+1),
    .07*ones(2,Nsides+1),zeros(2,Nsides+1)))

    hs2=streamtube(verts2(:,2),1,[1,Nsides]);
    set(hs2,'cdata',cat(3,.1*ones(2,Nsides+1),
    .1*ones(2,Nsides+1),zeros(2,Nsides+1)))

    hsS=streamtube(verts2(:,3),1,[1,Nsides]);
    set(hsS,'cdata',cat(3,zeros(2,Nsides+1),
    .6*ones(2,Nsides+1),zeros(2,Nsides+1)))
    if iB==nBranch %trunk
        hsT=streamtube([0, 0;0, 0;0, iB*spacing]',3,[1,Nsides]);
        set(hsT,'cdata',cat(3,.05*ones(2,Nsides+1),
    .05*ones(2,Nsides+1),0*ones(2,Nsides+1)))
    end
    % pause(.01) %use pause to see branches as placed.
end
axis tight
view(-37.5,30) % add light from default view (view(3))
camlight
lighting gouraud
shading interp
view(37.5,30) % add light from another direction
camlight
lighting gouraud
shading interp
view(0,90) % add light from another direction
camlight
lighting gouraud
shading interp
view(20,4) % choose final view angle

%%% Calculate Actual Mass, Diameter, Height, Volume, Bulk Density ----- %%%
Spec=3; %Third species is Juniper
a = [1.774758,2.171579,2.903705,2.956877];
b = [3.562158,4.450455,3.480897,3.037111];
mMin = [0.02585,0.025898,0.03472,0.031023];
mMax = [0.518337,0.404449,0.225163,0.228388];
m_dry = (betainv(rand(n_fuels,1),a(Spec),b(Spec))).*mMax(Spec);
xyz = ([vertsAll{:, :}])';
new_xyz = reshape(xyz,3,[]);
max_diam = max(max(new_xyz(1,:))-min(new_xyz(1,:)), max(new_xyz(2,:))...

```

```

    -min(new_xyz(2,:));
max_height = max(new_xyz(3,:));
Mdry = sum(m_dry);
dt = DelaunayTri(new_xyz'); %for density
[k,vol] = convexHull(dt); %for density
d_kg_m3 = (Mdry/1000)/(vol/100^3); %bulk density kg/m3
disp(['Actual/Target H: ' num2str(max_height) '/' num2str(height) ...
      ' D: ' num2str(max_diam) '/' num2str(diameter) ' Mdry: ' ...
      num2str(Mdry) '/' num2str(M_target) ' rho: ' num2str(d_kg_m3)])
close(h)

```


H. L-SYSTEMS FUEL PLACEMENT CODE FOR CHAMISE

This MATLAB code was used to generate chamise geometries discussed in Chapter 5.

```
% Generates 3-d, stochastic shrub with geometry similar to chamise.
% v1: +/- change theta, */! change phi
% v2: +/- change alpha, */! change beta
% v3: define size of arrays (saves memory and time); calculates volume
% v4: calculates bulk density
% v5: considers primary branch spacing (none overlapping); reorganized
%       code to have one big loop instead of several smaller ones;
%       strings specific to chamise added
% v6: graphs all points at once (faster); view to match picture for paper
% v7: splits all branches into 4-6 cm segments and assigns thicknesses;
%       number of primary branches calculated from correlations
% v8: uses different scripts
% v9: fewer primary branches, new correlations
% v10: fixes primary branch radius, plots segments in different colors
% Based on Prusinkiewicz, "The Algorithmic Beauty of Plants"
% Marianne Fletcher, March 2013

clear
close all

%% INPUTS
d_shrub = 140; % crown diameter (cm)
fuel_len = 4; % length of one fuel segment (cm)

plot_fig = 1; % Plot figure of shrub? 0=No; 1=Yes
save_fig = 0; % Save figure? 0=No; 1=Yes
plot_fuel = 1; % Plot figure of branch segments? 0=No; 1=Yes
save_fig2 = 0; % Save figure? 0=No; 1=Yes
filename = '04-24-d'; % Filename if figures are saved

% Color options
% Case 1: Fuel=green;           Non-fuel=brown;
% Case 2: Fuel=light green;    Non-fuel=dark green;
% Case 3: Different colors of green;
% Case 4: Black;
% Case 5: Fuel=orange;        Non-fuel=green
colors = 1;
%% VARIABLES
n = 3; % number of derivations

MC = .3;

% ANGLES (in radians)
```

```

max_angle = 77*pi/180; % average primary branch angle
st_dev(1) = 30*pi/180; % standard deviation for primary branch angle
delta = 30*pi/180; % average secondary/tertiary branch angle
st_dev(2) = 0*pi/180; % standard deviation for secondary/tertiary angle

% SCALE
scale = 0.45; % secondary length/primary length

% DISTANCES (cm)
shift = 13.1; % average distance of primary branches from center
dist = d_shrub/(2*sin(max_angle)); % primary branch length
st_dev(3) = 0; % standard deviation for primary branch length

% STRINGS
% Defines shape according to the following key:
% F one step forward
% + turn left by delta in x-plane
% - turn right by delta in x-plane
% * turn left by delta in y-plane
% ! turn right by delta in y-plane
% X location of rewriting
% NOTES ABOUT WRITING STRINGS:
% 'F's make up the main stem, and 'X's are the branches. So if the string
% were 'FFF', there would just be three straight lines connected
% end-to-end. However, 'X's do not connect end-to-end. The next segment
% after and 'X' starts at the same initial point as the 'X' rather than at
% the end point of the 'X' such as with an 'F'.
% The bottom line is:
% DO put +/-/!/ before 'X's
% DON'T put +/-/!/ before 'F's unless you want your branch to be bent
% If you are still confused, look at the document 'F vs. X' that should be
% in this same folder.
X1 = 'F+!XF+*X-*XFFF-!XXF';
X2 = 'F!X*-XF+*X!-XFFF+XX';
X3 = 'F-*X-!XFFF-XFF+*XXFF';
X4 = 'F-*XF+XFF+!X!XFF+*XX';
X5 = 'F!X+XFFF*X!-XFFFX';
% Counts numbers of X's and F's in strings.
X_f=zeros(5,1); X_x=zeros(5,1);
for i=1:5
    if i==1
        X=X1;
    elseif i==2
        X=X2;
    elseif i==3
        X=X3;
    elseif i==4
        X=X4;
    else
        X=X5;
    end
    for j=1:length(X)
        if X(j) == 'F'
            X_f(i,1)=X_f(i,1)+1;
        elseif X(j) == 'X'
            X_x(i,1)=X_x(i,1)+1;
        end
    end
end

```

```

end
end

%% NUMBER OF BRANCHES
height = (dist+dist*scale)/100; % approx. height (m)
fuel_weight = (0.286817639*exp(1.201245975*height))*1000; % total fuel weight
(gm)

% Predicts the fuel weights of each class based on the total fuel weight.
% The fuel classes are:
% 0 - 1/4"      "quart"
% 1/4" - 1/2"   "half"
% 1/2" - 1"     "one"
% 1" - 3"       "three"
fw_quart = (0.245570641*fuel_weight/1000+ 0.247667354)*1000; % (gm)
fw_half = (0.214064333*fuel_weight/1000-0.007333108)*1000; % (gm)
fw_one = (0.331204001*fuel_weight/1000-0.032277442)*1000; % (gm)
fw_three = (0.209161025*fuel_weight/1000-0.208056804)*1000; % (gm)
if fw_three < 0
    fw_three = 0;
end

thick_guess = mean(rand(10000,1).^(-1/2.612198509)-.45); % ave. thick from
distribution (mm)

% Dallan's correlation for fuel mass (gm).
m_quart = (-0.13575 + 0.136 * thick_guess + 0.127 * MC + 0.0178 *
fuel_len)/(1+MC);

% Mass of bigger stems, treated as cylinders (gm).
% density of chamise wood, 1.154 gm/cm^3, measured by Victoria Lansinger
2/7/13
m_half = 1.154 * pi * ((.635+1.27)/2*.5)^2 * fuel_len;
m_one = 1.154 * pi * ((1.27+2.54)/2*.7)^2 * fuel_len;
m_three = 1.154 * pi * (3.81/2)^2 * fuel_len;

% Estimated number in each class.
num_quart = round(fw_quart / m_quart);
num_half = round(fw_half / m_half);
num_one = round(fw_one / m_one);
num_three = round(fw_three / m_three);
num_total = num_quart+num_half+num_one+num_three;

% Percent of segments in each class.
quart = num_quart / num_total;
three = num_three / num_total;
half = num_half / num_total;

% Predicts total length of a primary branch (including lengths of all
% secondary and tertiary branches) and divides by fuel length to get the
% approximate number of segments per branch.
c=[-0.000119837 0.08202669 7.137025823 1110.252041];
fuel_branch=(c(1)*dist^3+c(2)*dist^2+c(3)*dist+c(4))/fuel_len;

% Number of primary branches
numb_branches = round(num_total/fuel_branch);

```

```

%% ARRAYS
% "Branch" refers to the full length of the branch
% "Segment" refers to the pieces of the branch that were cut up according
%   to the fuel length
x=zeros(1200,1); % x-coordinate of every branch
y=zeros(1200,1); % y-coordinate of every branch
z=zeros(1200,1); % z-coordinate of every branch
theta=zeros(1200,1);phi=zeros(1200,1); % 3-d angles of every branch
alpha=zeros(1200,1);beta=zeros(1200,1); %2-d angles of every branch
points=zeros(4000,6); % (x,y,z,phi,theta,length) of every segment

% Saves info before moving on the the next derivation
x_n=zeros(n,1);y_n=zeros(n,1);z_n=zeros(n,1);alpha_n=zeros(n,1);
beta_n=zeros(n,1);len_n=zeros(n,1);b_n=zeros(n,1);

dist_a=normrnd(dist,st_dev(3),numb_branches,n); % randomized distance

first_b=ones(1,2);count=0;countl=0;count_p=0; % counts place in arrays

%% PRIMARY BRANCHES
% SHIFT
% Assigns each primary branch a distance from the center of the shrub
shift_r = shift.*rand(numb_branches,1).^(1/3);
shift_x = shift_r*(1/sqrt(2));
shift_y = shift_r*(1/sqrt(2));

% LOCATIONS
% Dallan's code to assign phi and theta values.
branch_sections

%% GEOMETRY
for A = 1:numb_branches
    %% PART A: Sets up parameters for primary branches.
    % Initial coordinates and angles
    x(count+1) = shift_x(A); y(count+1) = shift_y(A); z(count+1) = 0;
    theta(count+1) = theta_primary(A); phi(count+1) = phi_primary(A);
    % Convert theta and phi to alpha and beta
    x0 = sin(phi(count+1))*cos(theta(count+1));
    y0 = sin(phi(count+1))*sin(theta(count+1));
    z0 = cos(phi(count+1));
    alpha(countl+1) = atan2(x0,z0);
    beta(countl+1) = atan2(y0,z0);

    % Last angle of current derivation
    alpha_n(1) = alpha(countl+1); beta_n(1) = beta(countl+1);
    countl = countl+1;

    choose_X = rand(1,n); % random string for each derivation
    count = count+1; % counts # of points in array
    n_current = 1; % current derivation number
    b = 1; % place in string
    turn = 0; % counts # of +/-/*!! in string
    loop = 1; % runs a continuous loop (until break)

    while loop > 0
        %% PART B: Generates the primary branch.

```

```

% String for current derivation
if choose_X(n_current) <= (1/5)
    X = X1;
    nmb_f = X_f(1); % number of 'F's in string
    nmb_x = X_x(1); % number of X's in string
elseif choose_X(n_current) <= (2/5)
    X = X2;
    nmb_f = X_f(2);
    nmb_x = X_x(2);
elseif choose_X(n_current) <= (3/5)
    X = X3;
    nmb_f = X_f(3);
    nmb_x = X_x(2);
elseif choose_X(n_current) <= (4/5)
    X = X4;
    nmb_f = X_f(4);
    nmb_x = X_x(2);
else
    X = X5;
    nmb_f = X_f(5);
    nmb_x = X_x(2);
end

% Randomizes strings for second and third derivations.
if n_current==2 && b>length(X)
    choose_X(n_current)=rand(1);
elseif n_current==3 && b>length(X)
    choose_X(n_current)=rand(1);
end

% Length of next step. This length is divided by the number of 'F's
% in the string (nmb_f), so the TOTAL LENGTH OF THE BRANCH DOES
% NOT CHANGE WITH THE LENGTH OF THE STRING.
dist_n = dist_a(A,n_current)/nmb_f*scale^(n_current-1);

if b <= length(X) % if all commands in string have not been
completed
    if X(b) == 'F' % one step forward
        % Converts alpha and beta to theta and phi
        x0 = sin(alpha(count1));
        if abs(alpha(count1)) > pi/2
            z0 = -sqrt(1-(sin(alpha(count1))^2));
        else
            z0 = sqrt(1-(sin(alpha(count1))^2));
        end
        y0 = z0*tan(beta(count1));
        r = sqrt(x0^2+y0^2+z0^2);
        phi(count+1) = acos(z0/r);
        theta(count+1) = atan2(y0,x0);
        % Next (x,y,z) coordinate using phi and theta from above
        x(count+1) =
x(count)+dist_n*cos(theta(count+1))*sin(phi(count+1));
        y(count+1) =
y(count)+dist_n*sin(theta(count+1))*sin(phi(count+1));
        z(count+1) = z(count)+dist_n*cos(phi(count+1));
        count = count+1; % # of elements in array
        b = b+1; % current step in string
    end
end

```

```

        % Separates branch into segments of length "fuel_len"
        num_segs = round(dist_n/fuel_len); % number of segments on
branch
        seg = zeros(num_segs,3); % (x,y,z) of each segment
        seg(1,:) = [x(count-1),y(count-1),z(count-1)]; % starting
point (initial point of branch)
        for i = 1 : num_segs - 1
            seg(i+1,1) =
seg(i,1)+fuel_len*cos(theta(count))*sin(phi(count)); % x
            seg(i+1,2) =
seg(i,2)+fuel_len*sin(theta(count))*sin(phi(count)); % y
            seg(i+1,3) = seg(i,3)+fuel_len*cos(phi(count)); % z
            % Puts all information into a single matrix
            points(count_p+1,1) = seg(i+1,1); % x
            points(count_p+1,2) = seg(i+1,2); % y
            points(count_p+1,3) = seg(i+1,3); % z
            points(count_p+1,4) = phi(count); % angles
            points(count_p+1,5) = theta(count);
            points(count_p+1,6) = fuel_len; % length
            count_p=count_p+1; % counts number of points in array
        end
        % Final point (end point of branch)
        points(count_p+1,1) = x(count);
        points(count_p+1,2) = y(count);
        points(count_p+1,3) = z(count);
        points(count_p+1,4) = phi(count);
        points(count_p+1,5) = theta(count);
        points(count_p+1,6) = (x(count)-
seg(end,1))/(cos(theta(count))*sin(phi(count))); %length
        count_p = count_p+1;
        elseif X(b) == '+' % left in x-plane
            alpha(count1+1) = alpha(count1)-normrnd(delta,st_dev(2),1,1);
            beta(count1+1) = beta(count1);
            b = b+1; count1 = count1+1;
            turn = turn+1; % # of +/-/*!!
        elseif X(b) == '-' % left in x-plane
            alpha(count1+1) = alpha(count1)+normrnd(delta,st_dev(2),1,1);
            beta(count1+1) = beta(count1);
            b = b+1; count1 = count1+1;
            turn = turn+1;
        elseif X(b) == '*' % right in y-plane
            alpha(count1+1) = alpha(count1);
            beta(count1+1) = beta(count1)-normrnd(delta,st_dev(2),1,1);
            b=b+1; count1=count1+1;
            turn=turn+1;
        elseif X(b)=='!' % left in y-plane
            alpha(count1+1) = alpha(count1);
            beta(count1+1) = beta(count1)+normrnd(delta,st_dev(2),1,1);
            b = b+1; count1 = count1+1;
            turn = turn+1;
        elseif X(b) == 'X'
            %% PART C: 'X' Command.
            if n_current < n % for all but last derivation
                % Saves current coordinates, angles, length of string,
and place in string.
                b n(n_current) = b; % place in string

```

```

x_n(n_current) = x(count); % x-coordinate
y_n(n_current) = y(count); % y-coordinate
z_n(n_current) = z(count); % z-coordinate
alpha_n(n_current) = alpha(count1-turn); % x-angle
beta_n(n_current) = beta(count1-turn); % y-angle
len_n(n_current) = length(X); %length of current string
n_current = n_current+1; % move to next derivation
b = 1; % starts at the beginning of the string
turn = 0; first_b(n_current-1) = count;
else % last derivation (does not rewrite)

% Randomizes segment lengths for last derivation
dist_n = dist_n*(1+(3-1).*rand(1));

% Treats 'X' essentially as an 'F'
% Converts alpha and beta to theta and phi
% See Amelia Rapp's Lab book p. 38 or "Angles.docx"
x0 = sin(alpha(count1)); % x-z plane
if abs(alpha(count1)) > pi/2
    z0 = -sqrt(1-(sin(alpha(count1))^2));
else
    z0 = sqrt(1-(sin(alpha(count1))^2));
end
y0 = z0*tan(beta(count1));
r = sqrt(x0^2+y0^2+z0^2);
phi(count+1) = acos(z0/r);
theta(count+1) = atan2(y0,x0);
% Next (x,y,z) coordinate using theta and phi above
x(count+1) = real(x(count)+dist_n*cos(theta(count+1))...
    *sin(phi(count+1)));
y(count+1) = real(y(count)+dist_n*sin(theta(count+1))....
    *sin(phi(count+1)));
z(count+1) = real(z(count)+dist_n*cos(phi(count+1)));
count = count+1; % # of elements in array
b = b+1; % place in string
% Separates branch into segments ('leaves')
num_segs = round(dist_n/fuel_len);
if dist_n/fuel_len < 1
    num_segs = 1;
    fuel_dist=dist_n;
else
    fuel_dist=fuel_len;
end
seg = zeros(num_segs,3);
seg(1,:) = [x(count-1),y(count-1),z(count-1)];
for i = 1:num_segs-1
    seg(i+1,1) =
real(seg(i,1)+fuel_dist*cos(theta(count))...
    *sin(phi(count)));
    seg(i+1,2) =
real(seg(i,2)+fuel_dist*sin(theta(count))...
    *sin(phi(count)));
    seg(i+1,3) =
real(seg(i,3)+fuel_dist*cos(phi(count)));
    points(count_p+1,1) =
seg(i+1,1);%(step(i,1)+step(i+1,1))/2; %#ok<*SAGROW>
    points(count_p+1,2) =

```

```

seg(i+1,2);%(step(i,2)+step(i+1,2))/2;
    points(count_p+1,3) =
seg(i+1,3);%(step(i,3)+step(i+1,3))/2;
    points(count_p+1,4) = phi(count);
    points(count_p+1,5) = theta(count);
    points(count_p+1,6) = fuel_dist;
    count_p=count_p+1;
end
points(count_p+1,1) = x(count);
points(count_p+1,2) = y(count);
points(count_p+1,3) = z(count);
points(count_p+1,4) = phi(count);
points(count_p+1,5) = theta(count);
points(count_p+1,6) = real((x(count)-
seg(end,1))/(cos(theta(count))*sin(phi(count)))));%fuel_dist;
count_p = count_p+1;

% Back track to continue with the next part of the code
x(count+1) = x(count-1);
y(count+1) = y(count-1);
z(count+1) = z(count-1);
alpha(count+1) = alpha(count-1);
beta(count+1) = beta(count-1);
theta(count+1) = theta(count-1);
phi(count+1) = phi(count-1);
turn = 0; count = count+1; count1 = count+1; %b=b+1;
end
else % for anything else in the string (spaces, brackets, etc.)
    b = b+1; % moves on to the next command, not infinite loop
end
else % if current derivation is complete
    if n_current > 1 && b_n(n_current-1)+1 <= len_n(n_current-1)
        % If it's not the first derivation and if all the commands
        % in the string of the previous derivation are not done.

        % Reload previously saved point to continue
        b = b_n(n_current-1)+1; % place in string
        n_current = n_current-1; % derivation
        x(count+1) = x(first_b(n_current)); % x-coordinate
        y(count+1) = y(first_b(n_current)); % y-coordinate
        z(count+1) = z(first_b(n_current)); % z-coordinate
        theta(count+1) = theta(first_b(n_current)); % angles
        phi(count+1) = phi(first_b(n_current));
        alpha(count+1) = alpha_n(n_current);
        beta(count+1) = beta_n(n_current);
        count = count+1; count1 = count+1;
        first_b(n_current) = count;
    else
        % If it has completed the first derivation or if all the
        % commands in the string of the previous derivation are
        % done.

        % The current derivation number keeps decreasing until
        % there is either a derivation that has not been completed
        % or until all of the derivations have been checked. If
        % all of the derivations are done, then the loop breaks
        % and the code continues done below.
    end
end

```

```

n_current = n_current-2; % tries the next lowest derivation
if n_current <= 0
    break
end

% Checks to see if all the commands in the string are
% completed.
b = b_n(n_current)+1;
while b > len_n(n_current)
    n_current = n_current-1;
    if n_current == 0
        break
    end
    b = b_n(n_current)+1;
end
if n_current == 0
    break
end

% If the code hasn't reached a break by this point, there
% is at least one derivation that isn't done yet, so it
% starts on that derivation where it left off.
x(count+1) = x_n(n_current); % x-coordinate
y(count+1) = y_n(n_current); % y-coordinate
z(count+1) = z_n(n_current); % z-coordinate
alpha(count+1) = alpha_n(n_current); % angles
beta(count+1) = beta_n(n_current);
count = count+1; count1 = count1+1;

end
continue
end
end
% Output progress
if round(A/10)*10 == A || A == numb_branches
    clc
    ['Completed primary branch ' num2str(A) ' of '
num2str(numb_branches)] %#ok<NOPTS>
end
end

%% LEAVES
% MASS, THICKNESS, AND WIDTH
nmb_leaves = count_p;

points = points(1:nmb_leaves,:); % deletes any empty rows
Leaf_thickness = zeros(nmb_leaves,1);
Leaf_width = zeros(nmb_leaves,1);
Leaf_Mass = zeros(nmb_leaves,1);

% Experimentally measured thickness max and min
max_thick = 3*2.54; min_thick = .03; % (cm)

% Sorts leaf properties according to distance from origin
leaf_r=sqrt(points(:,1).^2+points(:,2).^2+points(:,3).^2); % distance from
origin
height_decide=sortrows([leaf_r points],-1); % sorts according to radius
% All leaf coordinates, sorted by distance from origin

```

```

leaf_x=height_decide(:,2); % x-coordinate
leaf_y=height_decide(:,3); % y-coordinate
leaf_z=height_decide(:,4); % z-coordinate
leaf_angles=height_decide(:,5:6); % angles
leaf_len=height_decide(:,7); % lengths (cm)

% Percentages in each class were determined above. Specific number in each
% class determined by multiplying the percentage by the number of leaves.
quart = round(quart * nmb_leaves);
half = round(half * nmb_leaves);
three = round(three * nmb_leaves);
one = count_p - quart - half - three;

% Assigns thicknesses to each class.
Leaf_thickness(1:quart) = (rand(quart,1).^(-1/2.612198509)-.45); % (mm)
Leaf_thickness(quart+1:quart+half) = 0.635+(1.27-0.635).*rand(half,1).^2;
Leaf_thickness(half+quart+1:half+quart+one) = 1.27+(2.54-1.27).*rand(one,1);
Leaf_thickness(one+half+quart+1:one+half+quart+three) = 2.54+(max_thick-
2.54).*rand(three,1);

Alpha_Leaf_Mass = 0.0116;
Beta_Leaf_Mass = 0.1444;
A1 = 2.5;
A2 = 2;
for i=1:quart
    Leaf_width(i) = Leaf_thickness(i);
    %Dallan's Correlation: Leaf Mass (gm) = a + b * thickness(mm) + c *
MC(decimal) + d * length(cm)
    Leaf_Mass(i) = (-0.13575 + 0.136 * Leaf_thickness(i) + 0.127 * MC +
0.0178 * leaf_len(i))/(1+MC); % g
end
tot_quart=sum(Leaf_Mass); % total dry mass of burnable fuel (< 1/4")

% Bigger stems treated as cylinders
for i=quart+1:length(Leaf_thickness)
    Leaf_Mass(i) = 1.154 * pi * (Leaf_thickness(i) / 2) ^ 2 * leaf_len(i);
end

bush_mass=sum(Leaf_Mass);

% VOLUME
% Splits into 100 boxes in z-direction and adds volume
height_cut=max(leaf_z)/100; % height of each of the 100 boxes
volume=0;
min_x_temp=max(leaf_x); max_x_temp=min(leaf_x);
min_y_temp=max(leaf_y); max_y_temp=min(leaf_y);
for i=1:100
    min_z_temp=height_cut*(i-1); % bottom of current box
    max_z_temp=height_cut*i; % top of current box
    for j=1:nmb_leaves
        % Checks which segments are within the current box, and finds the
        % max/min of x and y.
        if leaf_z(j) >= min_z_temp && leaf_z(j) < max_z_temp
            if leaf_x(j) > max_x_temp
                max_x_temp = leaf_x(j);
            end
            if leaf_x(j) < min_x_temp

```

```

        min_x_temp = leaf_x(j);
    end
    if leaf_y(j) > max_y_temp
        max_y_temp = leaf_y(j);
    end
    if leaf_y(j) < min_y_temp
        min_y_temp = leaf_y(j);
    end
end
end
volume=volume+((max_x_temp-min_x_temp)*(max_y_temp-min_y_temp)*...
    (max_z_temp-min_z_temp));
max_x_temp = min(leaf_x);
min_x_temp = max(leaf_x);
max_y_temp = min(leaf_y);
min_y_temp = max(leaf_y);
end

% BULK DENSITY
bulk_density=bush_mass/volume;
bulk_density_kg=bulk_density/1000*100^3;
['Predicted: ' num2str(fw_quart) ' g; Actual: ' num2str(tot_quart) '
g.']*#ok<NOPTS>

%% PLOT
% Defines colors for plots.
if plot_fig == 1

    %COLORS
    switch colors
        case 1 % fuel=green; non-fuel=brown;
            fuel_color = 1/255 * [0 128 0];
            branch_color = 1/255 * [102 51 0];
        case 2 % fuel=light green; non-fuel=dark green;
            fuel_color = 1/255 * [0 255 0];
            branch_color = 1/255 * [0 96 0];
        case 3 % different colors of green;
            fuel_color = 1/255 * [104 137 59];
            fuel_color1 = 1/255 * [99 168 74];
            fuel_color2 = 1/255 * [82 120 72];
            branch_color = 1/255 * [86 91 51];
        case 4 % black
            fuel_color = [0 0 0];
            branch_color = fuel_color;
        case 5 % fuel=orange; non-fuel=green;
            fuel_color = 1/255 * [255 153 51];
            branch_color = [0 128 0];
    end

    figure
    hold on
    axis equal
    grid on

    %Plotting matrices: the first column in the initial point;
    % the second column is the end point
    a=1; b=quart;

```

```

    plotx1=[leaf_x(a:b) leaf_x(a:b)-
leaf_len(a:b).*cos(leaf_angles(a:b,2)).*sin(leaf_angles(a:b,1))];
    ploty1=[leaf_y(a:b) leaf_y(a:b)-
leaf_len(a:b).*sin(leaf_angles(a:b,2)).*sin(leaf_angles(a:b,1))];
    plotz1=[leaf_z(a:b) leaf_z(a:b)-leaf_len(a:b).*cos(leaf_angles(a:b,1))];

    a=quart+1; b=count_p;
    plotx=[leaf_x(a:b) leaf_x(a:b)-
leaf_len(a:b).*cos(leaf_angles(a:b,2)).*sin(leaf_angles(a:b,1))];
    ploty=[leaf_y(a:b) leaf_y(a:b)-
leaf_len(a:b).*sin(leaf_angles(a:b,2)).*sin(leaf_angles(a:b,1))];
    plotz=[leaf_z(a:b) leaf_z(a:b)-leaf_len(a:b).*cos(leaf_angles(a:b,1))];

    if colors == 3
        fc=randi(3,quart,1); % assigns random number to every fuel element
        color=sortrows([fc plotx1 ploty1 plotz1],-1); % sorts leaves by
random number
        % Splits fuel elements into three groups and plots those in
        % different colors.
        a=1; b=round(quart/3);

plot3(color(a:b,2:3)',color(a:b,4:5)',color(a:b,6:7)', 'Color',fuel_color,'lin
ewidth',1)
        a=b+1; b=round(quart*2/3);

plot3(color(a:b,2:3)',color(a:b,4:5)',color(a:b,6:7)', 'Color',fuel_color1,'li
newidth',1)
        a=b+1; b=quart;

plot3(color(a:b,2:3)',color(a:b,4:5)',color(a:b,6:7)', 'Color',fuel_color2,'li
newidth',1)
        plot3(plotx',ploty',plotz', 'Color',branch_color,'linewidth',1) %
segments > 1/4"
    else
        cmap = [fuel_color; branch_color];
        colormap(cmap);
        plot3(plotx1',ploty1',plotz1', 'Color',fuel_color,'LineWidth',1)
        plot3(plotx',ploty',plotz', 'Color',branch_color,'LineWidth',1)
    end

    xlim([-d_shrub/2-20 d_shrub/2])
    ylim([-d_shrub/2-30 20+d_shrub/2])
    zlim([0 height*100])

    camorbit(10,-80,'data')
    camorbit(90,0,'data')

    set(gca,'FontName','Times New Roman')
    set(gca,'FontSize',25)

    if save_fig == 1
        saveas(gcf,[filename '.jpg']);
%         saveas(gcf,filename,'tif')
        close
    end
end

```

```

% PLOT 2
if plot_fuel == 1
    figure
    hold on
    grid on
    axis equal
    red=[1 0 0];
    yellow=[1 1 0];
    green=[.0980 .5922 .1804];
    blue=[0 0 1];
    purple=[153/255 0 204/255];
    red_points=[leaf_x(1:quart) leaf_y(1:quart) leaf_z(1:quart)];
    yellow_points=[leaf_x(quart+1:quart+half) leaf_y(quart+1:quart+half)
leaf_z(quart+1:quart+half)];%zeros(nmb_leaves,3);
    green_points=[leaf_x(quart+half+1:quart+half+one)
leaf_y(quart+half+1:quart+half+one)
leaf_z(quart+half+1:quart+half+one)];%zeros(nmb_leaves,3);
    blue_points=[leaf_x(quart+half+one+1:quart+half+one+three)
leaf_y(quart+half+one+1:quart+half+one+three)
leaf_z(quart+half+one+1:quart+half+one+three)];%zeros(nmb_leaves,3);

plot3(red_points(:,1),red_points(:,2),red_points(:,3),'.','Color',red,'Marker
Size',5)

plot3(yellow_points(:,1),yellow_points(:,2),yellow_points(:,3),'.','Color',ye
llow,'MarkerSize',8)

plot3(green_points(:,1),green_points(:,2),green_points(:,3),'.','Color',green
,'MarkerSize',8)

plot3(blue_points(:,1),blue_points(:,2),blue_points(:,3),'.','Color',blue,'Ma
rkerSize',8)

    xlim([-d_shrub/2-20 d_shrub/2])
    ylim([-d_shrub/2-30 20+d_shrub/2])
    zlim([0 height*100])

    camorbit(10,-80,'data')
    camorbit(90,0,'data')

    set(gca,'FontName','TimesNew Roman')
    set(gca,'FontSize',25)

    if save_fig2 == 1
        saveas(gcf,['filename 'dot.jpg']);
        close
    end
end
end

```